OAK RIDGE
NATIONAL LABORATORY

MANAGED BY UT-BATTELLE
FOR THE DEPARTMENT OF ENERGY

Energy and Transportation Science Division

Oak Ridge National Laboratory Annual Progress Report for the Power Electronics and Electric Machinery Program

Mitch Olszewski, Program Manager

October 2011

UT-BATTELLE

ORNL-27 (4-00)

FY 2011

Oak Ridge National Laboratory
Annual Progress Report
for the Power Electronics
and Electric Machinery Program

Prepared by:

Oak Ridge National Laboratory

Mitch Olszewski, Program Manager

Submitted to:

Energy Efficiency and Renewable Energy
Vehicle Technologies Program

Susan A. Rogers, Technology Development Manager

October 2011

Contents

Acronyms and Abbreviations

2D	two dimensional
3D	three dimensional
ac	alternating current
Adc	amps direct current
APEEM	Advanced Power Electronics and Electric Motors (program, DOE)
AT	automatic transmission
bcc	body centered cubic
BIC	best-in-class
BNC	Bayonet-Neill-Concelman (connector)
CAN	controller area network
Cdg	drain-to-gate capacitance
Cds	drain-to-source capacitance
CF-trans-qZSI	current-fed trans-quasi-ZSI
CF-trans-ZSI	current-fed trans-ZSI
CSI	current source inverter
DBA	direct bonded aluminum
DBC	direct bonded copper
dc	direct current
DOE	U.S. Department of Energy
DPT	double pulse tester/testing
DUT	device under test
EDX	energy dispersive x-ray spectroscopy
EETT	Electrical and Electronics Technical Team (U.S. Drive)
EM	electric motor
emf	electromotive force
EMI	electromagnetic interference
ESC	electro-slag casting
ESL	equivalent series inductance
ESR	equivalent series resistance
EV	electric vehicle
FE	finite element
FEA	finite element analysis
GOSS	grain oriented silicon steel
GUI	graphical user interface
HEV	hybrid electric vehicle
HSG	hybrid starter-generator
ID	inner diameter

IGBT	insulated gate bipolar transistor
IMFP	isolated multiple flux path
IMMD	integrated modular motor drive
INV/CONV	inverter/converter
IPM	interior permanent magnet
JBS	junction barrier Schottky
Lp	parasitic inductance
MEC	magnetic equivalent circuit
M/G	motor/generator
mmf	magnetomotive force
MOSFET	metal-oxide semiconductor field-effect transistor
NFC	novel flux coupling
NIH	number-in-hand
Nm	Newton meter
OD	outer diameter
ORNL	Oak Ridge National Laboratory
PCU	power control unit
PD	power density (peak)
PE	power electronics
PEEM	Power Electronics and Electric Machines (subprogram, ORNL)
PEM	power electronics module
PEPL	Power Electronics Packaging Laboratory (ORNL)
PEV	plug-in electric vehicle
PF	power factor
PFC	power factor correction
PID	proportional-integral-derivative
PM	permanent magnet
PMSM	permanent magnet synchronous motor
PWM	pulse width modulated/modulation
R&D	research and development
R-L	inductor-resistor
RB	reverse-blocking
regen	regenerative braking
rms	root mean square
Rp	parasitic resistance
SF	specific force
SOA	state of the art
SJT	super junction transistor

SP	specific power (peak)
SPICE	Simulation Program with Integrated Circuit Emphasis
SPM	surface permanent magnet
SR	switched reluctance
SRM	switched reluctance motor
TC	thermal conductivity
THD	total harmonic distortion
Tj	junction temperature
Tjmax	maximum junction temperature
TMC	Toyota Motor Company
TSDPSR	total switching device power stress ratio
U.S. DRIVE	Driving Research and Innovation for Vehicle efficiency and Energy sustainability (cooperative research effort between DOE and industry partners)
UW	University of Wisconsin
V2G	vehicle-to-grid
Vac	volts of alternating current
Vdc	volts of direct current (operating voltage)
Vds	drain-to-source voltage
Vgs	gate-to-source voltage
VSATT	Vehicle Systems Analysis Technical Team (U.S. Drive)
VSI	voltage source inverter
VTP	Vehicle Technologies Program (DOE)
WBG	wide bandgap
WEG	water-ethylene glycol
ZCSI	Z-source current source inverter
ZSI	Z-source inverter

1. Introduction

The U.S. Department of Energy (DOE) announced in May 2011 a new cooperative research effort comprising DOE, the U.S. Council for Automotive Research (composed of automakers Ford Motor Company, General Motors Company, and Chrysler Group), Tesla Motors, and representatives of the electric utility and petroleum industries. Known as U.S. DRIVE (Driving Research and Innovation for Vehicle efficiency and Energy sustainability), it represents DOE's commitment to developing public-private partnerships to fund high risk–high reward research into advanced automotive technologies. The new partnership replaces and builds upon the partnership known as FreedomCAR (derived from "Freedom" and "Cooperative Automotive Research") that ran from 2002 through 2010 and the Partnership for a New Generation of Vehicles initiative that ran from 1993 through 2001.

The Oak Ridge National Laboratory's (ORNL's) Power Electronics and Electric Machines (PEEM) subprogram within the DOE Vehicle Technologies Program (VTP) provides support and guidance for many cutting-edge automotive technologies now under development. Research is focused on developing revolutionary new power electronics (PE), electric motor (EM), and traction drive system technologies that will leapfrog current on-the-road technologies. The research and development (R&D) is also aimed at achieving a greater understanding of and improvements in the way the various new components of tomorrow's automobiles will function as a unified system to improve fuel efficiency.

In supporting the development of advanced vehicle propulsion systems, the PEEM subprogram has enabled the development of technologies that will significantly improve efficiency, costs, and fuel economy.

The PEEM subprogram supports the efforts of the U.S. DRIVE partnership through a three phase approach intended to

- identify overall propulsion and vehicle related needs by analyzing programmatic goals and reviewing industry's recommendations and requirements and then develop the appropriate technical targets for systems, subsystems, and component R&D activities;
- develop and validate individual subsystems and components, including EMs and PE; and
- determine how well the components and subsystems work together in a vehicle environment or as a complete propulsion system and whether the efficiency and performance targets at the vehicle level have been achieved.

The research performed under this subprogram will help remove technical and cost barriers to enable the development of technology for use in such advanced vehicles as hybrid electric vehicles (HEVs), plug-in HEVs (PHEVs), battery electric vehicles, and fuel-cell-powered automobiles that meet the goals of the VTP.

A key element in making these advanced vehicles practical is providing an affordable electric traction drive system. This will require attaining weight, volume, efficiency, and cost targets for the PE and EM subsystems of the traction drive system. Areas of development include

- novel traction motor designs that result in increased power density and lower cost;
- inverter technologies involving new topologies to achieve higher efficiency with the ability to accommodate higher temperature environments while achieving high reliability;
- converter concepts that use methods of reducing the component count and integrating functionality to decrease size, weight, and cost;
- new onboard battery charging concepts that result in decreased cost and size;

- more effective thermal control through innovative packaging technologies; and
- integrated motor-inverter traction drive system concepts.

ORNL's PEEM research program conducts fundamental research, evaluates hardware, and assists in the technical direction of the VTP Advanced Power Electronics and Electric Motors (APEEM) program. In this role, ORNL serves on the U.S. DRIVE Electrical and Electronics Technical Team, evaluates proposals for DOE, and lends its technological expertise to the direction of projects and evaluation of developing technologies. ORNL also executes specific projects for DOE.

DOE's continuing R&D into advanced vehicle technologies for transportation offers the possibility of reducing the nation's dependence on foreign oil and the negative economic impacts of crude oil price fluctuations. It also supports the Administration's goal of deploying 1 million PHEVs by 2015.

Highlights

Task 2: Power Electronics Research and Technology Development

Task 2.1   Wide Bandgap Materials

- Acquired, tested, and characterized SiC metal-oxide semiconductor field-effect transistors (MOSFETs), super junction transistor switches, and junction barrier Schottky diodes both dynamically and statically over expanded temperature ranges.
- Optimized a traction drive model for use in determining the benefit of wide bandgap devices for automotive applications.
- Developed a SPICE[*] model for a 1,200 V, 33 A, SiC MOSFET for use in packaging efforts.

Task 2.2   Power Device Packaging

- Designed an integrated planar package power module structure featuring double sided planar interconnections and integrated cooling that offers cost reductions of 30% or more compared to state-of-the-art packages.
- Fabricated a 1,200 V, 200 A, phase leg using the new module, and completed thermal and electrical characterization.
- Developed a simulation program to comprehensively evaluate power module technologies.
- Established a thermal performance test station.
- Benchmarked four state-of-the-art power device packaging technologies.
- Manufactured four different types of power modules for other APEEM projects.

Task 2.3   Converter Topologies for Wired and Wireless Battery Chargers

- Wired charger
  — Developed a new approach that uses the onboard PE components to reduce the cost, weight, and volume of onboard chargers; accomplish galvanic isolation; and accommodate a wide range of battery voltages.
  — Completed a converter design for a 5 kW integrated wired charger with an estimated cost reduction of 80% compared to a stand-alone onboard battery charger.
- Wireless charger
  — Developed two converter topologies with reduced switch count and passive component requirements. Simulation results proved the concepts.

---

[*] Simulation Program with Integrated Circuit Emphasis.

Task 2.4 Inverter using Current Source Topology

- Completed a design for a 10 kW Z-source current source inverter based on the current-fed trans-quasi Z-source inverter using first generation reverse-blocking–insulated gate bipolar transistor (IGBT) technology. The design yields a specific power of 4.85 kW/kg, a power density of 14.2 kW/L, and efficiency of 97.7% in boost mode and 97.1% in buck mode.
- Test results with a 10 kW prototype demonstrate
  — capacitance reduction to 80 μF [200 μF for a voltage source inverter (VSI)],
  — output voltage capability range from 0–3 times the battery voltage (0–0.99× for a VSI),
  — output voltage total harmonic distortion of 6%−12 % (70%−200% for a VSI), and
  — high efficiency (more than 97% even at a relatively low source voltage of 250 V).

Task 2.5 A Segmented Drive System with a Small dc Bus Capacitor

- Demonstrated a 55 kW segmented inverter prototype with a 60% reduction of dc bus capacitance compared to a standard VSI.
- Tested prototype with both carrier based and space vector based pulse width modulation control methods to show
  — 55% to 75% reduction in capacitor ripple current,
  — 70% to 90% reduction in battery ripple current, and
  — 60% to 80% reduction in motor ripple current.
- Completed design and fabrication of a ring-shaped 55 kW segmented inverter that is suitable for integration with a motor.

Task 3: Electric Machinery Research and Technology Development

Task 3.1 A New Class of Switched Reluctance Motors without Permanent Magnets

- Developed, fabricated, and tested an unconventional switched reluctance machine design.
- Developed custom design software.
- Developed iterative self-learning pseudo-flux observer-based control algorithm capable of tracking/producing abstract current waveforms, which is essential for torque ripple control.
- Tested machine up to 5,000 rpm.

Task 3.2 Novel Flux Coupling Machine without Permanent Magnets

- Machined prototype motor parts; fabricated and assembled the motor.
- Completed locked rotor test on the prototype. It confirmed that the concept is workable. The full testing will be completed during FY 2012 due to scheduling issues with the Dyne cells in FY 2011.
- Completed studies on the issues with power factor performance of interior permanent magnet (IPM) motors.

Task 3.3 Motor Packaging with Consideration of Electromagnetic and Material Characteristics

- Analyzed ORNL benchmarking data on the 2010 Prius IPM, and extracted key parameters for development of an electrical equivalent d-q axis circuit model.
- Developed a computer model for the lamination material reluctivity to be used in magnetic equivalent circuit model and simulation.
- Developed baseline IPM technology trajectory.
- Developed a thermal model of the baseline IPM, and validated it against ORNL benchmarking data. The thermal model provides ORNL researchers a finite element analytical model for predicting IPM copper, lamination iron, and rotor magnet dissipation mechanisms.

Task 4: Systems Research and Technology Development

Task 4.1   Benchmarking of Competitive Technologies

- Conducted design/packaging studies of the 2011 Hyundai Sonata power converter unit, hybrid starter-generator, and primary motor.
- Assessed mass, volume, power density, and specific power of various hybrid system subsystems.
- Evaluated efficiency, performance, and other operational characteristics of the 2011 Sonata subsystems.

Task 4.2   High Power Density Integrated Traction Machine Drive

- Designed, built, and tested a 10 kW, six phase, 10-pole permanent magnet (PM) machine.
- Developed a modular integrated modular motor drive (IMMD) power converter that conforms to the dimensions of the 10 kW concept demo PM machine, providing a testbed for implementing the IMMD distributed control software.
- Tested ruggedness of selected IGBT at various temperatures, concluding that the device has good latch-up immunity and adequate short circuit capability for operation at 200°C.
- Designed and fabricated a 10 kW phase leg power module, and tested its electrical and thermal characteristics up to 200°C.
- Designed the gate driver boards and main board for the IGBT phase leg modules.

Task 4.3   Integration of Novel Flux Coupling Motor and Current Source Inverter

- Validated the concept of the integration of the novel flux coupling motor and the current source inverter through laboratory tests.
- Studied methods to increase the efficiency of the system.

Looking Forward

The following reports provide a detailed description of ORNL APEEM activities and technical accomplishments during FY 2011. Numerous project reviews, technical reports, and papers have been published for these efforts, and they are indicated at the end of each section for readers interested in pursuing details of the work. In collaboration with industry, universities, and national laboratories, ORNL continues to develop advanced PE and EM technologies for the next generation of automotive vehicles.

2.   Power Electronics Research and Technology Development

2.1   Wide Bandgap Materials

Principal Investigator: Madhu Sudhan Chinthavali
Oak Ridge National Laboratory
National Transportation Research Center
2360 Cherahala Boulevard
Knoxville, TN 37932
Voice: 865-946-1411; Fax: 865-946-1262; E-mail: chinthavalim@ornl.gov

DOE Technology Development Manager: Susan A. Rogers
Voice: 202-586-8997; Fax: 202-586-1600; E-mail: Susan.Rogers@ee.doe.gov

ORNL Program Manager: Mitch Olszewski
Voice: 865-946-1350; Fax: 865-946-1262; E-mail: olszewskim@ornl.gov

---

Objectives
- To keep up to date with the state-of-the-art wide bandgap (WBG) power devices and acquire, test, and characterize newer technology WBG power devices.
- Assess the system level impact of WBG semiconductor devices on hybrid electric vehicles.

Approach
- Evaluate device performance: Acquire, test, and characterize newer technology WBG power devices including the following:
  — Static characteristic tests
  — Dynamic characteristic tests
  — Behavioral modeling
- Develop behavioral SPICE[*] models for packaging projects: Specific device tests will be performed to extract the parameters required for behavioral SPICE models. These models will be used to study the parasitic parameters in a package.
- Perform inverter simulations with selected device models: The inverter simulations will be performed to evaluate the impact of the device performance at system level.
- Prepare a summary report that includes the test results of devices and SPICE modeling results to be incorporated into the annual DOE Vehicle Technologies Program report.

Major Accomplishments
- Acquired, tested, and characterized SiC metal-oxide semiconductor field-effect transistor (MOSFET), SiC super junction transistor (SJT), and SiC junction barrier Schottky (JBS) diodes.
- Developed SPICE model for a 1,200 V, 33 A SiC MOSFET.
- Developed a traction drive model to simulate the performance of the WBG devices over different drive cycles.

---

[*]Simulation Program with Integrated Circuit Emphasis.

Future Direction

- The state-of-the-art WBG power devices and newer technology WBG power devices will be acquired, tested, and characterized.
- SPICE models of the devices will be developed.

Technical Discussion

Device Testing

The new WBG devices acquired this year are SiC MOSFETs, SiC JBS diode copacks with silicon insulated gate bipolar transistors (IGBTs), and SiC SJTs. On-state characteristics and switching energy losses of the devices were obtained, and the voltage blocking capability of the devices over the wide temperature range was tested. The test results for these devices will be presented in the following sections. All the devices obtained were experimental samples.

1. 1,200 V, 35 A SiC JBS Diode

The static characteristics of a 1,200 V, 35 A SiC JBS diode were obtained over a wide temperature range (25°C–175°C) (Fig. 1). The on-state resistance over temperature is shown in Fig. 2. It is evident that the SiC JBS diode has a positive temperature coefficient. The leakage current of the diode at a blocking voltage of 600 V is about 0.5 uA at 25°C and increases to 350 μA at 175°C (Fig. 3). The leakage current increased dramatically from 150°C to 175°C. Fig. 4 shows the switching losses at 600 V.

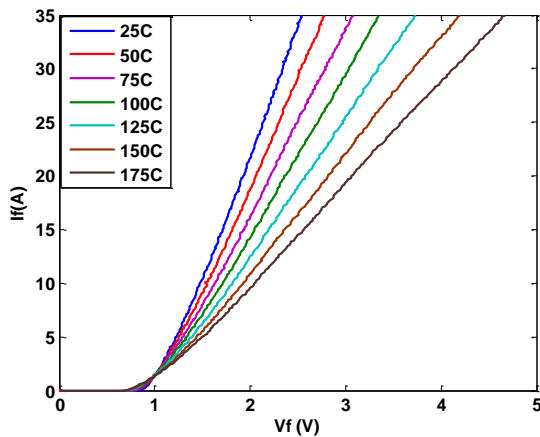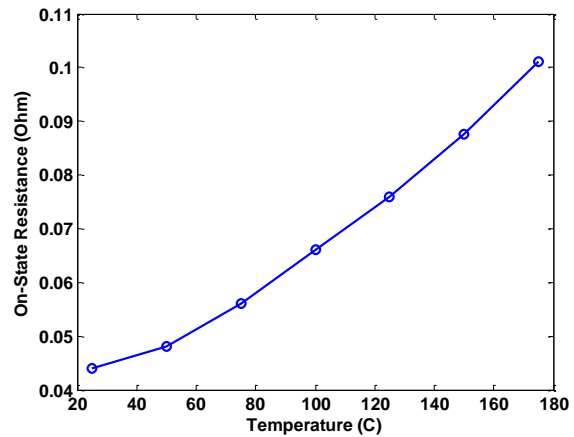**Fig. 1. Forward characteristic of 1,200 V, 35 A JBS diode.**

Fig. 2. On-state resistance of 1,200 V, 35 A JBS diode.

Fig. 3. Leakage current of 1,200 V, 35 A JBS diode.
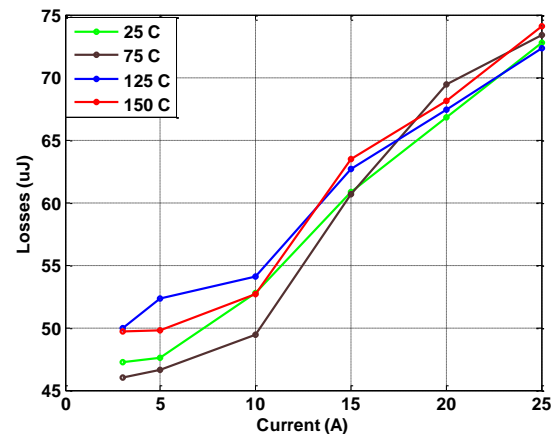
Fig. 4. Energy losses at 600 V.

6

2. 1,200 V, 100 A SiC JBS Diode

The static characteristics of a 1,200 V, 100 A SiC JBS diode were obtained over a wide temperature range (25°C–175°C) (Fig. 5). The on-state resistance over temperature is shown is Fig. 6. The diodes were specifically designed for high temperature operation. Figures 7 to 9 are the switching losses at different voltages and temperatures. As can be seen, the losses increase greatly with voltage; however, they decrease with current increases and stay almost constant with temperature.

Fig. 5. Forward characteristic of 1,200 V, 35 A JBS diode.
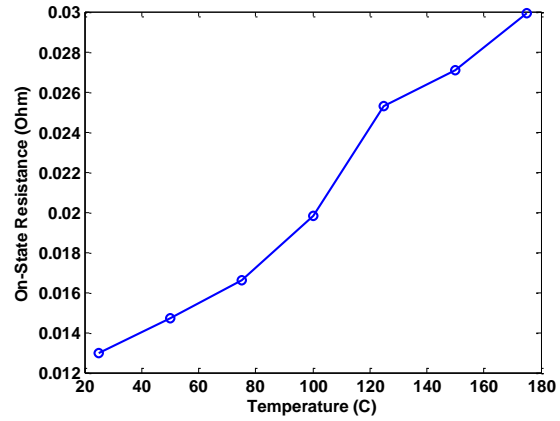
Fig. 6. On-state resistance of 1,200 V, 35 A JBS diode.
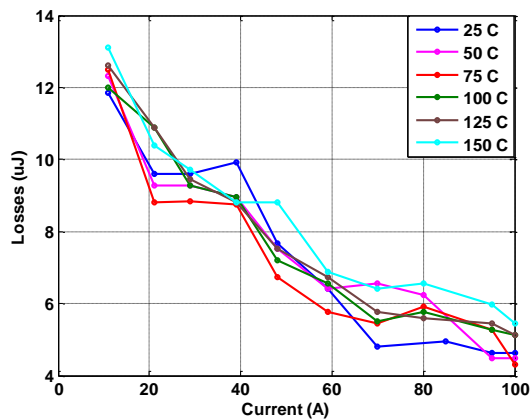
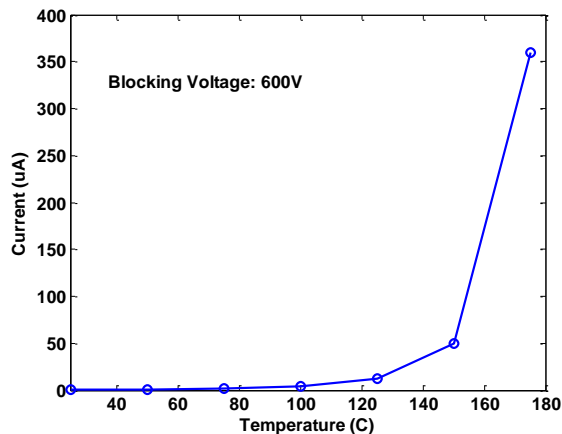**Fig. 7. Energy losses at 200 V.**

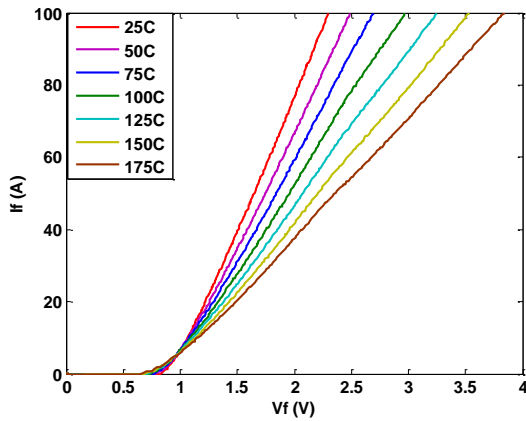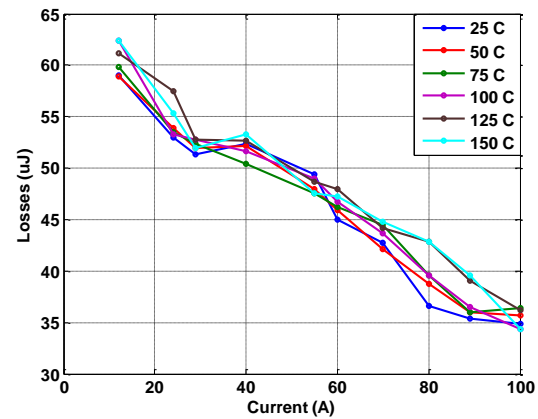**Fig. 8. Energy losses at 400 V.**
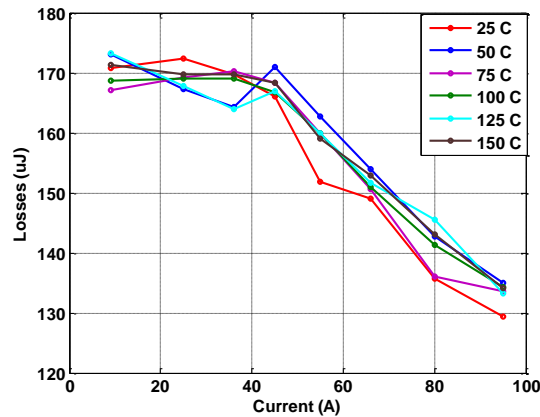
Fig. 9. Energy losses at 600 V.

3.   1,200 V, 20 A SiC MOSFET

Both static and switching characteristics of a 1,200 V, 33 A SiC MOSFET have been tested. Figure10 shows the forward characteristic at different temperatures. The on-state resistance has also been calculated accordingly and is shown in Fig. 11. One thing to be noticed is that the SiC MOSFET has a negative temperature coefficient around 50°C. This might be an issue when paralleling those devices because the current could not be shared evenly among devices. Figure 12 is the transfer function of the device over a wide temperature range at V_{ds} = 10 V. Figure 13 shows the threshold voltage obtained from the transfer curves. The threshold voltage decreases as temperature increases. Figure 14 is the leakage current at different temperatures for 600 V blocking voltage.
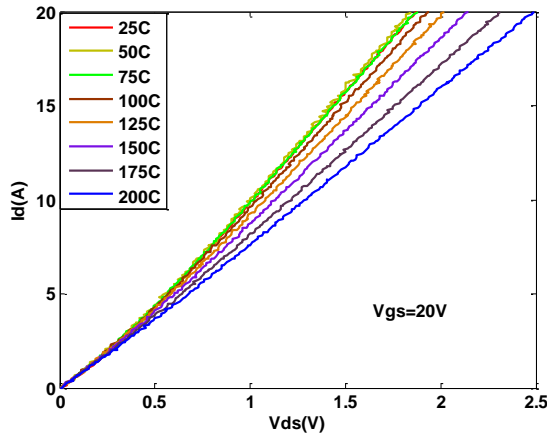
Fig. 10. Forward characteristic of 1,200 V, 33 A MOSFET.
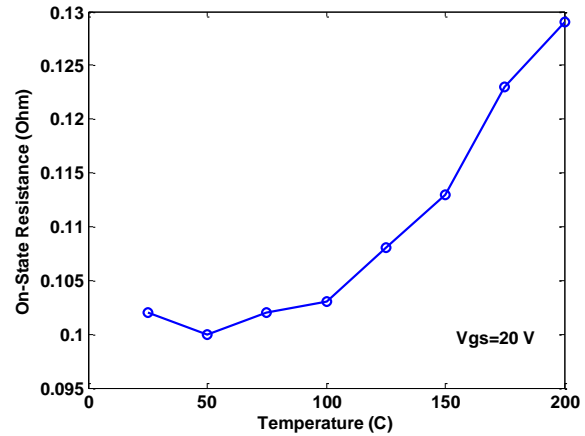
Fig. 11. On-state resistance of 1,200 V, 33 A MOSFET.
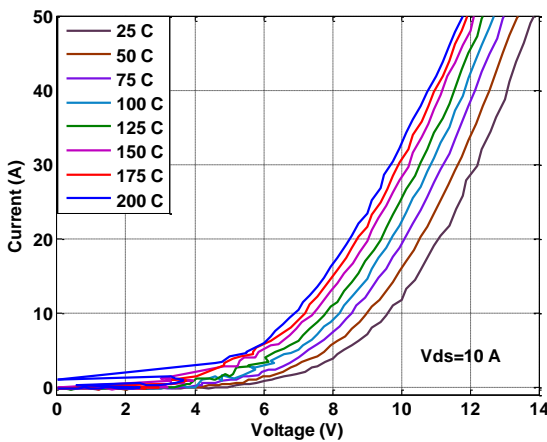
Fig. 12. Transfer characteristic of 1,200 V, 33 A MOSFET.
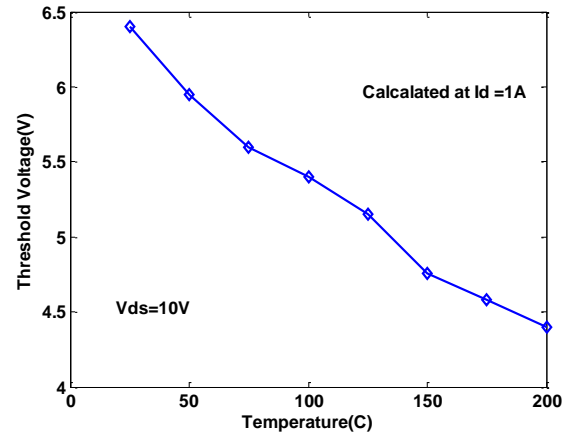
Fig. 13. Threshold voltage of 1,200 V, 33 A MOSFET.
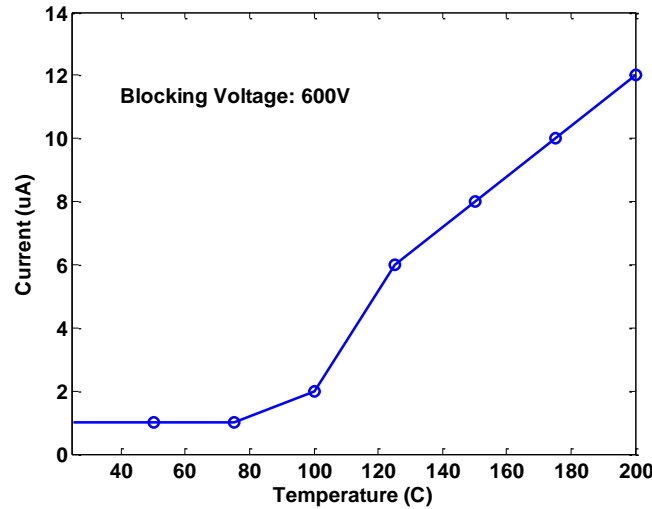
Fig. 14. Leakage current of 1,200 V, 33 A MOSFET.

Figure 15 is the switching waveform of the SiC MOSFET at 600 V and 12 A in a double pulse testing (DPT) circuit. The turn-on and turn-off energy losses were obtained with a load inductance of 140 μH, and a 1,200 V, 30 A SiC JBS diode was used as the clamping diode in the circuit. The gate driver used for this testing was a commercial gate driver IXDD414. The data were obtained at 600 V and 400 V dc for various currents from 25°C to 175°C. The total energy losses increase with increase in current; however, the losses do not change much with increase in temperature (Figs. 16 and 17).
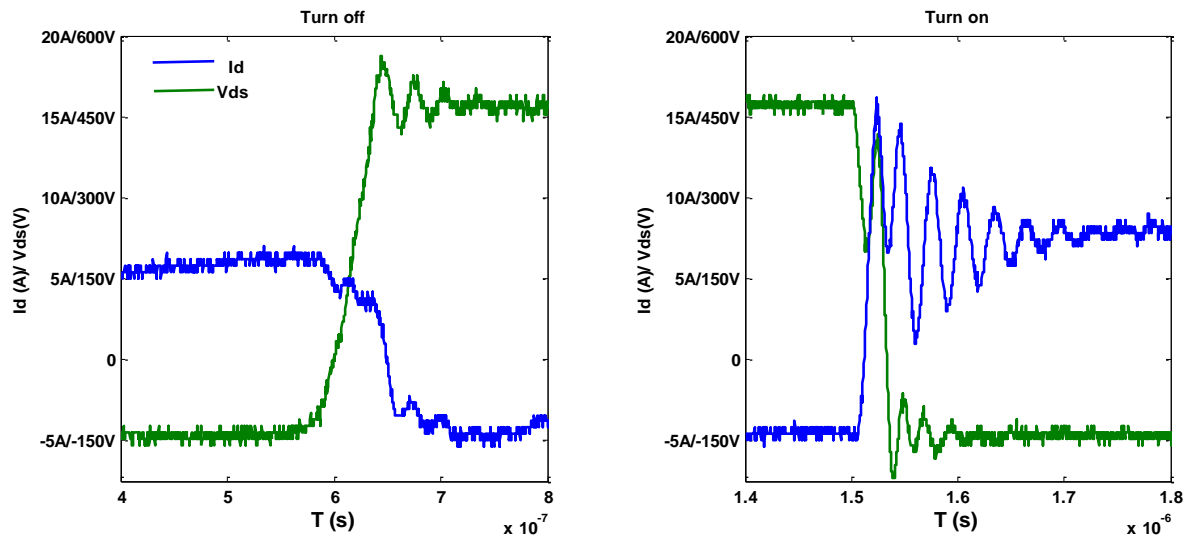
Fig. 15. Switching waveforms of 1,200 V, 33 A MOSFET.
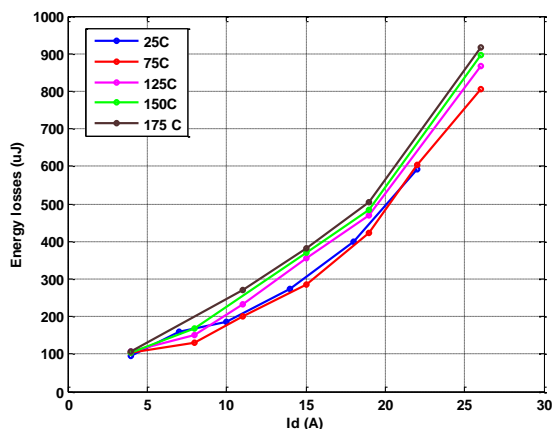
Fig. 16. Switching losses of 1,200 V, 33 A MOSFET at 400 V.
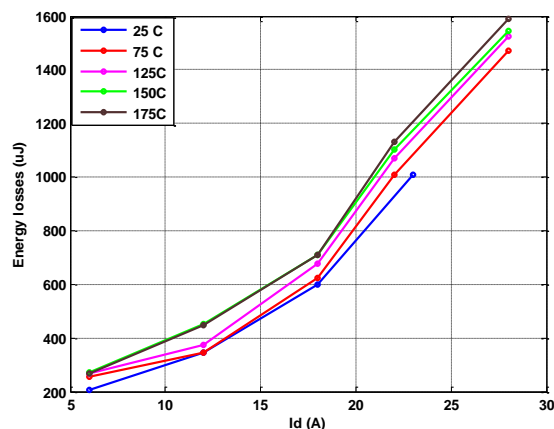
Fig. 17. Switching losses of 1,200 V, 33 A MOSFET at 600 V.

4. 1,200 V, 10 A SiC SJT

The SiC SJT is a current controlled normally off device. Figure 18 shows the forward characteristics of the SJT at different temperatures for a 350 mA base current. The gain of SJT was calculated correspondingly for different base current in the saturation region (shown in Fig. 19). It can be seen that the gain is decreasing with both temperature and collector current. Figure 20 is the on-state resistance of the SJT, which increases with temperature.
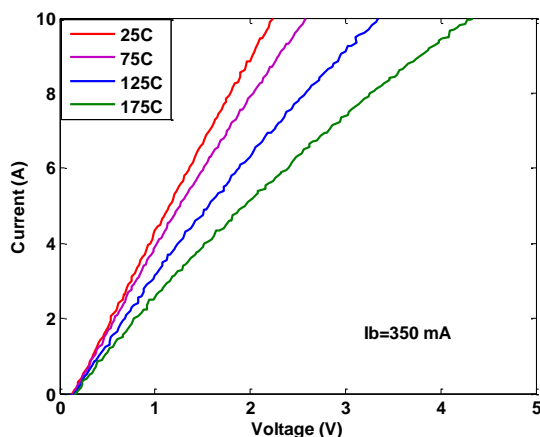
Fig. 18. Forward characteristic of 1,200 V, 10 A SJT.
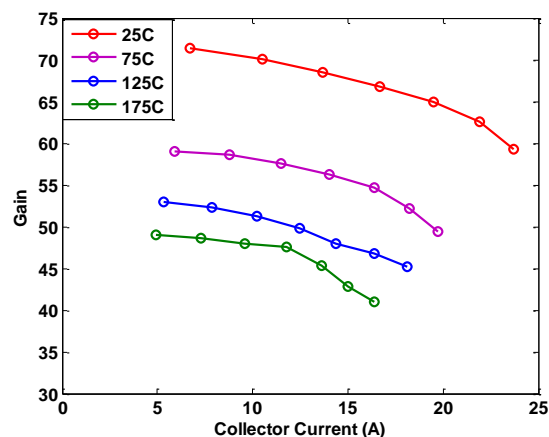
Fig. 19. Gain of 1,200 V, 10 A SJT.
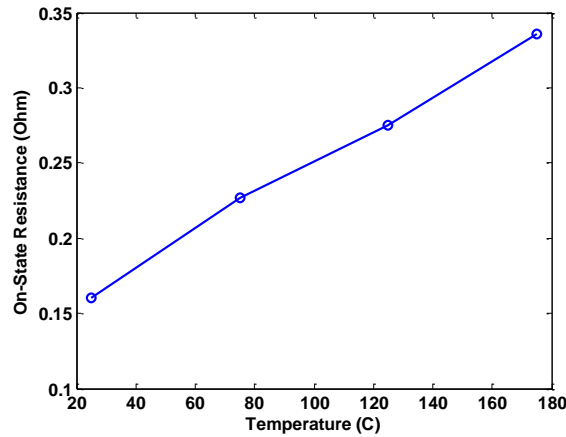
Fig. 20. On-state resistance of 1,200 V, 10 A SJT.

Device Modeling

1. PSPICE Model of SiC MOSFET

A behavioral model of a 1,200 V, 33 A SiC MOSFET was built in PSpice.[*] The parameters used to build the model were obtained from test data. The model has been verified through comparison of the simulation and testing data and will be discussed in detail in the following section.

The SiC MOSFET has three ports (gate, drain, and source), several internal capacitors, and several layers. The values of the internal capacitors change as the bias voltage changes. They affect the switch transient as these capacitors need to be charged or discharged every time the device is switched. The MOSFET has been simplified to be the equivalent circuit shown in Fig. 21. It includes a voltage controlled current source, three junction capacitors, reverse body diode, and other parasitic elements.
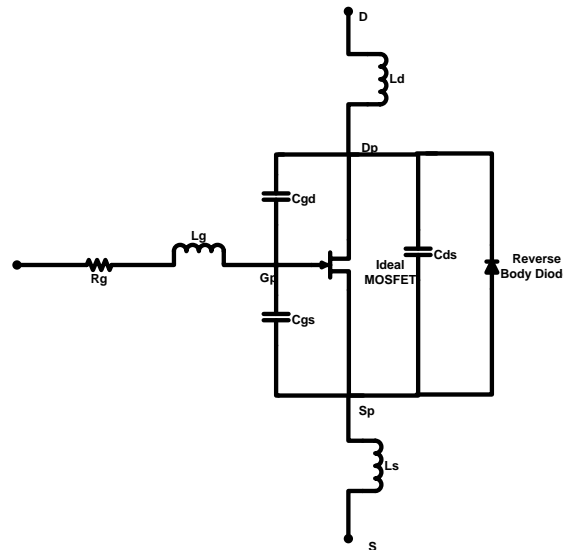
Fig. 21. Equivalent circuit of SiC MOSFET.

---

[*]PC version of SPICE.

Figures 22 and 23 show the relationship between junction capacitance [drain-to-source (C_{ds}) and drain-to-gate (C_{dg})] and drain-to-source voltage (V_{ds}). The corresponding equations are as follows.

$$C_{ds} = 10^{-12} * ((1781 * exp(-0.09048 * V_{ds}) + 420.8 * exp(-0.004418 * V_{ds})) \tag{1}$$

$$C_{dg} = 10^{-12} * ((1613.6 * exp(-0.0839 * V_{ds}) + 52.84 * exp(-0.00381 * V_{ds})) \tag{2}$$
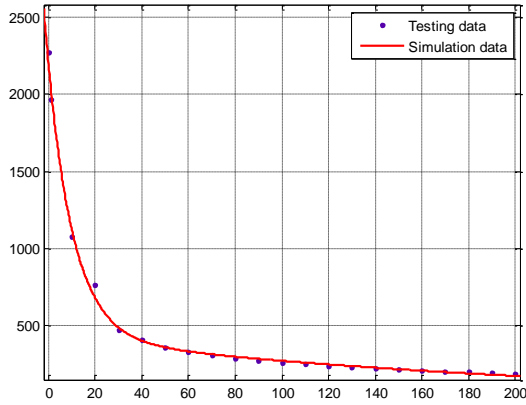
Fig. 22. Drain-to-source capacitance vs drain-to-source voltage.
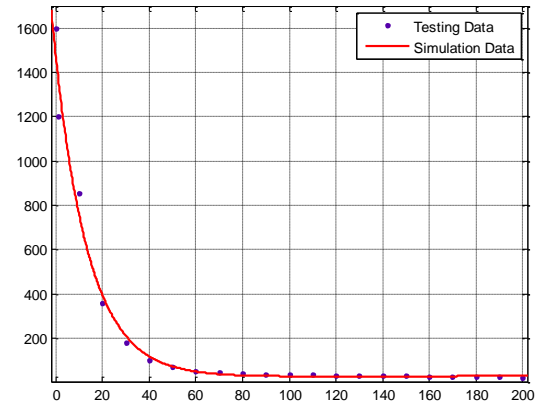
Fig. 23. Drain-to-gate capacitance vs drain-to-source voltage.

The following are the equations used to describe the voltage controlled current source. In these equations, λ is the channel-length modulation parameter; V_{TO} is threshold voltage; I_{DSAT} and V_{DSAT} are the saturation current and voltage, which are derived from[1,2]; *B* and *n* are constants that control the saturation current; and *K* and *m* are constants that control the saturation voltage.

$$I_D = 0 \qquad\qquad V_{GS} - V_{TO} \leq 0 \quad (Pinch - off) \tag{3}$$

$$I_D = I_{DSAT}(1 + \lambda V_{DS}) \qquad V_{DS} > V_{DSAT} \quad (Saturation\ region) \tag{4}$$

$$I_D = I_{DSAT}(1 + \lambda V_{DS}) * \left(2 - \frac{V_{DS}}{V_{DSAT}}\right) * \frac{V_{DS}}{V_{DSAT}} \qquad V_{DS} < V_{DSAT} \quad (Linear\ region) \tag{5}$$

$$V_{DSAT} = K(V_{GS} - V_{TO})^m \tag{6}$$

$$I_{DSAT} = B(V_{GS} - V_{TO})^n \tag{7}$$

The value of threshold voltage V_{TO} is directly from measured data. The values of *B*, *K*, *m*, *n*, and λ in the model are extracted from the forward curves of the device by solving linear equations with five points located at both linear and saturation regions from testing. All those parameters are temperature dependent.

Figure 24 is the comparison between simulation and testing for the forward characteristics at multiple gate voltages and temperatures with currents up to 70 A. Notice this is a 20 A rated device, so currents usually are lower. It can be seen that at lower current, higher temperature (125°C and 200°C) simulations have better agreement with testing. At room temperature, the simulation has an error less than 10% compared to the testing results, caused by curve fitting which will lose some accuracy at some operating

points. Figure 25 shows the on-state resistance calculated. Most of the resistance under a certain temperature is consistent; however, at room temperature the simulated resistance is higher than the testing results. Figure 26 shows the comparison of transfer characteristics between simulation and testing at different temperatures. The comparison shows good agreement.

The parasitic parameters, like inductance and resistance, were extracted using simulation to get a good match with the experimental data. As shown in Fig. 27, there are two dc inductances, L4 and L5. These two inductors affect the switching transient time and oscillation value. For L4 equals 200 nH and L5 equals 10 nH, the transient time has a good match, but the oscillation value is larger than the testing waveform, which is why a 2 Ω resistor R3 was added to the circuit to minimize the oscillation. Gate inductance L7 and drain inductance L3 also have influence on the transient time, but not as much as loop inductance. Values shown in the schematic are the final values used for the comparison. Figure 28 shows the comparison of switching voltage and current. The simulation results show some aspects of the actual switching behavior of the device in the circuit, like the overshoot and oscillation of both current and voltage and the transient time. However, some of the performance is not reflected in the simulation, like the double hump of the current and notch of voltage during turn-on. This could be caused because of some of the other parasitic parameters associated with the circuit that could not be evaluated.

25°C   125°C

200°C
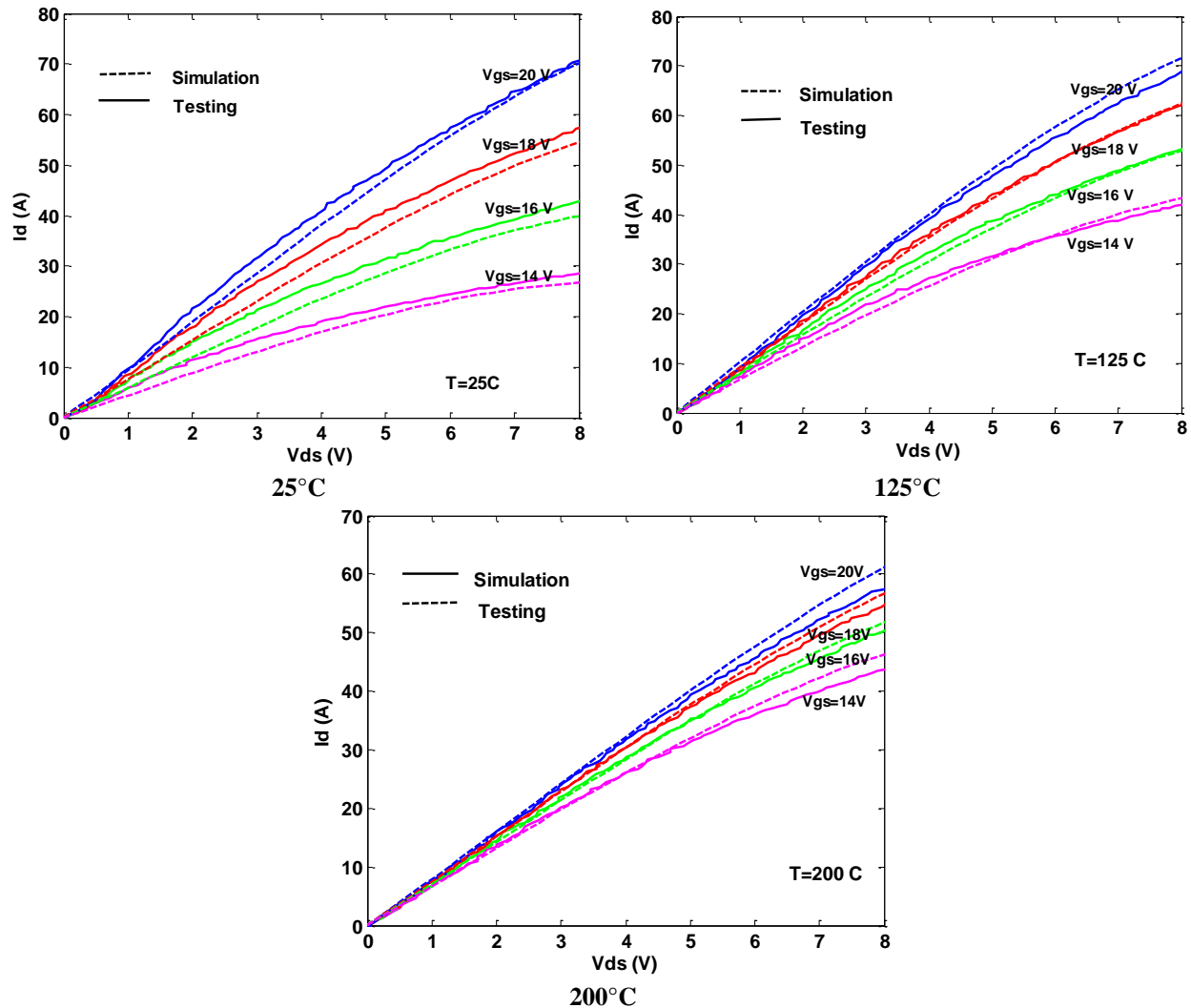
Fig. 24. Comparison at various temperatures of forward characteristics between testing and simulation.
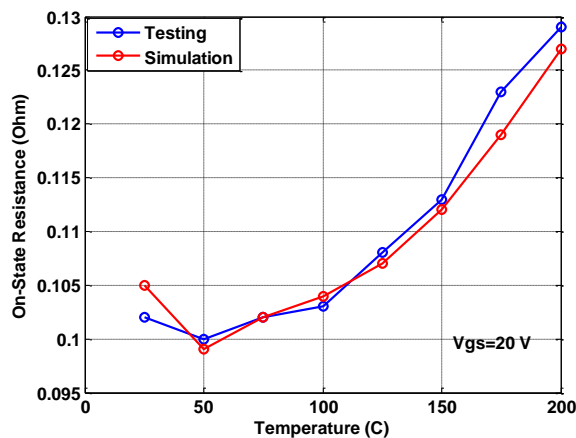
Fig. 25. Comparison of on-state resistance.
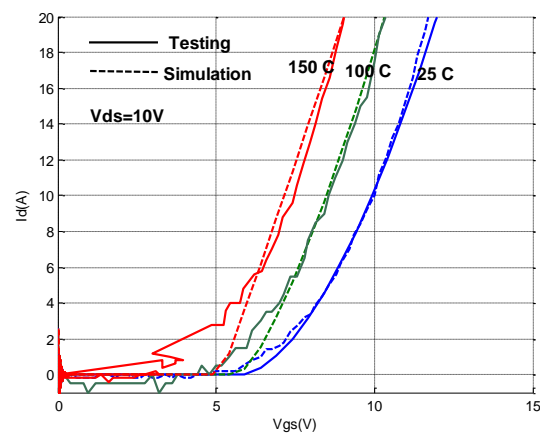
Fig. 26. Comparison of transfer characteristics.
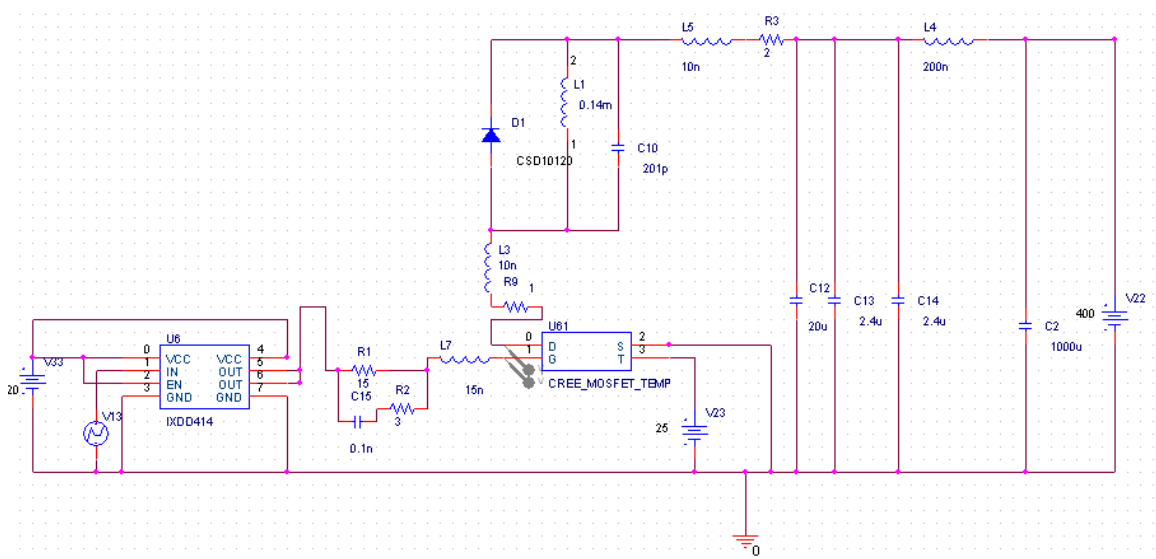
Fig. 27. Schematic of DPT in PSpice.
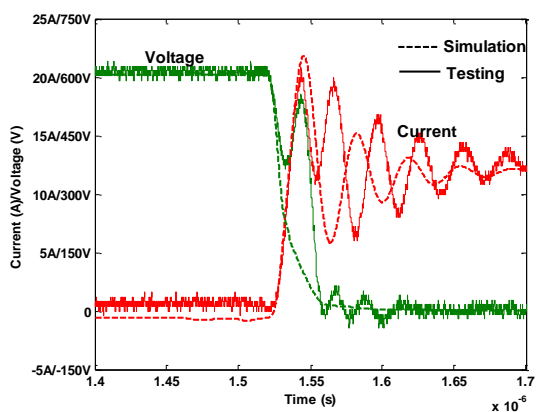
(a)
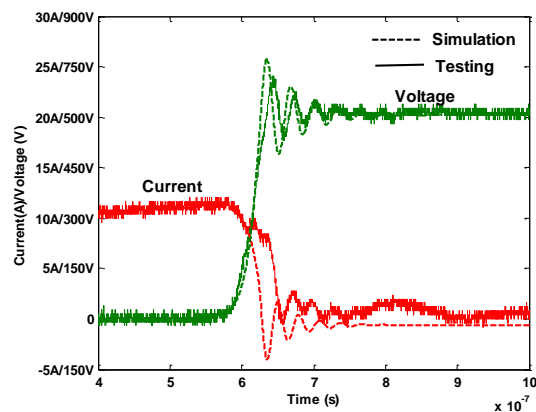
(b)

Fig. 28. Comparison of switching characteristics between testing and simulation: (a) turn-on; (b) turn-off.

2. Traction Drive Model

The traction drive model consists of two parts: (1) an electric motor/generator model that computes the current, voltage, and phase angle that will produce optimally 100% of the torque required at each time step and (2) an inverter loss model that computes the temperature dependent device losses associated with the voltages, currents, and frequencies demanded by the motor. The details of the motor model were presented in the FY 2010 annual report.

3. Inverter Loss Model

The inverter loss model was implemented by using silicon IGBT and SiC JBS diodes in a hybrid configuration. The temperature dependent conduction loss parameters, on-state resistance and voltage drop, and switching losses were obtained from testing the 1, 200 V, 100 A IGBT module. The details of the inverter model were also presented in the FY 2010 annual report.

Simulation Results

The drive model was simulated for the US06 drive cycle with silicon IGBT and diode models at switching frequencies of 10 kHz and 20 kHz and two different coolant temperatures, 70°C and 105°C. The drive model outputs time dependent, cycle average, and cumulative values of interest for all pertinent parameters. The average inverter efficiency and inverter losses over the drive cycle for 10 and 20 kHz with 70°C and 105°C cooling are shown in Table 1.

Table 1. Simulation results of traction drive for the US06 drive cycle

10 kHz		20 kHz	
Inverter efficiency (%)			
70°C	**105°C**	**70°C**	**105°C**
95.97	95.76	92.67	92.28
Inverter energy loss (kJ)			
70°C	**105°C**	**70°C**	**105°C**
536.4	565.2	1004.5	1061.5

The inverter efficiency corresponds to the losses of devices in the inverter only, and the losses in the boost converter are not included. For 10 kHz operation, the efficiency of the inverter decreased by only 0.21% for the 70°C to 105°C coolant temperature condition. For 20 kHz operation, the efficiency of the inverter decreased by 0.39% for the 70°C to 105°C coolant temperature condition. However, when the switching frequency was increased from 10 kHz to 20 kHz, the efficiency of the silicon IGBT and SiC diode hybrid inverter decreased by 3.3% and 3.48% at 70°C and 105°C coolant temperature, respectively.

Conclusion

Several new SiC MOSFETs, JBS diodes, and SJTs were acquired, tested, and modeled. The traction drive was sucessfully completed, and the simulation results for the Si-SiC hybrid inverter, developed based on 1,200 V, 100 A SiC JBS diode module testing, were presented. A behavioral SPICE model of a 1,200 V, 33 A SiC MOSFET was developed by obtaining the model parameters from testing the device. The SPICE model was validated through testing.

Patents

None.

Publications

M. Chinthavali, P. Ning, Y. Cui, and L. M. Tolbert, "Investigation on the parallel operation of the discrete SiC BJTs and JFETs," in Applied Power Electronics Conference (APEC), Dallas, 2011, pp. 1076–1083.

References

1. T. Sakurai and A. R. Newton, "A simple MOSFET model for circuit analysis," *IEEE Transactions on Electron Devices*, vol. 38, pp. 887–894, 1991.

2. N. Phankong, T. Funaki, and T. Hikihara, "A static and dynamic model for a silicon carbide power MOSFET," in *Power Electronics and Applications, 2009,* EPE '09, 13th European Conference, September 8–10, 2009, pp. 1–10.

2.2   Power Device Packaging

Principal Investigator: Zhenxian Liang
Oak Ridge National Laboratory
National Transportation Research Center
2360 Cherahala Boulevard
Knoxville, TN 37932
Voice: 865-946-1467; Fax: 865-946-1262; E-mail: liangz@ornl.gov

DOE Technology Development Manager: Susan A. Rogers
Voice: 202-586-8997; Fax: 202-586-1600; E-mail: Susan.Rogers@ee.doe.gov

ORNL Program Manager: Mitch Olszewski
Voice: 865-946-1350; Fax: 865-946-1262; E-mail: olszewskim@ornl.gov

Objectives

Overall project objectives
- Identify the limitations and shortcomings of existing device packaging approaches.
- Develop new packaging concepts for improved electrical performance, thermal management, reliability, and manufacturability.
- Complement other packaging and thermal management research efforts within the DOE Vehicle Technologies Program (VTP).

FY 2011 objectives
- Develop new power module packaging, including electrical, thermal, and thermomechanical performance evaluation and characterization and material/structure selection.
- Fabricate, test, and analyze sample modules.
- Continue to benchmark state-of-the-art technologies and share information.
- Provide packaging support for other DOE Advanced Power Electronics and Electric Motors (APEEM) projects.

Approach

- Optimize the new package structure, which incorporates advanced die attach, double sided cooling, and non-wire-bond interconnect, through simulation of its electrical, thermal, and thermomechanical properties.
- Based on the optimization information, fabricate a sample module. Fabrication will include process development and integration of substrate patterning, die attach, interconnect, encapsulation, etc.
- Test the fabricated sample electrically and thermally. Analyze the results for design verification and improvement.
- Implement an inverter-level package study.
- Benchmark promising new packaging concepts through survey, experimental analysis, and simulation.
- Develop key materials and processes such as paste materials and processes for sintering, substrates, and cooling though experimental tests and microstructural analysis.
- Provide packaging support for other projects: The support will mainly be through fabrication and testing of selected prototypes.
- Prepare a summary report that includes evaluation results (incorporate into the annual VTP report).

Major Accomplishments

- Designed an integrated planar package power module structure for automotive applications featuring double sided planar interconnection and integrated cooling (*Planar_Bond_All*).
- Fabricated a 200 A, 1,200 V phase leg planar bond power module prototype, and completed thermal and electrical characterization.
- Developed a simulation program to comprehensively evaluate the power module technology.
- Established a module thermal performance test station and performed tests.
- Benchmarked four state-of-the-art power device packaging technologies.
- Manufactured four different types of power modules for other APEEM projects.

Future Direction

Develop high temperature (up to 200°C), high reliability planar packaging through thermomechanical structure optimization, material tailoring, and process innovations.

Technical Discussion

Introduction

From a power electronics (PE) system point of view, the major criteria to appraise an automotive power module consist of its cost, reliability, functionality, power density, and efficiency. All these aspects are generally determined by its components (e.g., power semiconductors and package components) and manufacturing/processing technology. The power semiconductors include multiple power switches such as insulated gate bipolar transistors (IGBTs); metal-oxide semiconductor field-effect transistors (MOSFETs); and diodes made of Si, SiC, GaN, etc. The package components include the bonding wire and solder, power substrate, power and signal terminals, baseplate, encapsulate, thermal interface greases, etc. Power modules are made using all these diverse materials and multiple manufacturing processes. Figure 1 is a flowchart illustrating the relationship between the power module's performance criteria; electrical, thermal, thermomechanical, and mechanical properties; and components, materials, and manufacturing processes, with the electrical, thermal, etc. properties the critical link. These various properties can be further broken down into subcategories such as thermal impedance (resistance and capacitance), operation temperature, parasitic electric resistance, conductance, power cycling, thermal cycling/shock, vibration ruggedness, etc.
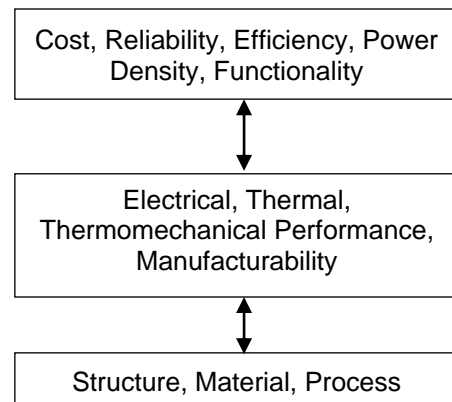
Fig. 1. Technology analysis flowchart for automotive power modules.

Looking at things in terms of these categories and their relationships makes evaluation of power module technologies to identify the shortcomings of existing technology and develop new power module concepts relatively easier.

Using this as a guideline, in FY 2011 ORNL developed a program dealing with the effects of the module's electrical, thermal, and thermomechanical performance on cost, efficiency, reliability, etc. Experimental setups were developed for characterizing these parameters and running simulations. Then a novel packaging structure was proposed, and an innovative packaging process technology was developed. Based on these, a new 200 A, 1,200 V phase leg power module prototype with tremendous improvement in performance and manufacturability was fabricated, resulting in considerable strides toward achieving power density and cost targets for PE systems. Furthermore, these automotive power modules were benchmarked with microstructure analysis tools in addition to thermal performance comparisons. Based

on in-house packaging capability, four types of power modules were prototyped for other APEEM projects.

Automotive Power Module Evaluation

To obtain the relationships between performance parameters and final criteria, an evaluation software program has been developed that incorporates a set of metrics (control factors) to represent the power module's performance based on standard operating conditions such as drive cycles. Figure 2(a) illustrates the computational flow chart of this program. The various parts are used to calculate the power semiconductor device's power loss and junction temperature with a certain die area under a typical driving cycle (in this case, the US06 drive cycle). The control factors include the module's thermal and reliability performance and semiconductor properties [Vce-J, (Tj), Esw-J(Tj)]; packaging parasitic electric parameters, Lp and Rp; thermal impedance, θja; and reliability characterization, N_f-ΔTj. Ultimately the program will be used to simulate power loss under various conditions, including change in junction temperature, ΔTj; maximum junction temperature, Tjmax; and IGBT/diode die size. Power loss data can be correlated to the module's efficiency; ΔTj and Tjmax can be used to assess lifetime (reliability) as well as coolant temperature. Die size data from these computations will be critical for calculating module cost (die costs are known to be a significant factor in overall power module cost).

This computational tool was used to perform a comprehensive evaluation of a conventional silicon IGBT module. As shown in Fig. 2(a), the US06 drive cycle over a 10 min regimen was selected as a standard operating condition for these simulations. The semiconductor characterization has been extracted. The thermal performance and thermal resistance versus die area relationship have been obtained by measurement and simulation. The module's reliability characterization, the number of thermal cycles to failure versus ΔTj or ΔTc (change in either junction or case temperatures) is based on experiment data along with Coffin-Manson modeling.

The IGBT power loss can vary greatly during one cycle, from 20 W to 230 W. To account for the total energy loss, the power loss is integrated for the total time duration. The dependence of this total energy loss on die area is shown in Fig. 2(b). As can be seen from the figure, increasing die area from 1 cm^2 to 3 cm^2 only reduces total energy loss by 5.6%. The main reason is that IGBTs have a cutoff voltage drop, Vce_0 (0.7 V), and the die area just affects the slope of I-V curve that is a minor part in conduction power loss.

The IGBT junction temperature variation, ΔTj, is dependent on both the die area and coolant temperature. The die area affects the IGBT maximum junction temperature, Tjmax, two ways: through power loss and through thermal impedance. Figure 2(c) shows the great dependence of Tjmax on die area. Because there is a rigid limitation on semiconductor operating temperature (Tjmax, 150°C for silicon devices), a minimum die area requirement can be set for specific cooling performance and coolant temperature. The computational program can also predict the penalty in die area if coolant temperature rises from 65°C to 105°C, a scenario in which the PE system shares a coolant loop with the internal combustion engine. So the tradeoffs in cost vs die area increase vs reduction of cooling loop requirements can be evaluated using the program.

To examine the power module lifetime vs die area, the temperature excursion, ΔT, with different die sizes has been calculated. Figure 2(d) shows the ΔTj distribution with a die size of 3 cm^2 during the 10 min drive cycle.
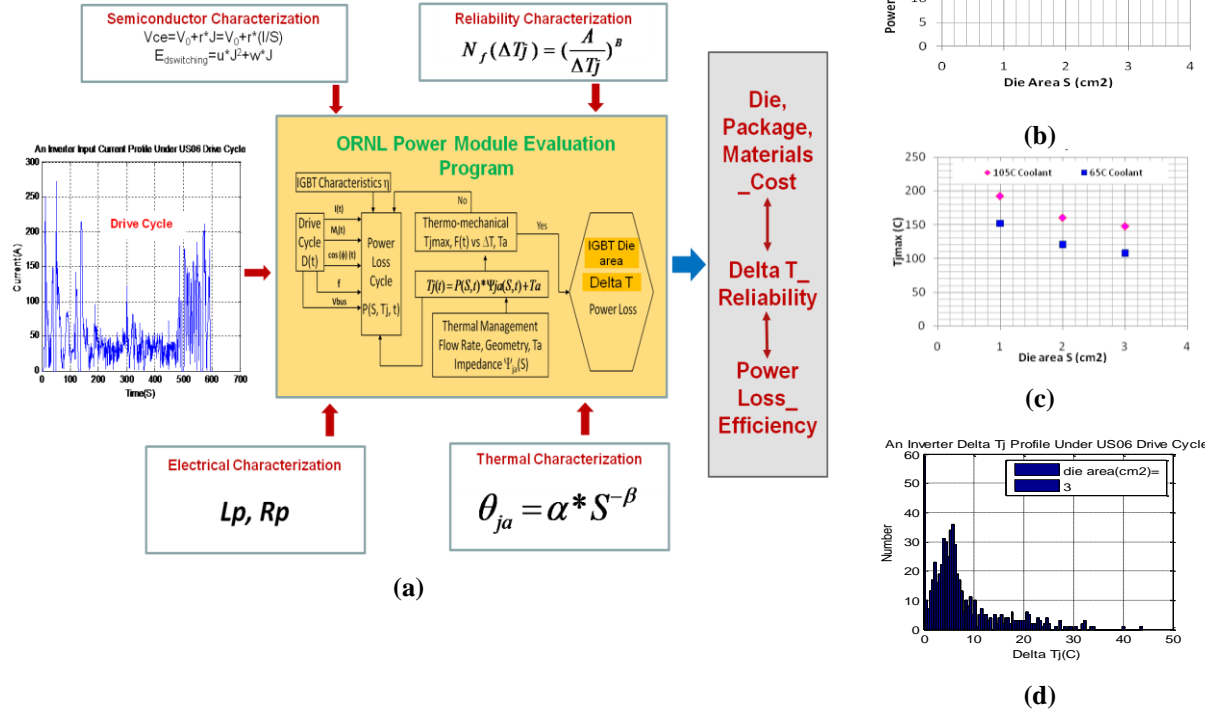
Fig. 2. ORNL automotive power module evaluation program: (a) computation flow chart of ORNL comprehensive evaluation program, showing individual components; (b) die area–power loss relationship; (c) die area–maximum junction temperature (Tjmax) relationship; (d) the number of times specific values of ΔTj occur during the US06 drive cycle.

In conclusion, the outputs from this program such as die size, power loss, and temperature and its excursion can be easily transferred to relationships of power conversion efficiency and reliability (lifetime) versus performance parameters. Using the algorithms developed as part of the ORNL automotive power module evaluation program, the best tradeoffs between the three major aspects of cost, efficiency, and lifetime can be made for a power module with specific technology.

Benchmarking Automotive Power Module Packaging Technologies

As described in the FY 2010 report, state-of-the-art automotive power modules are manufactured with different technologies. Many concepts for improvements in packaging structure, materials, and packaging process techniques have been pursued. All these advancements will affect the module's electrical, thermal, and thermomechanical performance, in turn leading to improvements in cost, reliability, and efficiency, as discussed in the previous section.

To comprehensively compare or benchmark advanced packaging technologies, in FY 2011 ORNL developed test techniques for characterization of various power module performance aspects. These data can be directly used in the evaluation program described previously. Figure 3 shows an example of these test techniques. Figure 3(a) shows the thermal impedance test facilities. The 2010 Toyota Prius (Prius 10) [1] and Infineon HP1 [2] module assemblies (power module + cold plate) were tested. Figure 3(b) shows a typical cooling down curve for IGBT junction temperature. The thermal impedance (resistance and time constant) can be extracted from it. Figure 3(c) presents the thermal time constant of three assemblies with five-order thermal network assumption. The difference between modules is attributable to the different

stacking components in the module structures. Figure 3(d) shows the thermal resistance of three module assemblies.
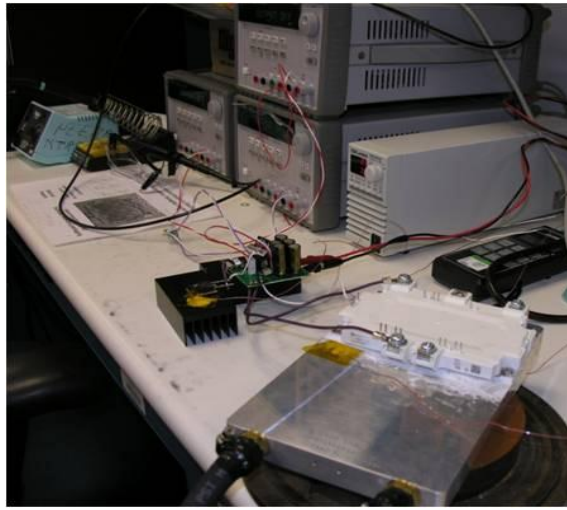
(a)
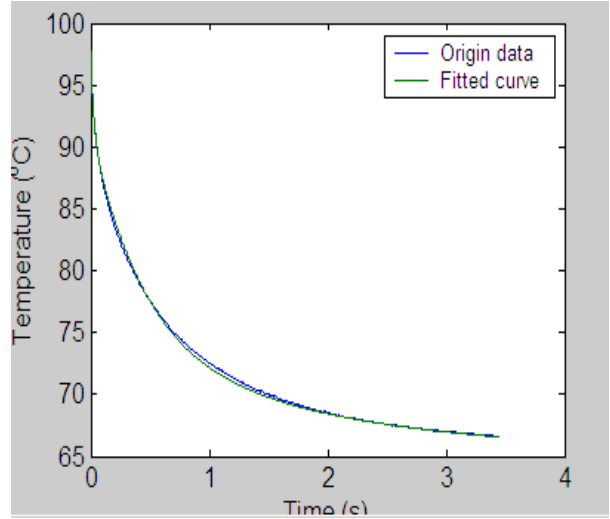
(b)
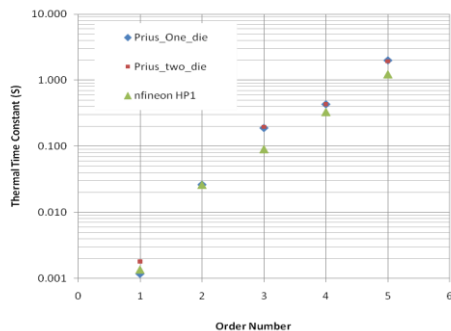
	Prius one die	Prius two die	Infineon HP1
τ1	0.00116023	0.00179598	0.001364815
τ1	0.02619172	0.0242483	0.026198585
τ1	0.18910741	0.19704433	0.090661831
τ1	0.43308792	0.43346337	0.330906684
τ1	2.00360649	1.94099379	1.229709788

(c)

	ToyotaPrius10_OneDie	ToyotaPrius10_TwoDie	InfineonHP1
Thermal Resitance (C/W)	0.4306	0.224	0.271
Die area (10xcm2)	0.109	0.219	0.198
Specific Thermal resistance (Cm2.C/W)	0.471	0.489	0.536
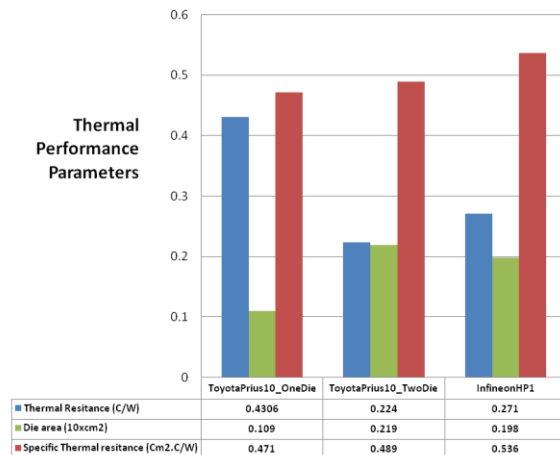
(d)

Fig. 3. Example of ORNL's comprehensive testing facilities/techniques: (a) thermal performance test setup, (b) typical cooling curves for a module assembly, (c) thermal time constant in a five-order network, and (d) thermal resistance comparison of power modules.

It is not fair to singularly compare packaging technologies by using thermal resistance data because of its dependence on die size. Therefore, a parameter referred to as "specific thermal resistivity," a product of die size and thermal resistance, was used to represent the package's thermal performance in Fig 3(d). It can be seen that there is little difference in the specific thermal resistance of a one-die device and a two-die device in Prius10 [0.471 cm^2•°C/W (one die) and 0.489 cm^2•°C/W (two die)] due to thermal spreading/coupling effects. The Prius10 offers 10% lower specific thermal resistance (0.489 cm^2•°C/W) than the Infineon HP1 one (0.536 cm^2•°C/W). This is attributable to its integrated cooling structure [direct bonded aluminum (DBA) bonded directly onto cold plate] compared to a conventional module mounted on a cold plate with thermal grease. The modules were also measured at different coolant temperatures (25°C, 65°C, 90°C, and 105°C). The thermal resistance of the HP1 module is 0.2234°C/W and

0.2211°C/W at 25°C and 105°C, respectively (only 1% difference). This illustrates that the effect of coolant temperature on a module's thermal resistance is negligible.

Figure 4 shows an example of parasitic electric parameters acquisition from the Prius10 module. A three-dimensional (3D) interconnection model was built [Figure 4(a)]. Using electromagnetic simulation software, the parasitic inductance (Lp) and resistance (Rp) associated with each section of the current paths were obtained, as shown in Fig. 4(b). For a power module, the sums of these parameters along the so-called main loop from the positive terminal through neutral to negative terminals are representative parameters for the package. For the Prius 10 module, they are Lp = 39.5 nH and Rp = 1.12 mΩ.

(a)	**(b)**
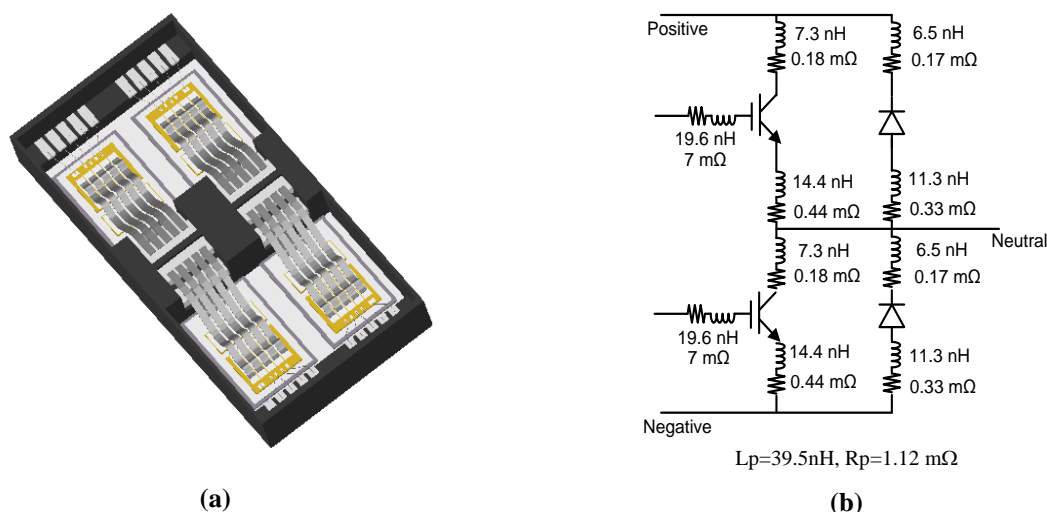
Fig. 4. Electrical performance simulation of the Toyota Prius10 power module: (a) 3D interconnection model and (b) parasitic electric parameters.

Packaging materials and the associated processing are critical factors in determining the mechanical and thermomechanical performance of power modules. During 2011, ORNL continued to perform microstructural analyses of selected packages. Figure 5 gives a few examples. Figure 5(a) shows the solder composition in the die attach layer in an Infineon HP1 module. This lead-free solder contains multiple elements such as tin, copper, and silver. The metallurgical compositions change also along the bond line. Among recent packaging advancements, the planar bond top interconnection of die, instead of wire bond, has become popular, such as that used in modules by Mitsubishi [3], IR [4], and Semikron [5]. The metallization on top of these dies is specially required to match with the bonding materials. Figure 5(b) shows the microstructure of the top metalized layer of a silicon IGBT die in the Mitsubishi TPM_II module, where a lead-free solder was used to bond a copper lead to the die. The metallization and bonding alloys have been identified by energy dispersive x-ray spectroscopy (EDX) and marked in the photo. The newly developed Nissan Leaf module [6] doesn't feature conventional direct bonded copper or DBA substrates; instead, a larger polymer insulation sheet is put on top of the cold plate. The power module built up on a metal frame (bus bar) is directly mounted on this layer with thermal grease, as shown in the photo in Fig. 5(c). Fourier transform infrared spectroscopy indicates that it is a silicone polymer. The EDX spectrum [Fig. 5(c), middle inset] discloses that it contains fluorine, calcium, carbon, and oxygen as part of its composition. Figure 5(d) shows the microstructure of a bonded copper tabs sandwich, which is designed to test the high temperature bonding capability of a polyimide paste/sheet. The photos give the details of bond line as well as failure modes under shear stress.

(a)

(b)

(c)

(d)
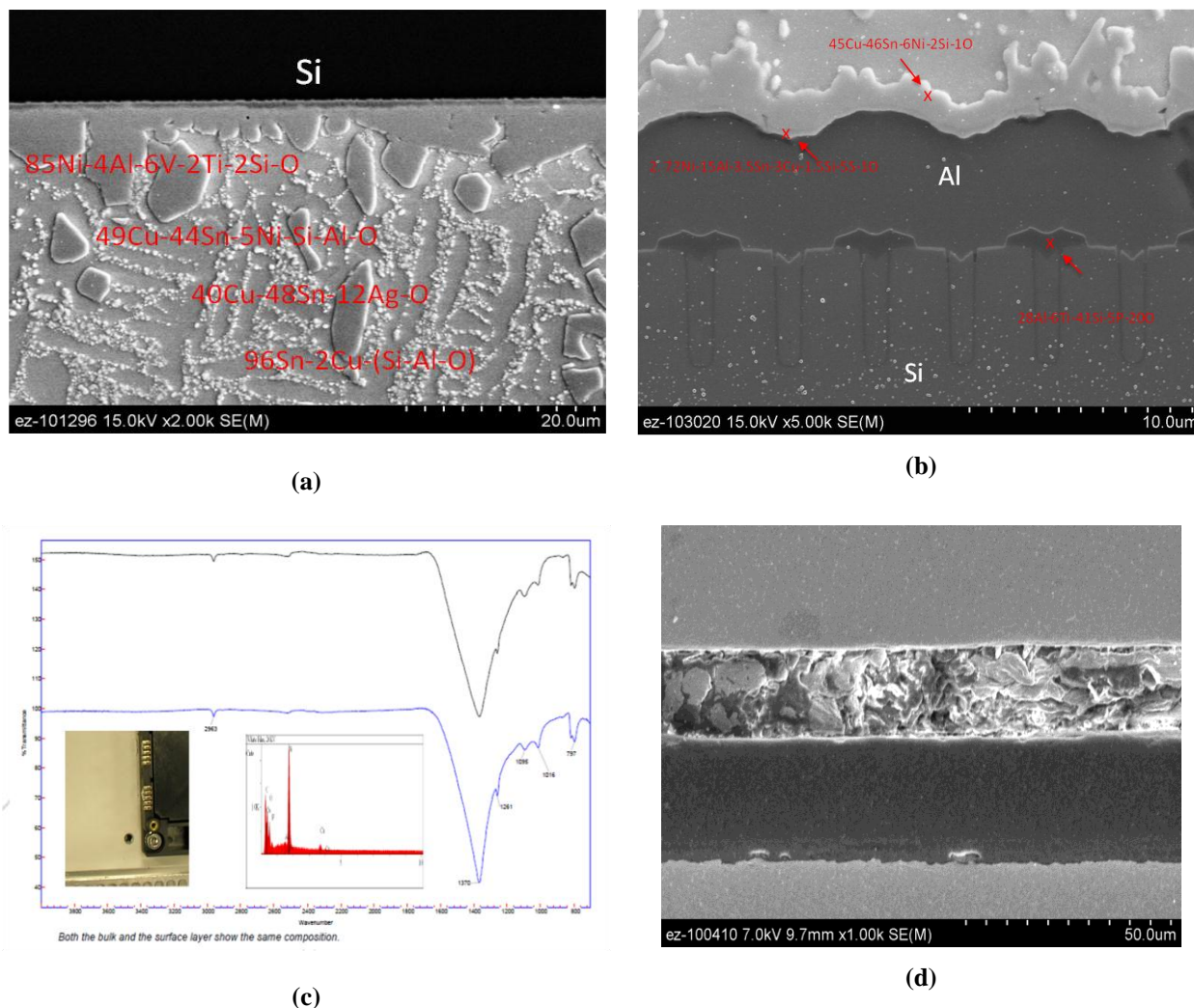
Fig. 5. Examples from microstructural analyses of packaging materials: (a) composition of die attach solder in Infineon HP1 module, (b) metallurgical composition on top of silicon die in Mitsubishi TPM_II, (c) insulator sheet in Nissan Leaf, and (d) a high temperature bonding polyimide layer.

New Automotive Power Module Packaging

An important objective of this project is to develop advanced automotive PE packaging technologies. To this end, multidisciplinary research has been performed including research on power module packaging processes and electrical, thermal, mechanical, and thermomechanical design and analysis.

Figure 6 illustrates a new 200 A, 1,200V phase leg power module, *Planar_Bond_All,* based on innovative ORNL packaging technology and fabricated at the NTRC packaging laboratory. The module features double sided planar electrical interconnections and integrated mini-coolers, resulting in tremendous improvement for automotive power modules.

(a)   **(b)**
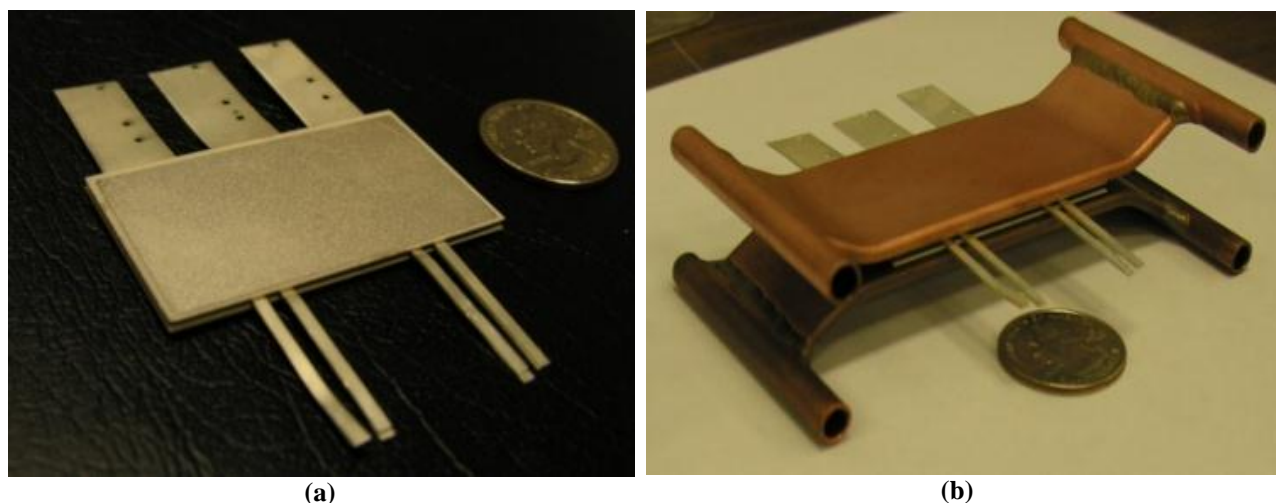
Fig. 6. Photos of the prototype of a 200 A, 1,200 V phase leg power module with (a) double sided planar interconnections and (b) integrated mini-coolers.

Planar_Bond_All is a paradigm shift in power module packaging technologies. It reduces the conventional multiple hybrid packaging processes to two steps, as shown in Fig. 7. In the first step, all the components are assembled into a fixture. The second step involves heating the assembly to form the bonds and create the final package. The simplicity of the process helps reduce costs and improve the manufacturability of the modules.

(a)   **(b)**
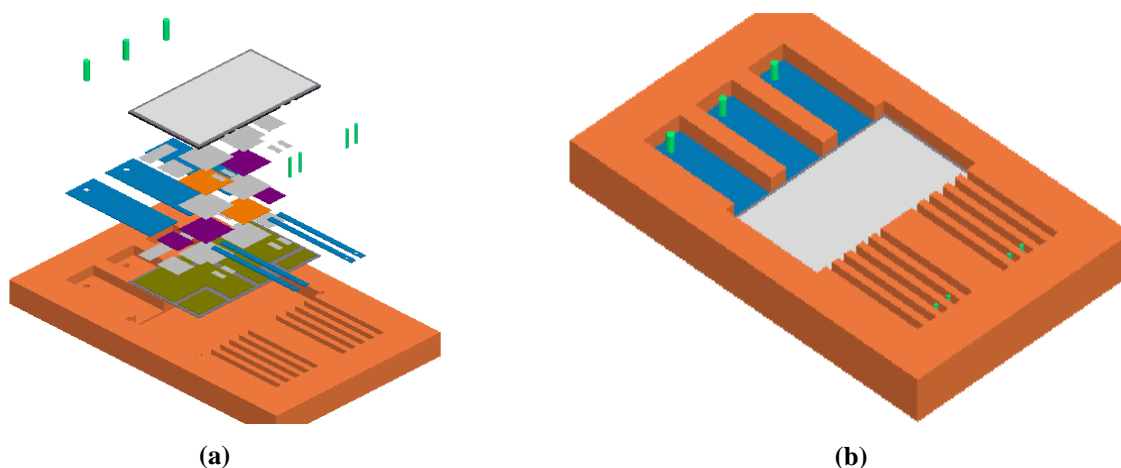
Fig. 7. *Planar_Bond_All* process flow: (a) assembling all components into a fixture; (b) heating of assemblies in oven.

Planar interconnection allows large contact and switch unit orientation of face up-face down switch die pairs (IGBT/diode) as depicted in Fig. 8(a), leading to lower parasitic electric parameters [Fig. 8(b)]. In comparisons with the Prius 10 [Fig. 8(c)], the *Planar_Bond_All* showed an 80% reduction in main path parasitic induction and resistance (Lp = 12.8 nH and Rp = 0.22 mΩ).

Figure 9(a) shows the temperature distribution for the *Planar_Bond_All* under typical application conditions. The double sided cooling reduces the specific thermal resistivity of the whole module assembly to 0.33 • cm^2 C/W, which is 30% lower than the Prius10 [Fig. 9(b)].

The improved performance and anticipated cost reduction of the *Planar_Bond_All* package should result in considerable strides toward achieving power density and cost targets for PE systems.

| (a) | (b) | (c) |
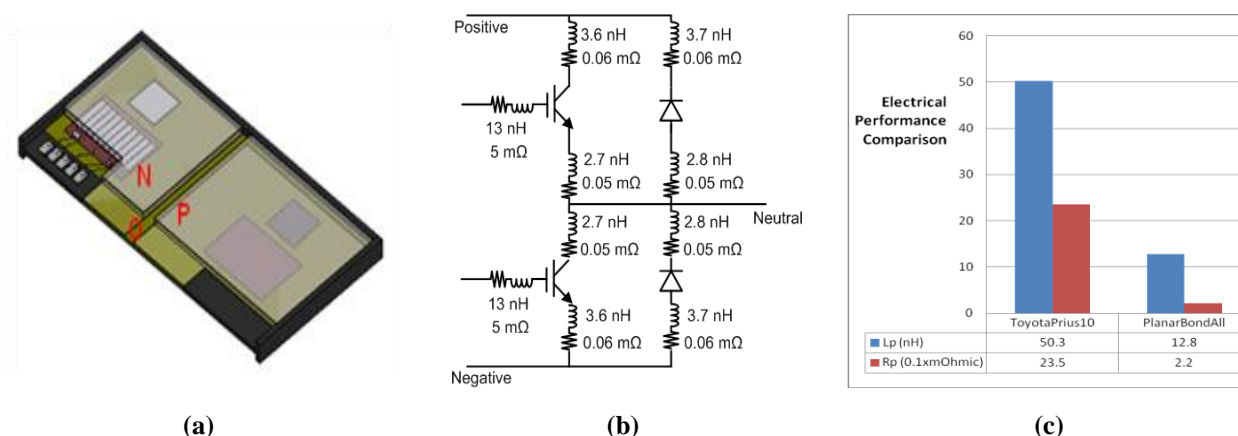
Fig. 8. Advantages of planar interconnection: (a) orientation of face up-face down switch die pairs, (b) parasitic electric parameters (main path Lp = 12.8 nH, Rp = 0.22 mΩ), and (c) comparison to Prius 10.

| (a) | (b) |
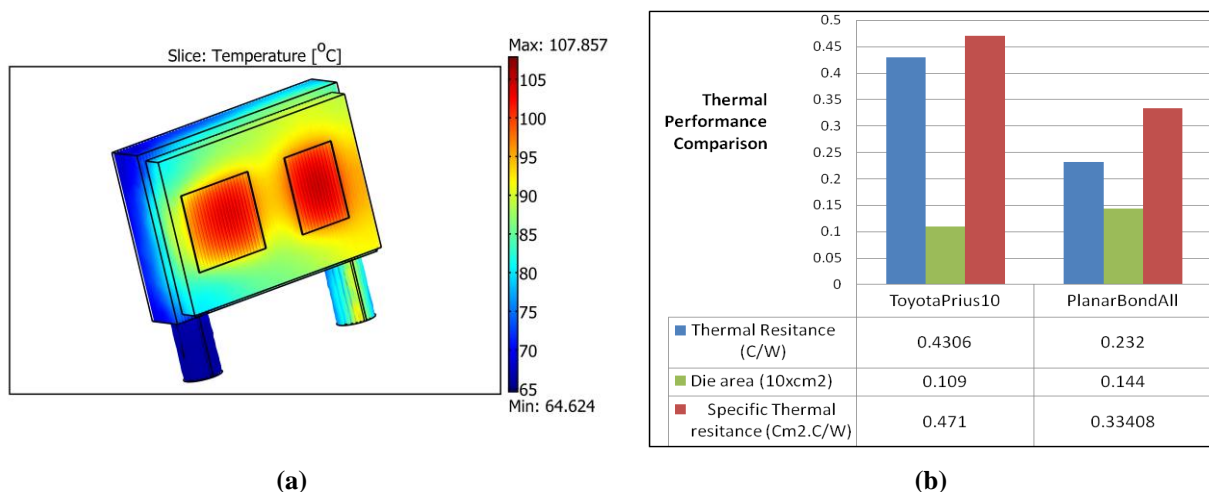
Fig. 9. Thermal performance characterization of ORNL planar bond power module: (a) temperature distribution from simulation; (b) test results and comparison to Prius 10.

Power Module Prototyping

The ORNL Power Electronics Packaging Laboratory (PEPL) supports projects for advancing packaging technology with materials development, structure optimization, and process innovation such as all planar bonding, double sided cooling, and coefficient of thermal expansion matching. Combining these technologies and advanced power semiconductors (Si, SiC, GaN, and diamond) produces PE modules with superior electrical performance, thermal management, high temperature operation, power density, and integration, which will improve cost-effectiveness, efficiency, and reliability of power conversion systems.

Equipped with modern facilities, PEPL provides advanced processing capabilities for PE module packaging. The laboratory includes (1) chemical processing stations for electrical or electroless thin metal plating, metal etching, parts cleaning, etc.; (2) class 100 clean operation bench and screen/stencil printer

for paste coating, assembling, etc.; (3) three furnaces for various large area semicondcutor die attach techniques (vacuum reflow, pressure assisted sintering, enviorment controlled reflow); (4) wire bonder machine for thick wire and ribbon bonding for interconnection; and (5) encapsulant set for polymer spin coating, dispensing, curing, etc. Based on these capabilities, we have completed fabrication of customized specific power module prototypes for other projects within the DOE APEEM program. Figure 10 presents examples of such modules. The prototypes offer flexibility of power semiconductor selection and package forms, which will greatly improve system efficiency and further integration.

(a)   (b)

(c)   (d)
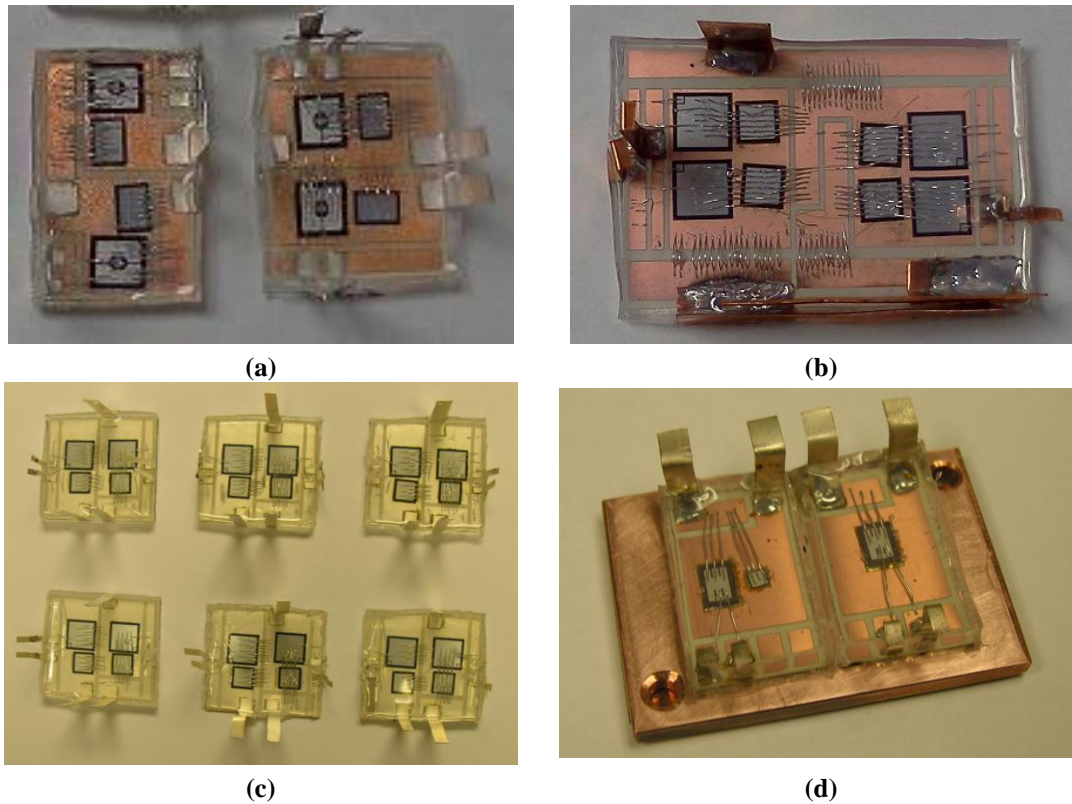
Fig. 10. Prototypes fabricated in the ORNL PEPL for other APEEM projects: (a) high power density integrated traction machine drive, (b) reduced stray inductance power module, (c) segmented drive phase legs, and (d) coupon for wide bandgap package.

Conclusion

In FY 2011, ORNL continued power device packaging research in three key areas: benchmarking, support for APEEM projects, and advanced power module development.

- Four advanced automotive power modules (Prius10, Infineon HP1, Mitusbishi TPM_II, and Nissan Leaf) have been benchmarked using ORNL's comprehensive automotive power module evaluation system.
- Four new prototype modules have been packaged for further system improvement.
- An innovative packaging technology has been invented featuring comprehensive improvement in performance, reliability, and cost effectiveness by structure optimization and material and processing development.
- A phase leg power module prototype with double sided planar interconnection and integrated heat exchangers has been developed. Initial analysis has confirmed its features of low parasitic electric parameters, low thermal resistance, and low manufacturing cost.

All these efforts contribute toward meeting 2015 DOE APEEM program challenging targets in PE systems cost, power density, and efficiency.

Patents

Zhenxian Liang, Fred Wang, Puqi Ning, and Laura Marlino, *Power Module Packaging with Double Sided Planar Interconnection and Heat Exchangers,* serial number 61/509312, filed 07/19/2011.

Publications

Zhenxian Liang, "Power Device Packaging," DOE VTP APEEM Kickoff Meeting, Oak Ridge, Tennessee, November 16–19, 2010.

Zhenxian Liang, Fred Wang, and Laura Marlino "Automotive Power Module Packaging: Issues and Technologies," APEC'11, Session 2.1, Fort Worth, Texas, March 8, 2011.

Zhenxian Liang, "Power Device Packaging," DOE AMR, Washington, DC, June 9, 2011.

Zhenxian Liang, Laura Marlino, and Fred Wang, "Challenges and Technologies of Power Semiconductor Module Packaging for Electric and Hybrid Electric Vehicles," SEMICON WEST'11 Keynote presentation, July 12, 2011.

Zhenxian Liang, Puqi Ning, Fred Wang, and Laura, Marlino, "Power Module Packaging with Double Sided Planar Interconnection and Heat Exchanger," ORNL PE Symposium, July 22, 2011.

Zhenxian Liang and Laura Marlino, "Power Semiconductor Module Packaging for Electric and Hybrid Electric Vehicles," Power Electronics Summit, Detroit, Michigan, Aug 8, 2011.

Zhuxian Xu, Ming Li, Fred Wang, and Zhenxian Liang, "Investigation of Si IGBT Operation at 200°C for Traction Application," ECCE'11, Phoenix, Arizona, September 19–22, 2011.

References

1. Natsuki Nozawa, Takeshi Maekawa, Shigeyuki Nozawa, and Ken Asakura, "Development of Power Control Unit for Compact-Class Vehicle," in Procs. 2009 SAE International Conference, p. 2009-01-1310.

2. Infineon Technologies, HybridPack 1, product information, available online at http://www.infineon.com/cms/en/product/power-modules-and-discs/hybridpack%E2%84%A2-modules/hybridpack%E2%84%A21/channel.html?channel=db3a3043136fc1dd011370f45ed90441.

3. Tetsuya Ueda, Naoki Yoshimatsu, Nobuyoshi Kimoto, Dai Nakajima, Masao Kikuchi, and Toshiaki Shinohara, "Simple, Compact, Robust and High-Performance Power module T-PM (Transfer-molded Power Module)," in *Proceedings of the 22nd International Symposium on Power Semiconductor Devices & ICs,* Hiroshima, Japan, June 6–10, 2010, pp. 47–50.

4. Hsueh-Rong Chang, Jiankang Bu, George Kong, and Ricky Labayen, "300 A, 650 V, 70 um Thin IGBTs with Double-Sided Cooling," in *Proceedings of The 23rd International Symposium on Power Semiconductor Devices & ICs,* San Diego, California, May 23–26, 2011, pp. 320–323.

5. Thomas Stockmeier, Peter Beckedahl, Christian Goebl, and Thomas Malzer, "Skin: Double side Sintering Technology for New Packages," in *Proceedings of the 23rd International Symposium on Power Semiconductor Devices & ICs,* San Diego, California, May 23–26, 2011, pp. 324–327.

6. Yoshinori Sato, Shigeaki Ishikawa, Takahito Okubo, Makoto Abe, and Katsunori Tamai, "Development of High Response Motor and Inverter System for the Nissan LEAF Electric Vehicle," International World Congress and Exhibition, Detroit, Michigan, April 12–14, 2011, paper 2011-01-0350.

2.3 Converter Topologies for Wired and Wireless Battery Chargers

Principal Investigator: Gui-Jia Su
Oak Ridge National Laboratory
National Transportation Research Center
2360 Cherahala Boulevard
Knoxville, TN 37932
Voice: 865-946-1330; Fax: 865-946-1262; E-mail: sugj@ornl.gov

DOE Technology Development Manager: Susan A. Rogers
Voice: 202-586-8997; Fax: 202-586-1600; E-mail: Susan.Rogers@ee.doe.gov

ORNL Program Manager: Mitch Olszewski
Voice: 865-946-1350; Fax: 865-946-1262; E-mail: olszewskim@ornl.gov

Objectives
- Overall project objectives
  — Develop a 5 kW integrated wired battery charger that fully utilizes the existing onboard power electronics components to reduce the cost, volume, and weight and simultaneously provide galvanic isolation and the capability of charging fully depleted batteries.
  — Develop converter topologies suitable for wireless charging systems and design, build, and test prototypes.
- Objectives for FY 2011 effort
  — Perform circuit simulation study and generate a converter design for a 5 kW integrated wired charger.
  — Develop converter topologies for wireless chargers through circuit simulation.

Approach
- Wired charger
  — Use the existing onboard power electronics components to reduce cost, weight, and volume and accomplish galvanic isolation.
- Wireless charger
  — Investigate converters suitable for wireless charging systems by simulation and bench tests. Converter topology candidates include the following:
    ► ac-dc plus dc-dc, and
    ► ac-ac plus ac-dc.
  — The following control methods for efficiency improvements will also be included:
    ► alternative resonant modes that can significantly reduce circulating current,
    ► soft-switching to reduce switching loss and electromagnetic interference (EMI) noises, and
    ► synchronous rectification to reduce conduction loss.

Major Accomplishments
- Wired charger
  — Developed a new approach that utilizes the onboard power electronics components to reduce the cost, weight, and volume of onboard chargers; accomplish galvanic isolation; and accommodate a wide range of battery voltages.
  — Proved the concept using detailed circuit simulations, and confirmed high power quality performance.

► Total harmonic distortion (THD) factors range from 2.8% to 6.6% and are less than 5% when charging rates are more than 1 kW.
► Power factors range from 97% to 99.6% and are greater than 98% when charging rates are more than 1 kW.

— Completed a converter design for a 5 kW integrated wired charger with an estimated cost reduction of 80% compared to a standalone onboard battery charger.

- Wireless charger
  — Developed two converter topologies with reduced switch count and passive component requirements. Simulation results proved the concepts.
  — Confirmed a high power factor resonant circuit was effective in reducing the circulating current and the associated losses. Simulation results showed reductions in the range of 70% to 75% for the current and 14% to 38% for the losses.

Future Direction

- Design, build, and test a 5 kW integrated wired charger prototype.
- Design, build, and test a 5 kW wireless charger converter prototype.
- Demonstrate a wireless charger prototype in a vehicle charging system.

Technical Discussion

Background

Plug-in electric vehicles (PEVs) are emerging as a pre–fuel-cell technology that offers greater potential to reduce oil consumption and carbon dioxide emissions than hybrid vehicles currently on the market. In PEVs, the energy storage capacity of the battery needs to be increased significantly to enable a driving distance of at least 40 miles in an all-electric mode, the distance needed to substantially reduce oil consumption for daily commuting. A charger is also required to replenish the battery after it is depleted, typically done overnight to leverage energy costs by taking advantage of off-peak electricity rates [1].

Stand-alone battery chargers, however, impose an extra cost on already expensive hybrid electric vehicles (HEVs) and have other limitations. A typical stand-alone battery charger for PEVs consists of a diode rectifier with power factor correction (PFC) and a unidirectional dc-dc converter (i.e., it can only charge the battery) that uses power semiconductor switches, diodes, inductors, and capacitors, as shown in Fig. 1. A charger with a low charging capability of 1 to 3 kW can cost almost 30% as much as the electric traction system for a mid-size PEV car (estimated at $300 to $400, about half of the DOE 2015 cost target of $660 for the entire traction drive system). The limited charging capability results in a long charging time (6–8 h), which could negatively impact the acceptance of PEVs. Moreover, most of the onboard chargers on the market are unidirectional [can only charge the battery but are not capable of vehicle-to-grid (V2G) support] to keep costs low.
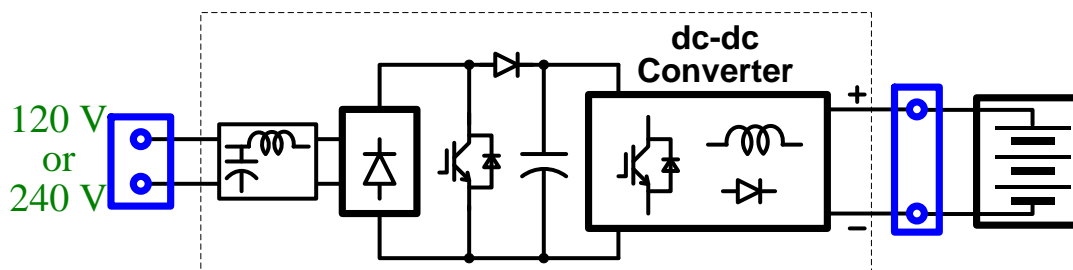
Fig. 1. A schematic showing major components in a stand-alone wired battery charger.

To minimize the cost of the charger while simultaneously providing other desirable functionalities such as V2G support and mobile power generation, a previous project finished in FY 2009 examined the use of

the power electronics and motors already aboard the vehicle to fulfill the charging requirements [2,3]. The project demonstrated that, compared with a stand-alone battery charger, this approach imposes virtually no additional cost or significantly reduces the cost, depending on the configuration of the onboard traction drive system. The proposed approach is to integrate the battery charging function into the traction drive system and eliminate or minimize the number of additional components. Because traction power inverters have a greater current-carrying capability, the integrated charger can reduce the charging time significantly. Another benefit of this approach is that it enables PEVs to function as mobile power generators and provide V2G support capabilities at little or no additional cost. An integral charger prototype (Fig. 2) utilizing a traction drive comprising a

**Fig. 2. An integral charger prototype utilizing a traction drive comprising a 55 kW motor inverter and a 30 kW generator inverter.**

55 kW motor inverter and a 30 kW generator inverter was demonstrated with (1) capability of providing charging power of 20 kW; (2) 90% cost reduction compared to a standalone charger; (3) high efficiencies of 93% to 97%; and (4) charging, mobile power generation, and vehicle-to-grid operations.

It has been found, however, that the integrated charger lacks galvanic isolation, which makes it difficult to meet safety requirements and the ability to charge "dead" batteries. One main task of this project is, therefore, to propose an integrated charger topology that utilizes the onboard traction drive system and the low-voltage converter to reduce the cost, volume, and size while simultaneously providing galvanic isolation and the capability to charge fully depleted batteries.

On the other hand, in the long term it is highly desirable to have charging systems that can transfer electric power from the grid to a vehicle to charge the batteries with minimal or no user intervention, not only because they offer ultimate convenience but also because they prevent users forgetting to plug in their vehicles. These desirable capabilities can be fulfilled with magnetically coupled wireless chargers. Until recently, conventional magnetically coupled systems required a gap of less than a centimeter. This is not practical for vehicles of the future. Power transferred by standing electromagnetic waves induced by the magnetic dipole of a loosely coupled air core transformer can theoretically provide the mechanism for this power transfer over a significant fraction of a meter without physical contact, eliminating the need for precision alignment between a vehicle and its power source. The air core is responsible for the loose coupling of this transformer's primary (transmitter) and secondary (receiver). By comparison, the wireless power transfer technology used by most systems on the market today is inductive power transfer, which uses a fair amount of magnetic core material to increase the coupling. Figure 3 illustrates a conceptual block diagram for wireless chargers based on a loosely coupled transformer in which an ac 50/60 Hz voltage is converted by the ac-ac converter into a high frequency voltage in the range of tens of kilohertz to several megahertz and transmitted to the onboard ac-dc converter through the loosely coupled transformer, where it is converted to a dc voltage and charges the battery.
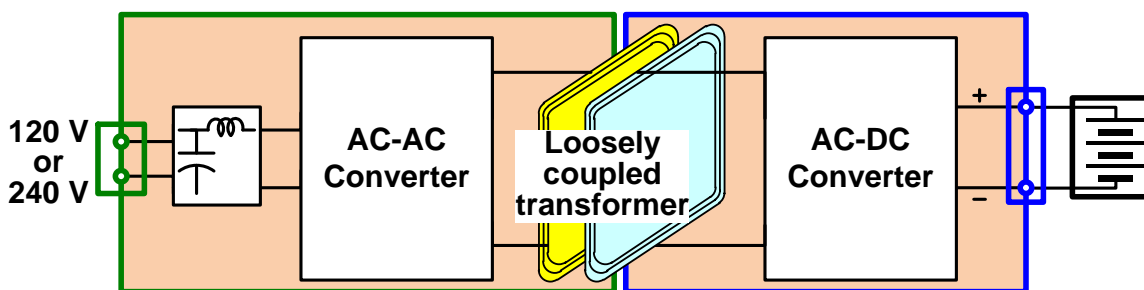
Fig. 3. A conceptual block diagram for wireless chargers based on a loosely coupled transformer.

ORNL is investigating an air core based wireless charger that is divided into two parts–one part installed in a vehicle with a receiver antenna and the other part positioned in garages or other charging stations with a transmitter antenna buried underground–and transfers power across the antennas without the need of plugging a cable into the vehicle. With the help of sensors and wireless communication systems, battery charging can be initiated and managed by a charger controller without user intervention other than parking a vehicle at a specified location. The ORNL work has been focused on antenna design and power transfer capability against misalignments of the antennas and has demonstrated power transfer greater than 4 kW in a full-scale laboratory apparatus (Fig. 4) with an efficiency of 95% from the transmitting antenna to a battery-like load with an antenna separation of 25.4 cm. Higher power transfer levels will only require components with higher voltage and current ratings. However, efficiency becomes a significant factor in overall cost. Converters with high efficiency and power factor and suitable for the wireless charging system are needed and thus developing such converter topologies is the second main task for this project.
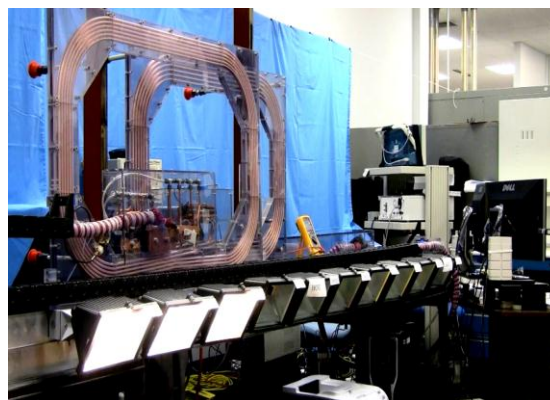
Fig. 4. ORNL laboratory test apparatus with alignment-adjustable antennas for wireless power transfer.

Integrated Wired Charger

Figure 5 shows the previous topologies for using the onboard electrical drive system (without galvanic isolation) to provide plug-in charging and mobile generation capabilities for HEVs. The new approach under investigation in this project will similarly utilize the traction drive system components but also add galvanic isolation. Details of the new circuit topology, however, will not be disclosed in this report because it is under patent review.

The onboard electrical drive system may consist of one or more electrical motor drive units, all connected to a common dc bus. Each motor drive unit typically employs a three phase inverter/converter (INV/CONV) and a three phase motor/generator (M/G) with a Y-connection of stator windings with a neutral point ($N_{M/G}$). At least one drive unit is coupled to the engine shaft through a mechanical transmission device. The basic idea is to use the M/Gs as inductors by connecting their neutral points to an external charging source to charge the battery or to external loads to supply power to them. The external charging source can be a dc or single phase or three phase ac power supply, depending on the number of onboard drive units. Figure 5(a) illustrates an arrangement for a series HEV in which two INV/CONVs and two M/Gs are used. For such vehicles, virtually no additional components except some wiring and connectors are required. An ac filter capacitor may also be needed to meet grid interface power quality requirements. For parallel HEVs, in which only one INV/CONV and M/G are used, two switches must be added, as shown in Fig. 5(b).

(a)   **(b)**
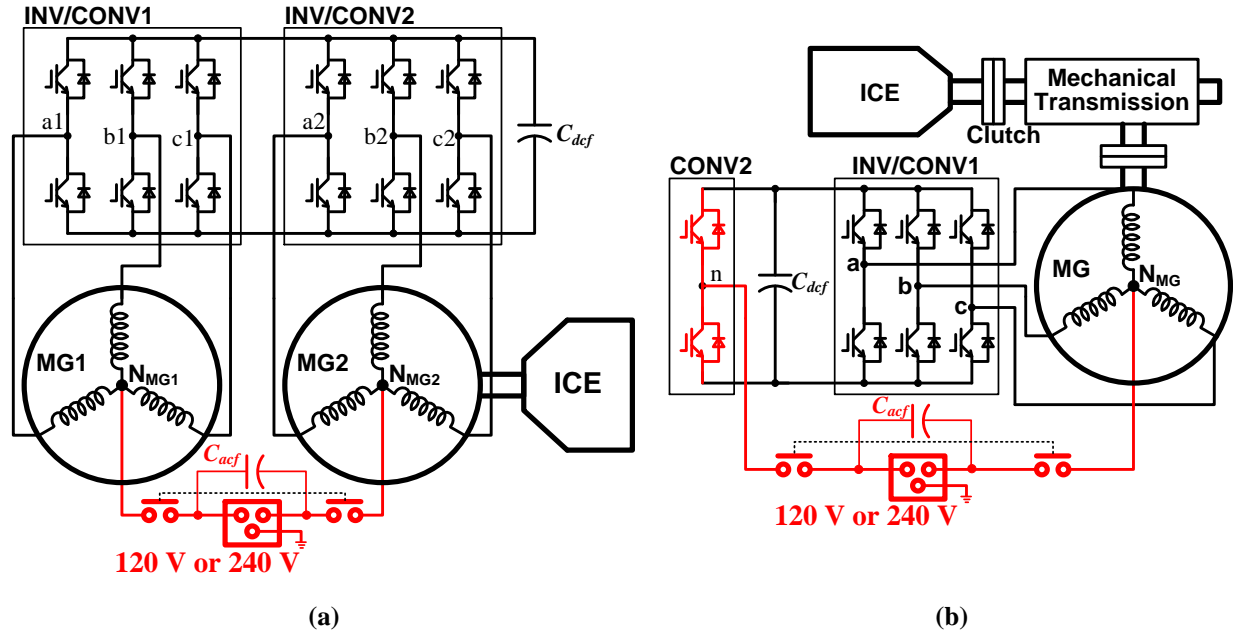
Fig. 5. The previous topologies for using the onboard electrical drive system to provide plug-in charging and mobile generation capabilities for HEVs: (a) for HEVs using two inverters and motors and (b) for HEVs using a single inverter and motor. (Red denotes added components.)

All the switch legs in each INV/CONV collectively function as a single switch leg and the M/G as an inductor (i.e., its stator zero sequence impedance network, consisting of three branches and each branch comprising the stator winding phase resistance and the stator phase leakage inductance). Together, the drive units form a single phase or multiphase converter, operating in the charging mode, to regulate the dc bus voltage. In the generation mode, the drive units form a single phase or multiphase inverter to supply external loads. In this mode, the M/G of the drive unit coupled to the engine shaft is driven by an engine to generate power to supply the dc bus and ultimately the external loads. Or power can be drawn from the battery for short operating intervals. An additional benefit of operating the three phase converters as single leg converters is the reduction in harmonic current components resulting from interleaving the gating signals of the three legs.

Detailed circuit simulations were performed in PSIM[*] to prove the concept and provide circuit design data for use in development of a prototype 5 kW integrated wired charger in FY 2012. Figure 6 gives simulation waveforms of input source voltage and current, "vs" and "is," and battery voltage and current, "Vbatt" and "Ibat," for charging at the rated power of 5 kW from a 240 V source showing capability for charging at the nominal battery voltage of 325 V [6(a)] and fully depleted battery voltage of 200 V [6(b)]. Figure 7 gives the same simulated waveforms for charging off a 120 V source at a rate of 2 kW, which is below half the rated power but slightly higher than the power limits of typical household 120 V outlets. The results again illustrate the capability for charging at the nominal [7(a)] and fully depleted [7(b)] battery voltage levels. In both cases, the input source currents are sinusoid shaped and are in phase with the source voltages because the charger produces very low THD factors but high power factors.

Figure 8 plots simulated THD factors against charging power, and Fig. 9 power factor vs charging power. The THD factors are in the range of 2.8% to 6.6% and lower than 5% when charging rates are more than 1 kW. The power factors are in the range of 97% to 99.6% and greater than 98% when charging rates are more than 1 kW.

---

[*]Simulation software from Powersim Inc.

The simulation results generated voltage and current requirements for the switches and passive components. A converter design for a 5 kW integrated wired charger incorporating these requirements was completed. From the bill of material, it was estimated that a cost reduction of 70% could be achieved compared to a stand-alone onboard battery charger.

(a)   **(b)**
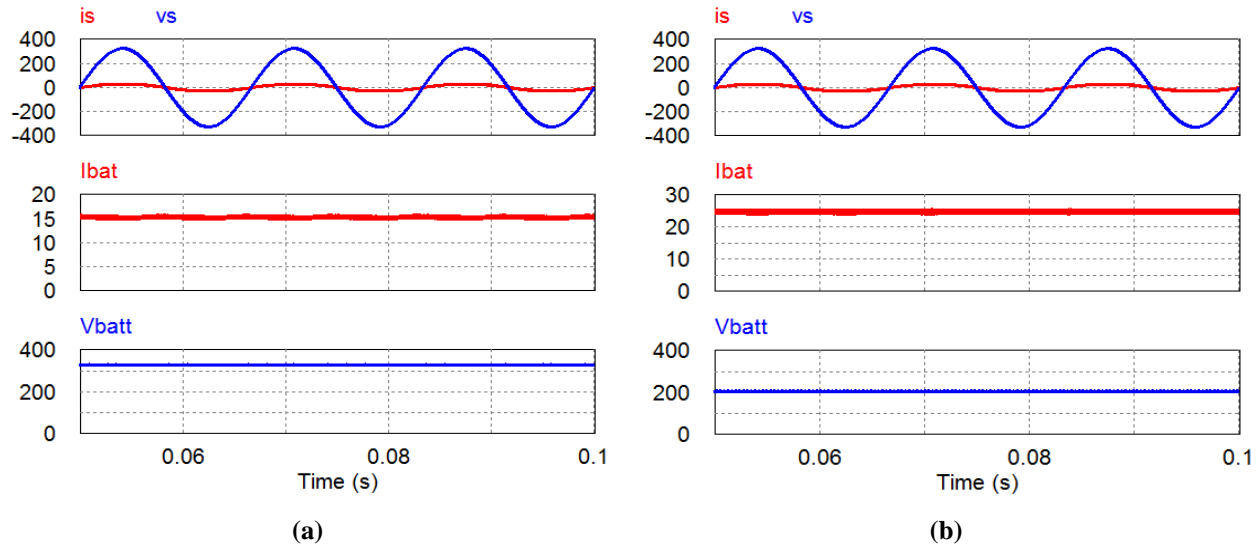
Fig. 6. Simulation results for charging at 5 kW from 240 V input showing capability for charging at (a) nominal battery voltage of 325 V and (b) fully depleted battery voltage level of 200 V.

(a)   **(b)**
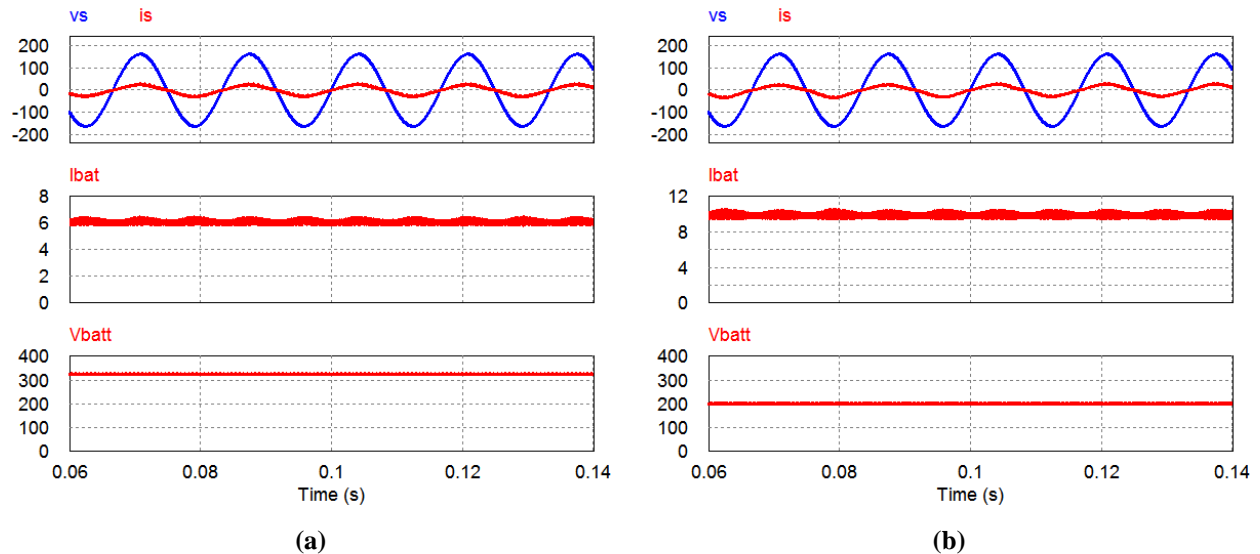
Fig. 7. Simulation results for charging at 2 kW from 120 V input showing capability for charging at (a) nominal battery voltage of 325 V and (b) fully depleted battery voltage level of 200 V.
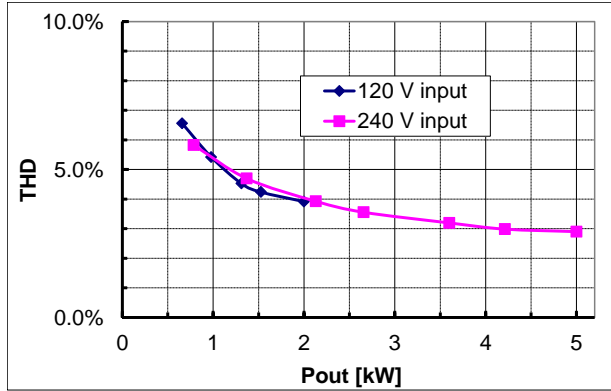
Fig. 8. THD vs charging power.
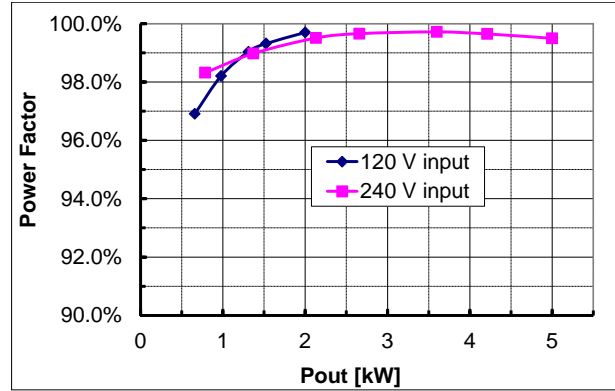
Fig. 9. Power factor vs charging power.

Wireless Charger

A converter topology study through simulation was carried out. In particular, two new topologies with reduced switch count and passive components were investigated through modeling and simulation. The first one comprises an ac-dc and dc-dc converter, and the second one is based on ac-ac-dc conversion. Details of the topologies will not be discussed in this report because they are under patent review. Compared to a typical wireless charger converter shown in Fig. 10, the proposed converters can either reduce the number of switches or significantly reduce the dc bus capacitance. In addition, an investigation on resonant circuit designs was also conducted to minimize the reactive power requirements by the air core transformer through increasing its power factor, thus reducing the circulating current and losses in the resonant circuit and converter and increasing the system efficiency. Furthermore, the following efficiency improvement techniques were included in the topology study: (1) soft switching to reduce switching loss and EMI noises and (2) synchronous rectification to reduce conduction loss.
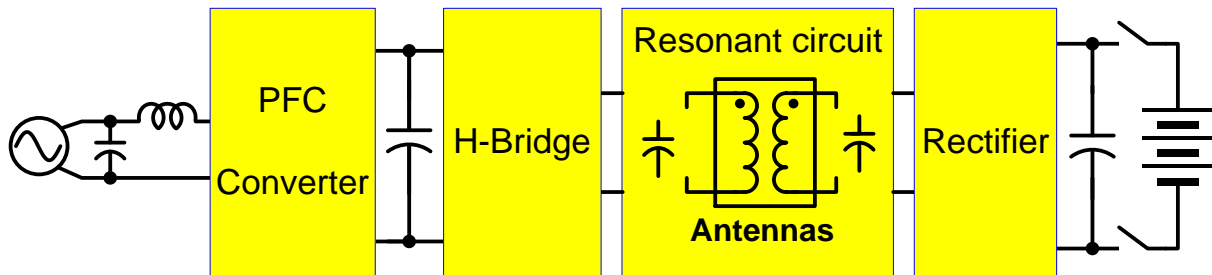
Fig. 10. A simplified block diagram for a typical wireless charger converter.

Figure 11 shows typical simulated operating waveforms for the ac-dc + dc-dc converter: source voltage and current, dc bus voltage, and high frequency output current to the transformer. The source current is sinusoidal and in phase with the source voltage, indicating a low THD and high power factor. Figure 12 gives typical simulation results for the ac-ac-dc converter: source voltage and current, high frequency ac link voltage, and high frequency output current to the transformer. Again, the source current is sinusoidal and in phase with the source voltage. These simulation results confirmed the operating principles of the converters.
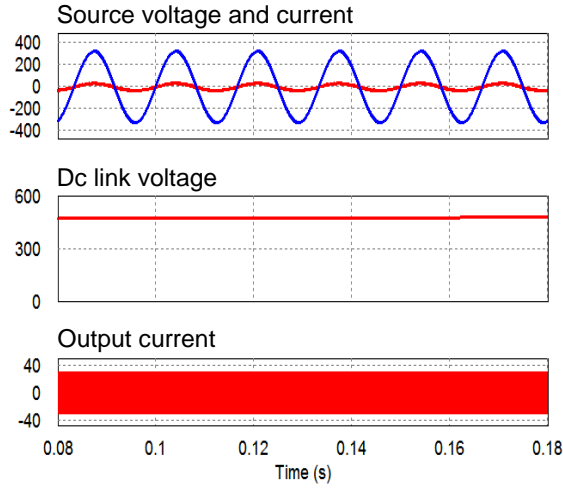
Fig. 11. Simulated operating waveforms for the ac-dc + dc-dc converter.
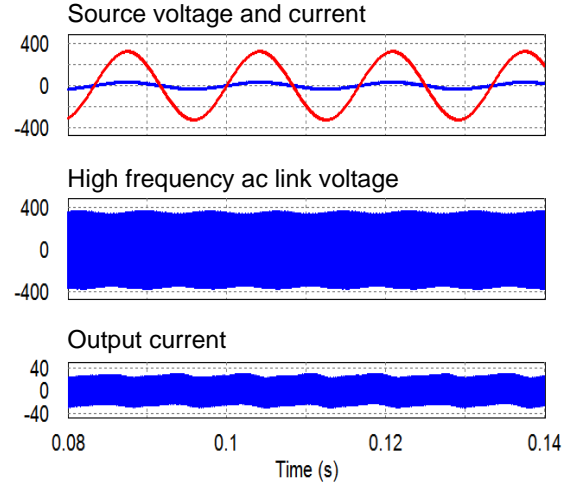
Fig. 12. Simulation results for the ac-ac-dc converter.

Figure 13 gives simulation results for charging the battery at the rated power of 5 kW to show the impact of the power factor of the resonant circuit on the primary current in which "vs" and "is" are source voltage and current; "Vbatt" and "Ibat" battery voltage and current; and "vab" and "io" primary voltage and current. Figure 13(a) is for a low power factor resonant circuit that produced a high primary current of io = 64.33 Arms, while Fig. 13(b) is for a high power factor resonant circuit that significantly reduced the primary current of io to 19.33 Arms.

(a)

(b)
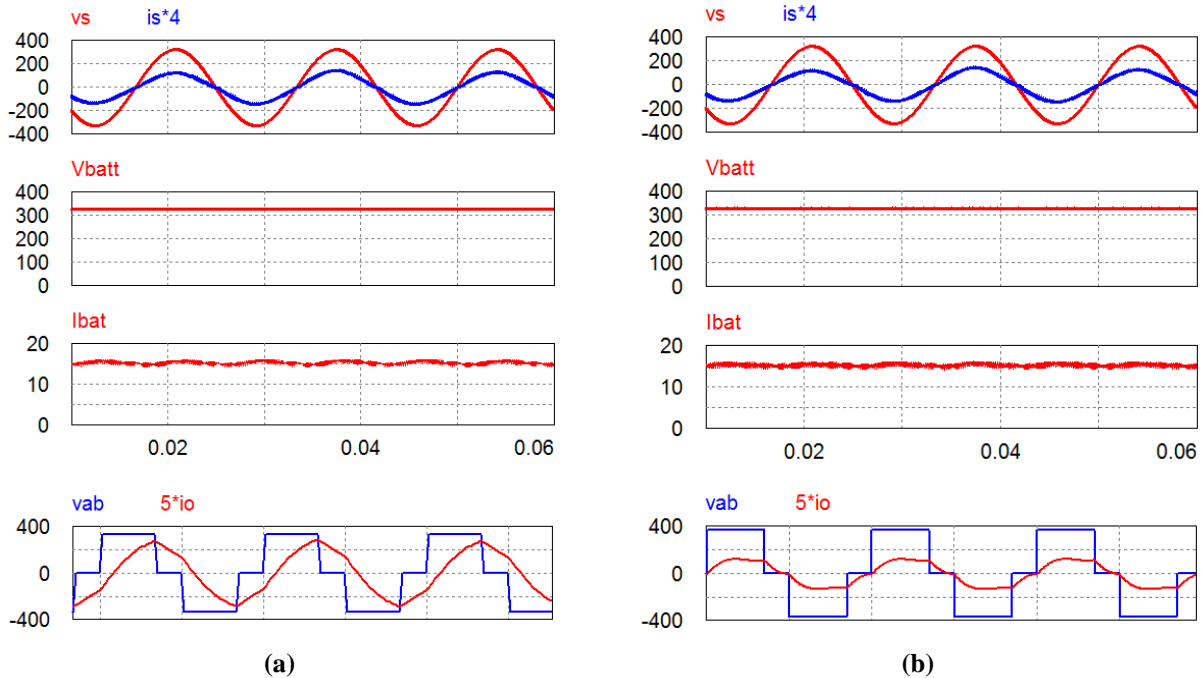
Fig. 13. Simulation results for charging at 5 kW showing the impact of the power factor of the resonant circuit on the primary current for (a) a low power factor resonant circuit that produced a high primary current of 64.33 Arms and (b) a high power factor resonant circuit that produced a significantly lower primary current of 19.33 Arms.

Figure 14 gives simulation results for charging the battery at half the rated power of 2.5 kW. With the low power factor resonant circuit, the primary current of io = 63.07 Arms remains at almost the same level for charging at 5 kW, while io is reduced to16.42 Arms for the high power factor resonant circuit. In both cases, the source currents are sinusoidal and in phase with the source voltages, indicating low THD factors and high power factors.

<div align="center">(a)   (b)</div>
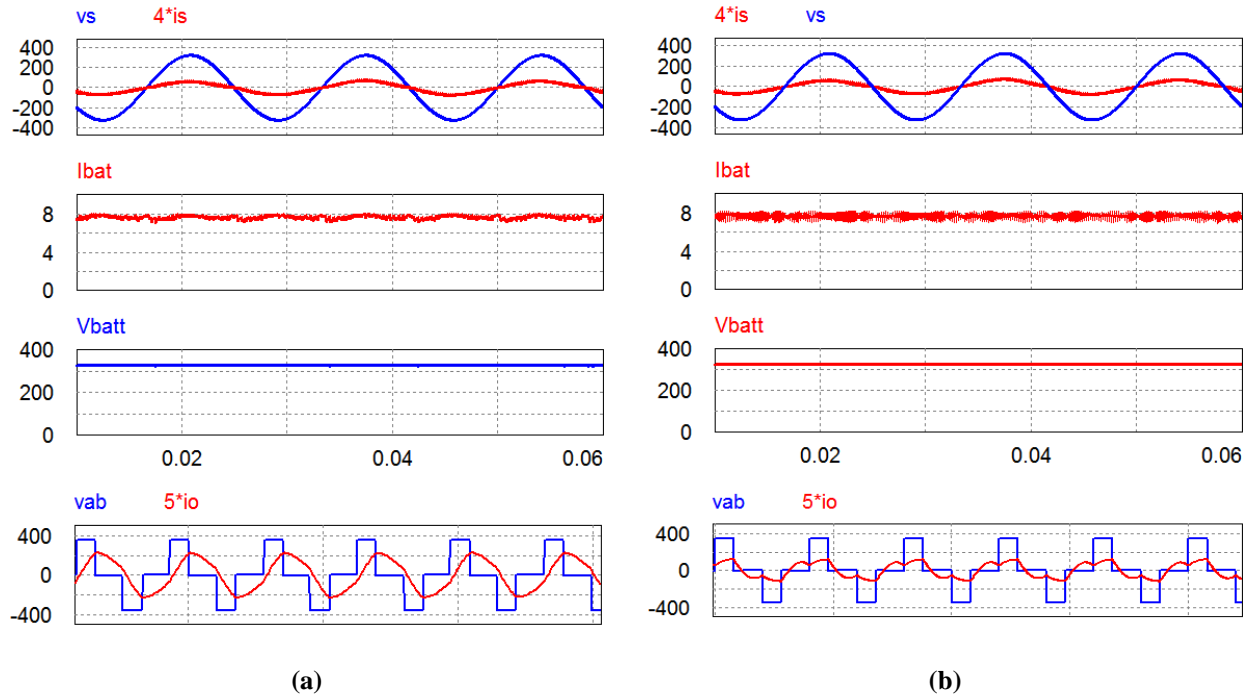
Fig. 14. Simulation results for charging at 2.5 kW showing the impact of the power factor of the resonant circuit on the primary current for (a) the low power factor case, resulting in a primary current of 63.07 Arms, and the high power case, with a primary current of 16.42 Arms.

The lower primary current levels with the high power factor resonant circuit lead to lower losses. For a comparison of losses and primary currents between the two resonant circuits, Fig. 15 plots the losses and primary current of the high power factor resonant circuit as percentages of those for the low power factor resonant circuit at various charging rates. The chart shows a range of 25% to 30% for the current and 62% to 86% for the losses. The chart also illustrates a significant reduction in the losses with the high power factor resonant circuit that increases as the charging power decreases.
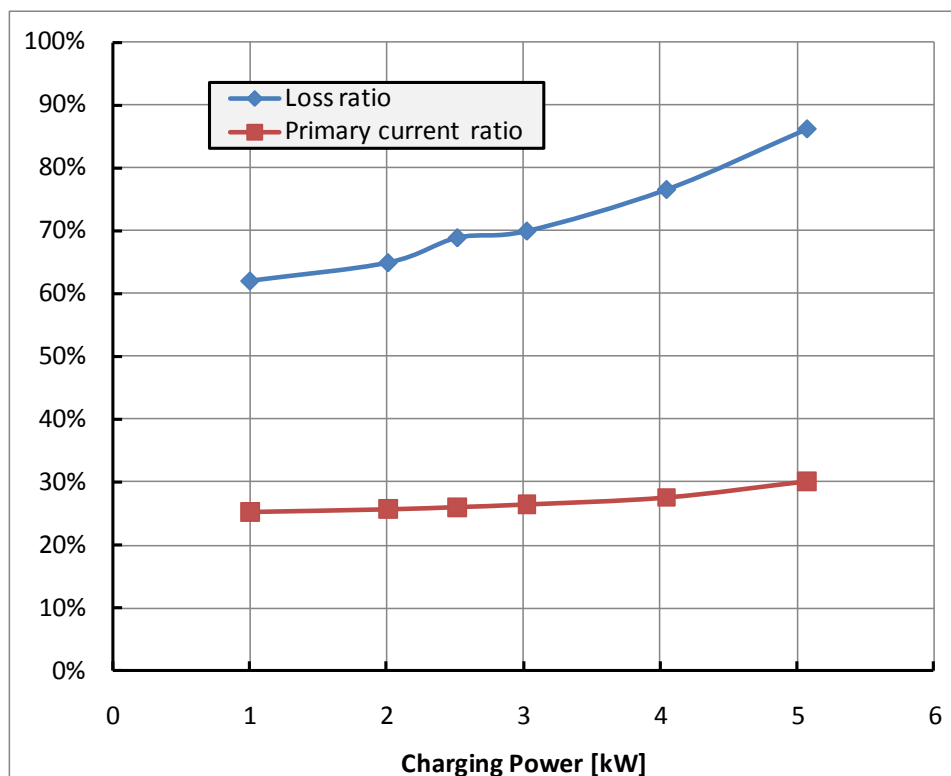
**Fig. 15. Comparison of losses and primary currents between the high power
factor and low power factor resonant circuits at various charging rates.**

Conclusion

This project extends the previous approach of using the onboard power electronics components to provide plug-in charging functionality. The new approach under investigation in this project similarly utilizes the traction drive system components to reduce the cost, weight, and volume but also accomplishes galvanic isolation. Detailed circuit simulations were carried out, and the simulation results proved the concept and showed high performance in meeting the utility connection requirements for power quality: (a) THD factors are in the range from 2.8% to 6.6% and lower than 5% when charging rates are more than 1 kW and (b) the power factors are in the range from 97% to 99.6% and greater than 98% when charging rates are more than 1 kW. Based on the simulation results a converter design for a 5 kW integrated wired charger was completed with an estimated cost reduction of 80% compared to a stand-alone onboard battery charger.

Two converter topologies with reduced switch count and passive component requirements for wireless chargers were also investigated through modeling and simulation. A high power factor resonant circuit was found effective in reducing the circulating current and the associated losses. Simulation results showed reductions in the range of 70% to 75% for the current and 14% to 38% for the losses.

Patents

G. J. Su, Invention disclosure 201002409, "AC-DC Power Conversion Apparatus and Method," March 2011.

Publications

None.

<u>References</u>

1. *Advanced Batteries for Electric-Drive Vehicles*, Report 1009299, Electric Power Research Institute: Palo Alto, California, May 2004.

2. G. J. Su, US Patent 7,733.039B2, *Electric Vehicle System for Charging and Supplying Electrical Power,* June 8, 2010.

3. L. Tang and G. J. Su, "A Low-Cost, Digitally-Controlled Charger for Plug-In Hybrid Electric Vehicles," *IEEE Energy Conversion Congress and Exposition (ECCE)*, September 20–24, 2009, San Jose, California, pp. 3923–3929.

2.4   Inverter Using Current Source Topology

Principal Investigator: Gui-Jia Su
Oak Ridge National Laboratory
National Transportation Research Center
2360 Cherahala Boulevard
Knoxville, TN 37932
Voice: 865-946-1330; Fax: 865-946-1262; E-mail: sugj@ornl.gov

DOE Technology Development Manager: Susan A. Rogers
Voice: 202-586-8997; Fax: 202-586-1600; E-mail: Susan.Rogers@ee.doe.gov

ORNL Program Manager: Mitch Olszewski
Voice: 865-946-1350; Fax: 865-946-1262; E-mail: olszewskim@ornl.gov

Objectives

- Overall project objectives
  — Develop novel Z-source current source inverter (ZCSI) topologies that combine the benefits of ORNL's current source inverter (CSI) efforts and Michigan State University's work on Z-source inverters (ZSIs) to significantly reduce cost and volume through the integration of voltage boost, inverter, regenerative braking (regen), and plug-in electric vehicle charging functions.
- Objectives for FY 2011 effort
  — Perform a simulation study on ways to reduce passive component requirements for ZCSI on the selected ZCSI topology.
  — Design, assemble and test a 10 kW ZCSI setup using reverse-blocking (RB) insulated gate bipolar transistors (IGBTs) to validate the simulation study.

Approach

- Use ORNL's CSI with a quasi-Z network of passive components to enable
  — single stage voltage buck and boost power conversion,
  — battery charging,
  — safe operation in open- and short-circuit events,
  — reduction of total capacitance,
  — supply of sinusoidal voltages and currents to the motor, and
  — extension of constant-power speed range without using a dc-dc boost converter.
- Eliminate antiparallel diodes with RB-IGBTs.

Major Accomplishments

- Confirmed through simulation that using the modulation signal angle control method can significantly increase the output voltage to the point that is only limited by the voltage rating of the switches in the inverter, thus eliminating the need for high numbers for the turns ratio of the coupled inductor.
- Completed a design for a 10 kW ZCSI based on the current-fed trans-quasi-ZSI (CF-trans-qZSI) using first generation RB-IGBT technology. The design yields a specific power of 4.85 kW/kg, power density of 14.2 kW/L, and efficiency of 97.7% in boost mode and 97.1% in buck mode. With next generation RB-IGBT technology, the efficiency numbers can be increased to 98.7% and 98%, respectively.
- Test results with a 10 kW prototype demonstrate the following:
  — Capacitance reduction to 80 µF [200 µF for a voltage source inverter (VSI)]

— Output voltage capability range from 0 to 3 times the battery voltage (0–0.99× for a VSI)
— Output voltage total harmonic distortion (THD) factors of 6%–12% (70%–200% for a VSI)
— High efficiency (more than 97% even at a relatively low source voltage of 250 V)

Future Direction

- Design, fabricate, and test 55 kW ZCSI prototypes when new RB switching devices become available.

Technical Discussion

Background

Current electric vehicles (EVs) and hybrid electric vehicles (HEVs) use a type of inverter called a voltage source inverter (VSI) [Fig. 1(a)]. The VSI, while well suited to operate off a battery as the voltage source, possesses several drawbacks that make it difficult for it to meet the U.S. DRIVE goals for inverter volume, lifetime, and cost established by the U.S. Department of Energy and its industrial partners. The VSI requires a very high performance direct current (dc) bus capacitor to maintain a near ideal voltage source and absorb the ripple current generated by the switching actions of the inverter. The root mean square (rms) value of the ripple current can reach 50% to about 80% of the motor current. Concerns about the reliability of electrolytic capacitors have forced HEV makers to use film capacitors, and currently available film capacitors that can meet the demanding requirements of this environment are costly and bulky, taking up one-third of the inverter volume and making up one-fifth of the cost. The reliability of the inverter is also limited by the capacitors and further hampered by the possible shoot-throughs of the phase legs making up a VSI [S_1–S_2, S_3–S_4, and S_5–S_6 in Fig. 1(a)]. Steep rising and falling edges of the pulse width modulated (PWM) output voltage generate high dv/dt related electromagnetic-interference noises, cause motor insulation degradation due to the voltage surges resulting from these rapid voltage transitions, produce high frequency losses in the windings and cores of the motor, and generate bearing-leakage currents that erode the bearings over time. Furthermore, for the VSI to operate from a low voltage battery, a bidirectional boost converter is needed.

All these problems can be eliminated or significantly reduced by the use of another type of inverter, the CSI [Fig. 1(b)]. The CSI requires no dc bus capacitors and uses only three alternating current (ac) filter capacitors of a much smaller capacitance. The total capacitance of the ac filter capacitors is estimated to be about one-fifth that of the dc bus capacitors in the VSI. In addition, the CSI offers many other advantages important for EV/HEV applications: (1) it does not need antiparallel diodes in the switches, (2) it can tolerate phase leg shoot-throughs, (3) it provides sinusoid-shaped voltage output to the motor, and (4) it can boost the output voltage to a higher level than the source voltage to enable the motor to operate at higher speeds. These advantages could translate into a significant reduction in inverter cost and volume, increased reliability, a much higher constant-power speed range, and improved motor efficiency and lifetime. Furthermore, by significantly reducing the amount of capacitance required, the CSI based inverter with silicon IGBTs will be able to substantially decrease the requirements for cooling systems and, further, could enable air-cooled power inverters in the future when silicon carbide based switches become commercially viable.
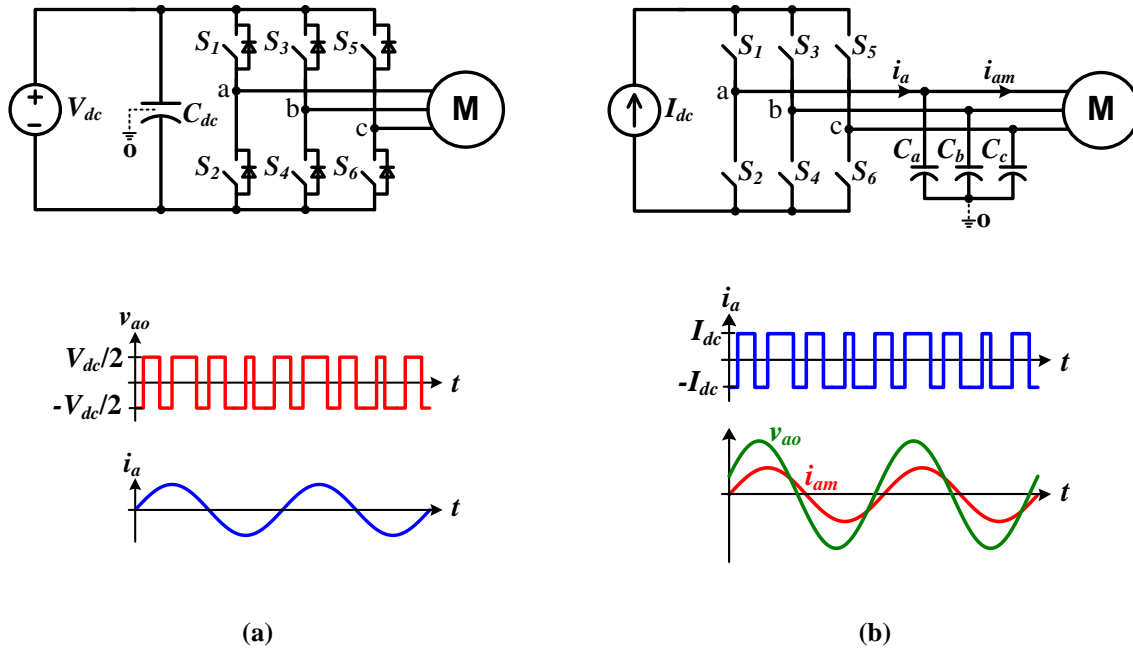
Fig. 1. Schematics of the two types of inverters and typical output voltage and current waveforms: (a) VSI and (b) CSI.

Two factors, however, have so far prevented the application of CSIs in HEVs. The first is the difficulty of incorporating batteries into a CSI as energy storage devices while controlling the motor at low speeds; the second is the limited availability of power switches that can block voltages in both forward and reverse directions. However, IGBTs with RB capability are being offered as engineering samples [1, 2], and the technology is rapidly reaching the maturity needed for commercial production. This project aims to take advantage of the latest technologies to remove the remaining hurdles and bring the CSI to HEV applications by offering new inverter topologies based on the CSI but with novel schemes to incorporate energy storage devices. Two approaches have been examined: one uses a V-I converter and the other uses a passive Z-network of inductors, capacitors, and diodes. The former, although it requires switches, has the advantage of being able to be applied in multiple-motor traction drive systems. This report discusses the work in FY 2011 on the latter approach.

Z-Network Based Current Source Inverter

Two new Z-network based CSI (ZCSI) topologies, CF-trans-qZSI and CF-trans-ZSI, were developed in FY 2010. The CF-trans-qZSI was selected for prototype development in FY 2011. Figure 2 shows a schematic drawing of the CF-trans-qZSI. The inverter topology uses a passive Z-network consisting of a diode, D_1; a capacitor, C_1; and coupled inductors, L_1 and L_2. In addition, a contact switch is used for selecting between the motor/generator (M/G) and a charger port that can be plugged into a single- or three-phase grid to charge the battery. Compared to previous ZCSIs, the new topologies eliminate one capacitor and can extend the constant-power speed range by increasing the coupled-inductor turns ratio to provide a higher voltage boost ratio. Compared to the traditional CSI, the ZCSIs can buck and boost the output voltage in a single stage, charge the battery during regen operation, and tolerate open-circuit conditions in the CSI bridge.
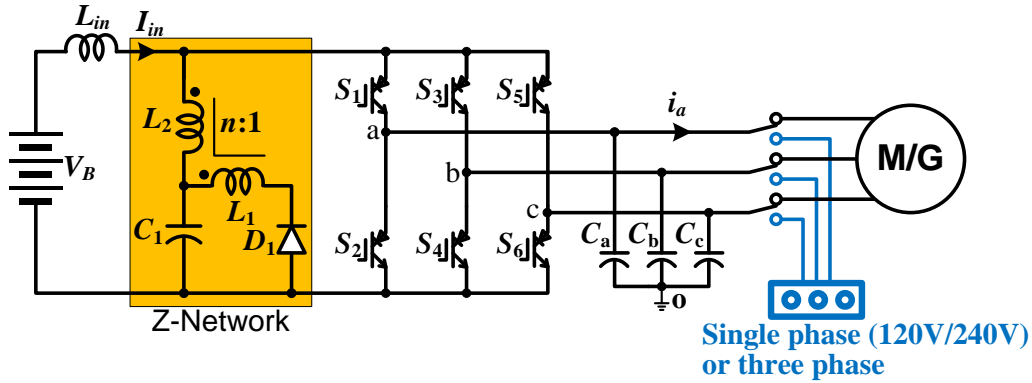
Fig. 2. Schematic of the CF-trans-qZSI with PHEV battery charging ability.

ZCSIs introduce a new zero current state, open-circuit zero state, in which all switches are turned off, in addition to the short-circuit–zero current vector and use this new current vector to step down the output voltage (buck mode) and perform the regenerative function to charge the battery. To control the duty ratio of the open–circuit zero state, in addition to the traditional CSI control method, two open-circuit–zero state references are added to the current references, as shown by the shaded intervals in Fig. 3. During these intervals, the shoot-through zero states, in which both switches, S_1 and S_2, are conducting, are changed to open-circuit zero state by turning off both switches.
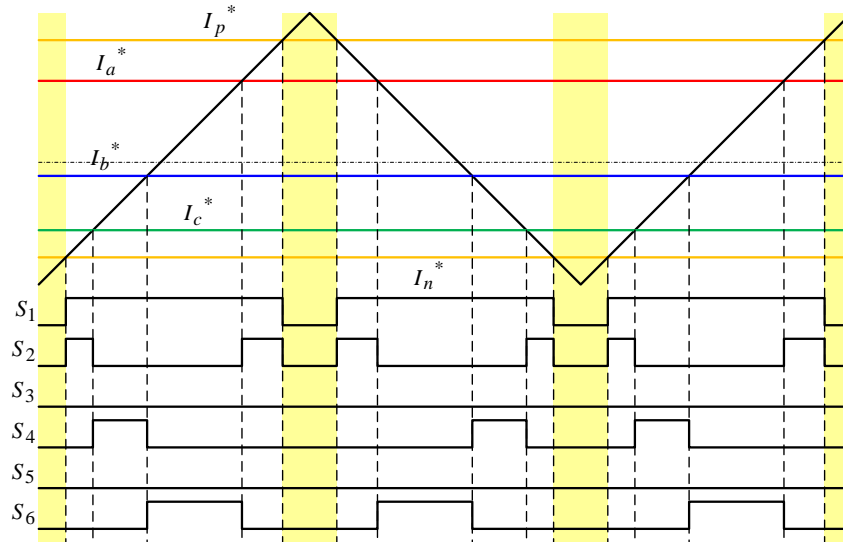
Fig. 3. PWM control method with open-circuit–zero state references inserted.

Depending on how the open-circuit–zero state reference is generated, there are three ways to insert it: (1) simple boost control, in which two straight lines are added as the open-circuit–zero state reference; (2) maximum boost control, which uses the envelop of the three phase current references; and (3) constant boost control, in which the reference is produced by injecting a third harmonic into the current commands, as shown in Fig. 4. The maximum boost control transfers the entire shoot-through–zero state interval to open-circuit zero state, while the simple boost and constant boost control have the same open-state duty cycle over every switching cycle.

42
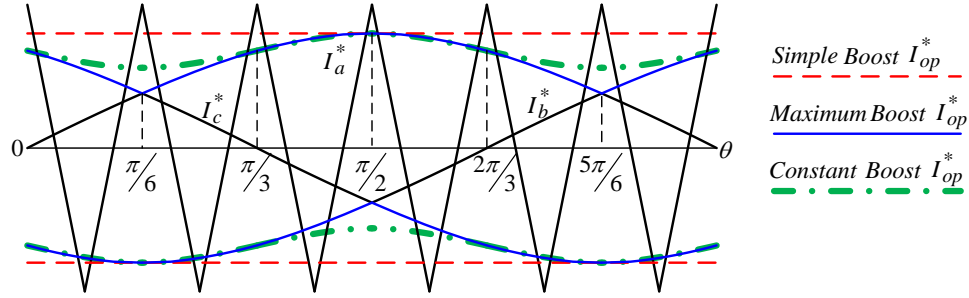
Fig. 4. PWM control methods using three different references to generate the open-circuit zero state.

Figure 5 shows the equivalent circuits of the CF-trans-qZSI for the three operation states: active, shoot-through zero, and open-circuit zero. Figure 5(a) shows the active state, in which the inverter operates in one of the six active states and the diode, D_1, (ref. Fig. 2) is not conducting. Figure 5(b) shows the shoot-through zero state, in which one of the inverter legs is short-circuited and the diode, D_1, is not conducting. Figure 5(c) shows the open-circuit zero state, in which all the switches of the inverter are off and the motor is disconnected from the battery. The diode, D_1, is conducting during this state.
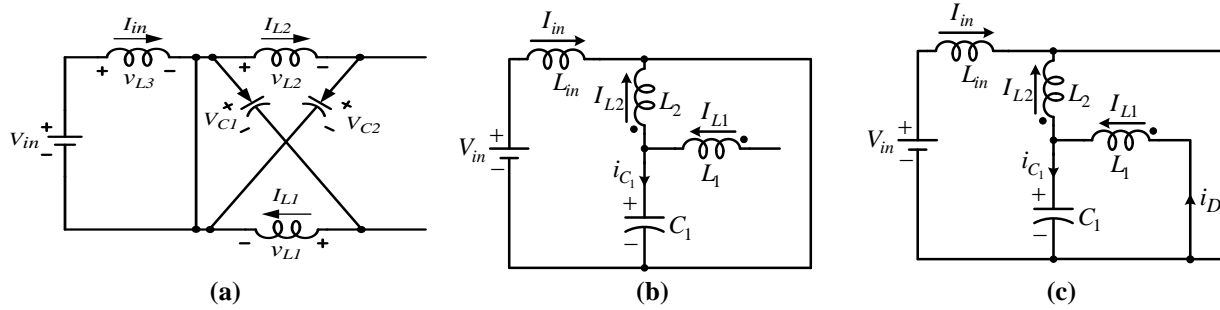
Fig. 5. CF-trans-qZSI equivalent circuit: (a) active state, (b) shoot-through zero state, and (c) open-circuit zero state.

The dc voltage gain of the CF-trans-qZSI can be derived from the equivalent circuits as

$$\frac{V_{out}}{V_{in}} = \frac{1 - D_{op}(n+1)}{D_A} \quad,$$

where n is the turns ratio of the coupled inductor and D_A and D_{op} represent the duty cycles for the active and open-circuit states, respectively.

For a turns ratio of 2 (i.e., $n = 2$) and taking into account that $D_A + D_{op} + D_{sh} = 1$, the above equation becomes

$$\frac{V_{out}}{V_{in}} = \begin{cases} \dfrac{1}{D_A} & \text{if } D_{op} = 0 \\[2ex] 3 - \dfrac{2}{D_A} & \text{if } D_{sh} = 0 \end{cases} \quad,$$

where D_{sh} represents the short-circuit–zero state duty ratio.

Figure 6 shows the dc output voltage gain of the CF-trans qZSI. There are three operation regions, A, B, and C. In region B the inverter operates in the motoring mode and can produce an equivalent dc output voltage in the range of 0 to $3V_{in}$. Region C is the regen region, as indicated by the negative output voltage gain. In this region, the inverter can operate as a PWM rectifier and plug in the grid to charge the battery. Region A is a prohibited region because the diode of the Z-network will conduct automatically, interrupting the proper operation of the inverter. The output voltage will get distorted due to the unwanted conduction of the diode. If it is desired to extend the motoring operation region, the diode will have to be replaced with an RB switch. Alternatively, increasing the transformer turns ratio can also extend the motoring operation region. In addition, the line marked "Mode 1" represents the motoring operation region boundary on which no open-circuit zero states are introduced and the highest voltage gain is achieved. The line marked "Mode 2" is the regen region boundary line where all the shoot-through zero states are replaced by open-circuit zero states. During this mode, the inverter produces the lowest possible voltage.
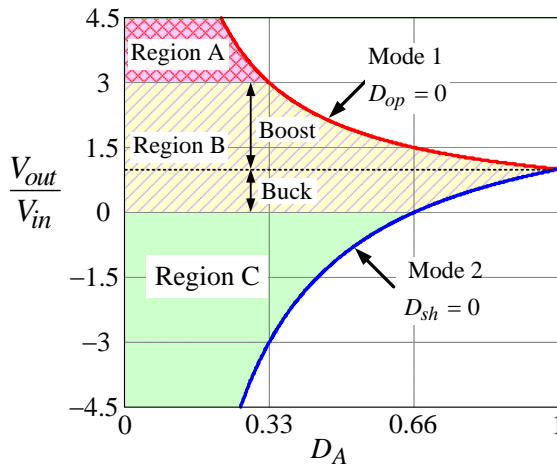
Fig. 6. CF-trans-qZSI dc output voltage gain.

Table 1 summarizes the open-circuit duty cycle, D_{op}, voltage and current gains corresponding to the modulation index, M, for the three control strategies. In the table, n is the turns ratio of the coupled inductor and $\cos\theta$ is the power factor (PF) of the motor.

Table 1. Comparison of the three different control strategies

Control method	D_{op}	Voltage gain	Current gain
Simple boost	$1 - M$	$\dfrac{4}{3M \cos\theta}[M(n+1) - n]$	$\dfrac{M}{M(n+1) - n}$
Maximum boost	$1 - \dfrac{3\sqrt{3}M}{2\pi}$	$\dfrac{4}{3M \cos\theta}\left(\dfrac{3\sqrt{3}M}{2\pi}(n+1) - n\right)$	$\dfrac{2\pi M}{3\sqrt{3}M(n+1) - 2n\pi}$
Constant boost	$1 - \dfrac{\sqrt{3}M}{2}$	$\dfrac{4}{3M \cos\theta}\left(\dfrac{\sqrt{3}M}{2}(n+1) - n\right)$	$\dfrac{2M}{\sqrt{3}M(n+1) - 2n}$

Figure 7 plots the output line-to-line peak voltage gain of the CF-trans-qZSI versus the modulation index at n = 2 and PF = 1 for the three control methods. The simple boost method produces the narrowest operation area, while the maximum boost method leads to a slightly wider regen area than that of the constant boost scheme.
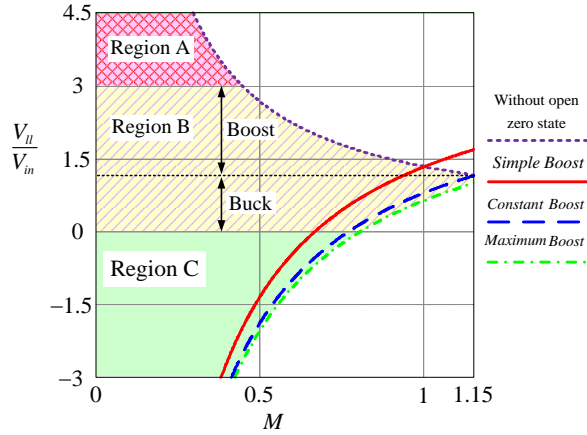
Fig. 7. Output voltage gain at $n = 2$ vs modulation index for the three control methods.

Table 2 shows the switching device stress comparison. The product of the line current, I_{l_rms}, and the maximum input voltage, V_{max}, is used as the base for the power. Because the maximum boost control may lead to discontinuous buck and boost modes, the constant boost control is used to calculate the total switching device power stress ratio (TSDPSR).

Table 2. Switching device stress

Switching device voltage stress, V_S	$(n+1)V_{max}$
Diode voltage stress, V_D	$\left(1 + \dfrac{1}{n}\right)V_{max}$
Switch average current stress, I_{ave}	$\dfrac{\sqrt{2}}{3}I_{l\_rms}$
Diode average current stress, I_D	$\dfrac{\sqrt{2}n(2-\sqrt{3}M)}{\sqrt{3}M}I_{l\_rms}$
Average TSDPSR, $(6V_SI_{ave} + V_DI_D)/V_{max}I_{l\_rms}$	$4\sqrt{2} + \dfrac{2\sqrt{2}n(2-\sqrt{3}M)}{\sqrt{3}M}$
Switching peak current stress, I_{pk}	$\dfrac{2\sqrt{2}}{\sqrt{3}M}I_{l\_rms}$
Diode peak current stress, I_{Dpk}	$\dfrac{2\sqrt{2}n}{\sqrt{3}M}I_{l\_rms}$
Peak TSDPSR, $(6V_SI_{pk} + V_DI_{Dpk})/V_{max}I_{l\_rms}$	$\dfrac{24\sqrt{2} + 4\sqrt{2}n}{\sqrt{3}M}$

Using Phase Angle Control to Extend the Boost Voltage Factor

Because the voltage boost gain is limited by the turns ratio, n, of the coupled inductor, higher voltage boost ratios require a higher n, which is not desirable because it increases the size and weight of the coupled inductor and generates high leakage inductance that causes high transient voltages. There is another way to increase the voltage gain without increasing n.

The voltage, V_{out}, is determined by

$$V_{out} = \frac{3}{4}V_{ll\_pk}M\cos\theta \ ,$$

where V_{ll_pk} and θ are the line-to-line peak voltage and phase angle of modulation signal. For a given V_{out}, decreasing leads to a higher V_{ll_pk}, effectively raising the voltage boost ratio defined as V_{ll_pk}/V_{in}. This method of increasing the output voltage is suited for controlling motors in the field weakening region to extend the motor constant power speed range. A simulation study was carried out, and the results indicated that by using this control method, the output voltage can be increased significantly and is only limited by the voltage rating of the switches in the inverter.

10 kW ZCSI Design, Fabrication, and Test

A design for a 10 kW ZCSI using the CF-trans-qZSI topology was generated for the following conditions.

- Peak power rating: 10 kW
- Battery voltage, V_{in}: 265 V
- Output line-to-line voltage: 0~500 V
- Switching frequency: 7.5 kHz
- Coupled inductor turns ratio: 2

Based on the calculated voltage stress of 780 V and current stresses of 44 A peak and 13 A average for the switches, an RB-IGBT rated at 1,200 V and 50 A should be chosen. The RB-IGBT engineering sample from Fuji that contains 18 switches with those ratings is used to estimate the losses and efficiency of the inverter design. At $V_{ce(sat)} = 2.8$ V and an average switch current of 13 A, conduction losses of the six switches are estimated to be 109.2 W. Assuming the RB-IGBT switching loss is proportional to the peak current, the total switching loss of the six devices under 7.5 kHz switching would be 101.2 W in the boost mode and 67.5 W in the buck mode. The estimated volume and weight of a six-pack RB-IGBT module are 0.047 L and 0.144 kg, respectively.

Based on the calculated diode voltage stress of 390 V and current stresses of 21 A peak and 7.1 A average, a diode rated at 600 V and 30 A could be sufficient for the design. The readily available diode from Microsemi (APT2X101D60J, dual diode rated at 600 V and 100 A) was, however, chosen for the design. The weight and volume of the diode are 0.029 kg and 10.45 mL, respectively. The diode conduction and reverse recovery losses are estimated at 9.95 W and 1.57 W, respectively.

Requirements for the Z-network capacitor are 300 V, 18.1 Arms, and 50 µF. To meet the ripple current requirement, the Electronic Concepts film capacitor, 5MPA1506K, was chosen for the design, giving a capacitance of 50 µF, a volume of 0.163 L, and a weight of 0.213 kg. The loss due to the electric series resistance is 0.55 W.

Requirements for the Z-network coupled inductors, L_1 and L_2, are 69 µH/14.7 Arms and 280 µH/10.4 Arms, respectively. With the selected amorphous core, AMCC-40, and 14 turns for L_1 and 28 turns for L_2, the resulting coupled inductor has $L_1 = 68$ µH, $L_1 = 274$ µH, core weight of 0.53 kg, core loss of 46.7 W, copper loss of 33.8 W, litz wire weight of 0.073 kg, and a total inductor volume of 0.101 L.

Requirements for the input inductor, L_{dc}, are 38 A and 310 µH. With the selected amorphous core, AMCC-50, and 30 turns, the resulting inductor has inductance of 315 µH, core weight of 0.586 kg, core loss of 9.8 W, copper loss of 10.26 W, litz wire weight of 0.102 kg, and a total inductor volume of 0.152 L.

The voltage stress of the output ac filter capacitors is around 300 Vrms, and the required capacitance is 10 µF per phase. The film capacitor made by Genteq Capacitors, 41L6100, rated at 330 Vac and 10 µF, was selected. Using three of these capacitors gives a total volume of 0.154 L and weight of 0.138 kg.

A water-cooled heat sink about twice the size of the switch module was chosen for the design. The volume and weight of the heat sink are 0.079 L and 0.248 kg, respectively.

Figure 8 is a three-dimensional drawing of the 10 kW ZCSI design. Table 3 provides a summary of component volumes and weights and the resulting power density. Figure 9 shows inverter volume breakdown by component; the capacitors and inductors are the major volume-contributing parts, constituting 81% of the total inverter volume. Figure 10 illustrates weight breakdown by component; the inductors contribute the most to the inverter weight (63%).
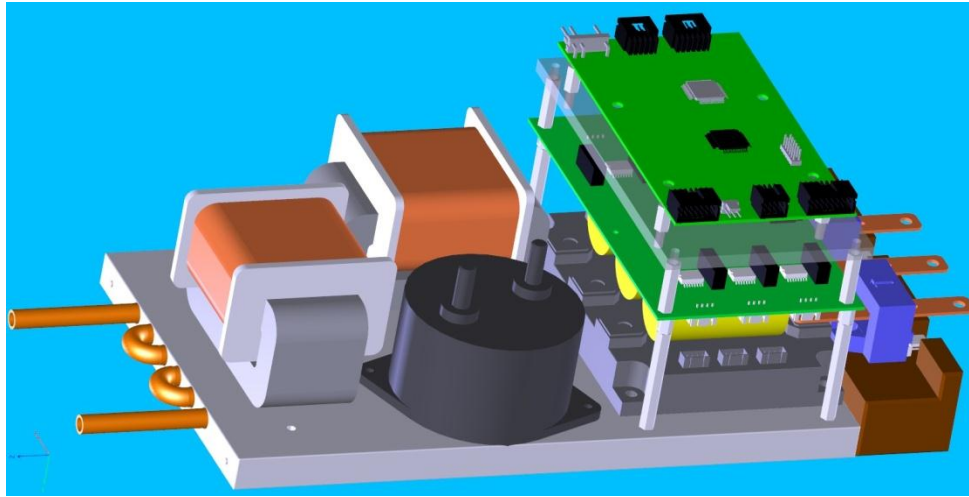
Fig. 8. A three-dimensional drawing of the 10 kW ZCSI design.

Table 3. Summary of component volume, weight, and power density for the 10 kW inverter design

	Switches	**Diode**	**Capacitors**	**Inductors**	**Heat Sink**	**Total**	**Power Density**
Weight (kg)	0.144	0.029	0.351	1.291	0.248	2.063	4.85 kW/kg
Volume (L)	0.047	0.010	0.317	0.253	0.079	0.706	14.16 kW/L
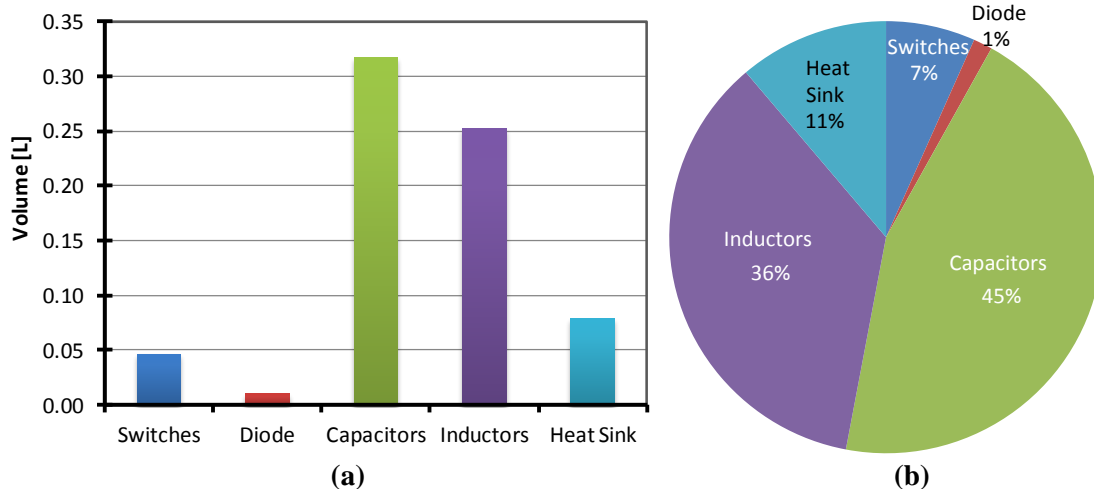
Fig. 9. Volume breakdown by component for the 10 kW ZCSI design: (a) component volume in liters; (b) component percentage of total.
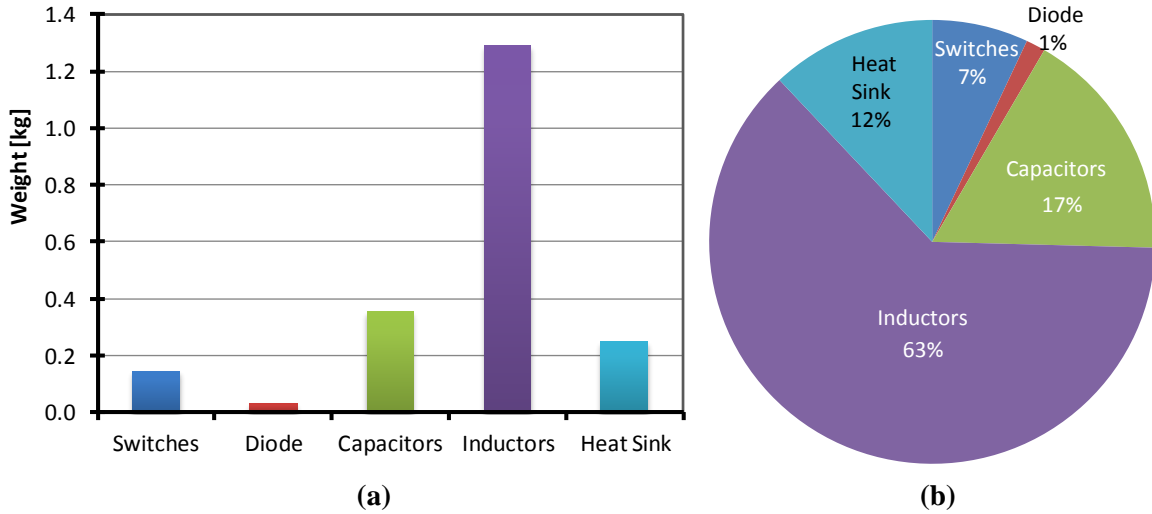
Fig. 10. Weight breakdown by component for the 10 kW ZCSI design: (a) component weight in kilograms; (b) component percentage of total.

Table 4 shows loss breakdown in boost mode and buck mode. As the Z-network is not activated in the boost mode, losses in the coupled inductor, diode, and capacitor are negligible. The estimated efficiency is 97.7% in boost mode and 97.1% in buck mode. The switching device loss is the major contributor to the total loss. To achieve higher power density and reduce the size of the inductor, the switching frequency should be increased. But the device switching loss will also increase, negatively impacting the converter efficiency. Currently available first generation RB-IGBT technology was used in this design. Assuming 100% reductions in switching and conduction losses with next generation RB-IGBTs, the boost mode and buck mode efficiency numbers can be increased to 98.7% and 98%, respectively. Further, future wide bandgap based devices, which can switch at high frequencies while still maintaining low switching losses, can be used to shrink the size of the inductors and improve the power density and efficiency.

Table 4. Summary of component loss and efficiency for the 10 kW ZCSI design

	Switches	**Diode**	**Capacitors**	**Inductors**	**Total**	**Efficiency**
Boost Mode (W)	210.4			20.06	230.46	97.70%
Buck Mode (W)	176.7	11.52	0.550	100.60	289.37	97.11%

A 10 kW prototype was fabricated using the design and tested. Figure 11 shows a photo of the 10 kW ZCSI prototype. An 18-pack RB-IGBT rated at 600 V and 200 A was available and thus used to assemble the prototype. The control scheme was implemented with a Texas Instruments digital signal processor, TMS320F28335, and a complex programmable logic device for synthesizing the gate control PWM signals. Figures 12 and 13 show experimental waveforms of input voltage, V_{in}; output line-to-line voltages, V_{ab} and V_{bc}; input current, I_{in}; and output currents, i_a and i_c, for the 10 kW ZCSI prototype operating in boost and buck modes. Figures 14 and 15 show experimental waveforms for charging a capacitor-resistor load at source voltages of 60 V in the boost mode and 120 V in the buck mode, illustrating the buck and boost capability of the ZCSI based charger. All the output voltage waveforms are sinusoidal with very low THD factors (in the range of 6%−12%). Figure 16 shows an efficiency chart at $V_{in} = 250$ V, indicating a maximum efficiency of 97.6%.
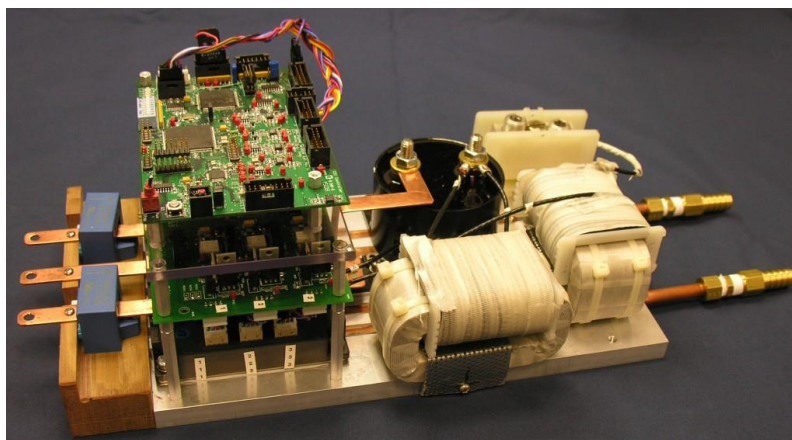
Fig. 11. Photo of the 10 kW ZCSI prototype.
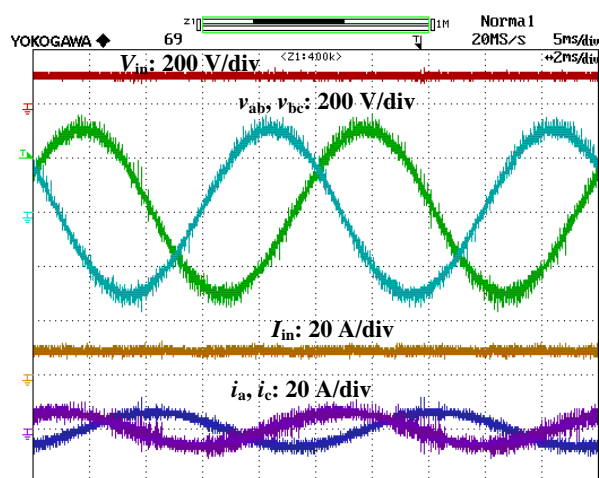
Fig. 12. Test waveforms in the boost mode showing a voltage boost factor of 3.
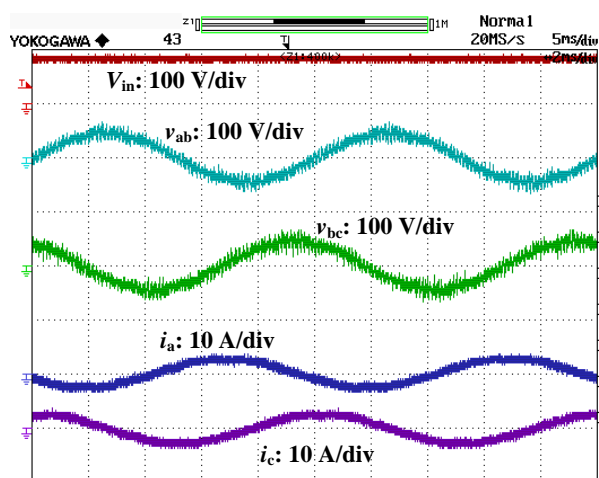
Fig. 13. Experimental waveforms in buck mode.
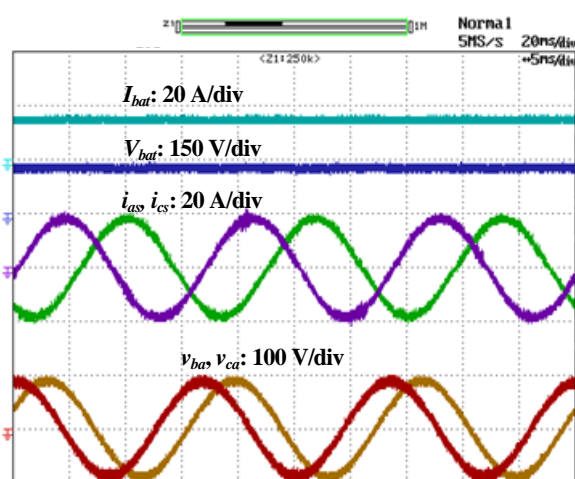
Fig. 14. Test waveforms for charging in boost mode.
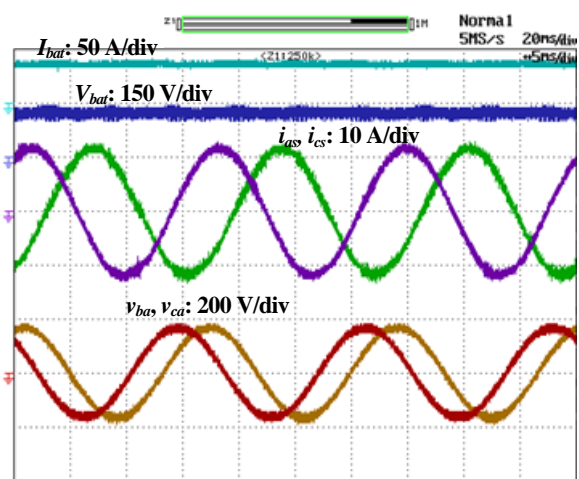
Fig. 15. Test waveforms for charging in buck mode.
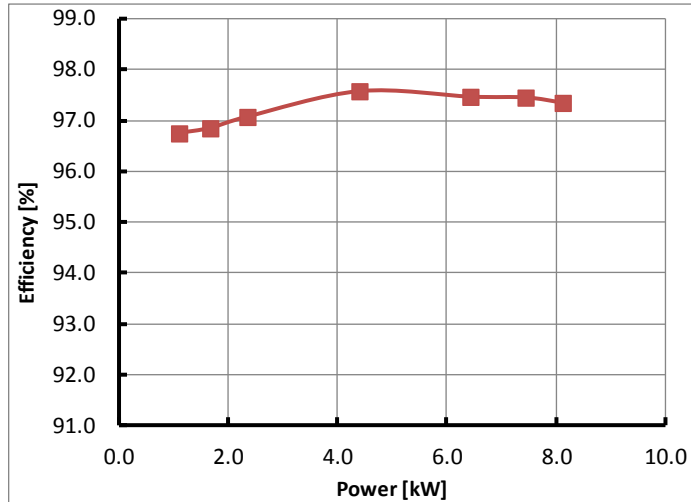
Fig. 16. Efficiency chart.

Conclusion

A simulation study verified that using the modulation signal angle control method can significantly increase the output voltage to the point that it is only limited by the voltage rating of the switches in the inverter, thus eliminating the need for high numbers for the turns ratio of the coupled inductor.

A 10 kW ZCSI based on the CF-trans-qZSI was designed using the first generation RB-IGBT technology, fabricated, and tested. The design yields a specific power of 4.85 kW/kg, power density of 14.2 kW/L, and efficiency of 97.7% in boost mode and 97.1% in buck mode. With next generation RB-IGBT technology, it is estimated the efficiency numbers can be increased to 98.7% and 98%, respectively. Test results with the 10 kW prototype demonstrate the following.

- Capacitance reduction to 80 µF (200 µF for a VSI)
- Output voltage capability range from 0 to 3 times the battery voltage (0–0.99× for a VSI)
- Output voltage THD factors of 6%−12% (70%−200% for VSI)
- High efficiency (more than 97% even at a relatively low source voltage of 250 V)

Patents

G. J. Su, *Power Conversion Apparatus and Method,* application US12/399,486, March 6, 2009, patent pending.

Publications

G. J. Su and L. Tang, "A Current Source Inverter Based Motor Drive for EV/HEV Applications," presented at the SAE 2011 World Congress, 2011-01-0346, April 21–25, 2011, Detroit, Michigan.

G. J. Su and L. Tang, "Current Source Inverter Based Traction Drive for EV Battery Charging Applications," presented at the 7th IEEE Vehicle Power and Propulsion Conference (VPPC '11), September 6–9, 2011, Chicago, Illinois.

L. Tang and G. J. Su, "A Novel Current Angle Control Scheme in a Current Source Inverter Fed Surface-Mounted Permanent Magnet Synchronous Motor Drive," in *3rd IEEE Energy Conversion Congress and Exposition (ECCE 2011)*, September 17–22, 2011, Phoenix, Arizona, pp. 2358–2364.

References

1. M. Takei, Y. Harada, and K. Ueno, "600 V-IGBT with Reverse Blocking Capability," in *Proceedings of IEEE ISPSD '2001*, 2001, pp. 413–416.

2. E. R. Motto, et al., "Application Characteristics of an Experimental RB-IGBT (reverse blocking IGBT) Module," in *Proceedings of IEEE IAS 2004 Annual Meeting*, 2004, pp. 1504–1544.

2.5   A Segmented Drive Inverter Topology with a Small dc Bus Capacitor

Principal Investigator: Gui-Jia Su
Oak Ridge National Laboratory
National Transportation Research Center
2360 Cherahala Boulevard
Knoxville, TN 37932
Voice: 865-946-1330; Fax: 865-946-1262; E-mail: sugj@ornl.gov

DOE Technology Development Manager: Susan A. Rogers
Voice: 202-586-8997; Fax: 202-586-1600; E-mail: Susan.Rogers@ee.doe.gov

ORNL Program Manager: Mitch Olszewski
Voice: 865-946-1350; Fax: 865-946-1262; E-mail: olszewskim@ornl.gov

Objectives

- Overall project objectives
    — Design, develop, build, and test a 55 kW integrated segmented traction drive system that can reduce the inverter dc bus ripple current and thus the capacitance by at least 60%.
    — Address the 2015 inverter target of 12 kW/kg and the 2020 inverter target of 13.4 kW/L.
    — Eliminate the capacitor related hurdle for high temperature operations.
- Objectives for FY 2011 effort
    — Test the 55 kW segmented inverter prototype developed in FY 2010 with a higher dc bus voltage for higher power levels and motor speeds.
    — Test the 55 kW segmented inverter prototype with space vector based pulse width modulation (PWM) schemes.
    — Design and fabricate a 55 kW segmented inverter that is suitable for integrating with a motor.

Approach

- Use a segmented drive system topology that does not need additional switches or passive components but can significantly reduce the dc link ripple current and the amount of capacitance.
- Perform simulation study of various PWM schemes using commercial circuit simulation software to assess their impact on the capacitor ripple current.
- Design, build, and test a 55 kW inverter prototype to experimentally validate the simulation study.
- Integrate the segmented inverter and motor into a single package drive system to eliminate cable connections and reduce the drive system cost.
- Test, characterize, and refine a 55 kW prototype of an integrated segmented inverter-motor drive system (FY 2012).

Major Accomplishments

- Demonstrated a 55 kW segmented inverter prototype with a 60% reduction of dc bus capacitance compared to a standard voltage source inverter (VSI).
- Tested prototype with both carrier based and space vector based PWM control methods to show
    — 55% to 75% reduction in capacitor ripple current,
    — 70% to 90% reduction in battery ripple current, and
    — 60% to 80% reduction in motor ripple current.
- Completed design and fabrication of a ring-shaped 55 kW segmented inverter that is suitable for integration with a motor.

— Finite element analysis (FEA) results indicated satisfactory thermal performance of a toroidal heat exchanger design.
— Use of heavy copper printed circuit board technology for interconnecting the power modules eliminated the need for bus bars and greatly simplified the inverter assembly steps

Future Direction

— Test, characterize, and refine the 55 kW integrated segmented inverter and motor drive prototype developed in FY 2011.

Technical Discussion

Background

The dc bus capacitor is an indispensable component for maintaining a stable dc bus voltage and smooth battery current for the voltage source inverter (VSI) based traction drive systems in electric vehicles (EVs), hybrid EVs (HEVs), and plug-in HEVs. Figure 1 is a schematic drawing of the standard VSI based drive system. The VSI, mainly comprising six power semiconductor switches—typically insulated gate bipolar transistors (IGBTs)—and a dc bus filter capacitor, switches the battery dc voltage to produce a desired set of three phase ac voltages according to a chosen PWM scheme. The ac voltages in turn regulate the motor current to control the motor torque and speed. In doing the switching operations, the inverter generates large ripple components in the dc link current, i_{inv}, thus necessitating the use of the dc bus filter capacitor to absorb the ripple currents and suppress voltage transients, which occur on the dc bus at every instant of inverter switching and, if not sufficiently constrained, are detrimental to the battery life and reliability of the semiconductor switches in the inverter.
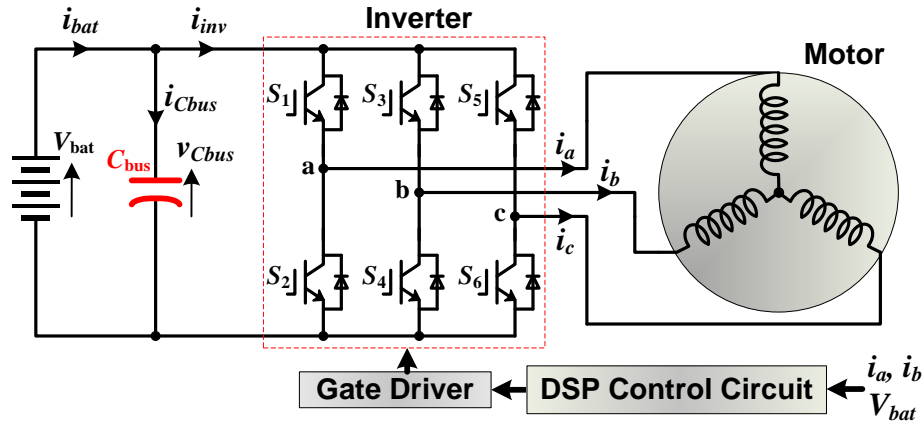
Fig. 1. Standard VSI based drive system in HEVs.

Figure 2 shows simulated motor currents, i_a, i_b, and i_c; capacitor ripple currents, i_{Cbus} and $i_{Cbus(rms)}$; inverter dc link current, i_{inv}; battery current, i_{bat}; and bus voltage, v_{Cbus}, in a typical 55 kW HEV inverter. The capacitor ripple current reaches as large as 200 Arms, which is more than 70% of the motor current. As a result, a bulky and costly dc bus capacitor of about 1,000 µF is required to prevent this large ripple current from flowing into the battery and to maintain a smooth dc bus voltage. Even with the large bus capacitor, there is still a relatively large ripple component of 70 A peak-to-peak in the battery current, i_{bat}.

Concerns about the reliability of electrolytic capacitors have forced HEV makers to use self-healing film capacitors, and currently available film capacitors that can meet the demanding requirements are costly and bulky, taking up one-third of the inverter volume and making up one-fifth of the cost. The dc bus capacitor, therefore, presents significant barriers to meeting the requirements of the USDRIVE program goals for inverter volume, lifetime, and cost established by DOE and its industrial partners [1].

i_a i_b i_c **(280 Arms)**

i_{Cbus} $i_{Cbus(rms)}$

i_{inv} i_{bat}

v_{Cbus}
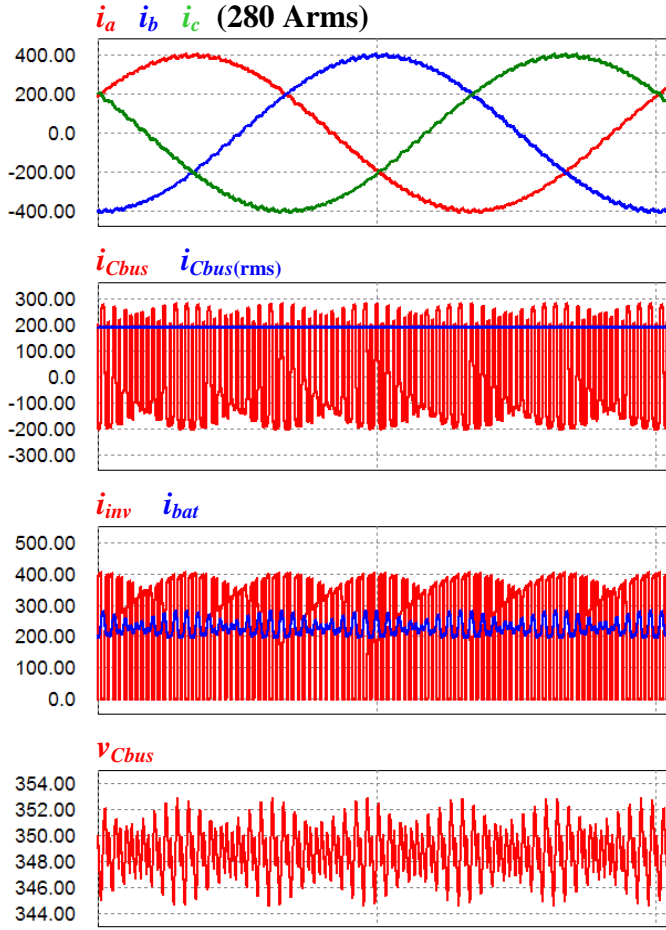
Fig. 2. Simulated waveforms in the standard VSI based drive system.

The large ripple currents become even more problematic for the film capacitors in high temperature environments as their ripple current handling capability decreases rapidly with rising temperatures, as indicated in Fig. 3 for one of the best film capacitors at 150 µF available on the market. For example, as the ambient temperature rises from 85°C to 105°C, weight, volume, and cost of capacitors could increase by a factor of 5 due to the decrease of ripple current capability from 50 A to 11 A.

To help achieve the USDRIVE targets, there is thus an urgent need to minimize this bulky component by significantly reducing the inverter ripple current. A much smaller dc bus capacitor would also enable inverters to operate at higher temperatures. The following factors, however, make this a difficult task: (1) increasing the switching frequency, which is one of the anticipated benefits with future wide-bandgap-based switches, has little impact on the bus capacitor ripple currents because the capacitor ripple currents depend on the motor peak current, although so increasing switching frequency does reduce the dc bus voltage and motor current ripples, and (2) the major components of the capacitor ripple currents have frequencies of multiples of the switching frequency (nf_{sw}) or their side bands ($nf_{sw} \pm f_m$, $nf_{sw} \pm 2f_m$, …), as given by the equation below and illustrated in Fig. 4. The high frequency nature makes it impractical to actively filter out the ripple components because doing so requires the use of very high switching frequencies in the active filter.

$$i_{inv} = I_{dc} + \sum_{k=0}^{\infty} \sum_{n=1}^{\infty} I_{n,k} \sin[2\pi(nf_{sw} \pm kf_m)t + \alpha_{n,k}]$$

where

f_{sw} is inverter switching frequency,
f_m is motor current fundamental frequency,
I_{dc} is dc component,
$I_{n,k}$ is ripple current amplitude,
$\alpha_{n,k}$ is ripple current phase angle.

**Fig. 3. Film capacitor ripple current capability vs ambient temperature
(Electronic Concepts UL31 Series) [2].**
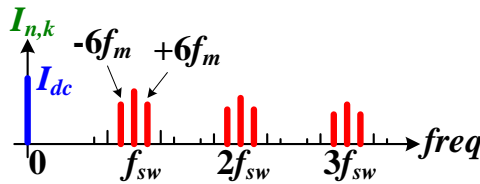
**Fig. 4. Ripple components in the dc
link current in the standard VSI based
drive system.**

Features of the Proposed Segmented Drive

A segmented drive system (Fig. 5) that does not add switches or passive components has been developed in this project to significantly reduce the ripple current and thus the requirement on bus capacitance. Because the technology is under patent review, details of the topology will not be shown in this report. However, the segmented topology does not need additional switches or passive components but enables the use of optimized PWM schemes to significantly reduce the dc link ripple current generated by switching of the inverter output currents. In addition, integrated inverter/motor packaging techniques are being explored to reduce inverter/motor connection cable length.

The uniqueness of this technology is that, while being able to significantly reduce the capacitor ripple current and bus capacitance, it *does not*

- need additional silicon or passive (L or C) components,
- need additional sensors, or
- add control complexity.
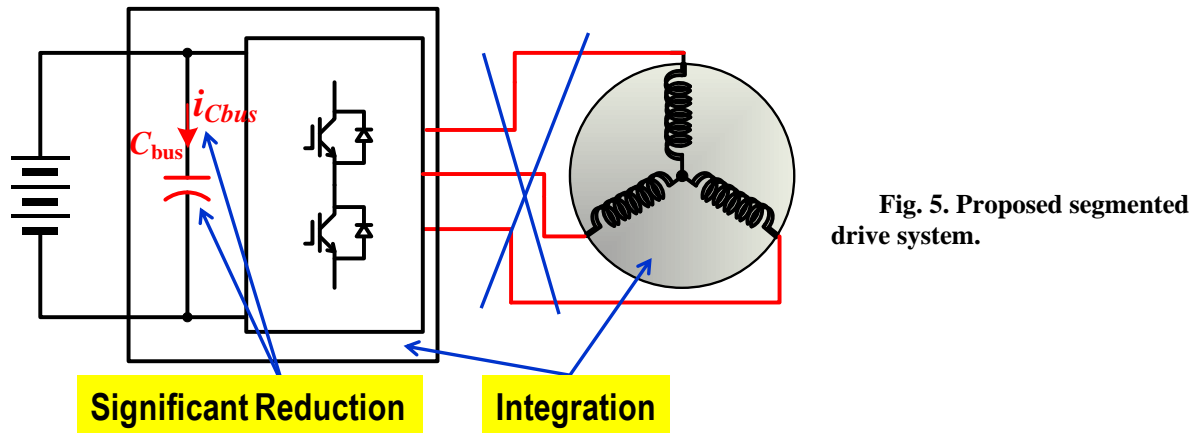
Fig. 5. Proposed segmented drive system.

The following positive impacts are expected.

- Substantially reduced bus capacitance (at least 60%) and thus reduced inverter volume and cost.
- Reduced battery losses and improved battery operating conditions (by eliminating battery ripple current).
- Significantly reduced motor torque ripples (up to 50%).
- Reduced switching losses (by 50%).
- Improved high temperature operating capability.

A simulation study using PSIM carried out in FY 2009 has validated the segmented drive concept and indicated that the bus capacitance can be reduced by 60% from that needed for a standard VSI. The simulation results also show that, compared to the standard inverter configuration, the segmented drive inverter can achieve (1) more than 65% reduction in capacitor ripple current, (2) 80% reduction in battery ripple current, (3) 70% reduction in dc bus ripple voltage, and (4) 50% reduction in motor ripple current.

Inverter Prototype Design and Test Results

Incorporating the simulation study, a 55 kW prototype was designed, built, and tested in FY 2010. A 55 kW baseline standard VSI was also designed for comparison. Both designs use the same IGBT modules, purchased from Powerex, and the same water-cooled cold plate, measuring 6 in. by 7 in., for fixing and cooling the IGBT modules. Capacitor requirements for the segmented inverter are 400 µF and are fulfilled with two film capacitors, each rated at 500 V and 200 µF. In comparison, a total amount of capacitance of 1,000 µF is needed for the baseline VSI design and is furnished with five film capacitors, each rated at 500 V and 200 µF. The capacitors are mounted on an aluminum heat sink attached to the cold plate. Because of the larger capacitance requirement (more than twice that of the segmented inverter), the baseline design requires a significantly larger heat sink for mounting the capacitors. Table 1 gives a comparison of heat sink size and capacitor volume for the two designs. Figure 6 shows a photo of the assembled 55 kW segmented inverter prototype. A Texas Instruments 32 bit fixed-point digital signal processor chip, TMS320F2812, is used to implement the motor control and PWM switching schemes.

**Table 1. Comparison of heat sink sizes and capacitor volumes of 55 kW segmented
inverter and baseline standard inverter designs**

	Baseline	**Segmented**
Heat sink footprint (in.)	$6 \times 7 + 6.6 \times 9.6$	$6 \times 7 + 6.6 \times 2.2$
Capacitor volume	**1.39 L**	**0.56 L** $\longrightarrow$ a 60% reduction
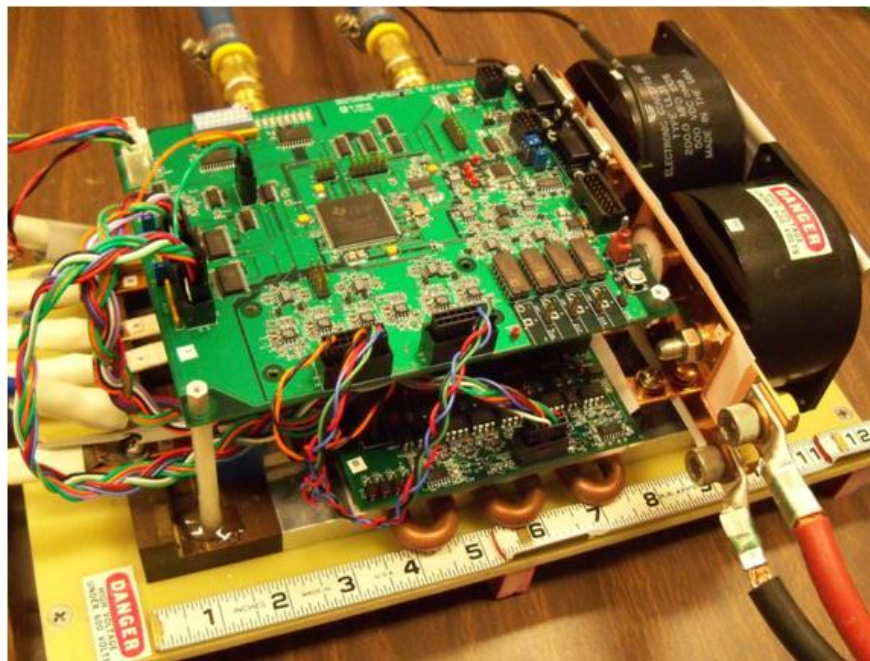
Fig. 6. A 55 kW segmented inverter prototype.

During FY 2010, the prototype was first tested with an inductor-resistor (R-L) load bank with nominal circuit parameters of 0.45 mH and 1.6 Ω. A dc power supply was used to simulate a 300 V battery. For comparison, the prototype was reconfigured as the baseline VSI, but without the added capacitors, and tested at the same load conditions. Because the limitation of the maximum dc power supply voltage renders the inverter unable to supply the rated voltage to the load bank, the R-L load tests were performed with power levels up to 27 kW. The prototype was then tested with a commercial, off-the-shelf, induction motor rated at 15 HP, 230 Vrms, 37.5 Arms, 91 Nm, and 1,175 rpm. The motor is in delta connection and has six pole pairs. Again due to the limitation of the maximum dc power supply voltage of 300 V, tests could not be done at the rated speed region. All the tests were performed with carrier based PWM schemes.

In FY 2011, as a dc power supply with a maximum output voltage of 450 V became available, R-L load tests were conducted at a higher inverter dc bus voltage and power levels up to 43 kW. Tests were then repeated with space vector based PWM schemes, and the results were similar to those with the carrier based PWM methods. Figure 7 plots the capacitor ripple currents at various levels of input dc power for both the baseline and segmented inverters. The graph shows the same results as the tests in FY 2010 did [i.e., the segmented inverter offers a significant reduction of capacitor ripple current (in the range of 55% to 75%)].
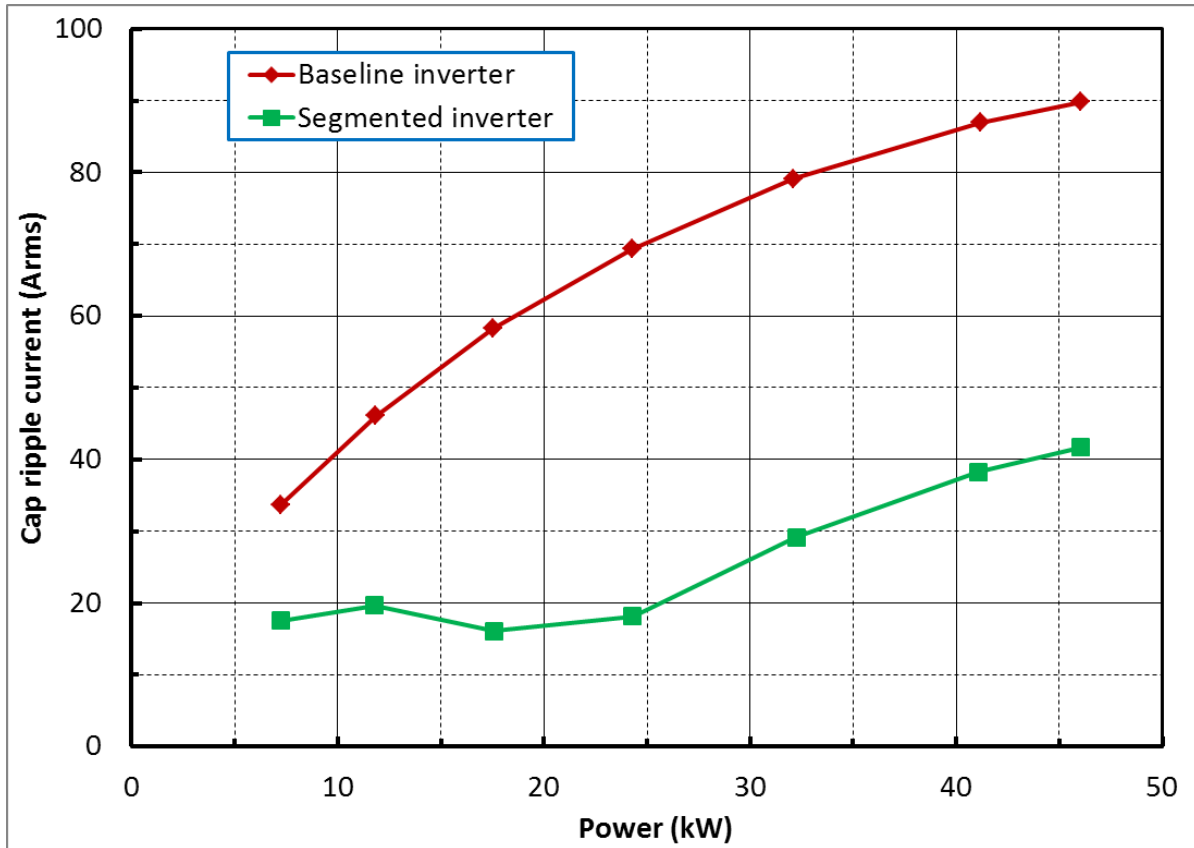
Fig. 7. Comparison of capacitor ripple current vs dc input power for an R-L load.

Figure 8 plots the battery ripple currents at various levels of input dc power for both the baseline and segmented inverters. Again, the segmented inverter offers a significant reduction of battery ripple current (in the range of 70% to 80%).

The prototype was then tested again with the commercial off-the-shelf induction motor at a higher dc bus voltage that enabled the inverter to operate the motor at the rated speed of 1,175 rpm. The motor tests were also repeated with the space vector PWM schemes, and nearly identical results were obtained. Figure 9 shows battery current, I_{bat}; motor currents, i_a, i_b, and i_c; and capacitor ripple current, i_{Cbus}, at 1,185 rpm and rated torque of 91 Nm for the baseline inverter and the segmented inverter. The measured capacitor ripple currents are 31.72 Arms for the baseline inverter and 13.87 Arms for the segmented inverter, and the measured peak-to-peak battery ripple currents are 35 A and 10 A, respectively. These measurements show a reduction of 56% for capacitor ripple current and 71% for battery ripple current with the segmented inverter. The motor current waveforms also illustrate significantly lower ripple components with the segmented inverter. Figure 10 plots the capacitor ripple currents at various levels of load torque vs motor speed for both the baseline and segmented inverters. Again, the segmented inverter offers a significant reduction of capacitor ripple current, in the range of 55% to 75%, at the rated torque; 50% to 70% at 75% of rated torque; and 50% to 60% at 50% of rated torque. It is also worth noting that the maximum ripple current with the baseline VSI approaches the rated motor current of 37.5 Arms.
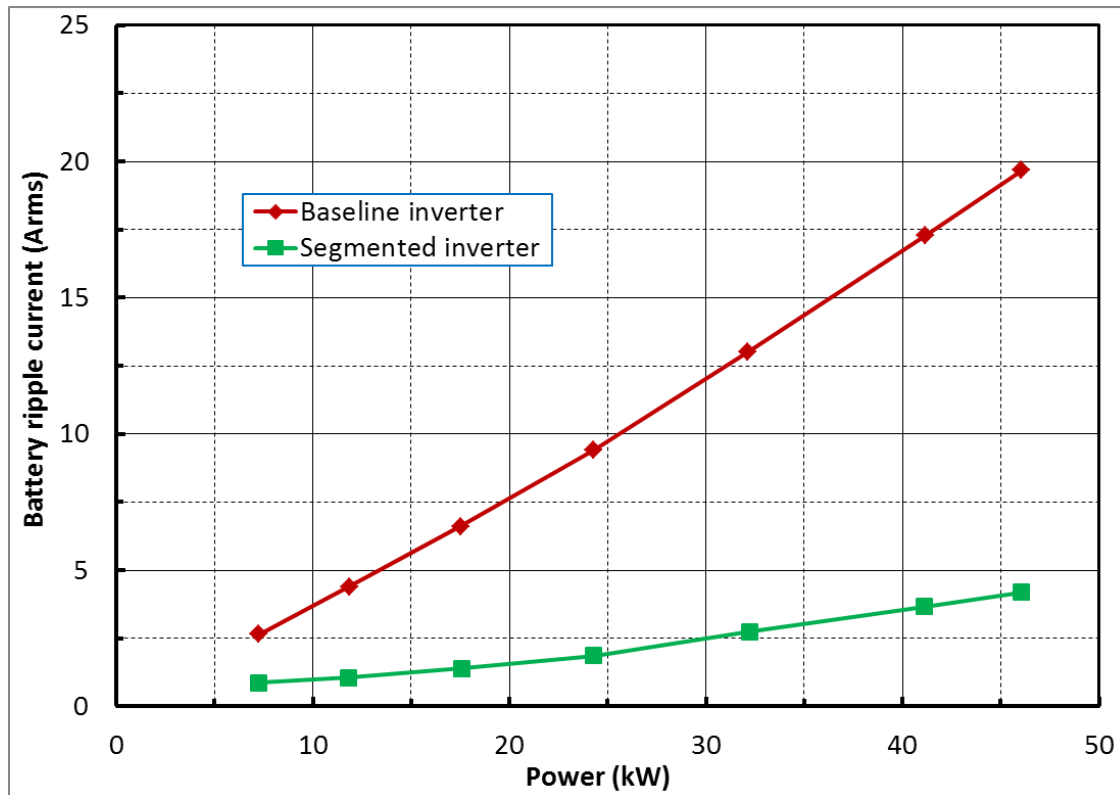
Fig. 8. Comparison of battery ripple current vs dc input power for an R-L load.

I_{bat}:
50A/div

i_a, i_b, i_c:
50A/div

i_{Cbus}:
50A/div

Baseline inverter   **Segmented inverter**
$i_{Cbus(rms)}$: 31.72 Arms; I_{bat}, **p-p ripple**: 35 A $i_{Cbus(rms)}$: 13.87 Arms; I_{bat}, **p-p ripple**: 10 A
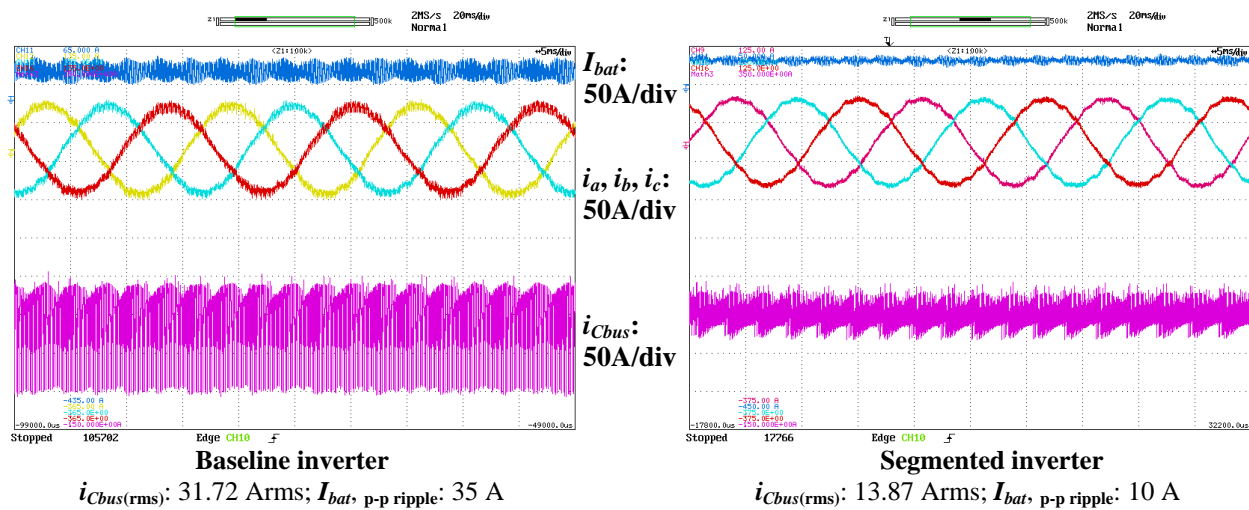
Fig. 9. Waveforms with an induction motor at 1,185 rpm and rated torque of 91 Nm showing a reduction of 56% for capacitor ripple current [$i_{Cbus(rms)}$] and 71% for peak-to-peak battery ripple current (I_{bat}, p-p ripple) with the segmented inverter.
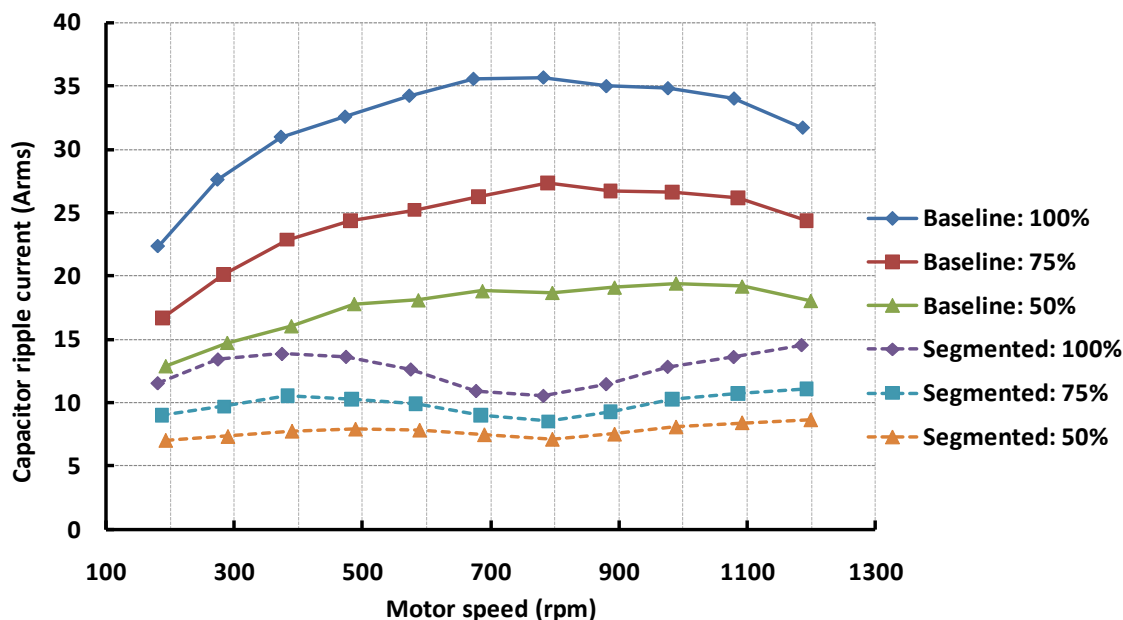
Fig. 10. Comparison of capacitor ripple current vs motor speed at load torque of 100%, 75%, and 50% of rated torque of 91 Nm.

Table 2 shows estimated performance improvements when the technology is applied to the 2009 Toyota Camry motor inverter: 40% and 35% increases in specific power and power density, respectively, and 11% decrease in cost ($/kW). It also indicates that the segmented inverter would exceed the DOE 2015 target for specific power and the 2020 target for power density.

Table 2. Estimated performance improvements[a]

	Camry inverter			Segmented inverter		
	Weight (kg)	**Volume (L)**	**Cost ($)**	**Weight (kg)**	**Volume (L)**	**Cost ($)**
Bus Cap	3.57	2.6	182	1.43	1.04	73
Others	3.99	3.36	728	3.99	3.36	737
Subtotal	7.56	5.96	910	5.42	4.4	810
Metrics	**kW/kg**	**kW/L**	**$/kW**	**kW/kg**	**kW/L**	**$/kW**
	9.3	11.7	13	12.9	15.9	11.6
DOE targets	12	12	5	14.1	13.4	3.3
		2015			2020	

[a]Assumptions: Camry inverter: capacitor costs 20%
                 Segmented inverter: a reduction of 60% in bus capacitor requirements

Segmented inverter performance on significant DOE targets highlighted.

Design and Fabrication of a 55 kW Inverter Prototype for Integrating with a Motor

One of the goals of the project is to develop an integrated segmented inverter and motor traction drive system (Fig. 11) that can substantially reduce cost, volume, and weight of the drive system through a reduction of the dc bus capacitance by 60% and elimination of cable connections between the inverter and motor. Toward this goal, a ring-shaped segmented inverter that is suited to be integrated into typical cylindrical motors was designed and fabricated. Figure 12 shows three-dimensional drawings of the hardware design for the 55 kW prototype. The design comprises a toroidal heat exchanger with circular water channels, IGBT modules, a dc bus capacitor board that is constructed using heavy copper printed circuit technology and also functions as bus bars to interconnect the IGBT power modules, and a gate

drive and control logic board. The toroidal heat exchanger has an outer diameter of 9 in., inner diameter of 4 in., and thickness of 0.75 in. Although the required capacitance was fulfilled using multiple discrete block capacitors for this prototype design, a custom built ring-shaped capacitor would fully use the spaces and thus reduce the inverter volume. Such a capacitor is under examination and will be used in a refined design. Also, the gate drive board is divided into six identical arc sections to save design time and cost. Future designs could put all the gate drive and control circuits on a single ring-shaped board.
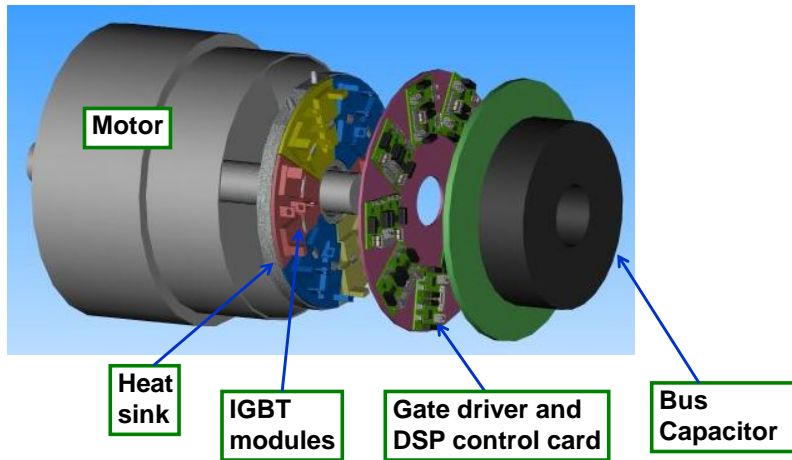
Fig. 11. Design concept for an integrated segmented inverter-motor.
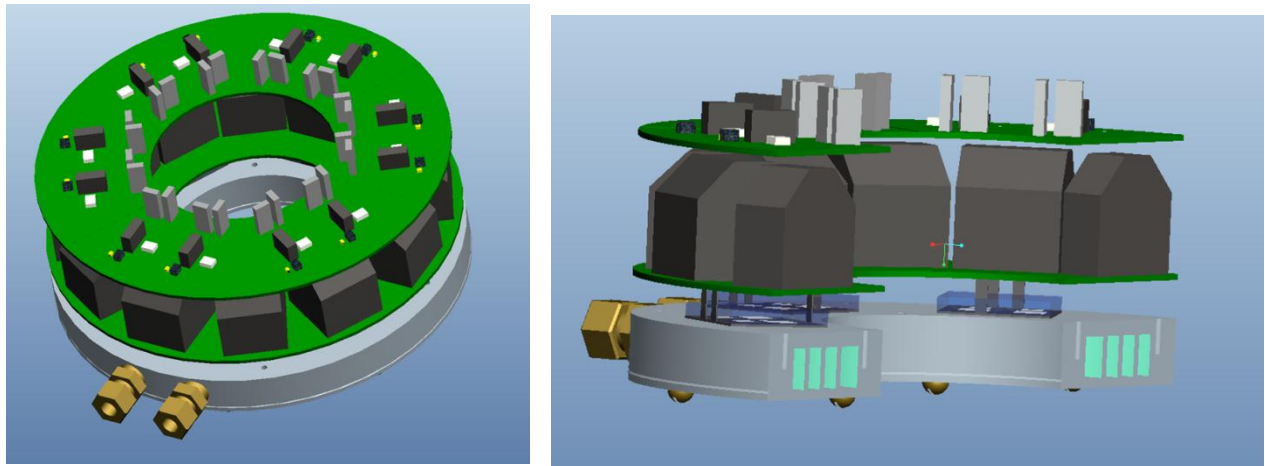
Fig. 12. Hardware design for a 55 kW ring-shaped segmented inverter that is suited to be integrated with typical cylindrical motor prototypes.

The IGBT modules (Fig. 13) were designed and packaged at the ORNL packaging laboratory using ABB IGBT and diode dies rated at 1,200 V and 75 A. The dies are soldered on a rectangular aluminum oxide double bond copper substrate with a footprint of 1.5 in. by 1.38 in. The modules use wire bonds for interconnections and are potted with a type of relatively high temperature silicone gel. A double side cooled, "wirebondless," planar IGBT module is under development at ORNL and could be used in future prototype designs, which could substantially improve thermal performance and decrease parasitic resistance and inductance.

FEAs were carried out to evaluate the thermal performance of the toroidal heat exchanger. Inlet water flow was set to 0.2 m/s. Water properties were that of a 66°C water-ethylene glycol (WEG) mixture. Water flow was solved then coupled with the heat transfer. The cooling chamber material was aluminum, with a thermal conductivity (TC) of 160 W/(m/K). The silicon chip, with a TC of 163 W/(m/K), was mated to a copper plate with a copper TC of 400 W/(m/K). The chip-copper set was mated to Duralco thermally conductive adhesive with a TC of 5.8 W/(m/K). The chip was set to produce a total of 165 watts of waste heat. This waste heat was applied as a volumetric heat load. The WEG was set to an inlet temperature of 70°C. The FEA (Fig. 14) gave a maximum junction temperature of 110.7°C, well below the typical safe operation limit of 125°C. FEA results indicated that the toroidal heat exchanger design presents a relatively low pressure drop, with the bulk of it occurring at the narrow inlet and outlet fixtures. This provides an opportunity for further optimization of the cooling channels in terms of

Fig. 13. ORNL packaged IGBT module.

the number and width of the channels for higher coolant temperature operations. A feasibility study will be carried out once the FEA results are validated by prototype testing in FY 2012 to assess the possibility of using the motor coolant for the inverter with a heat-transfer-enhanced heat exchanger design, higher junction temperature silicon switches, and better power module packages.

Fig. 14. FEA results for the toroidal heat exchanger.

After the FEA results showed satisfactory thermal performance with the toroidal heat exchanger design, a 55 kW ring-shaped segmented inverter was fabricated (Fig. 15). The use of heavy copper printed circuit board technology for interconnecting the power modules eliminates the need for bus bars and greatly simplifies the inverter assembly steps. Testing of the prototype is planned for FY2012.

Fig. 15. A 55 kW ring-shaped segmented inverter prototype that is suited to be integrated into typical cylindrical motors.

Conclusion

The 55 kW segmented inverter prototype with a 60% reduction of dc bus capacitor developed in FY 2010 was successfully tested with both R-L load and an induction motor at higher power levels and motor speeds. Test results show a significant reduction of 55% to 75% in capacitor ripple current, reduction of 70% to 90% in battery ripple current, and reduction of 60% to 80% in motor ripple current. The tests were then repeated with space vector based PWM schemes, and the same results were obtained. Moreover, with the segmented inverter a lower switching frequency can be used to increase the inverter efficiency while still maintaining a low level of harmonic components in motor currents, even for low inductance motors such as permanent magnet motors.

One of the objectives for the project is to demonstrate an integrated segmented inverter and motor traction drive system that can substantially reduce system cost, volume, and weight through a reduction of the dc bus capacitance by 60% and elimination of cable connections between the inverter and motor. Toward this goal, a 55 kW ring-shaped segmented inverter that is suited to be integrated into typical cylindrical motors was designed and fabricated. FEA results indicated satisfactory thermal performance with the toroidal heat exchanger design. Testing of the prototype is planned in FY 2012.

Patents

G. J. Su, *Electrical Motor/Generator Drive Apparatus and Method,* App. serial no. 12/887,110, filing date: September 21, 2010.

Publicantions

None.

References

1. U.S. Department of Energy, *Electrical and Electronics Technical Team Roadmap*, December 7, 2010, available online at http://www1.eere.energy.gov/vehiclesandfuels/about/partnerships/roadmaps-other_docs.html.

2. Electronic Concepts, Inc., Electronic Concept Datasheets, available online at http://www.ecicaps.com/capacitors/features/ul3-series-unlytic-lt-sup-gt-reg-lt-sup-gt-ul3-ul31-ul32-ul34-ul35-series .

3. Electric Machinery Research and Technology Development

3.1 A New Class of Switched Reluctance Motors Without Permanent Magnets

Principal Investigator: Tim Burress
Oak Ridge National Laboratory
National Transportation Research Center
2360 Cherahala Boulevard
Knoxville, TN 37932
Voice: 865-946-1216; Fax: 865-946-1262; E-mail: burressta@ornl.gov

DOE Technology Development Manager: Susan A. Rogers
Voice: 202-586-8997; Fax: 202-586-1600; E-mail: Susan.Rogers@ee.doe.gov

ORNL Program Manager: Mitch Olszewski
Voice: 865-946-1350; Fax: 865-946-1262; E-mail: olszewskim@ornl.gov

Objectives

- Overall Objectives
  — Develop, design, build, and test an unconventional traction drive that
    ▪ has no permanent magnet (PM) material;
    ▪ has lower torque ripple and acoustic noise than that of a conventional switched reluctance motor (SRM); and
    ▪ maintains the low cost, simplicity, and power density of the conventional SRM.
  — Obtain operational characteristics for finalized design and compare with targets:
    ▪ power density: 5 kW/L (2015 DOE target),
    ▪ specific power: 1.3 kW/kg (2015 DOE target), and
    ▪ cost between $7/kW and $4.7/kW (2015 and 2020 targets, respectively).

- FY 2011 Objectives
  — Construct prototype.
  — Characterize prototype machine parameters.
  — Develop and prepare drive/controller hardware and software.
  — Conduct comprehensive motor testing in dynamometer test cell to determine performance, efficiency, torque ripple, and acoustic noise characteristics.

Approach

- Select preferred design approach for novel switched reluctance (SR) machine.
  — Analyze basic feasibility of various novel SR machine designs.
  — Conduct finite element analysis (FEA) to obtain motor characteristics.
  — Develop preliminary novel control schemes.
  — Simulate final designs with basic dynamic model.
  — Obtain estimated capabilities of torque and power as a function of speed.
  — Choose preferred design approach based on preliminary cost assessments, FEA, and dynamic simulation results.
- Perform detailed design and simulation of selected design approach.
  — Conduct structural, thermal, and acoustic noise modeling.
  — Adjust design approach as necessary.

- — Investigate potential to apply air-gap enhancements.
  - — Carry out comprehensive dynamic simulations.
  - — Refine novel control algorithm and investigate potential to apply other novel control techniques.
  - — Obtain accurate capabilities of torque and power as a function of speed
- Build and test SRM prototype and novel control technique.
  - — Determine power density, specific power, and cost based on results from dynamometer tests.

Major Accomplishments

- Developed unconventional SR machine design.
- Verified through simulations that the design meets 2015 performance targets with less than 5% torque ripple.
- Developed custom software to accomplish various tasks.
  - — Two universal dynamic simulators.
    - ▪ Parametric: efficient means to optimize control and design parameters.
    - ▪ FEA: capable of conducting dynamic electromagnetic and structural simulations.
  - — Automated FEA based geometric optimization.
  - — Complex multivariable, multiobjective optimization of control waveforms as a function of speed and torque.
- Achieved near-zero torque ripple for low and moderate torque levels (up to 150 Nm).
- Developed iterative self-learning pseudo-flux observer-based control algorithm.
  - — Capable of tracking/producing abstract current waveforms.
- Tested machine up to 5,000 rpm.
  - — Results lower than expected, but accounting for steel degradation, results are close to simulations.

Future Direction

- This project will not be funded by the DOE Vehicle Technologies Program beyond FY 2011, but several potential prospects exist for the continuation of this work.

Technical Discussion

Background

Because of the high and unpredictable cost and availability of rare earth PMs, which are used in most hybrid vehicle applications today, many automotive manufacturers have a common interest in the use of electric machines which do not use these materials. Although PM motors are not easily surpassed with respect to efficiency and power density, other competitive motor technologies exist which can have lower cost per power rating (dollars/kilowatt). Of the alternative motor technologies, the SRM offers the simplest rotor configuration, which is advantageous in terms of material cost, manufacturing cost, speed capability, and reliability. The highly nonlinear behavior and unusual control methods associated with the SRM require the use of sophisticated and computationally intensive software programs to fully optimize its design and operation. Therefore, the SRM is a relatively young motor technology, in terms of research and development, as opposed to other technologies such as the induction motor. Two primary drawbacks of the SRM are the level of torque ripple and the acoustic noise inherently associated with the SRM's doubly salient stator and rotor geometry. The intent of this project is to apply novel design techniques that significantly reduce torque ripple and acoustic noise while maintaining the intrinsic benefits of the SRM.

Existing torque ripple and acoustic noise reduction techniques typically incur significant compromises of things such as peak torque, torque–power density, material/manufacturing costs, and/or design complexity. A conventional SRM with eight stator teeth and six rotor teeth is shown in Fig. 1(a). If the rotor is assumed to be rotating clockwise, the two stator teeth without a superimposed yellow "X" are the only stator teeth that would have excited windings if a conventional control scheme were used. That is, only two (25%) of the eight stator teeth are active during this instant. As the rotor position continues to

increase in the clockwise direction, coils of two additional stator teeth are excited, and thus 50% of the stator teeth are active at that instant. However, this condition is maintained only for a short duration, and only 25% of the stator teeth are active beyond this short duration, giving a low average of active stator teeth.

(a) **(b)**
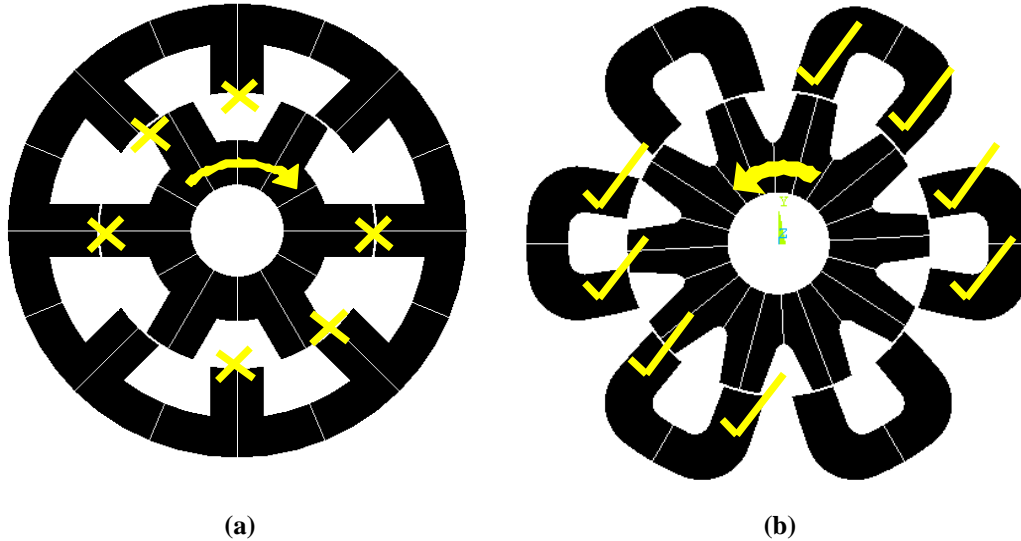
Fig. 1. Active stator teeth of (a) a conventional SRM and (b) an unconventional SRM.

After observing the low amount of active air-gap area within the conventional SRM, it seemed that novel concepts could be used to increase the average number of active stator teeth that are producing productive torque to more readily distribute the torque production and thereby reduce torque ripple. Because the fundamental means in which torque is produced in an SRM relies on the magnetic saliency of the stator and rotor, it can be difficult to increase the number of active stator teeth without compromising the reluctance ratio between aligned and unaligned rotor positions. This is a result of introducing stator and/or rotor teeth within a closer proximity of each other, thereby promoting detrimental flux leakage through undesired paths, which typically decreases the overall torque capability of the machine. Therefore, the proposed general approach uses isolated multiple flux paths (IMFPs) to carry out the tasks mentioned above while seeking to minimize counterproductive flux flow by means of magnetic path isolation. Because the permeability of steel approaches that of air as magnetic saturation increases in the steel, it is not possible to have completely isolated magnetic paths in this type of application, particularly since the SRM often operates in the saturation region for applications requiring high power density. Therefore, these types of hardware approaches must be incorporated carefully in such a way that the natural operation and control of the motor inhibits the detrimental tendencies of leakage and undesired flux paths.

In FY 2009, a wide variety of designs which use this technique were developed and analyzed for feasibility. Based on comparisons of estimated performance, size, cost, and manufacturability, the most feasible geometry was chosen to be the focus of FY 2010 development efforts. As shown in Fig. 1(b), 8 of 12 stator teeth are typically active at the indicated rotor position for counterclockwise motoring operation. As the rotor continues to rotate, only 4 of 12 stator teeth are active for a brief period of time and then 8 of 12 stator teeth are active again. Therefore, on average, at least 50% of the stator teeth are active in this unconventional SRM versus roughly 33% in a conventional SRM. While many more characteristics should be considered in making a direct comparison, this quick observation reveals the potential of the design to facilitate greater overlap of torque production among the phases compared with a conventional SRM.

Dynamic Simulators

To have the capability to fully assess the overall impact of the variation of a range of design parameters, two separate universal dynamic simulators were developed. The simulators are universal in the sense that they can simulate various motor designs, even other types of motors, with slight modification to the simulator. An FEA based simulator was developed for design optimization such that most of the design parameters are variable and the corresponding design geometry, mesh, boundary conditions, and constraints are generated in an automated manner. This simulator is well suited for integration with other types of analyses such as integrated structural and thermal FEA. The other simulator is similar in nature, but is better suited for control optimization and uses a differential equation based machine model developed by ORNL.

Extensive efforts were made to ensure that the impacts of saturation, mutual coupling, and other interactions between phases were fully realized. It is common for designers to neglect these phenomena, but the acknowledgement of these aspects is particularly important for this unconventional design approach. Both simulators have the capability to work in various modes such as current, torque, or speed regulated operation so that the simulation is conducted as if the design were in actual operation in a vehicle. Figure 2 shows a graphical user interface (GUI) that was developed to provide an effective way to operate the dynamic simulators and generate and edit waveforms which are supplied and returned from the simulator code.
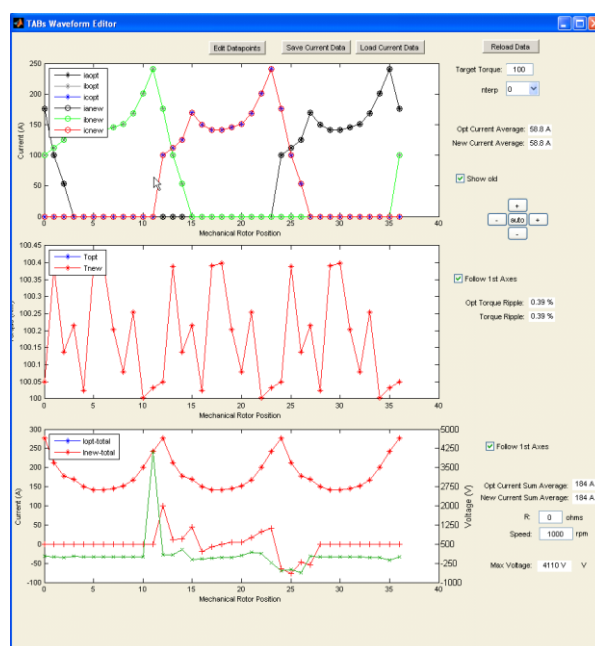
Fig. 2. GUI developed to operate dynamic simulators.

Control Algorithm Development

The dynamic equation based simulator is particularly useful for optimizing control conditions such as maximum torque per amp, minimum torque ripple, and maximum efficiency. A considerable amount of effort was devoted to the development of control optimization codes for operation with near-zero torque ripple. Since torque is a function of three currents and position, the currents at each position can be chosen to meet the desired torque reference, provided that current and voltage constraints are not violated. Therefore, this approach requires dynamic modeling to ensure that the required voltage does not exceed the amount available from the dc link. The resulting problem is nonlinear multivariable, multiobjective optimization with nonlinear constraints. Attempts were made to use optimization algorithms including

various genetic and neural networking techniques, but computational times were tremendous and there was difficulty in obtaining globally optimal solutions, as local solutions were often presented despite the use of a global algorithm. Therefore, ORNL developed an algorithm termed the "brute-force" method, based on the unconventional manner in which the problem is approached using this method. The method involves the automated generation of an initial solution for the desired conditions followed by development of a series of solutions that fall within the given constraints. At this point, the brute-force method finds the optimal solution and verifies that it is a global solution, or another iteration is commenced. It is estimated that about 10,000 lines of code were written to carry out this task in which recursive functionality is used to explore solution regions. The overall result is a collection of reference waveforms for points throughout the entire operation region.

Solutions obtained from the brute-force method were analyzed with the dynamic equation based simulator, with the results for less than 5% torque ripple conditions indicated by the blue trace in Fig. 3. Torque ripple can be defined in various ways, and in this case, it is based on the quadratic mean of the ripple divided by the average torque multiplied by 100. This method was used as opposed to using single values such as the maximum and minimum torque, which do not fully incorporate all aspects of the torque waveform. For example, a torque spike with very short duration could be present in the torque waveform, and the latter torque ripple calculation would be greatly affected although the inertia of the system would most likely render the spike to be minimally consequential. A torque level of about 170 Newton meters (Nm) is achievable at low speeds with a torque ripple level of 5%. At 4,000 rpm, the machine is capable of producing 125 Nm, which is a power level of 52.4 kW, with a torque ripple of only 5%. Calculations which include copper and iron losses indicate that the efficiency of the motor under these conditions is about 94.5%. As speed increases, the power capability decreases if the torque ripple is limited to 5%. But at higher speeds, it may be possible to alleviate the torque ripple constraints based on the increased momentum associated with these speeds.
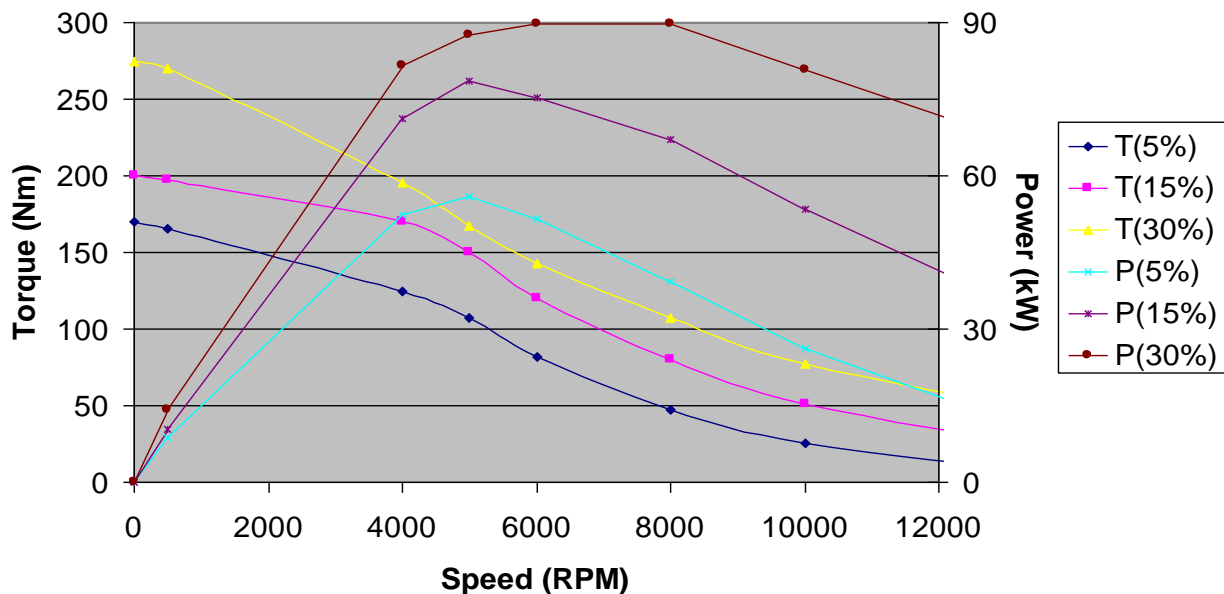
Fig. 3. Torque and power versus speed.

Continuous conduction control can greatly increase the output power of an SRM at moderate and high rotor speeds as a higher amount of current is applied in the torque production region (for the motoring operation mode). This is achieved by not requiring the current in each stator tooth to reach zero during each electrical cycle. Because current is not zero when the rotor rotates beyond the alignment position,

negative torque is applied to the shaft, and thus this control mode does not operate with utmost efficiency, but it can greatly increase the power capability of the machine. This is particularly relevant to vehicle propulsion applications, wherein the average required power is relatively low for normal driving conditions and only short durations of high power demand are required for situations such as passing other vehicles or merging with high-speed traffic. However, there may be issues associated with acoustic noise during this type of operation.

The additional traces shown in Fig. 3 represent the torque and power capabilities of the machine with torque ripple percentages that are greater than 5%. Simulations indicate that the machine can produce about 75 kW at 8,000 rpm with a torque ripple of 20% and more than 90 kW at 8,000 rpm with a torque ripple of 30%. Simulations also show that the machine is capable of operating beyond 15,000 rpm. The size of the machine used in these simulations matches that of the second generation Prius, with roughly a 10 in. stator outer diameter and a 3.3 in. stack length. This particular design is well suited for an application similar to that of the primary motor of the Camry hybrid electric vehicle (HEV), where a gear reducer is used to increase the torque capability while the high speed operation results in improved power density. These simulation results indicate that this design approach could potentially offer a competitive alternative to PM machines in HEVs.

Structural, Modal, and Acoustic Assessments

Mechanical analyses were conducted to perform design optimization and validation in terms of structural integrity and minimal acoustic signature. Force vector results from electromagnetic FEA studies were used to establish proper loading conditions and boundary conditions for these mechanical FEA studies. As peak loading conditions were applied, stress analyses were conducted on the components within the assembly. As structural improvements were incorporated into the design in response to these studies, the impacts upon the electromagnetic characteristics were assessed in separate analyses, as necessary.

Advantages of IMFP Design

In unconventional IMFP SRMs, air or other nonmagnetic materials provide magnetic isolation between segments which would otherwise have a direct path in which flux traverses. Fig. 4 shows examples of the flux paths for a conventional 12-8 (12 stator poles and 8 rotor poles) SRM [4(a)] and an unconventional 12-10 SRM [4(b)]. The flux path of the conventional 12-8 SRM, indicated in light orange, travels an angular distance of 90° through the stator back-iron (yoke) from pole to pole. The unconventional IMFP 12-10 uses short, localized flux paths (also indicated in light orange).

<table>
<tr><td>(a)</td><td>(b)</td></tr>
</table>
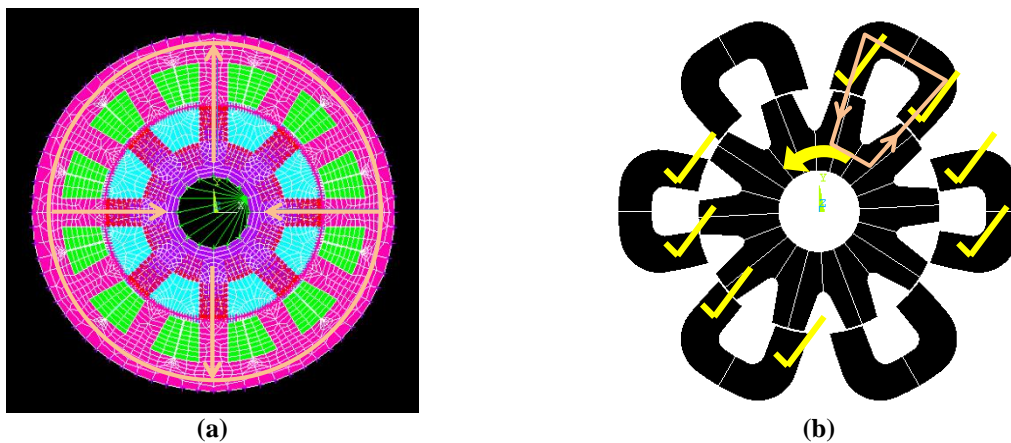
Fig. 4. Flux paths in (a) conventional 12-8 and (b) unconventional IMFP 12-10 SRMs.

Three major loss components in electric machines are hysteresis, eddy current, and copper losses. Hysteresis and eddy current losses are roughly proportional to the length of the flux path. Therefore, the IMFP has a noticeable advantage over conventional designs because the flux path length is much shorter. Furthermore, hysteresis loss (heat) is generated from molecular friction when magnetic particles in the steel are subject to a reversal of magnetic field. For certain IMFP configurations, such as the 12-10, there is essentially no flux reversal in the stator pieces. This is a significant advantage when compared with conventional flux reversal frequencies that are 3 or more times the electrical frequency because all phases share the same back-iron. Additionally, SRMs in general have a smaller amount of wasted copper at the end-turns because the phase windings do not overlap each other and thus can have lower copper (I^2R) losses than what is typical for PM or induction machines with distributed windings.

Conventional winding arrangements in SRMs consist of single coils individually wrapped around each stator tooth, as shown in Fig. 5. This winding arrangement can be used on the unconventional IMFP 12-10 (and other IMFP arrangements), with a coil wrapped around each of the 12 stator teeth. In this case, each pair of coils on the U-shaped stator pieces is typically connected in series, and these can be connected in series or parallel with other coils in the same phase. However, the segmented pieces of the IMFP provide another option for coil placement. A coil can be "yoke-wound" on each stator piece, as indicated in Fig. 6. The coil can be strategically wound such that the impact upon the radial size of the machine is minimal. This is achieved by allowing the conductors of the outermost portion of the coil to spread wide across the outermost arc of the stator pieces. It can be assumed that area "A1" and area "A2" (Fig. 6) should be about equal, and because the arc of A2 is much greater than the arc of A1, the radial width of the outermost coil is much smaller.
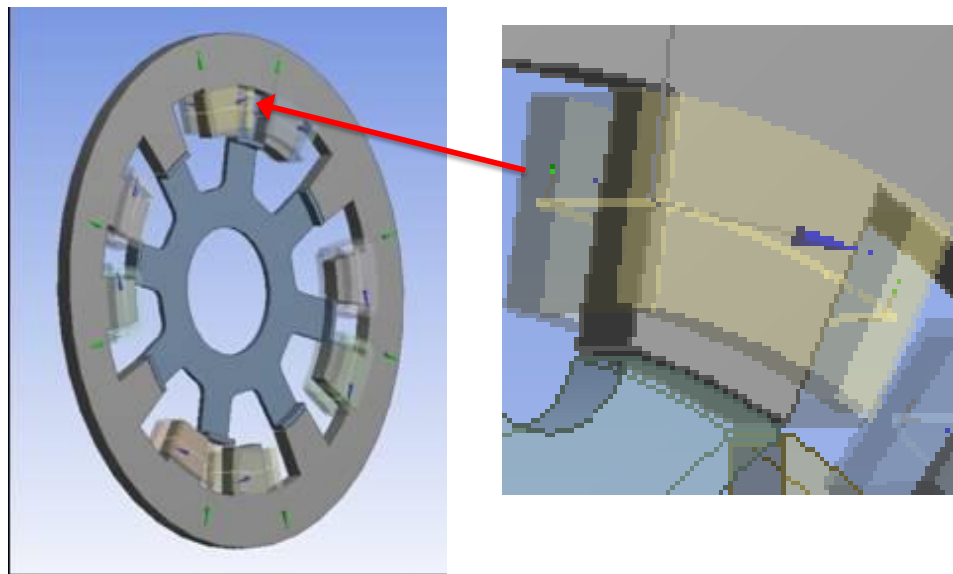
Fig. 5. Conventional SRM tooth winding.
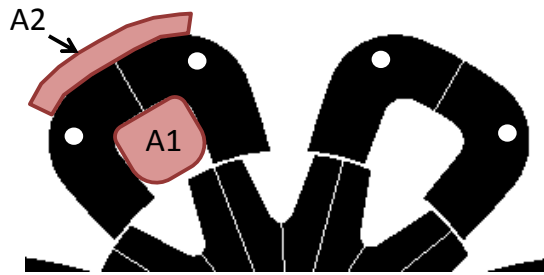
Fig. 6. Yoke-wound IMFP 12-10 SRM.

Although the significance of the transition from conventional tooth-wound coils to yoke-wound coils seems minimal, there are many advantages that can be gained from this transition.

1. Improved heat transfer. Copper has a thermal conductivity that is about 40 times higher than steel, and thus the wire on the outer arc of the pieces can interface with a cooling infrastructure. Normally, the heat in motors has to travel through the steel before reaching a heat exchanging interface (often aluminum for hybrid vehicles). For the IMFP, heat generated by copper losses has a good thermal conduction path directly to the heat exchanger. Note that because the windings are not a solid piece of copper, but actually insulated copper wires, the observed benefit will not be 40 times higher. Removal of heat is essential for obtaining high power densities—which is important for vehicle applications, among many other applications. Therefore, this improvement of heat transfer leads to improved power densities and specific powers as higher output power can be obtained with an equivalently sized motor.

2. Wider stator and rotor teeth. The stator teeth can be much wider because the conductors are not located outside of the teeth on the U-shaped pieces. This allows for the torque production from each phase to be more broad, increasing the overlap of torque production among phases. This can also increase the overall torque, and facilitates the reduction of torque ripple and opens up more opportunities to reduce acoustic noise from a controller/software standpoint. The rotor teeth would also likely be wider as the stator teeth are wider. Therefore, the teeth in the motor are more mechanically substantial and will not vibrate and create acoustic noise as much as thin teeth would.

3. Higher fill factor. More conductors can be located in the middle of the "U" because two coils do not share this volume. Because the yoke-wound approach has one single coil, the issue of winding two coils in place or installing two prewound coils onto the stator teeth is avoided. These latter approaches require compromises on fill factor. Additionally, high voltage applications may require the two coils to be separated with insulation material to keep the coils electrically isolated and mechanically protected from vibration. And ultimately, fill factor is also a key factor in obtaining high power density and/or specific power.

4. Facilitation of acoustic noise damping techniques. Because the space between the U-shaped stator pieces is void, there is opportunity to incorporate noise damping countermeasures into this void. For example, an epoxy or rubber-like substance could be inserted between the pieces to dampen the noise, which may allow some the acoustic energy to be dissipated in the damping compound as opposed to being transmitted through the chassis/support structure.

5. Other ways to use void between stator pieces. Other unexplored uses of the void between the U-shaped pieces include the integration of coolant passages (air or liquid), addition of separate coils, use of non-rare-earth magnets to counteract leakage, and location of power electronics/controls.

6. Winding manufacturability. The U-shaped stator pieces can be wound before they are installed in the motor, and they can be wound directly by simply "chucking" the pieces such that they can be rotated while wire is wrapped around them. This method was used during the fabrication of the prototype. The tooth-wound approach allows for the stator pieces to be wound before they are installed in the motor, but the coils would typically be prewound and then slid onto the stator teeth. Finally, the tooth-wound approach requires the interconnection of the two separate coils on each stator piece, while this is avoided with the yoke-wound technique.

Fabrication and Assembly of IMFP SRM

High tolerance parts for the IMFP SRM were fabricated externally by tool shops and lamination manufacturers. Figure 7(a) shows the SRM assembly with star-shaped end bells, a stator containment ring with integrated cooling channels, end plates, a stainless steel shaft, and custom swaging tool. The swaging tool was used to simultaneously compress the rotor laminations and fold a rigid retention lip to hold the laminations in place. Rotor and stator laminations are shown in Fig. 7(b), where the stainless steel shaft with a 2 in. outer diameter is also visible. With a rotor outer diameter of about 6 in. and stator outer diameter of about 10 in., the lamination dimensions are similar to that of Toyota designs. The laminations were combined into a 3.0 in. stack, which is shorter than the 2004 Prius stack length of 3.3 in. and slightly longer than the 2007 Camry stack length of 2.8 in. Both rotor and stator laminations are 0.014 in. thick and are made of nonoriented M19 steel with a C5 coating for electrical insulation.

| (a) | (b) |
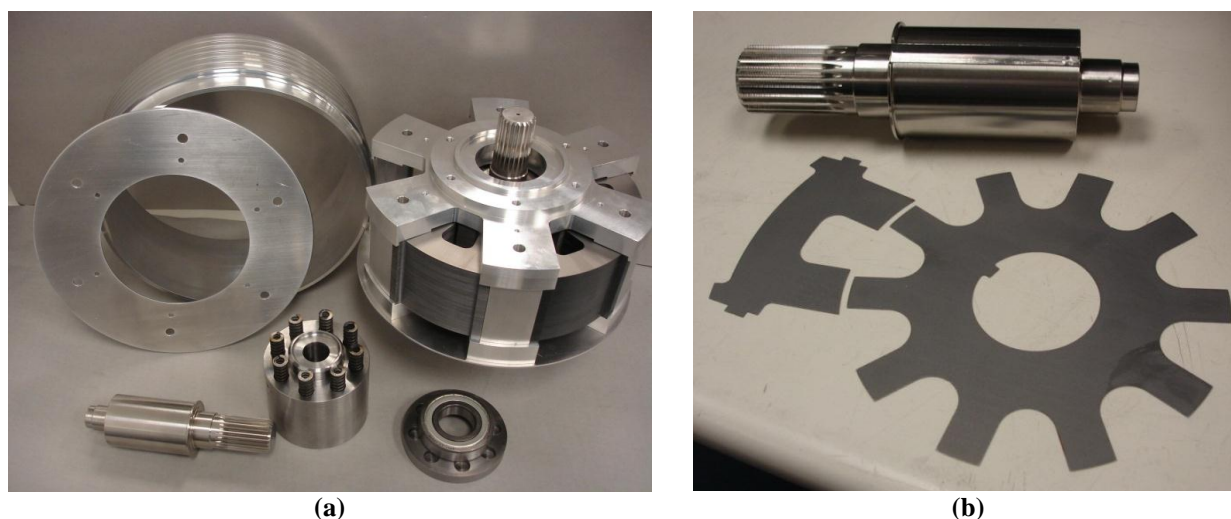
Fig. 7. High tolerance parts for the IMFP SRM: (a) fabricated parts and (b) stator and rotor laminations with rotor shaft.

A custom in-house winding system was developed to clamp, hold, and rotate the stator piece and compress the windings to improve fill factor and form it to mate with the stator containment ring. The first batch of stator windings incurred some hi-pot test failures, and the stator pieces were rewound with special care at sharp bending radii. Mylar was used as a slot liner, with 0.005 in. and 0.010 in. thick pieces being applied, depending on the location. The windings were vacuum impregnated with a variant of Dolph's thermal-setting varnish. Opposing stator coils, shown in Fig. 8(a), were connected in series with two coils per phase. These could have been connected in parallel, and other possibilities include the use of switchable windings to obtain high torques at low speed and to extend the speed range of the machine.

| (a) | (b) |

Fig. 8. IMFP SRM final assembly: (a) winding installation and (b) finished IMFP SRM.

Characterization

Control optimization software developed by ORNL uses machine parameters to determine optimal control conditions throughout the entire torque and speed range. These machine parameters (namely torque and flux linkages) vary as a function of rotor position and three independent currents. With the need to collect 1,500 data points which include many high-current situations, a system was developed to automatically step and lock the rotor in desired positions as sequences of current combinations were applied to the windings. This system required a substantial amount of time to develop, but was crucial in obtaining motor parameters without experiencing over-temperature conditions. Figure 9 shows locked rotor torque measurements for single phase excitation plotted against position. These measurements are significantly lower than what simulations indicated. A clear comparison can be made by computing a ratio of simulated locked rotor torque over measured locked rotor torque. This ratio is plotted versus dc current in Fig. 10 for single phase (pink trace) and multiple phase (yellow trace) excitation. This graph indicates that the measured torque-per-current ratio is relatively close to simulated values for very low currents, but the ratio decreases significantly with increasing current. At 200 A, the measured torque values are 25% and 35% lower than simulated torque capabilities for multiple phase and single phase excitation, respectively. These results suggest that the steel starts magnetically saturating at a much lower current level than simulations indicate. Premature saturation results in lower torque capability and ultimately lower efficiency. Locked rotor simulations are simple and usually accurate as there is no impact from eddy current, hysteresis, and I^2R losses. These results were verified with multiple FEA software packages, and therefore, it can be reasonably assumed that the quality of the steel laminations is inferior.
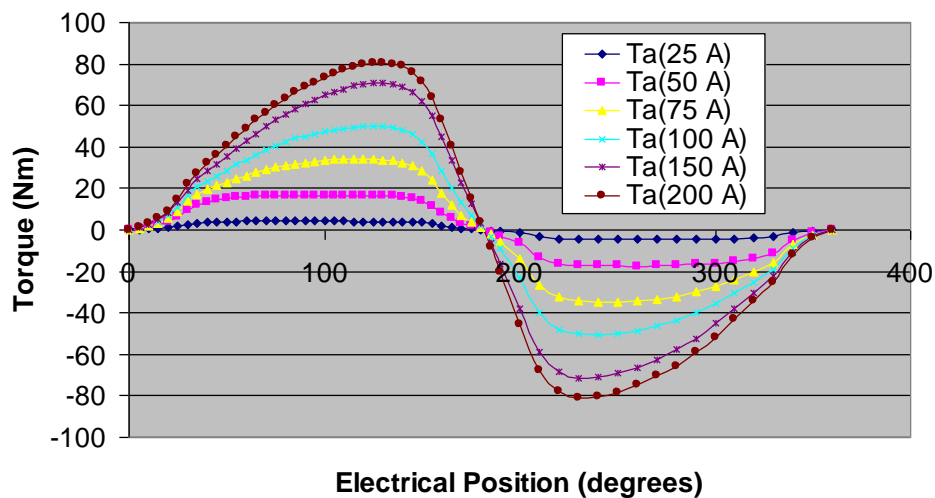

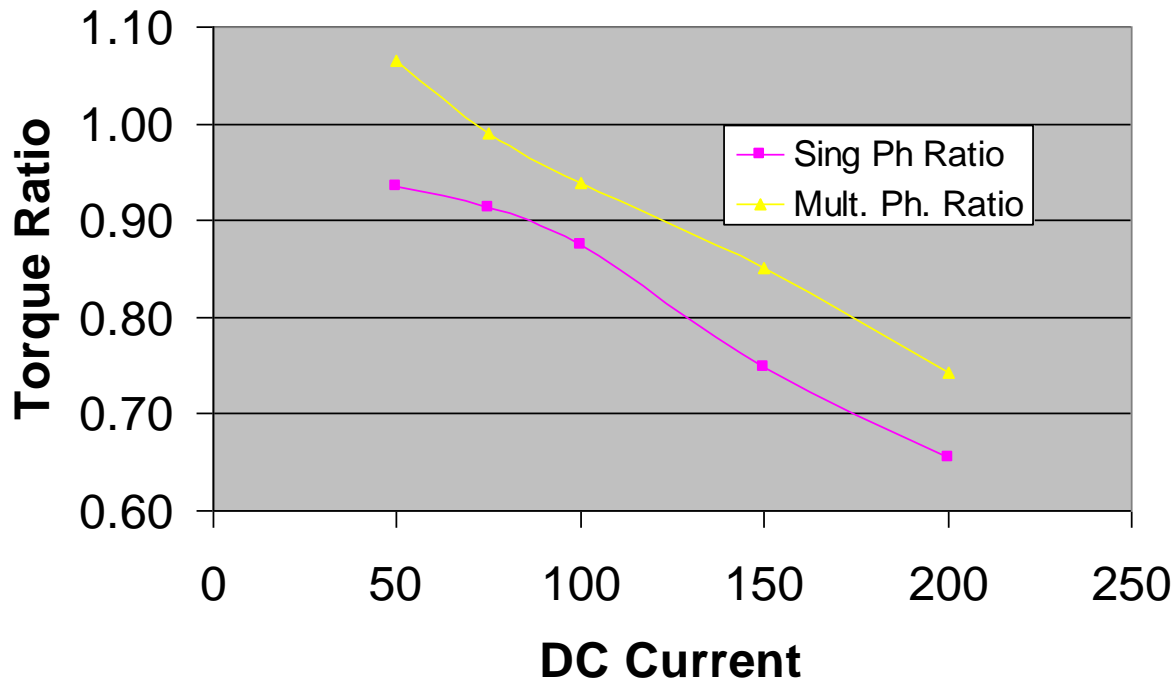**Fig. 9. Single phase locked rotor torque.**

Fig. 10. Ratio of simulated/measured locked rotor torque.

Drive/Controls Implementation and Test Results

The inverter drive shown in Fig. 11(a) was developed on a previous project for a four phase 8-6 SRM and was used to drive the three phase IMFP 12-10 SRM. A face-mounting system was used where the IMFP SRM was face-mounted to a torque meter and the torque meter was face-mounted to the dynamometer, as shown in Fig. 11(b). The circuit diagram in Fig. 12(a) depicts two IGBTs and two diodes per phase, which is the same as a conventional inverter except the diodes are not antiparallel diodes. Several switching schemes are available, but an interleaved switching technique was used which is capable of applying +Vdc and –Vdc (when rectifying) as well as a zero volt loop which alternates between upper and lower IGBTs, thereby dispersing heat generation. Additionally, the effective switching frequency in the winding is 2 times that of the individual IGBT switching frequency, which facilitates improved current control and reduced acoustic noise. A comprehensive control system console, shown in Fig. 12(b), was developed to allow convenient manipulation of various control parameters. Original control methods involved a conventional current feedback loop with proportional-integral-derivative (PID) regulation. To mitigate torque ripple, optimal current profiles typically have significant transients which are difficult for a conventional PID current loop to track. In addition to transient references, the influence of electromagnetic interference, current transducer bandwidth, and position measurement resolution are also factors in the performance of the current loop. Therefore, a self-learning pseudo-flux-observer control algorithm was developed to more readily anticipate and generate the appropriate control signals needed to track the optimal current profile. The uppermost and middle graphs visible in the control console shown in Fig. 12(b) show successful tracking of a demanding current profile.
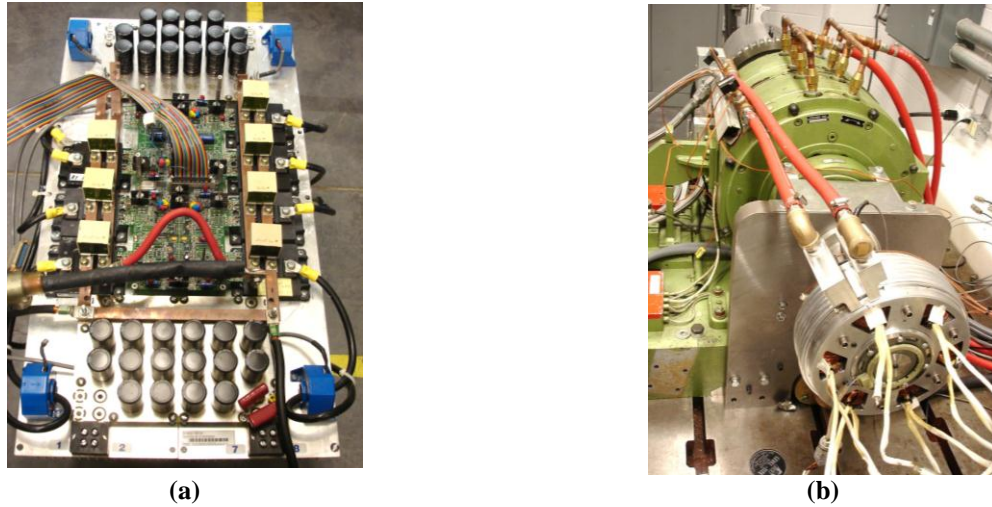
(a)   (b)

Fig. 11. Test setup: (a) inverter used to drive the IMFP SRM and (b) dynamometer installation.

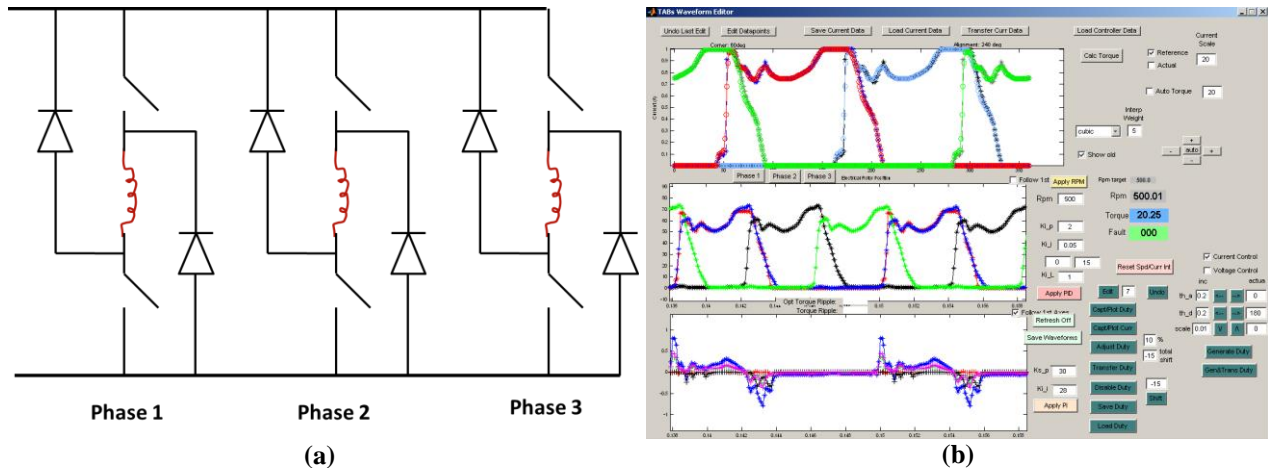(a)   (b)

Fig. 12. Drive controls: (a) converter diagram and (b) control console.

The motor was designed for operation with a dc link voltage of 650 V, but tests were limited to 400 V to ensure that potential failures did not occur as time limitations became eminent. For the same reasons, phase currents were limited to 200 Arms and rotational speed was limited to 5,000 rpm. An ethylene-glycol coolant temperature regulator was used to maintain the coolant temperature at 65°C during most of the tests. An efficiency map is shown in Fig. 13, with portions above 5,000 rpm being extrapolated. Motor efficiency is comparable to many benchmarked PM machines for low to moderate loads and low speeds (less than 750 rpm) and reaches 90% at 3,500 rpm with a peak efficiency measurement of 93%. However, efficiency values are relatively low between 1,000 and 3,000 rpm in comparison with most PM machines, which is no surprise when considering the low torque-per-current that was observed in locked rotor tests. Peak torque and peak power curves for 400 V are shown in Fig. 14, with a peak power level of 23.4 kW at 3,000 rpm. Also shown in Fig. 14 are peak torque and power curves for 650 V, which were extrapolated from 400 V operational data. The curves indicate that the motor can produce a power level of about 38 kW. Torque-ripple levels at these peak power conditions reached about 15% to 20%, which is much higher than simulations indicated. This is also a detriment that was likely caused by inferior electrical steel properties. Because the torque-per-current was observed to be about 0.75 of the simulated

locked rotor torque, peak power capability with the expected steel quality can be roughly estimated to be 38 kW times a factor of 1/0.75, which is 50.7 kW.
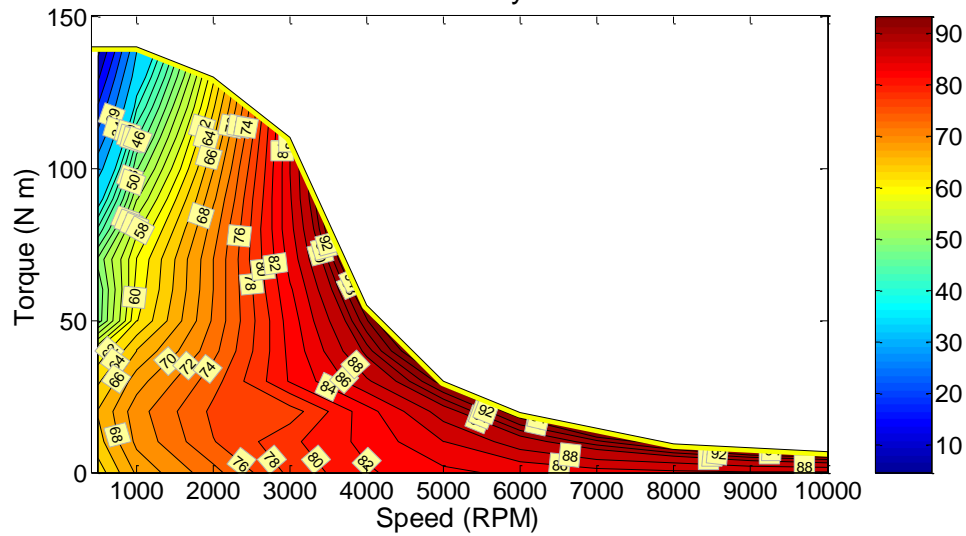
Fig. 13. Motor efficiency measurements.
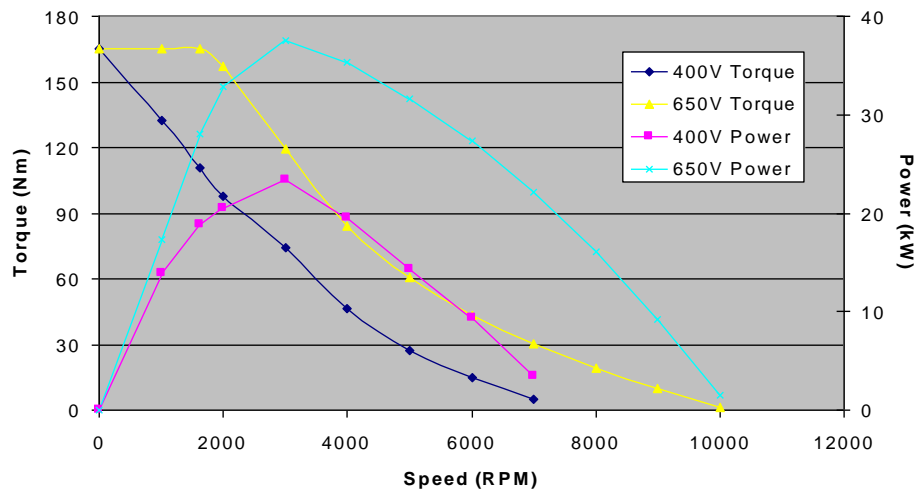
Fig. 14. Motor torque and power capability.

Using the measured and estimated power levels previously discussed, power densities and specific power values were generated using a volume of 8.5 L and a mass of 36 kg (Table 1). While 400 V power capabilities result in low power densities and specific power, estimated 650 V capabilities put the design close to DOE 2015 targets. If estimations with improved steel are used (50.7 kW), DOE 2015 targets are surpassed and DOE 2020 power density is surpassed. In Table 2, a similar comparison is made with systems that have been benchmarked at ORNL. Tested power densities at 400 V compare closely with the 2011 Hyundai Sonata, and expected 650 V power densities fall short of 2010 Prius power densities, whereas anticipated improved steel estimations place the power density and specific power above the 2010 Prius. The SRM has the advantage of reduced end-turn volume, but the axial length of the motor may need to be increased to modify the structure to mitigate potential eddy current impacts upon efficiency.

Table 1. Comparison of ORNL IMFP SRM power density and specific power with DOE targets

Parameter	ORNL IMFP 400 V SRM (23.4 kW)	ORNL IMFP 650 V SRM (38 kW)	ORNL IMFP 650 V SRM (50.7 kW) (estimation with improved steel)	DOE 2015 targets	DOE 2020 targets
Peak power density, kW/L	2.8	4.5	6.0	5.0	5.7
Peak specific power, kW/kg	0.7	1.1	1.4	1.3	1.6

Table 2. Comparison of ORNL IMFP SRM power density and specific power with benchmarked systems

Parameter	ORNL IMFP SRM 400V, (23.4 kW)	ORNL IMFP SRM 650V, (38 kW)	ORNL IMFP SRM 650V, (50.7 kW) (estimation with improved steel)	2011 Sonata (30 kW)	2010 Prius (60 kW)	2006 Honda Accord (12 kW)	2004 Prius (50 kW)
Peak power density, kW/L	2.8	4.5	6.0	3.0	4.8	1.5	3.3
Peak specific power, kW/kg	0.7	1.1	1.4	1.1	1.6	0.5	1.1

Conclusion

- Created design optimization tool for SRMs.
    — Automated geometric optimization, meshing, and application of boundary conditions.
    — Interfaced with existing FEA software package.
- Generated control optimization software.
    — Parameterized dynamic nonlinear three phase modeler.
    — Optimizes with respect to speed and torque ripple.
- Achieved encouraging simulation results.
    — 52.4 kW (125 Nm at 4,000 rpm) with 5% torque ripple and 93% efficiency.
    — 75 kW at 8,000 rpm with 20% torque ripple.
    — 90 kW at 8,000 rpm with 30% torque ripple using continuous conduction.
    — Stress and modal analyses verified design feasibility in qualitative acoustic noise assessments.
- Tested machine up to 5,000 rpm.
    — Results lower than expected, but accounting for steel degradation, results are close to simulations and address DOE targets.
    — Torque ripple improved, but still not to desired level observed in simulations.

Patents

T. Burress and C. Ayers, *Isolated Multiple Flux Path Reluctance Motors with Yoke-Wound Coils and Wedge Supports,* Serial number 61/509,213, filed 7/19/2011, patent pending.

Publications

None.

3.2   Novel Flux Coupling Machine without Permanent Magnets

Principal Investigator: John Hsu
Oak Ridge National Laboratory
National Transportation Research Center
2360 Cherahala Boulevard
Knoxville, TN 37932
Voice: 865-946-1325; Fax: 865-946-1262; E-mail: hsujs@ornl.gov

DOE Technology Development Manager: Susan A. Rogers
Voice: 202-586-8997; Fax: 202-586-1600; E-mail: Susan.Rogers@ee.doe.gov

ORNL Program Manager: Mitch Olszewski
Voice: 865-946-1350; Fax: 865-946-1262; E-mail: olszewskim@ornl.gov

Objectives

- Research the feasibility of an electric motor, without permanent magnets (PMs), that has the potential to replace the interior PM (IPM) motor in hybrid electric vehicles and plug-in hybrid electric vehicles.
- Create a novel flux coupling machine (NFC-machine) with the following characteristics.
  — Is brushless.
  — Contains no rotor windings.
  — Has no PM material.
  — Is an adjustable field synchronous machine.
  — Retains both rotor-excitation torque and reluctance torque productions.
- Produce a motor that meets or comes close to DOE's 2020 motor targets for cost, weight, volume, and efficiency.

Approach

- Based on the FY 2010 identification of the advantages and weaknesses of the most advanced IPM motors available in the market today,
  — develop and fabricate a prototype motor that retains the advantages of IPM motors without the use of rare earth PMs and
  — overcome the disadvantages such as the nonadjustable field, low permissible temperature, and the low power factor at peak power of the IPM machines.

Major Accomplishments

- Completed engineering drawings that were based on the results of a significant number of electromagnetic and mechanical simulations.
- Completed prototype NFC-motor parts machining, fabrication, and assembly.
- Completed locked rotor test on the NFC-machine prototype.
  — Confirmed that the novel NFC-machine concept is a workable concept.
  — Full testing scheduled to be completed during FY 2012 (scheduling issues with the Dyne cells prevented completion by the end of September 2011).
- Completed study on the power factor of IPM motors during the period the prototype motor was fabricated and machined.
- Based on the power factor study of the IPM motor, determined the technical approach for better power factor of the NFC-machine was feasible (discussed in detail later in this report).

Future Direction

- DOE funding for this project ended this fiscal year. Any issue observed from the full test will be recorded and used as we seek industry partners to bring this novel achievement to the market.

Technical Discussion

The prototype NFC-motor is shown in Fig. 1. Its overall size based on the active materials (13.6 L) is about the same as the Toyota Camry motor (13.9 L).
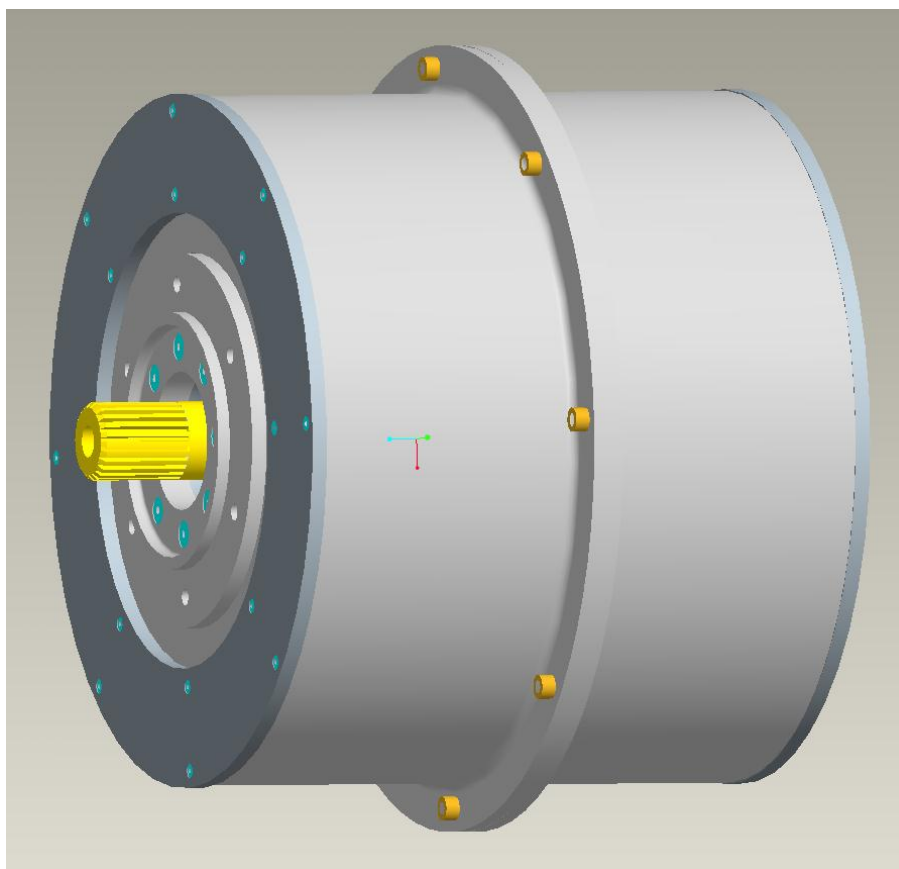
Fig. 1. Prototype NFC-motor.

Locked-Rotor Tests

Figure 2 shows the results of the locked rotor torque versus load angle tests for the prototype NFC-motor at 100 Stator winding currents with field excitation currents changed from 0 A to 6 A. The torque curves do not go up much when the field excitation current exceeds 3 A. This indicates that the magnetic saturation becomes significant at higher field excitation currents.

Figure 3 shows the results of similar tests, under similar conditions, for the Toyota Camry IPM motor. The prototype NFC-motor's peak torque of 86 Nm at 100 A stator winding current (with 6 A field excitation current) shown in Fig. 2 compares favorably with the peak torque of 85 Nm at 100 A shown in Fig. 3 for the Toyota Camry IPM motor.
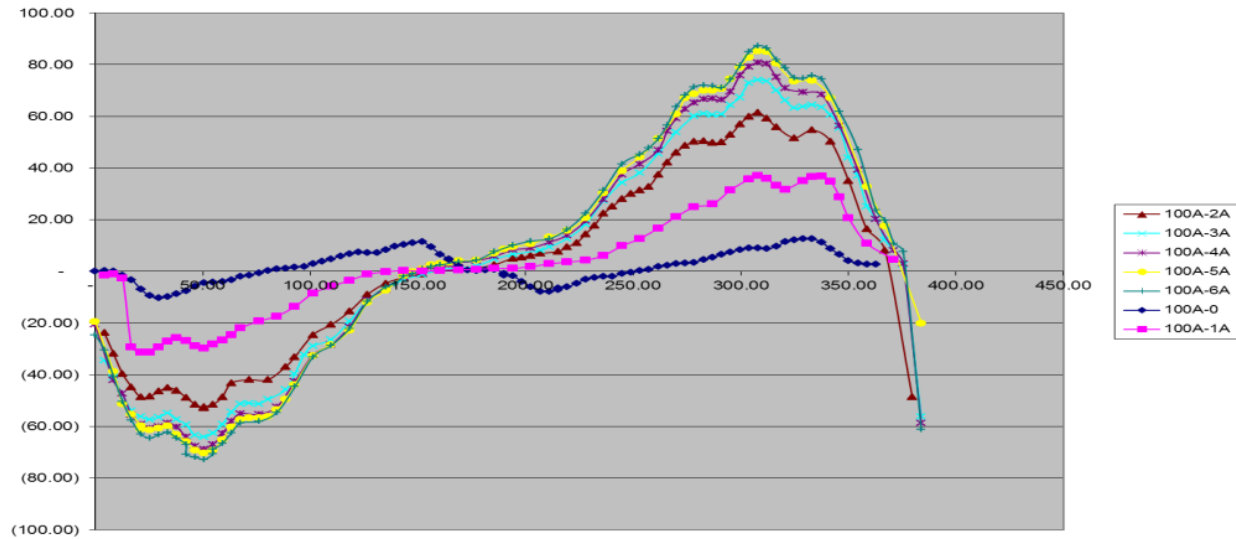
Fig. 2. Results of locked rotor torque versus load angle tests at 100 A stator current with field excitation currents changed from 0 A to 6 A.
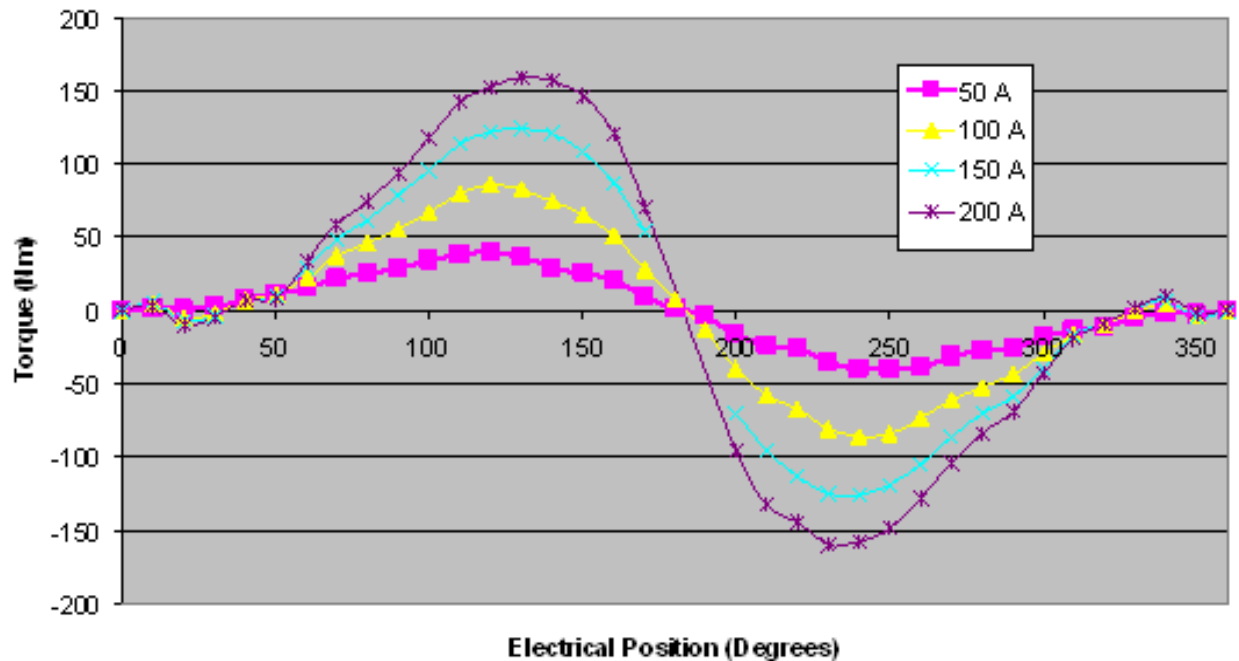
Fig. 3. Results of locked rotor torque versus load angle tests of Toyota Camry IPM motor.

Figure 4 shows the results of locked rotor torque versus load angle tests of the prototype NFC-motor at 150 A stator current with field excitation current at 0, 3, and 6 A. As this figure shows, the peak torque at 6 A excitation current is 106 Nm. For the Camry motor the peak locked rotor torque shown in Fig. 3 at 150 A stator winding current is 122 Nm. Based on this comparison, the NFC-motor saturates more rapidly than the Camry motor.

Comparing Figs. 2 and 4, the increase of the excitation current seems to be more effective for the additional torque when the stator winding current goes up.
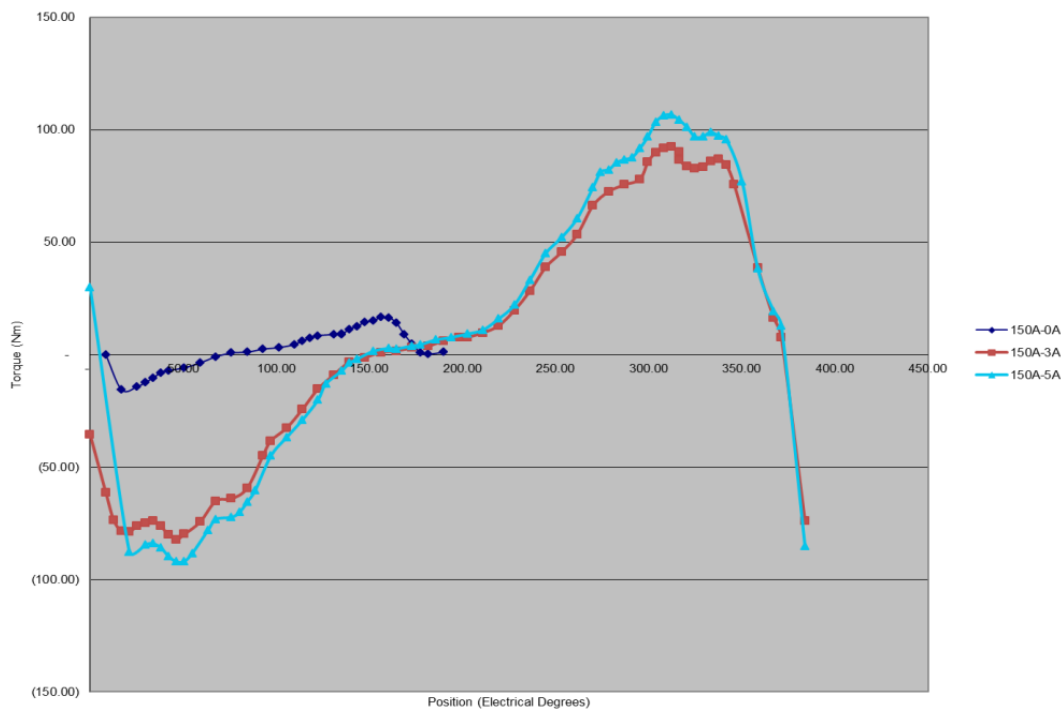
Fig. 4. Prototype NFC-motor tested locked rotor torques versus load angle at 150 A stator current with field excitation current at 0, 3, and 6 A.

Tests conducted at 240 A stator winding current and 8 A field excitation current give 132 Nm locked rotor torque. This is proportionally lower than the 160 Nm predicted in the theoretical performance simulation shown in Fig. 5. However, this magnetic saturation problem can be overcome in future designs.
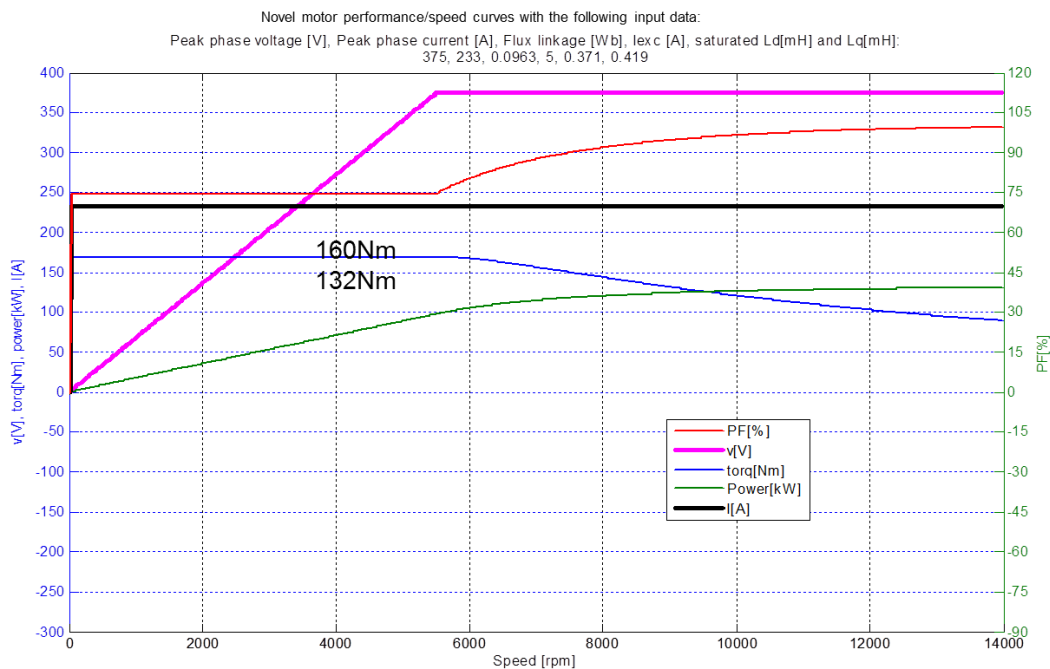
Fig. 5. Simulated prototype NFC-motor performance versus speed.

Study on Power Factor of IPM Motors for Guiding Arrangement of NFC-Machine Reluctance Poles

The Toyota Camry and Lexus motors are IPM motors. Figure 6 shows the direct (d) and quadrature (q) axes of their rotor laminations. The d-axis flux of any of these IPM motors has to go through rare earth PMs that have a low permeability value roughly equal to the permeability of air. Therefore this d-axis flux path is difficult for the flux created by the stator winding current to go through as compared to the q-axis flux path without the blocking from the PM. The basic knowledge for power factors of wound-field synchronous machines can be viewed from [1]. Additional information on the Toyota Camry and Lexus motors can be found in references [2] and [3].
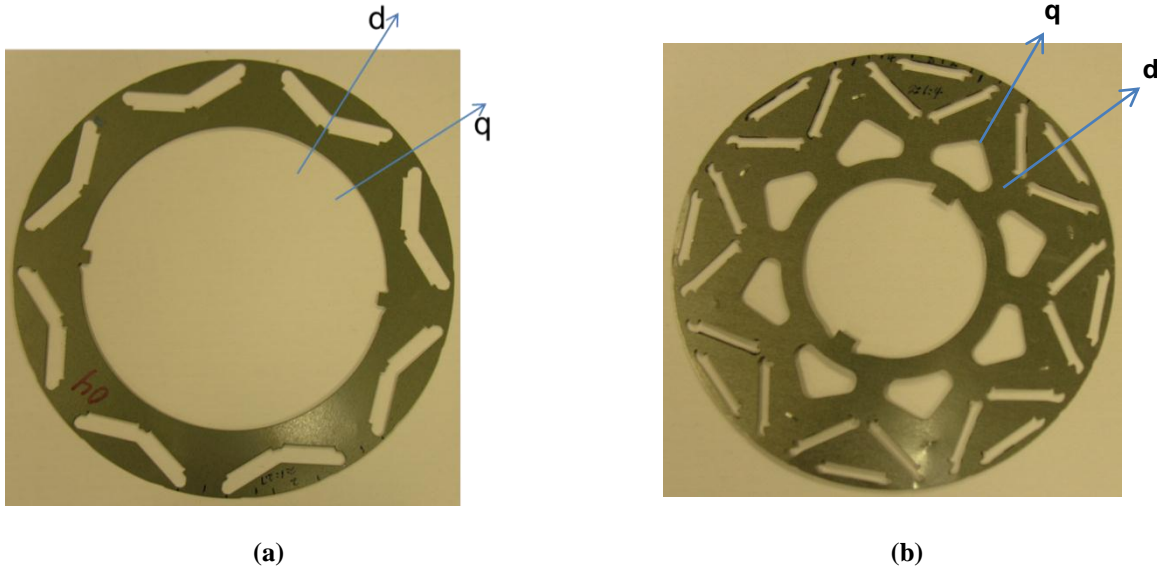

(a)   **(b)**

Fig. 6. Locations of rotor direct (d) and quadrature (q) axes of typical IPM motors: (a) Toyota Camry and (b) Lexus.

Based on the definition of inductance, L, that is the ratio of the flux linkage of the stator winding divided by the stator winding current, the inductance of the stator winding for the d-axis flux, *Ld*, is lower than that of the q-axis. The mathematical expression for the comparison of inductance values of the rare earth IPM motors is as follows:

$$Ld < Lq \; . \tag{1}$$

Low power factor at peak power of IPM motors. Some test reports indicate that the power factor at peak power of IPM motors can be as low as 0.45. The reason is that the IPM peak torque versus load angle, δ, is changed greatly according to the motor torque equation:

$$Power = 3\frac{VE}{\omega L_d}\sin\delta + 3V^2\frac{(L_d - L_q)}{2\omega(L_d L_q)}\sin 2\delta \; . \tag{2}$$

When *Ld < Lq,* the second term of Eq. (2) becomes negative; the negative sin 2δ term makes the peak torque located at δ greater than 90°. The corresponding peak torque versus load angle, δ, is shown in Fig. 7. These curves are taken from previous testing performed on the 2004 Prius. They show that the reluctance torque is about 70% of the PM torque.
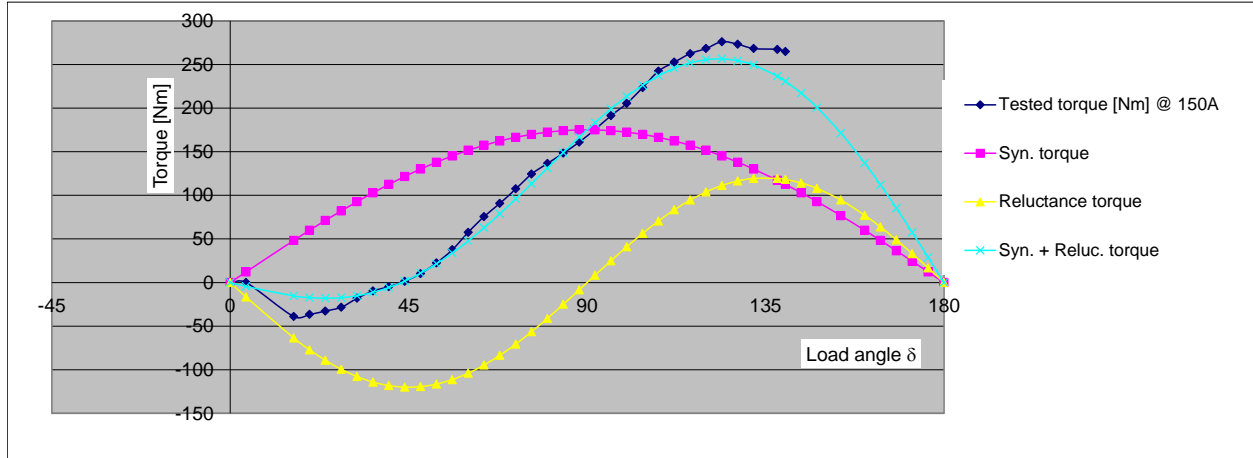
Fig. 7. When *Ld < Lq,* peak torque (or peak power) is at load angle, δ, greater than 90°.

The stator winding voltage phasor, *V,* must be balanced with the phasor sum of the back-electromotive force (emf), *E,* and reactance voltage drops, $V_{reactance\ drops}$, in the stator winding. The phasor of the back-emf, *E,* is lagging behind the winding voltage, *V,* by δ degrees. This results in the diagram of the voltage phasors shown by the darker plots for the *Ld < Lq* case in Fig. 8.

From the phasor of the reactance voltage drop, $V_{reactance\ drops}$, the stator winding current, I, for *Ld < Lq* can be seen to be roughly 90° lagging . The power factor angle, φ, can be obtained from the diagram. The power factor angle, φ, is large, causing the power factor, cos(φ), to be low at peak powers for rare earth IPM motors.

Reluctance Poles Arrangements for U-Machines

Because there is no PM in the rotor of the NFC-machine to block the flux produced by the stator winding current, the NFC-machine can be designed for either the *Ld < Lq* case or for the *Ld > Lq* case.

When the option of an *Ld > Lq* design is selected, the corresponding *Ld > Lq* peak torque (or peak power) is at a load angle, δ, less than 90° as shown in Fig. 9.

The assessment of power factor at peak power is shown by the lighter plots in Fig. 8. The angle between the motor winding voltage, *V,* and the motor winding current, *I,* for *Ld > Lq* is significantly less than the IPM *Ld < Lq* case; hence a higher power factor at peak power can be obtained.
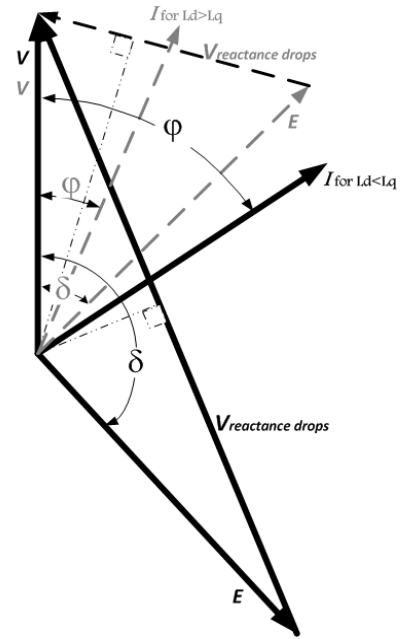
Fig. 8. Phasor diagrams for (a) the *Ld < Lq* case (darker plots) and (b) the *Ld > Lq* case (lighter plots).
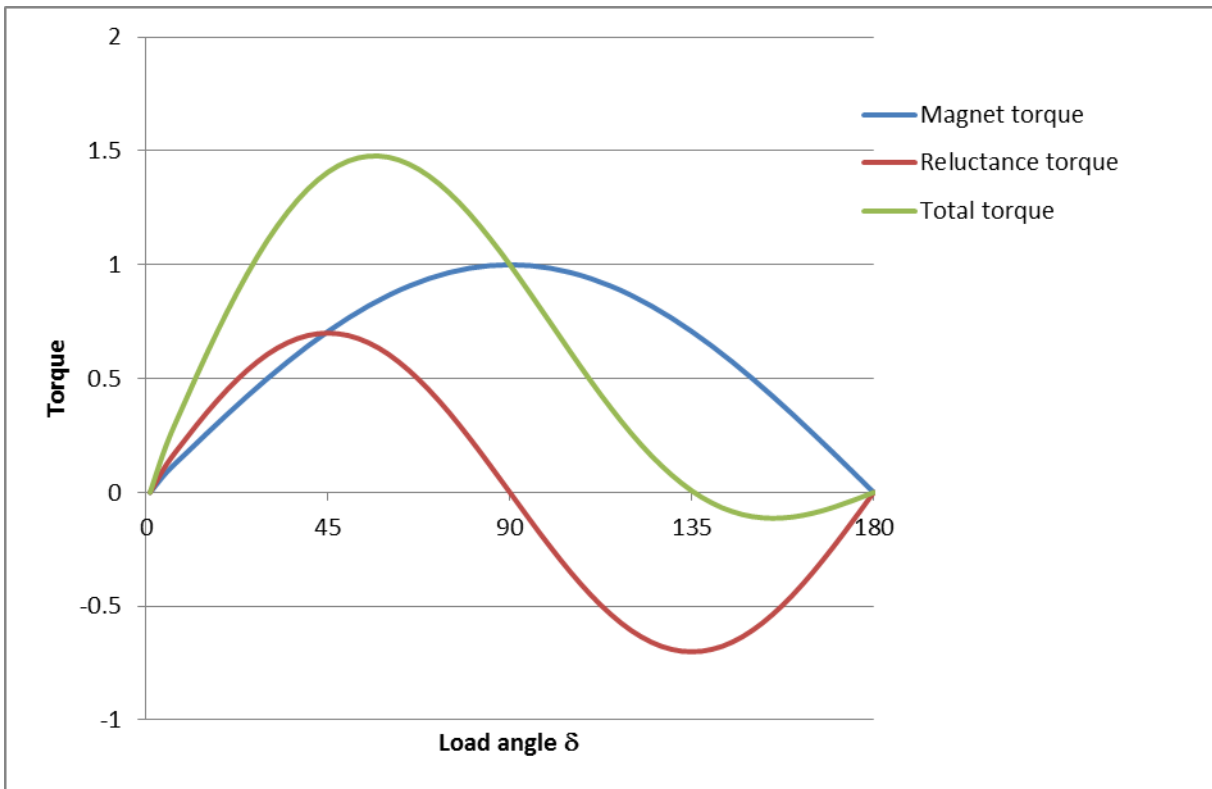
Fig. 9. When *Ld* > Lq, peak torque (or peak power) is at a load angle, δ, less than 90°.

Conclusion

- This DOE project has created a new topology for a motor without PMs, brushes, or rotor windings. Additionally, the machine contains adjustable windings.

- Initial tests confirm the practical validity of the novel flux coupling concept.

- Adjustable field excitation of the NFC-machine can improve the power factor and consequently lower motor and inverter currents.

- The magnetic saturation shows up earlier than the simulation predicts; however, this saturation problem can be overcome in future designs.

- In view of the rapid cost increase of rare earth PMs, the NFC-machine without PMs may reduce cost per kilowatt of the vehicle drive motors by 75% or more.

- The NFC-machine can operate at higher temperatures because there is no PM related temperature limitation.

- Integration of the NFC-machine and the current source inverter may further lower the drive system cost.

Patents

J. S. Hsu, ID-2505, *Combined Electric Machine and Current Source Inverter Drive System,* serial number 61/417,906, filed 11/30/2010.

J. S. Hsu, ID-2522, *Multilevel Windings,* serial number 61/433,546, filed 1/18/2011.

J. S. Hsu, ID-2670, *Arc Suppression for Reactive-Circuit Switches* filed 2011.

Publications

Internal and DOE review meeting publications only.

References

1. A. E. Fitzgerald, Charles Kingsley, Jr., and Stephen D. Umans, *Electric Machinery,* McGraw-Hill Book Company, Fourth Edition, 1983.

2. T. A. Burress, C. L. Coomer, S. L. Campbell, L. E. Seiber, L. D. Marlino, R. H. Staunton, and J. P. Cunningham, *Evaluation of the 2007 Toyota Camry Hybrid Synergy Drive System,* ORNL/TM-2007/190, January 2008 (Revised April 2008).

3. T. A. Burress, C. L. Coomer, S. L. Campbell, A. A. Wereszczak, J. P. Cunningham, L. D. Marlino, L. E. Seiber, and H. T. Lin, *Evaluation of the 2008 LEXUS LS Hybrid Synergy Drive System,* ORNL/TM-2008/185, January 2009.

3.3   Motor Packaging with Consideration of Electromagnetic and Material Characteristics

Principal Investigator: John M. Miller
Oak Ridge National Laboratory
National Transportation Research Center
2360 Cherahala Boulevard
Knoxville, TN 37932
Voice: 865-946-1469; Fax: 865-946-1262; E-mail: millerjm@ornl.gov

DOE Technology Development Manager: Susan A. Rogers
Voice: 202-586-8997; Fax: 202-586-1600; E-mail: Susan.Rogers@ee.doe.gov

ORNL Program Manager: Mitch Olszewski
Voice: 865-946-1350; Fax: 865-946-1262; E-mail: olszewskim@ornl.gov

Objectives

Motor continuous power ratings become increasingly important as traction drives become more electrified. Motor packages need to be developed to satisfy the requirement for increased continuous power, including consideration of electromagnetic effects and new material characteristics. In light of this, for FY 2011 the key objectives were as follows.

- Characterize a state-of-the-art (SOA) interior permanent magnet (IPM) electric machine for use as the baseline comparator.
- Establish the technology trajectory of the baseline IPM based on designs from the last 7 years.
- Develop a complete model of the baseline IPM, including fully characterized electromagnetic parameters.
    — Assess its leakage inductance for future alternative winding design comparisons.
    — Compare performance to laboratory measurements.
- Develop a thermal model, including material characteristics, of the baseline IPM and compare results to laboratory measurements.

Approach

- Use the 2010 Prius 60 kW IPM traction motor benchmarking data [1] and available dynamometer mapping point data to construct an equivalent circuit model of the baseline machine.
- Assess the electromagnetic and material characteristics of the baseline IPM as a means for improving motor continuous power rating (complements National Renewable Energy Laboratory motor cooling project).
- Establish technology trajectory of SOA IPM designs through comprehensive review of ORNL archived benchmarking reports [1, 2]. Apply the design comparisons to the overall objective of this project to identify areas for future exploitation to improve continuous power rating relative to peak power.
- Develop a thermal model of the baseline IPM using material characteristics, and compare simulation results to ORNL dynamometer thermal rise test data.
- Establish directional guidelines based on FY 2011 project electric-magnetic-thermal results for use in a follow-on FY 2012 prototype IPM design project having a goal to deliver higher continuous power. The work is supported by ORNL materials specialists in lamination steels (shear rolled, graded silicon, other) and thermal materials (epoxy composites, others).
- Assess alternative winding designs suitable for FY 2012 design program.

Major Accomplishments

- Analyzed ORNL benchmarking data on the 2010 Prius IPM, and extracted key parameters for development of an electrical equivalent d-q axis circuit model. The main reluctance torque production mechanisms obtained from the saturation dependent inductances $L_{qds}(I_s)$ resulted in a high accuracy torque prediction model.
- Developed a computer model for the lamination material reluctivity to be used in the magnetic equivalent circuit (MEC) model and simulation.
- Developed the baseline IPM technology trajectory showing highly optimized magnetic flux, electric matching of machine to source voltage, and virtually constant power loss of stator copper for the 7 years of products evaluated. The implication is that the IPM supporting thermal management system evolved little over the interim.
- Developed a thermal model of the baseline IPM, and validated it against ORNL benchmarking data. The thermal model provides ORNL researchers a finite element analytical model for predicting IPM copper, lamination iron, and rotor magnet dissipation mechanisms.
- Established directional guidelines for the FY 2012 machine design improvement to demonstrate higher continuous power rating.

Future Directions

- During FY 2012 initiate design alternatives for the baseline IPM rotor and stator laminations to decrease magnetic loss. Perform detailed deformation sequences on shear rolled lamination steel for higher GOSS (grain oriented silicon steel) texture and lower losses to transverse and rotational flux. Include in the design and simulation work the material properties of new composite epoxy and other thermal management materials.
- Fabricate testable prototypes of the FY 2012 IPM design, and validate improved continuous power rating based on new lamination steel, improved conductor and winding design, and thermal management materials.
- Fabricate one stator with new lamination steel, and compare performance to baseline IPM.
- During FY 2013 perform fabrication and testing of thermal materials.

Technical Discussion

Development of Baseline IPM Electrical Model

The 2010 Prius [Toyota Motor Company (TMC)] traction motor rated at 60 kW (Fig. 1) was selected as the baseline machine because it represents a SOA IPM technology according to ORNL benchmarking data. Essential electrical parameters were extracted from the dynamometer test data so that a comprehensive electrical model could be compiled for future use as a comparator for alternative magnetic and thermal materials and for performance comparisons. Dynamometer testing data were taken using the TMC production inverter power stage and ORNL's inverter controller. A point of interest regarding TMC's IPM designs is that all have been 48 slot, eight pole, and three phase using 0.3 mm lamination steel but various rotor permanent magnet (PM) designs from straight (2003) and single "V" to one double V in the 2008 Lexus hybrid.

Table 1 summarizes the electromagnetic design of the baseline IPM, a 2010 Prius traction motor rated at 60 kW; 13,500 rpm; and 205 Nm. Based on the electromagnetic mass (22.74 kg), the specific power of this design is: SP = 2.64 kW/kg and compares very favorably with the DOE 2020 target of 1.6 kW/kg.
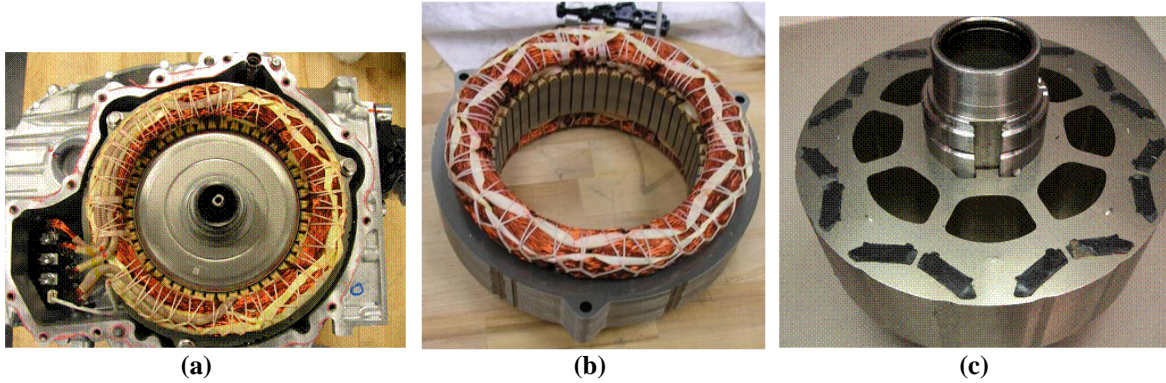
(a)   **(b)**   **(c)**

Fig. 1. 2010 Prius traction motor: (a) assembly, (b) stator, and (c) rotor.

Table 1. Dimensional data on the baseline IPM[a]

ODs (mm)	IDs (mm)	Gap (mm)	ODr (mm)	Stator stack (mm)	Rotor stack (mm)	Stator mass (kg)	Stator copper (kg)	Rotor mass (kg)	PM mass (kg)
264	162.4	0.73	160.4	50.8	50.165	10.36	4.9	6.7	0.78

[a]Abbreviations: ODs = outer diameter-stator, IDs = inner diameter-stator, and ODr = outer diameter-rotor.

ORNL benchmarking data taken on the baseline IPM [1] provided sufficient test data for a convenient characterization and mapping point (5,000, 60) for a speed of 5,000 rpm and continuous torque of 60 Nm. This mapping point was selected because it represents the 30 kW continuous operating power at rated voltage and is also the point of highest efficiency of this IPM, as demonstrated in Table 2. The power factor (PF) angle at this mapping point was 35.88°, giving PF = 0.81, a relatively low value but realistic for the IPM at this load condition.

Table 2. Measured data from dynamometer test

U_{dc} (V_{dc})	I_{dc} (A_{dc})	P_e (kW)	P_m (kW)	U_{an} (V_{rms})	I_{an} (A_{rms})	m (Nm)	n (rpm)	η (#)
652.4	50.8	32.9	31.4	310	43	60	5,000	0.954

In operation the IPM stator current vector, I_s, is placed along the maximum torque per ampere line, which for this machine is at the torque angle listed in Table 3. In addition to the torque angle, γ (angle of current relative to q-axis), the IPM will operate with a stator voltage vector that satisfies the machine reactance at this speed. The resulting power angle, δ (angle of stator voltage vector relative to the q-axis), is such that δ = γ + θ.

Table 3. IPM angles needed to construct phasor diagram at mapping point

Torque angle (γ)	PF angle (θ)	Power angle (δ)	Phase displacement (a)	Electrical angle $(θ)_e$
33.34°	35.88°	88.06°	2π/3 radian	$ω_e t$

The relationship of the inverter drive voltage limit, U_s; current limit, I_s; and electromagnetic torque are conveniently shown as circle diagrams. The circle diagram for the SOA baseline IPM is shown in Fig. 2, where the current circle represents the full extent of current vector control over the d-q plane. A segment of the torque hyperbolae and the speed dependent voltage ellipses for three different operating speeds, the mapping point at 5,000 rpm and higher speed ellipses for 9,000 and 13,000 rpm, are also plotted on this

same scale. The fact that the inverter runs out of voltage control and/or current as speed increases is very evident from the figure. In fact, referring to the maximum current circle diagram one can see that the controller would follow a maximum torque per ampere trajectory down the I_s vector until that vector falls inside the voltage ellipse for that speed, thereby satisfying both the inverter voltage and current limit.

Baseline IPM parameter values

r_s=	66mΩ	λ_m=	121mWb
U_{an}=	310 V_{rms}	I_{an}=	177 A_{rms}
$I_s(A)$	L_{ds} (mH)	L_{qs} (mH)	$I_{ch}(A)$
75	0.874	3.10	138
150	0.787	1.78	154
250	0.672	1.03	180
L_{ls}=	0.170		

(a)　　　　　　　　　　(b)　　　　　　　　　　(c)
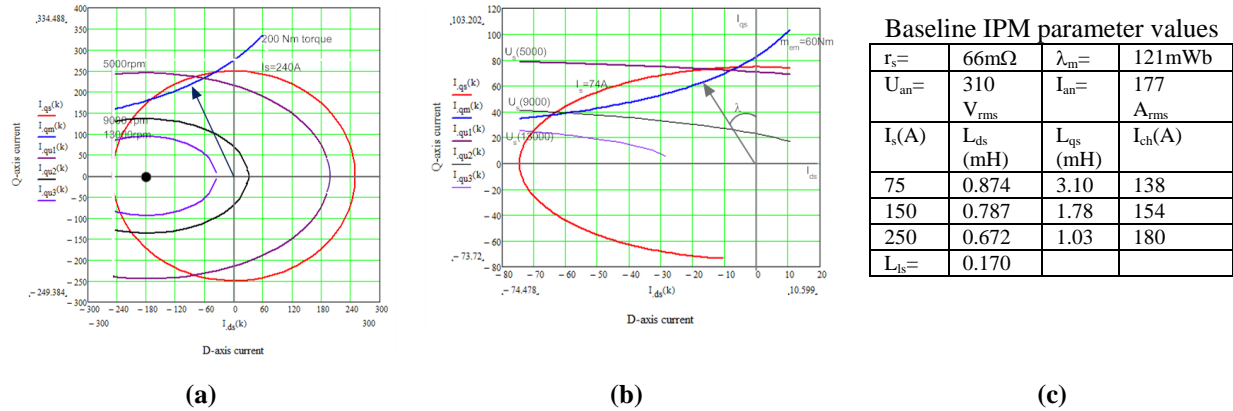
Fig. 2. Baseline IPM circle diagrams: (a) maximum capability and (b) situation at mapping point. The table, (c), shows the extracted parameter values for the baseline IPM.

The IPM characteristic current, I_{ch}, is shown as the solid circle in these diagrams. The parameter table in Fig. 2 highlights the fact that for nonlinear magnetics the characteristic current is a function of loading and moves away from the origin with increasing stator current, but inside the maximum controllable stator current circle. This is very important because as long as the IPM characteristic current remains within the inverter maximum current rating, it will not be damaged under inverter faults such as loss of gating signals at high speed resulting in uncontrolled generation mode. As shown in Fig. 2, the baseline SOA IPM always has its characteristic current well within the current circle and voltage ellipse, even at the highest operating speed.

Figure 3 summarizes the baseline IPM modeling work showing the resultant phasor diagram at the mapping point (5,000, 60) at a phase current of 43 A_{rms}, phase voltage of 310 V_{rms}, and power of 32 kW. The diagram also illustrates some interesting controller behavior in the power angle magnitude, which, being a few degrees larger than what is needed, could potentially improve the PF at this operating point. The modeled torque is nearly the same as the measured.

(a)　　　　　　　　　　　　　　　　　　(b)
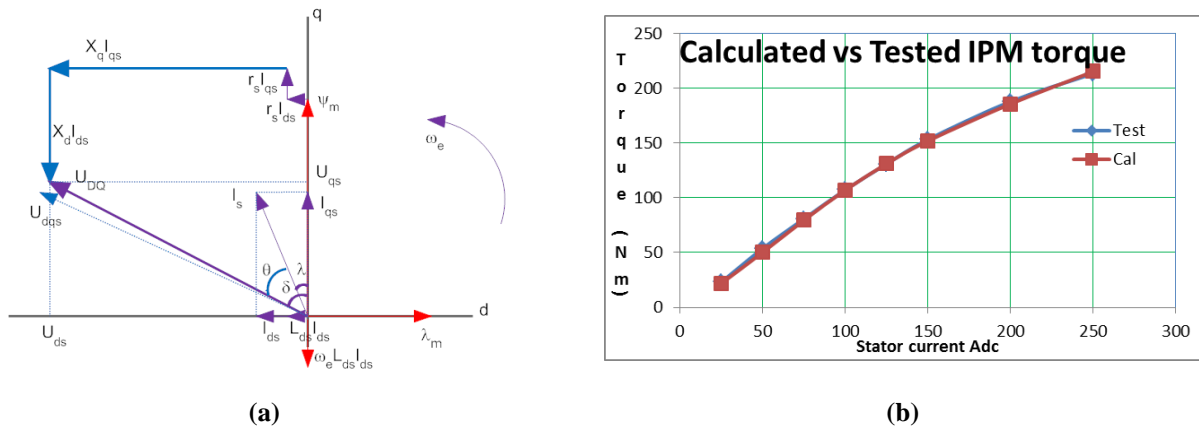
Fig. 3. Summary of modeling work: (a) SOA IPM phasor diagram at (5,000 rpm, 60 Nm) and (b) measured vs estimated torque.

90

The electrical model concludes with a summary of the synchronous inductance variations with stator current loading and the modeled versus calculated electromagnetic torque of this IPM. Table 4 summarizes the findings and shows that calculated electromagnetic torque using the d-q axis inductances that are functions of stator current agrees very well with laboratory measured torque.

**Table 4. SOA IPM calculated torque and inductance parameter versus stator current**

I_s (A$_{dc}$)	m_{em_meas} (Nm)	m_{em_cal} (Nm)	$L_{ds}*(I_s)$ (mH)	$L_{qs}*(I_s)$ (mH)
25	23	21.8	0.93	4.73
50	53.7	50.2	0.9	3.815
75	80.8	79.6	0.874	3.104
100	107.3	107.1	0.845	2.55
125	131	131.2	0.816	2.118
150	153.2	152	0.787	1.783
200	188	185.9	0.73	1.317
250	213.6	215.4	0.672	1.035

Development of Baseline IPM Magnetic Model

Motor packaging work is not complete without an assessment of the flux path material utilization. This turns out to a very useful approach from which the electrical model behavior can be better understood (e.g., why the synchronous inductances exhibit the nonlinearities noted in Table 4). This essentially boils down to the particular machine design specification and material characteristics for low silicon, nonoriented, lamination steel. Lamination steel magnetization is inverse modeled using reluctivity (ν) rather than permeability to iteratively determine the magnetic field strength in the machine element as a function of flux density, $H(B) = \nu(B)$. Using the popular M19 motor grade steel (JFE35JN250) as the baseline case, it was found that a simple power law expression resulted in a very good fit of the steel intensive variable, its magnetic field strength as a function of extensive variable, and flux density. Figure 4(a) illustrates the fit of $\nu(B)$ to the manufacturer's data (diamond markers). The fit is excellent, especially in the highly nonlinear knee region where the IPM mainly operates.
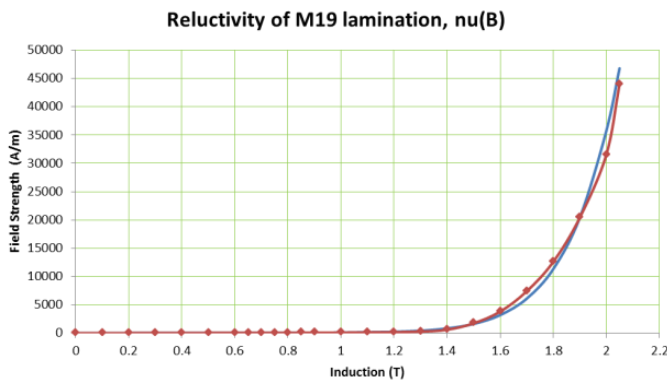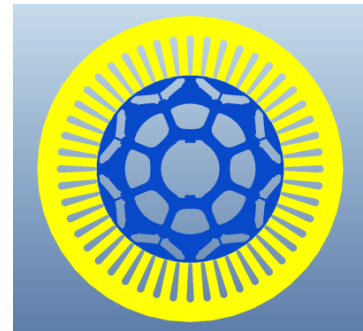
(a)   (b)

Fig. 4. Reluctivity model of (a) lamination steel and (b) lamination design.

An MEC model was developed to identify the main contributors to the nonlinearity in machine inductances and also to find those areas in which the majority of the permanent magnet and armature

reaction magnetomotive forces (mmfs) were consumed. Figure 5 summarizes the MEC model in both its simulation and physical context.

<div align="center">(a)   (b)</div>
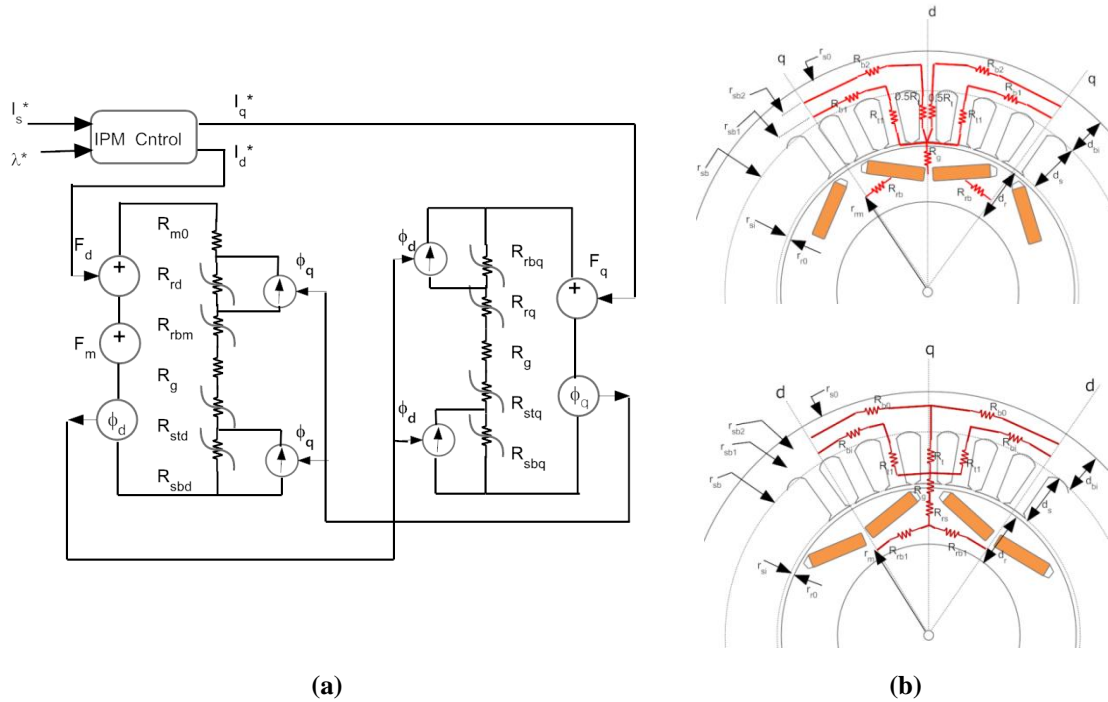
Fig. 5. MEC model of the baseline IPM: (a) circuit simulation model and (b) magnetic element model.

Another purpose for the MEC model was to better understand the rotor magnet V configuration being aligned with and tangent to the d-axis and q-axis flux contours. Finite element analysis (FEA) with the rotor magnet pockets redefined as lamination steel confirmed this—the V is indeed oriented in this manner, having the magnet slabs orthogonal to d-axis flux and tangent to q-axis flux as shown graphically in Fig. 6. Figure 7 shows the corresponding MEC model derived d-axis and q-axis mmf distributions with stator current loading in the various regimes of the IPM (i.e., the stator and rotor steel, the air gap, and the magnet cavities). The MEC model accounts for PM leakage flux in rotor posts and bridges as 9.5% of its mmf and 14% of its flux per magnet or twice that per pole (i.e., 28% leakage flux on each pole). This is in very good agreement with FEA showing 26% flux leakage via posts and bridges in each pole. PM leakage flux in IPMs is a concern given the fact that hybrid vehicle grade NdFeB magnets have 20%−25% Nd and 6%−9% Dy content at 2011 prices of $275/kg and $920/kg, respectively.

It is clear from the MEC model that the IPM rotor saturates most in both d-axis and q-axis; therefore it is the dominant factor in setting the magnetizing inductance variation with stator current. Because of the magnet pockets the variation in $L_{ds}(I_s)$ is much shallower than for the mostly iron q-axis flux path.

IPM Technology Trajectory and Evaluation Areas

This project explored the technology trajectory of the TMC IPM electric machines developed for its hybrid vehicle products in the Prius, Camry, and Lexus vehicle lines. Our findings are that little has changed in the electromagnetic design of these IPMs over the course of the past decade. This is understandable for serial production automotive components as running changes can be very expensive. In light of this, TMC has remained with a three phase, eight pole, 48-slot basic design. Related work on electric machines indicates that eight pole designs do indeed represent a more optimal choice. Table 5

summarizes the salient points of the technology trajectory mapping. In this analysis the electric machine design trends are shown in terms not only of power and torque rating but also of basic attributes such as stator bore to stator stack ratio (OD_s/h) and air gap radius (r_g). Stator bore diameter to stator stack ratio is a fundamental electric machine metric. Another important electric machine metric is aspect ratio that defines the relative deviation from unity of the ratio of stack to pole pitch. Most fundamental of all is the ability of an electromagnetic design to develop a high level of rotor surface shear force (N) per unit mass (kg) termed specific force, SF. SF is fundamental since the lever arm contribution of air gap radius needed to determine torque is eliminated from the metric. The key metrics used in technology trajectory mapping are shaded in Table 5.

(a)   (b)
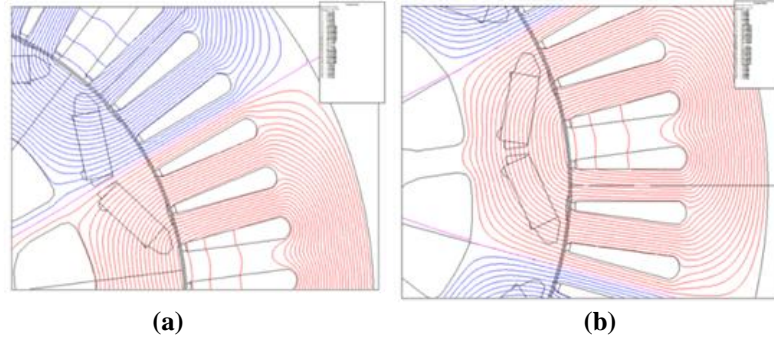
Fig. 6. PM placement relative to the d- and q-axes (I_s = 100 A):
(a) FEA for d-axis; (b) FEA for q-axis.

(a)   (b)

(c)
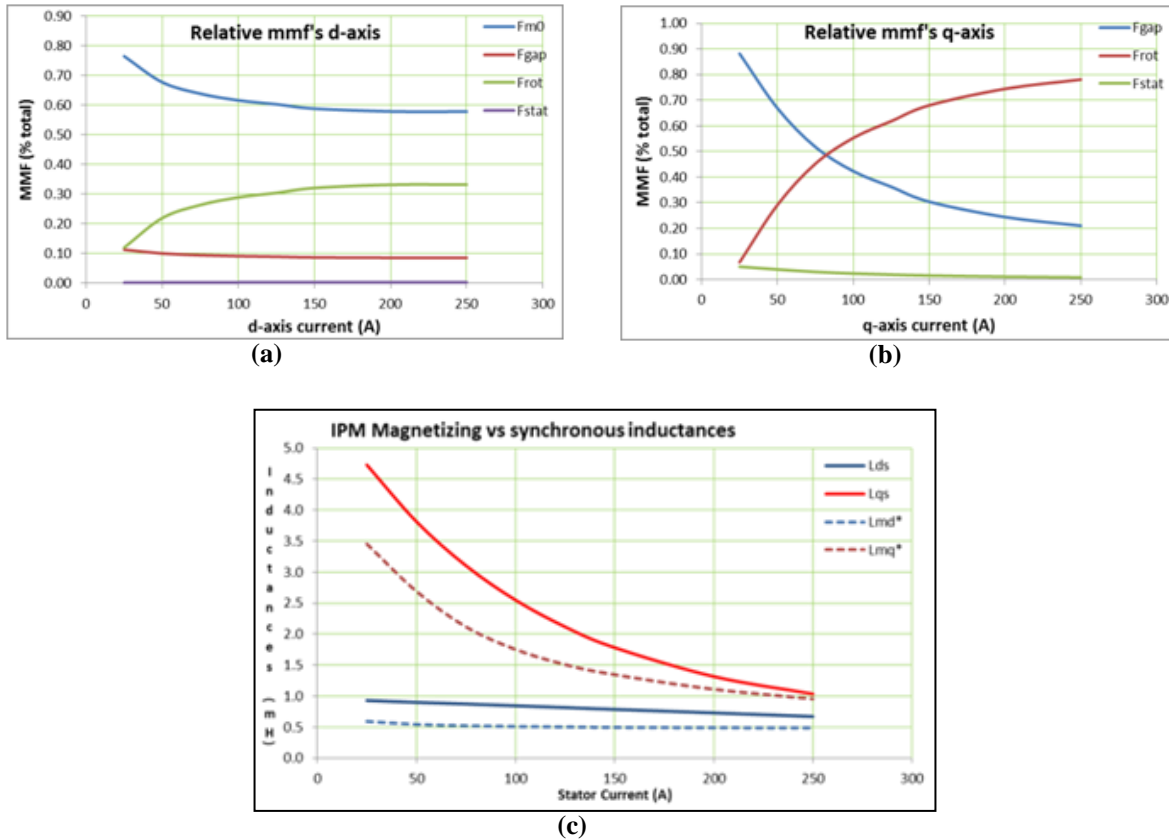
Fig. 7. Mmf distribution breakdown for (a) d-axis and (b) q-axis and (c) inductance comparison for the machine inductance electrical model vs the MEC model.

Table 5. SOA IPM calculated torque and inductance parameter versus stator current

Attribute	Unit	Model			
		2004 Prius	2007 Camry	2008 Lexus	2010 Prius
Peak power, P_{pk}	kW	50	70 (105)	110 (165)	60
Peak torque, m^{pk}	Nm	400	270	300	205
Stator bore: OD_s/h	#	1.92	2.64	0.95	3.16
Mid-gap radius, r_g	mm	80.98	80.98	65.44	80.47
Aspect, $\gamma_s = \dfrac{h}{\tau_p}$	#	1.32	0.95	1.35	0.77
Gap flux: $\bar{B}_g = \dfrac{\Phi_g}{\tau_p h}$	T	0.446	0.453	0.434	0.442
SF	N/kg	136.8	123.3	149.4	112.3
Current density, J_{Cu}	A_{ms}/mm^2	26.25	17.05	16.29	27.35
Copper, P_{Cu}	kW	6.47	6.97	6.24	6.65
Inverter switches, J_{Si}	A_{pk}/cm^2	94.7	124.7	131.6	109.7

The first of the key metrics is aspect ratio or stack/pole pitch, from which the TMC designs can be seen to vary about unity for the production years evaluated (i.e., h/τ_p=1.0). This in itself is of considerable value as the IPM designs tend to a square aspect ratio, which is a known design criterion for both performance and efficiency. The next key metric is average air gap flux density, which tends to be nearly constant over all the electric machines evaluated, with less than ±2.2% variation. This is an extremely small variation over the applications and machine power ratings being evaluated. Therefore, an interim conclusion on trajectory is that aspect ratio and average air gap flux are essentially constant. This is not the case for the SF metric, which varies from 112 N/kg to about 150 N/kg. An SF value of 110 to 120 N/kg is typical of the best induction and variable reluctance electric machines. The real benefit of the high energy permanent magnets used is the capacity of these IPMs to reach SF values of 137 to 150 N/kg, truly high performance.

The remaining three metrics relate to the thermal management system and the power inverter. The first of these thermal metrics is the current density in the copper (J_{Cu}), which not surprisingly aligns with the winding scheme of S-P-P-S going left to right on this table row (P=parallel, S=series). The two series wound stators have the highest current density at maximum loading, while the two parallel wound stators have the lowest peak current density. However, the total copper losses (P_{Cu}) in the machines studied are very nearly identical. This may be intentional on TMC's part and a capacity limitation of their vehicle thermal management system.

The final metric considers the current density in the power inverter semiconductor switches that appears to follow a criterion of J_{Si}=115 + 14%/-17% A/cm^2 for the insulated gate bipolar transistors in use. The correlation with switch current density, if there is any, appears to be with machine SF generation. But that is more coincidence than anything else. A plausible explanation may be taken from the mission requirements of the IPMs studied: (1) Prius is designed for moderate driving, an urban dynamometer driving schedule; (2) Camry is designed for more performance; and (3) Lexus is a premium brand designed for the US06 drive cycle and aggressive driving. Following that rationale, the power converter switch current density number is in proper alignment with vehicle mission requirements.

The main conclusions to be drawn from this trajectory mapping are that few changes have taken place at the electromagnetic level and basically no changes at the materials level over the last 7 years. This puts emphasis on this program's technical direction that advancements on electric machines now must occur at the materials level, specifically focusing on lower loss and inexpensive lamination steel and thermal

compounds. Therefore, when the program moves into its second year in FY 2012, the focus will be on lamination steel and thermal materials using the 2010 Prius IPM as the baseline comparator. The following section summarizes work to date on the baseline electric machine thermal model.

Development of baseline IPM thermal model

Thermal analysis and modeling is based on Fourier's law of heat transfer. Heat transfer in the dynamic state involves a generation rate, an outflow, and storage over any volume under consideration. Our interest is higher efficiency during continuous operating mode, which means the heat generation is balanced by conduction and convection mechanisms so that Fourier's law becomes the vector Poisson's equation. Thermal FEA essentially solves the vector Poisson equation in each mesh element's volume:

$$q_g + \nabla \cdot (k\nabla T) = \rho c_p \frac{\partial T}{\partial t} \ \left(W/m^3\right); \ \ Q = h_c A_s \delta T \ (W) \ ,$$

where, $k[=]\frac{W}{mK}$; $\rho[=]\frac{kg}{m^3}$; $c_p[=]\frac{J}{mK}$; $h_c[=]\frac{W}{m^2 K}$; $Q[=]W$. And in steady state, $\nabla^2 T = -\frac{q_g}{k}$ the vector Poisson equation is solved in the analysis software Flux2D.

Figure 8 illustrates the IPM pole area and slot model for analysis of iron and copper loss. The slot area is lined with Nomex paper (10 mil), and the equivalent copper conductor area is modeled according to the number-in-hand (NIH) winding pattern and coil turns (N_c) showing representative magnet wire insulation content suited to a 220°C rated wire.

| (a) | (b) |
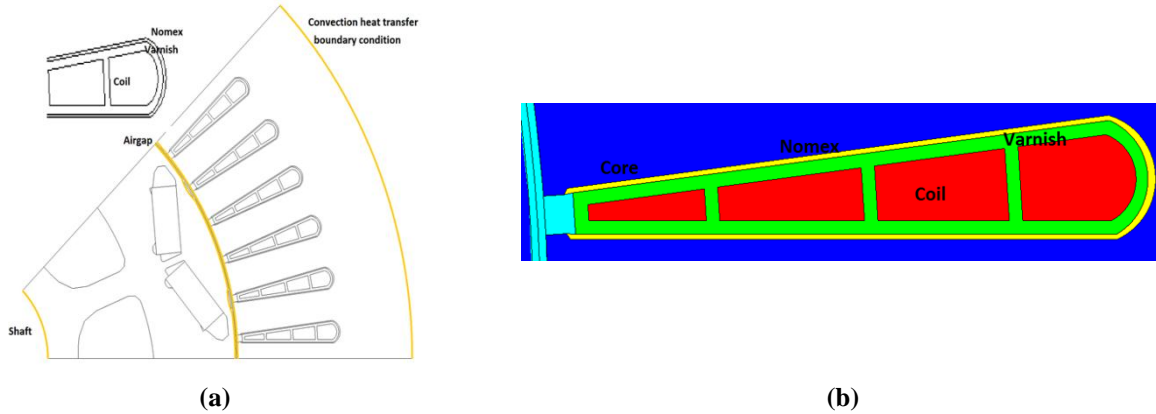
Fig. 8. One-eighth model pole area (a) and slot model (b) used for thermal analysis of the baseline machine.

The heat source, q_g, consists of the lamination core plus copper loss. Heat conduction in this two-dimensional (2D) analysis consists mainly of the core, coil, and insulating material paths. A convection coefficient is applied to the rotor at the mapping point condition (5,000 rpm, 60 Nm) given $I_s = 43$ A$_{rms}$ applied to the stator windings. A constant thermal conduction boundary condition is applied at the rotor shaft, and a constant convection coefficient is applied at the stator OD. The simulation was then run and the stator OD boundary condition modified until the simulated temperature rise was in agreement with laboratory test data. The boundary condition 155 W/m^{2}K < h$_c$ < 200 W/ m^{2}K resulted in good agreement between simulation and measurement.

Copper loss is computed as the Joule heating due to phase current flow in the winding conductors, corrected for temperature as $R_{ph} = 77(1 + 0.00393(100 - 21°C)) = 100.9$ mΩ at T=100°C and the corresponding power dissipation as $P_{cu} = 3 \times I_s^2 \times R_{ph} = 559.7$ W.

Lamination steel core loss is computed using the Berttoti formula (Fig. 9), a modified Steinmetz relation that includes the usual hysteresis component ($\propto f$) and eddy current contribution ($\propto f^{3/2}$) plus an additional eddy current term containing material properties $\sigma = 5.96 \times 10^7 \, (\Omega m)^{-1}$, d = 0.3 mm, p = 7,700 kg/m^3 and k_h is the coefficient of hysteresis loss and k_e is the coefficient of additional eddy current loss. At the mapping point the core loss heat generation turns out to be P_{core} = 421 W determined using the following where M_s is the stator core mass in kilograms:

$$P_{core} = \left\{ k_h B_m^2 f + \frac{\pi^2 \sigma d^2}{6\rho} (B_m f)^2 + k_e (B_m f)^{3/2} \right\} M_s \ (W) \ .$$

At the mapping point the IPM mechanical shaft power, P_m=31kW at η=96%, implies a power dissipation, Pd=1292 W [using P_d=((1-η)/η)P_m)]. The net result then is that $P_d = P_{cu} + P_{fe} + P_{mech}$ → P_{mech} = 1,292 − 559.7 − 421 = 311.3 W for bearing friction, windage friction, and stray losses. Stray load losses are not well quantified at this point but can be partitioned into friction components along with error in copper and core loss due to harmonics, skin effects, and proximity effects.

Summarizing the thermal model performance at the stated mapping point results in the heating shown in Fig. 10 when the rotor convection coefficient, h_c, is 65 W/m^{2}K, and the stator OD boundary condition, h_c, is 155 W/m^{2}K. After 32 minutes the stator temperature has equilibrated to a final value of T_{copper} = 141°C.

(a)

(b)

(c)

(d)
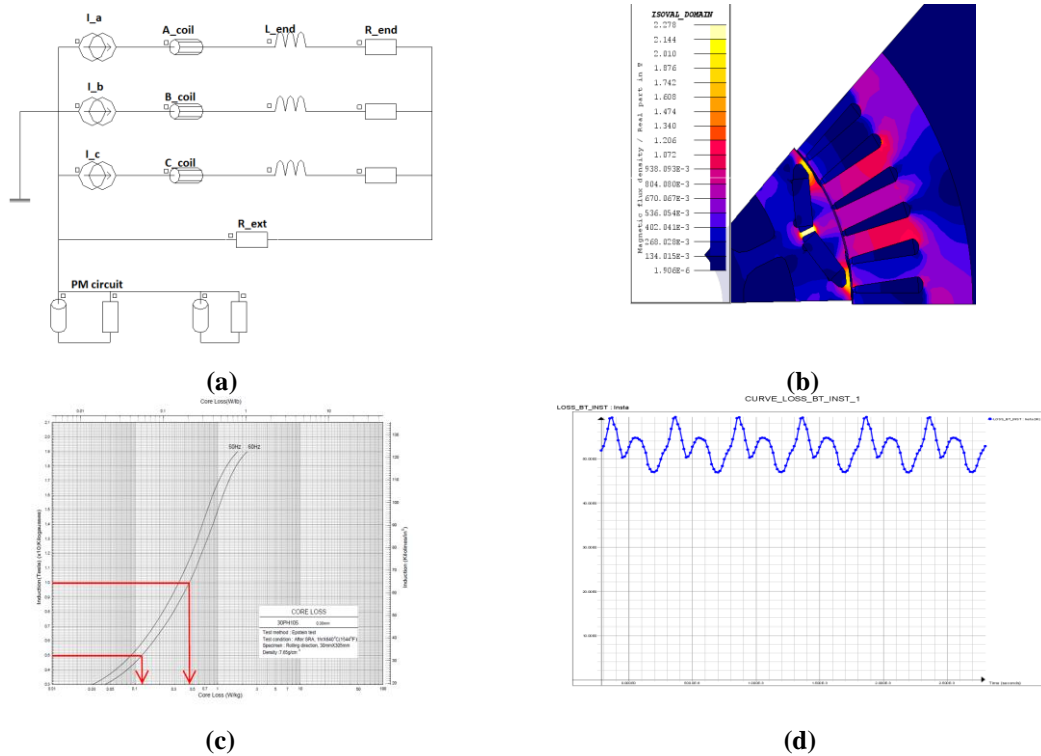
Fig. 9. Derivation of core loss coefficients for Berttoti formula: (a) per pole electrical model, (b) corresponding pole flux density plot, (c) material characteristics, and (d) resultant core loss.
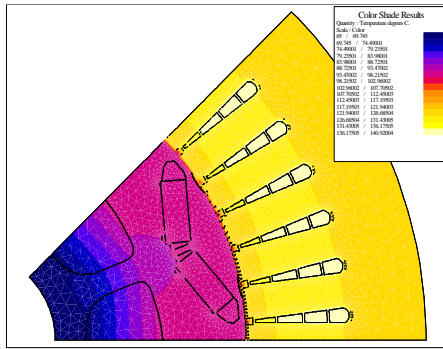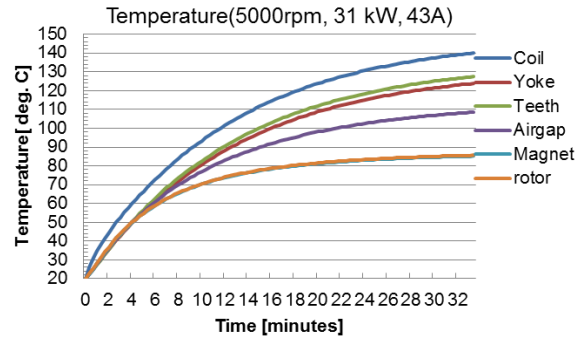
Fig. 10. Thermal model result at mapping point after 32 min.

Benchmarking data is not available at the selected IPM mapping point but is available at a power level of 25 kW (3,000 rpm, 79.6Nm) and I_s= 54A_{rms}. Measured stator coil temperature at this power level was 134°C at 34 min given a power dissipation in the machine of 1,275 W. Simulation at this same point showed a stator coil temperature of 138°C at 34 min into the test as summarized in Fig. 11. At this test point the rotor convection coefficient h_c = 65 W/m²K and stator OD boundary condition were reset to h_c = 180 W/m²K to match the test data. This adjustment is needed in 2D simulation.

(a)
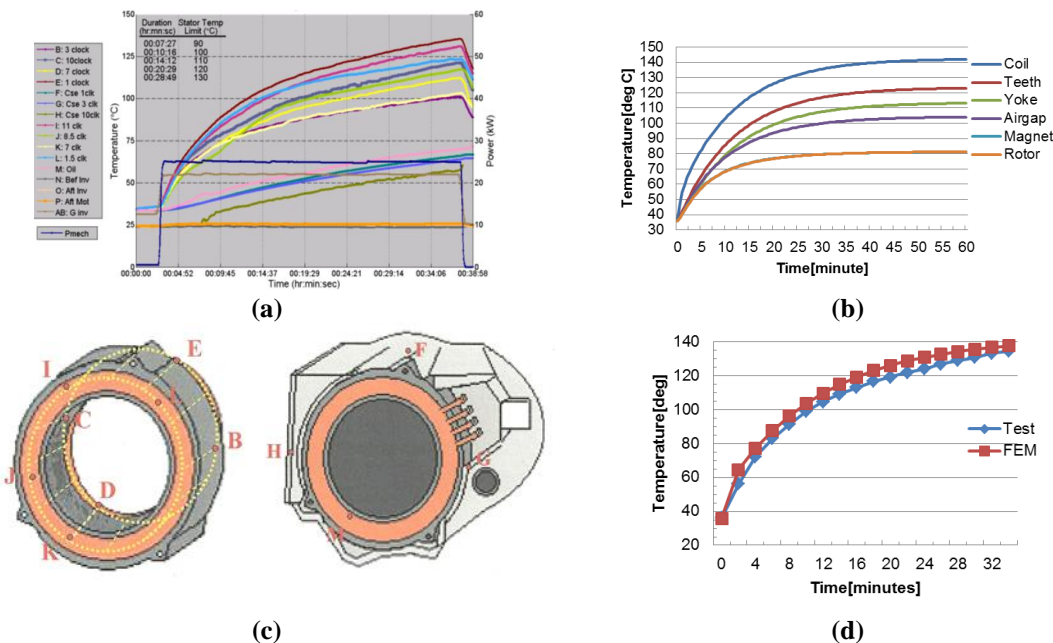

(b)

(c)

(d)

Fig. 11. Thermal model result at tested point after 34 min: (a) measured temperatures, (b) simulated temperatures, (c) thermocouple locations, and (d) comparison to test data.

The thermal evaluations are ongoing and will be extended to remove the stator OD boundary constraint on heat conduction by replacing this with the actual lamination stack to aluminum case with coolant jacket. The thermal analysis will also need to be three dimensional (3D) because end turn and rotor windage contribute significantly to heat rejection.

Electromagnetic and Thermal Mapping for Material Improvements

The mapping activities in this program are focused on identification of material improvements that will enhance the continuous power rating of the traction motor. In the program work this year that meant a focus on performance at the mapping point (5,000 rpm, 60 Nm). To understand the lamination steel needs

in terms of its crystal structure, or GOSS texture, the stator lamination flux density is computed as a vector trajectory over a rotor pole pair. The (x,y) components of the flux vector are shown in Fig. 12 at five evaluation points in the lamination steel.

Flux vector plots for 90 mechanical degrees of rotation show flat to shallow ellipse patterns where the flux essentially pulsates in magnitude with fixed or nearly fixed spatial direction. This happens in the center of the teeth and at the stator OD in the back iron. At the base of each tooth and base of the slot in the back iron the situation is very different, with the flux vector showing a strong circular polarization. The flux pattern at the tip of the stator tooth was very surprising, exhibiting a strong pulsating character with superimposed 540° of circular polarization at each magnetic polarity.

During FY 2012 the program will continue from this point and build a magnetothermal coupling model to better quantify the core losses. This will be a level of refinement beyond the Flux2D Berttoti evaluation within each mesh element. The essentials of this approach are to compute the material loss for each component of the flux vector as shown in Fig. 13(a) in matrix form with reluctivity tensor. This is illustrated graphically in Figs. 13(a) and 13(b), where the flux density vector and its attendant field strength are shown.
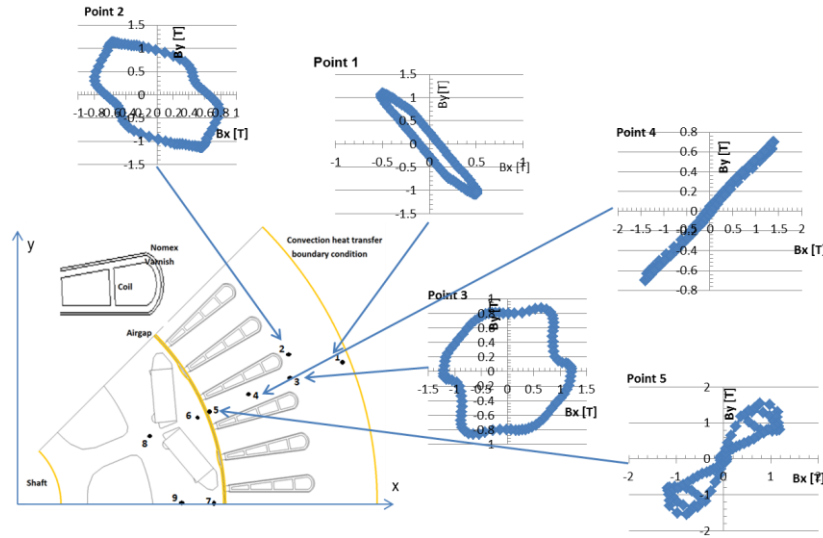
Fig. 12. Flux vector at representative points in the IPM stator.

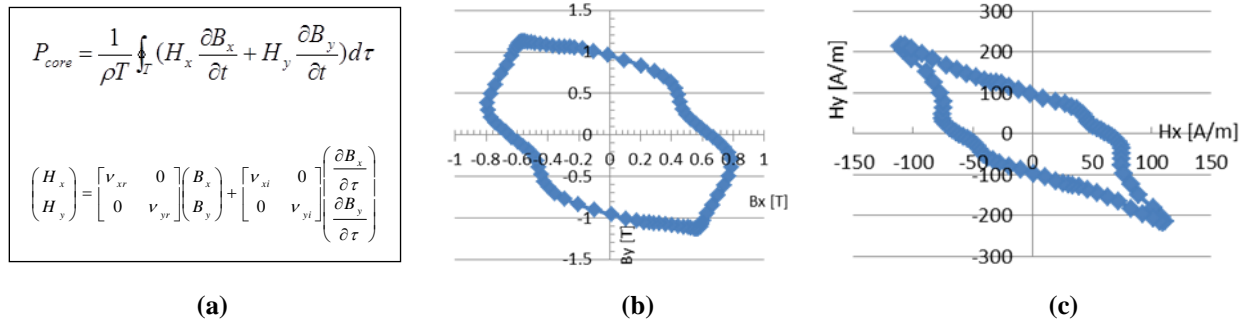**(a)**   **(b)**   **(c)**

Fig. 13. Illustration of the magnetothermal coupling method: (a) calculation of material loss for flux vector, (b) flux density locus at point 2, and (c) magnetic field intensity at point 2.

As the project moves into FY 2012, the pressing materials question for new lamination steel and its processing is to determine whether its crystal structure can be zonally oriented so that aligned, transverse, and circular polarized flux will contribute minimal losses. The first round of inquiry into this question will consist of deformation sequences in the steel processing stage, including evaluating the benefits of the shear rolling process and annealing steps. The FY 2012 project will also explore electroslag casting (ESC) as a means to obtain body centered cubic (bcc) crystal structure of <100> aligned axis and <100> in transverse axis. There will also be an investigation of alternative conductor designs such as Mitsubishi's rectangular magnet wire.

Electric-Magnetic-Thermal Directional Guidelines for IPM Optimization

During FY 2011 the baseline IPM was also evaluated for thermal performance enhancement using epoxy matrix composite (EMC) materials for stator winding potting. Investigation focused on EMCs with thermal conductivities ranging from 0.5 to 20 W/mK. The baseline IPM was loaded at the maximum copper power dissipation of 6.65 kW and the structure simulated for thermal profiles in steady state. Figure 14 illustrates three representative simulation runs with thermal conductivity, K, such that $0.2 < K < 20$ W/mK. Our interest in thermal materials is motivated by the desire to improve heat conduction, and higher K-factor materials have higher thermal diffusivity, D, that in turn contributes to reduced thermal time constant, τ_{th}. The relationships are $D = \frac{K}{\rho c_p}; \quad \tau_{th} = \frac{\rho c_p}{K} S_A$, where ρ = density, c_p = specific heat, and S_A = active area.

| (a) | (b) | (c) |
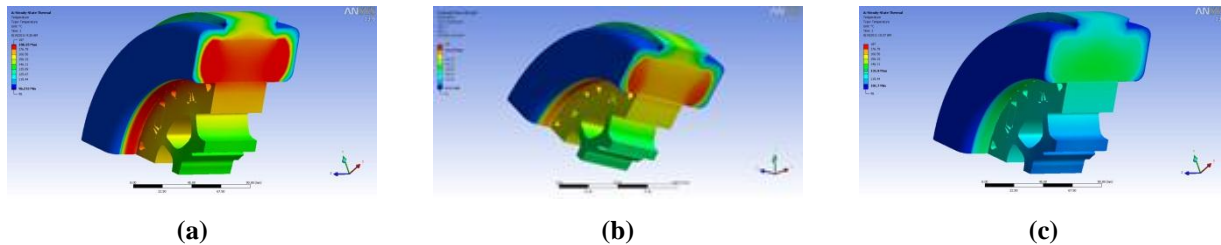
Fig. 14. Illustration of IPM thermal profiles of EMC potted windings (P_d = 6.65 kW and $T_{coolant}$ = 105°C): (a) K = 0.5, (b) K = 2, and (c) K = 20.

For the K = 0.5 case [Fig. 14(a)], the end winding potting temperature is 96°C and core temperature at the end winding sides is 186°C. For the K = 2.0 case [Fig. 14(b)], the end winding potting temperature is 97°C and core temperature at the end winding sides is 174°C. For the K = 20 case [Fig. 14(c)], the end winding potting temperature is 101.7°C and core temperature at the end winding sides is 131.9°C. The key finding here is that for the same coolant temperature of 105°C, the higher the thermal conductivity, K, the higher the end turn temperature is and the lower the stator core temperature at the end turn sides. The implication is that the higher the thermal conductivity of the EMC material, the more uniform the overall stator temperature becomes. Reviewing the sequence of thermographs, it is also apparent that the EMC properties affect magnet temperature.

<u>Conclusion</u>

During its first year, this project has made significant progress toward meeting the objectives set out during the FY 2011 kickoff. The overarching objective of this motor packaging work was to develop an electromagnetic model for the baseline IPM and to evaluate the benefits possible from improved magnetic steel and thermal materials. This has been accomplished and the results presented in this report. The stage is therefore set to build on this modeling and materials work for quantitative evaluation in FY 2012, specifically in the evaluation of efficiency improvement potential from novel core steel processing

methods and the inclusion of modern thermal potting materials. The key objectives met include the following.

- Completed characterization of the TMC 2010 Prius traction drive motor, a 60 kW IPM design. The key finding is that torque saturation occurs due to reduction in reluctance torque with stator current—diminished Lqs-Lds magnitude because of q-axis saturation.

- Completed technology trajectory by mapping the design changes introduced by TMC into its hybrid vehicle product line traction motors. The period of evaluation covered 2003 to 2010 and Prius, Camry, and Lexus models. The bottom line is that fine tuning adjustments were made to winding designs (series and parallel), rotor magnet configuration (straight, single V, and double V, but no U shapes), and overall OD to stack ratio. Essentially no material changes were made, and TMC elected to stay with a proven P = eight pole, m = three phase, Qs = 48 slot design using t_{lam} = 0.3 mm thickness. Some insights included the fact that all the designs evaluated maintained near 0.44 T on average mid-gap flux density, an aspect ratio that is nearly square, and use of multiple round conductor bundles (NIH), contributing to skin effect cut-in frequencies greater than 13 kHz.

- Completed building the IPM model based on characterization of winding resistance, synchronous inductance versus current, magnet flux linkage, and assessment of end turn leakage inductance. Using the model parameters, the simulated torque versus current was shown to very accurately match laboratory measured torque (obtained from FY 2010 benchmarking at ORNL).

- Completed an initial thermal model based on material characteristics, and defined what the stator boundary conditions needed to be to match characterization data temperature measurements. However, only initial evaluations of coolant jacket performance were obtained because the thermal model was done in 2D FEA and 3D FEA is needed to resolve the end winding dissipation via automatic transmission fluid splash. The project did include 3D FEA thermal modeling of the benefits of EMC as a guide for FY 2012 materials development.

During FY 2012 the focus of the Motor Packaging with Consideration of Electromagnetic and Material Characteristics project will be on material characterization and design suitable for the IPM stator, specifically the evaluation of both shear roll processing of lamination steel for bcc crystal orientation in rolling and transverse directions so that local core loss contributions due to radial, circumferential, and circular polarized flux are minimized. The FY 2012 work will also investigate high silicon content ESC for suitability for an IPM. One IPM stator will be fabricated, wound, and tested for comparison to the baseline IPM performance. Thermal materials such as EMC will continue to be modeled and evaluated, but because of budget restrictions, prototype builds and evaluation will not take place until FY 2013.

Patents

New project; none to date.

Publications

J. M. Miller, "New Materials and Processes Lead Way to PEV Traction Motor Efficiency Improvement," presented at the Wisconsin Electric Machines and Power Electronics Consortium (WEMPEC) 30th Annual Review Meeting, University of Wisconsin-Madison, May 18–19, 2011.

References

1. T. Burress, *Evaluation of the 2010 Toyota Prius Hybrid Synergy Drive System*, ORNL/TM-2010/253, Oak Ridge National Laboratory, March 2011.

2. C. Ayers, *Evaluation of 2004 Toyota Prius Hybrid Electric Drive System*, ORNL/TM-2004/247, Oak Ridge National Laboratory, November 2004.

3. E. C. Lovelace, T. M. Jahns, and J. H. Lang, "A Saturating Lumped-Parameter Model for an Interior PM Synchronous Machine," *IEEE Transactions on Industry Applications,* Vol. 38(3), pp. 645–650, May/June 2002.

4. E. C. Lovelace, T. M. Jahns, J. Wei, T. Keim, J. H. Lang, D. D. Wentzloff, P. J. McCleer, F. Leonardi, and J. M. Miller, "Design and Experimental Verification of a Direct-drive Interior PM Synchronous Machine Using a Saturable Lumped-Parameter Model," IEEE 37th Industry Applications Society Annual Meeting, Pittsburg, Pennsylvania, October 13–18, 2002, pp. 2486–2492.

5. M. A. Rahman, T. A. Little, and G. R. Slemon, "Analytical Models for Interior-Type Permanent Magnet Synchronous Motors," *IEEE Transactions on Magnetics,* Vol. Mag-21(5), pp. 1741–1743, September 1985.

6. N. Bianchi and S. Bolognani, "Magnetic Models of Saturated Interior Permanent Magnet Motors based on Finite Element Analysis," in *Proceedings of the IEEE 33rd Industry Applications Society Annual Meeting,* St. Louis, Missouri, October 12–15, 1998, pp. 27–34.

7. M. A. Rahman, P. Zhou, D. Lin, and M. F. Rahman, "Measurement of Parameters for Interior Permanent Magnet Motors," in *Proceedings of the IEEE Power and Energy Society General Meeting,* Calgary, Alberta, Canada, July 26–30, 2009, pp. 1–4.

8. P. Zhou, D. Lin, G. Wimmer, N. Lambert, and Z. J. Cendes, "Determination of d-q Axis Parameters of Interior Permanent Magnet Machine," *IEEE Transactions on Magnetics,* Vol. 46(8), pp. 3125–3128, August 2010.

9. E. C. Barnes, "An Experimental Study of Induction Machine End-turn Leakage Reactance," *AIEE Transactions,* Vol. 70, pp. 671–679, 1951.

10. R. D. Findlay, N. Stranges, and D. K. MacKay, "Losses Due to Rotational Flux in Three Phase Induction Motors," *IEEE Transactions on Energy Conversion,* Vol. 9(3), pp. 543–549, September 1994.

11. W. A. Pluta, "Specific Total Loss Components Under Axial Magnetization in Electrical Steel Sheets with Different Degree of Goss Texture," *IEEE Transactions on Magnetics,* Vol. 44(11), pp. 3832–3835, November 2008.

12. J. R. Brauer, "Magnetic Diffusion Times for Infusion and Effusion in Nonlinear Steel Slabs and Cylinders," *IEEE Transactions on Magnetics,* Vol. 43(7), pp. 3181–3188, July 2007.

13. ASTM International (ASTM), *Standard Test Method for Alternating Current Magnetic Properties of Materials Using the Wattmeter-Ammeter-Voltmeter Method, 100 to 10,000 Hz and 25-cm Epstein Frame*, A 348/A 348M-05, ASTM: West Conshohocken, Pennsylvania, 1991.

14. Bo yang, *Development of Thermal Models for Permanent-Magnet Traction Motors,* MS thesis, Royal Institute of Technology, Stockholm, Sweden, July 2009.

15. Sami Ruoho et.al., "Temperature Dependence of Resistivity of Sintered Rare-Earth Permanent-Magnet Materials," *IEEE Transactions on Magnetics,* Vol. 46(1), pp.15–20, January 2010.

16. Heesung Yoon, Inhyun Kim, Pan Seok Shin, and Chang Seop Koh, "Finite Element Implementation of a Generalized Chua-Type Vector Hysteresis Model and Application to Iron Loss Analysis of Three-Phase Transformer," *IEEE Transactions on Magnetics,* Vol. 47(5), pp. 1122–1125, May 2011.

17. W. L. Soong, *Thermal Analysis of Electrical Machines: Lumped-Circuit, FE Analysis and Testing,* Power Engineering Briefing Note Series, PEBN 6, University of Adelaide, School of Electrical and Electronic Engineering, Australia, May 20, 2008, pp. 21–22 (available online at http://www.eleceng.adelaide.edu.au/research/power/pebn.

18. Wojciech A. Pluta, "Specific Total Loss Components Under Axial Magnetization in Electrical Steel Sheets with Different Degree of Goss Texture," *IEEE Transactions on Magnetics*, Vol. 44(11), pp. 3832–3835, November 2008.

4. Systems Research and Technology Development

4.1 Benchmarking of Competitive Technologies

Principal Investigator: Tim Burress
Oak Ridge National Laboratory
National Transportation Research Center
2360 Cherahala Boulevard
Knoxville, TN 37932
Voice: 865-946-1216; Fax: 865-946-1262; E-mail: burressta@ornl.gov

DOE Technology Development Manager: Susan A. Rogers
Voice: 202-586-8997; Fax: 202-586-1600; E-mail: Susan.Rogers@ee.doe.gov

ORNL Program Manager: Mitch Olszewski
Voice: 865-946-1350; Fax: 865-946-1262; E-mail: olszewskim@ornl.gov

Objectives

- Provide status of nondomestic hybrid electric vehicle (HEV) technologies through assessment of design, packaging, fabrication, and performance during comprehensive evaluations.
    - Compare results with other EV technologies.
    - Distribute findings in open literature.
- Support U.S. DRIVE program planning and assist in guiding research efforts.
    - Confirm validity of the program technology targets.
    - Provide insight for program direction.
- Produce a technical basis that aids in modeling/designing.
- Foster collaborations with the Electrical and Electronics Technical Team (EETT) and the Vehicle Systems Analysis Technical Team (VSATT).
    - Identify unique electric machine/inverter/converter/drive-train technologies.
    - Ascertain what additional testing is needed to support research and development (R&D).

Approach

- Choose vehicle subsystem.
    - Evaluate potential benchmarking value of various HEVs.
    - Consult with original equipment manufacturers as to which system is most beneficial.
- Perform system level tear down.
    - Determine volume, weight, specific power, and power density.
    - Assess design and packaging improvements.
    - Conduct tests upon magnets and capacitors.
- Prepare components for experimental evaluation.
    - Develop interface and control algorithm.
    - Design and fabricate hardware necessary to conduct tests.
    - Instrument subsystems with measurement devices.
- Evaluate hybrid subsystems.
    - Determine peak and continuous operation capabilities.
    - Evaluate efficiencies of subsystems.
    - Analyze thermal data to determine assorted characteristics.

Major Accomplishments

- Selected and procured the 2011 Hyundai Sonata because it is the first hybrid to be sold in the United States by Hyundai Motor Company, which in 2010 ranked 4th in the world in motor vehicle production volume.
- Conducted design/packaging studies of the 2011 Hyundai Sonata power control unit (PCU), hybrid starter-generator (HSG), and primary motor, which revealed a wide range of design characteristics and R&D efforts that differ considerably from that of Toyota hybrids.
- Bypassed the 2011 Hyundai Sonata motor inverter controls to allow full control over testing conditions while using the Sonata's insulated gate bipolar transistor (IGBT) driver board to ensure consistent inverter operation.
- Assessed mass, volume, power density, and specific power of Sonata hybrid subsystems.
- Evaluated efficiency, performance, and other operational characteristics of the 2011 Sonata subsystems.
- Communicated effectively with EETT and VSATT to aid in discerning project direction, test plan, and test results.

Future Direction

- Continue benchmarking efforts with a focus on technologies of interest to DOE, EETT, and VSATT.
- Incorporate approaches similar to that of previous benchmarking studies while working to suit the universal need for standardized testing conditions.

Technical Discussion

The 2011 Hyundai Sonata hybrid is the first hybrid to be added to Hyundai's product line, and the Sonata's hybrid drive train is also used in the 2011 Kia Optima hybrid. Although the vehicle was scheduled to be released in the fall of 2010, release dates were delayed several times and sales began in select metropolitan areas in January of 2011. ORNL obtained parts in the February–April timeframe even though the vehicle was not available at the local dealership. Parts arrived with February production dates stamped upon them. Hyundai refers to their drive system as the "Hybrid Blue Drive," and it includes a 30 kW primary permanent magnet (PM) motor and an 8.5 kW HSG. The PCU, shown in Fig. 1, includes inverters for these two motors as well as a converter which steps the 270 V hybrid battery voltage level down to the standard 12 V supply level. Overall, the hybrid subassemblies include more off-the-shelf components than hybrids made by Toyota and Honda. A comparison of the 2010 Toyota Prius, 2007 Toyota Camry, and 2011 Hyundai Sonata PCUs is shown in Fig. 1, with total masses and volumes of 13.0 kg and 16.2 L, 17.4 kg and 11.7 L, and 11.8 kg and 10.6 L, respectively. Although the Sonata PCU is shorter, dc and three phase interconnects make it slightly wider than the Prius and Camry PCUs. It should be noted that the combined motor and generator inverter power capabilities of the Sonata (38.5 kW) are much lower than the Prius (~90 kW) and Camry (~120 kW). Also note that there is not a converter which boosts the hybrid battery voltage in the Sonata, as there is in the 2010 Prius PCU (but not the Camry).

As indicated in the left portion of Fig. 2, the 270 V to 12 V dc-dc converter is located in the uppermost compartment of the Sonata PCU. The HSG and primary motor inverters and their periphery are located in the lowest compartment of the PCU. A cast aluminum serpentine heat exchanger/cold plate with cooling fins is integrated into the chassis of the lower compartment, and this is sealed with the nearly flat surface of the upper compartment. An ethylene glycol cooling loop (separate from the engine cooling loop) flows through the PCU and HSG, with a reservoir and pressure relief cap located on top of the PCU, which is visible in Fig. 2. The three phase interconnects for the HSG and primary motor are also shown in Fig. 2.
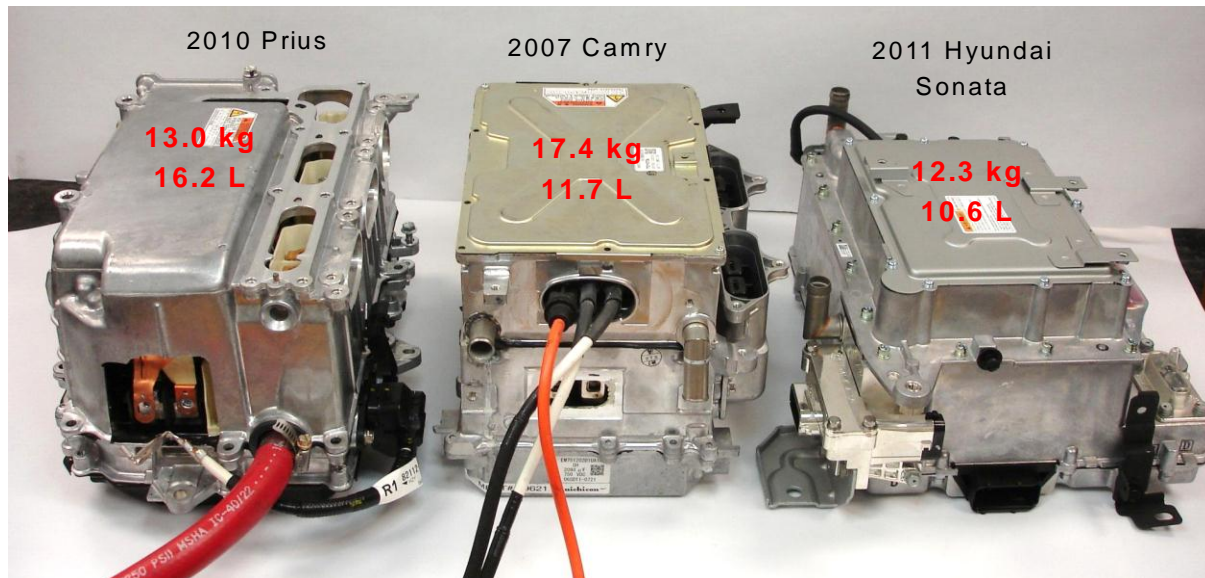
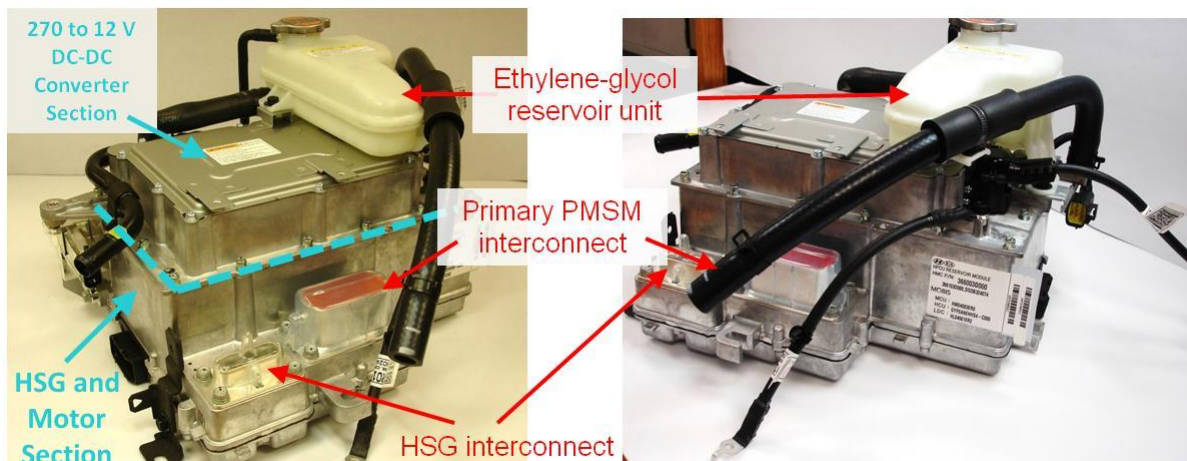**Fig. 1. Comparison of 2010 Prius, 2007 Camry, and 2011 Hyundai Sonata PCUs.**

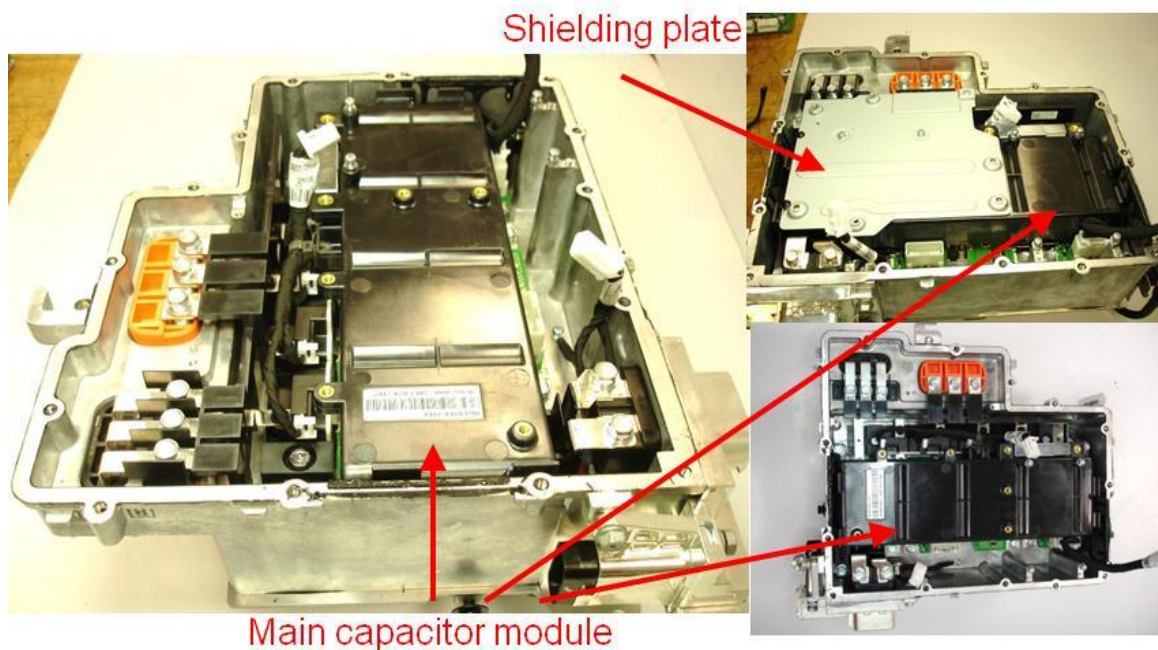

Fig. 2. 2011 Hyundai Sonata PCU.

Most of the components in the bottom compartment of the PCU, visible in Fig. 3, are mounted upside down when the PCU is installed in the vehicle. This allows the 270–12V converter and the inverters to share the cast aluminum heat sink. Two power and communication connectors are located on the bottom sides of the PCU, and the 270 V battery interconnect (with safety interlock pins) is also near the bottom of the PCU. One of the power and communication connectors is mounted to a board labeled "Inverter MCU," which does not connect or interface with any other components in the PCU. It is possible that this is the control board for the three phase oil pump, which is discussed later in this report. The larger board visible in Fig. 3 is also labeled "Inverter MCU" and serves as the control and power regulation board for the HSG and primary motor inverters. As indicated, several well-known integrated circuits are used for the controls, power supply, and feedback. Tamagawa chips, observed in all PCUs benchmarked thus far, are used to supply and decode resolver signals to provide position feedback from the HSG and primary motor.
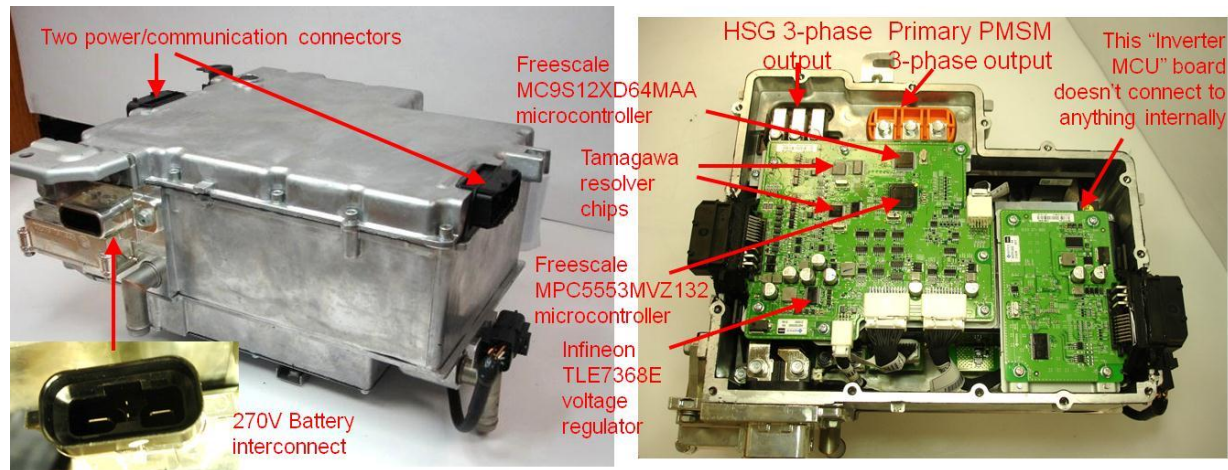
Fig. 3. Bottom compartment of 2011 Hyundai Sonata PCU.

A substantial shielding plate, seen in Fig. 4, is located below the control boards and the main capacitor to mitigate influence of electromagnetic interference (EMI) generated by IGBT switching transients, which could cause significant issues in control circuitry and ultimately system operation. The main capacitor module includes a 600 V, 680 µF capacitor and two additional integrated 0.28 µF capacitors and has a total mass of 1.72 kg and volume of 0.96 L. The 2010 Prius capacitor module is rated at 750 V and 888 µF, with a mass and volume of 1.79 kg and 1.45 L. One of the 0.28 µF capacitors is connected to the PCU chassis and the other is connected to the dc link. Bus bars are integrated into the Sonata's capacitor module, which connects the 270 V interconnect to the two power electronics modules, and a dc-link bleed resistor is mounted on the side of the module. An x-ray image of the capacitor, shown in Fig. 5, indicates that eight capacitor cells are used to form the 680 µF capacitor.

Fig. 4. Bottom compartment of 2011 Hyundai Sonata PCU with control boards removed.
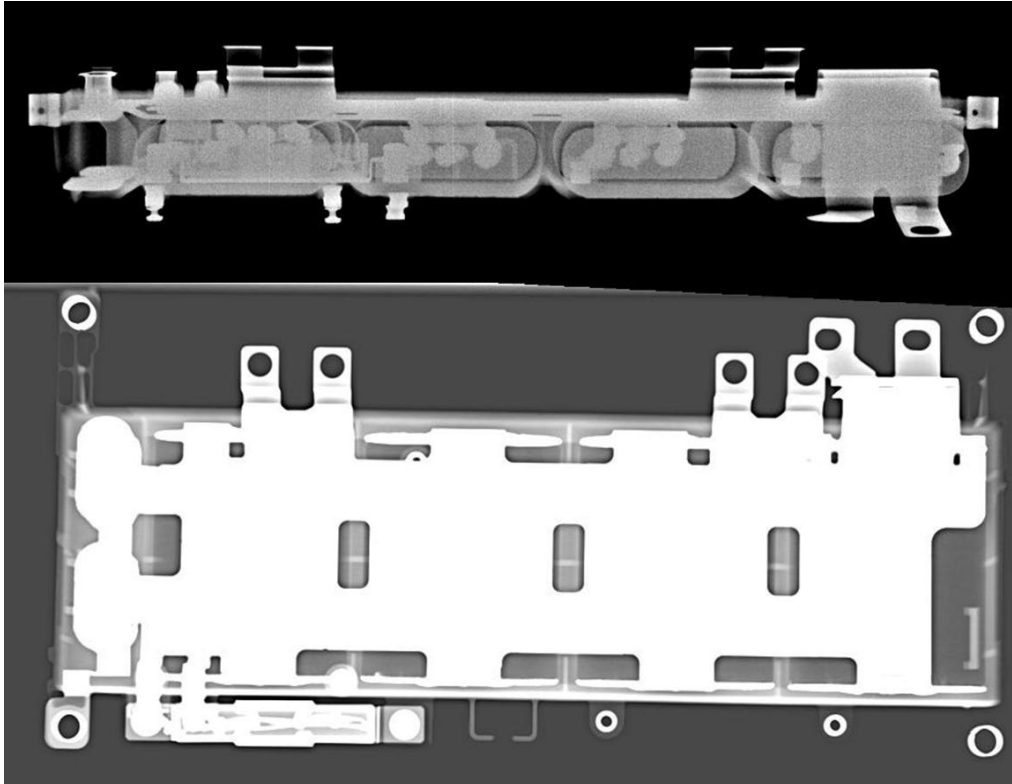
Fig. 5. Main capacitor of 2011 Hyundai Sonata PCU.

After the main capacitor module is removed (Fig. 6), the power electronics modules (PEMs) and driver boards for the HSG and primary motor are accessible. A bus bar infrastructure is used for both three phase inverter outputs and includes two LEM HAH1DR-500S-SP1 500 A current transducers for the primary motor and two LEM HAH1DR-300S-SP1 300 A current transducers for the HSG. It is interesting to note that despite the significant difference between the HSG and primary motor power ratings (8.5 kW versus 30 kW, respectively), the size and packaging of the PEMs are identical. A closer look at a PEM is given in Fig. 7, where specific components of the driver board are indicated. The white modules are labeled "HIG-FeB1" and are identical in appearance to Infineon's HybridPack1 PEMs. With the gate driver board and thin white plastic plate removed, the IGBTs and diodes of the HSG and primary motor PEMs are visible in Fig. 8. Dimensions of the IGBTs and diodes are shown in millimeters, and the motor IGBTs and diodes are 1.85 and 1.88 times larger than the HSG IGBTs and diodes, respectively. Note that the ratio of power ratings is 30 kW/8.5 kW = 3.53, indicating that the generator IGBTs and diodes are likely oversized. There are 12 IGBTs and 12 diodes in each PEM with cross-sectional areas of silicon of about 960.2 mm^2 and 1,194.5 mm^2 for the HSG and primary motor, respectively, with a total of 2,154.7 mm^2 for both PEMs. Only one buffer is used for two parallel IGBTs, and they also share the same gate signal trace. This may entail imbalance between IGBT activity due to the slight impedance discrepancy between each IGBT and the buffer output. Three surface-mounted thermistors are located near the outer edge of the PEM. Only the centermost thermistor is monitored for over-temperature conditions.
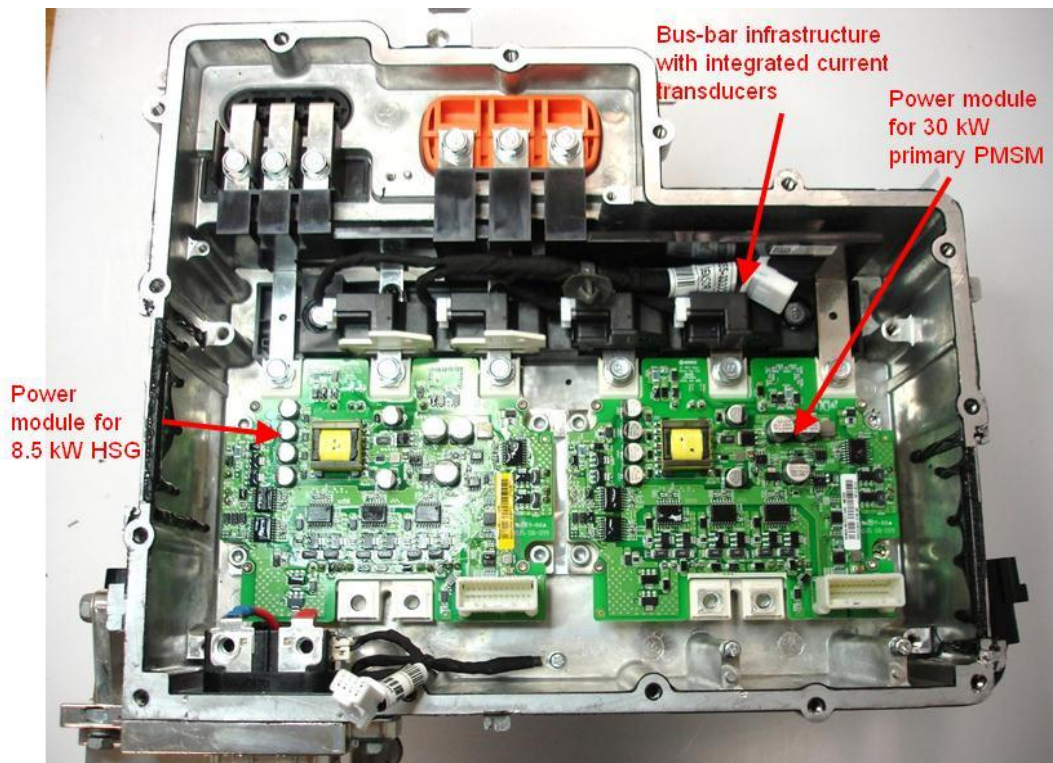
Fig. 6. Bottom compartment of 2011 Hyundai Sonata PCU with main capacitor removed.
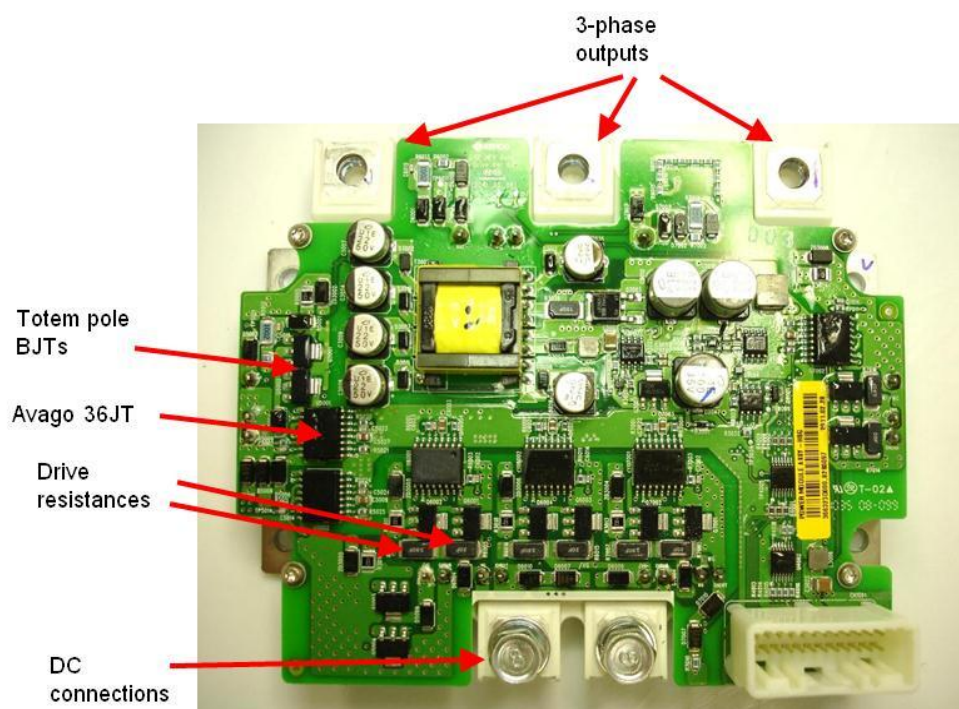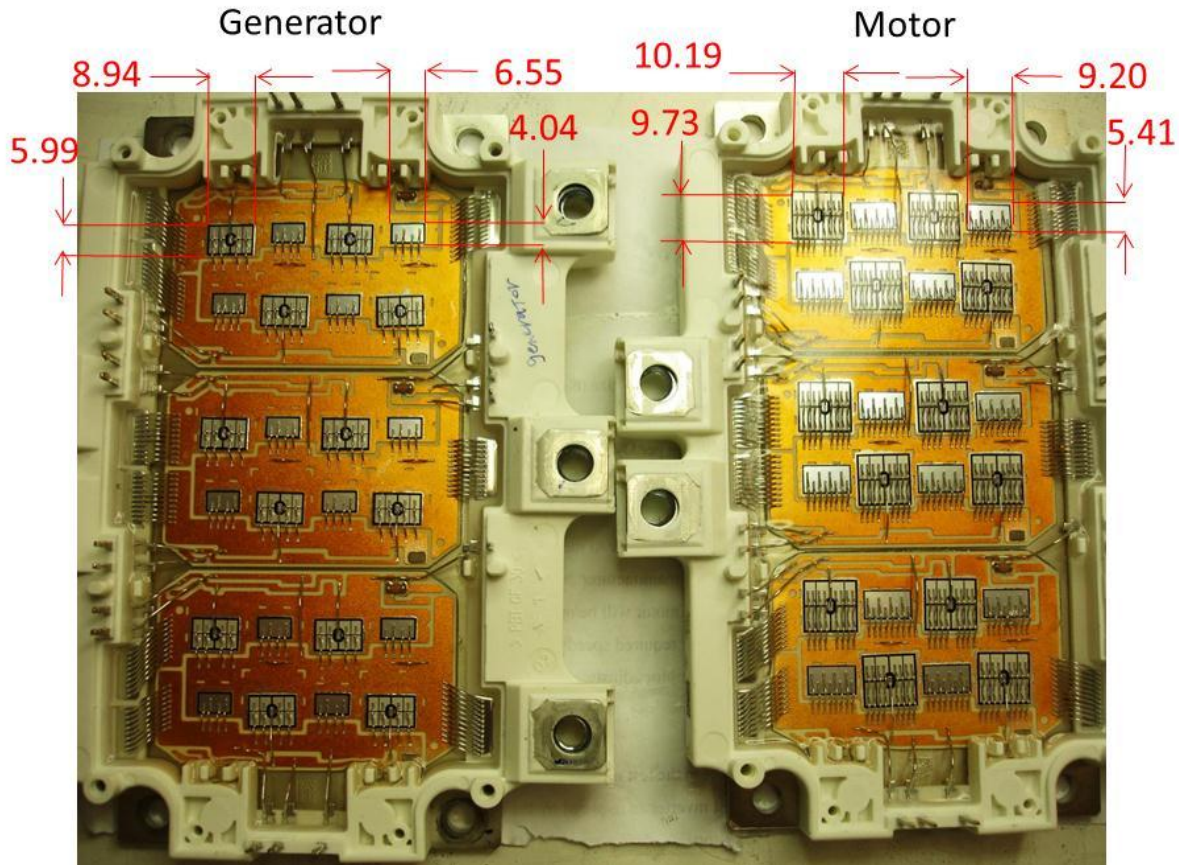

Fig. 7. 2011 Hyundai Sonata PEM with driver board.

Fig. 8. 2011 Hyundai Sonata PEM with driver board removed.

The 2011 Hyundai Sonata hybrid drive system includes an HSG which is similar in size to a conventional alternator. The HSG is also connected to the engine crankshaft pulley like a conventional alternator, yet the belt is more substantial than most standard belts. Some U.S. made hybrids have a similar starter-alternator arrangement, yet it is operated on the 12 V system which is likely inferior to the Sonata's 270 V HSG system in terms of efficiency, power density, and specific power. With a power rating of 8.5 kW, the HSG is a three phase interior PM (IPM) machine that can develop 43 Nm of torque to absorb energy from the engine to recharge the 270 V battery and to start the engine for cold starts and in-driving restarts (e.g., so the engine can be stopped when the vehicle is at rest). The stator, shown in Fig. 9, has 36 stator slots which form six poles, and the distributed windings have a thermistor installed to prevent overheating. A resolver with relatively small outer diameter is used for position feedback, and it has a 12-pole stator and a rotor with three lobes. The stator is enclosed in a water jacket in which ethylene glycol is circulated as it travels from the coolant inlet port to the coolant outlet port. There is not a significant separator between the coolant inlet and outlet ports (both of which are visible in Fig. 10), so it seems that the angle of the inlet is intended to project the coolant in such a manner that the coolant does not bypass the loop around the HSG. As the HSG was disassembled, a seal for the water jacket with preexisting damage was discovered. Details will be discussed in a later section of this report.
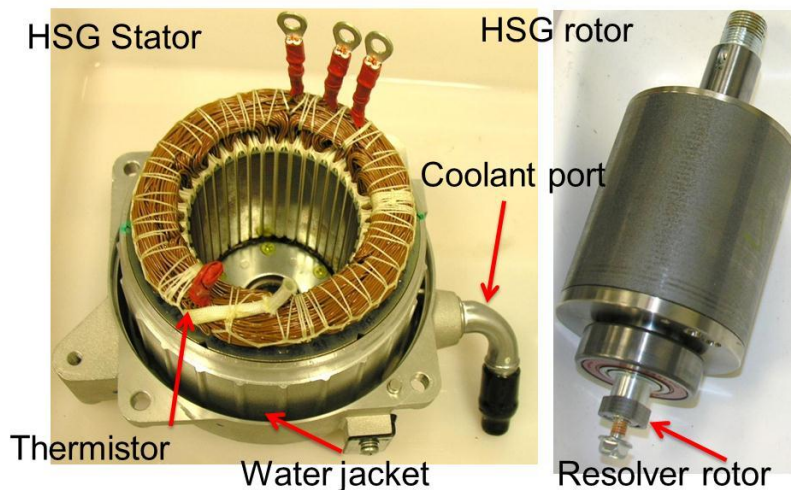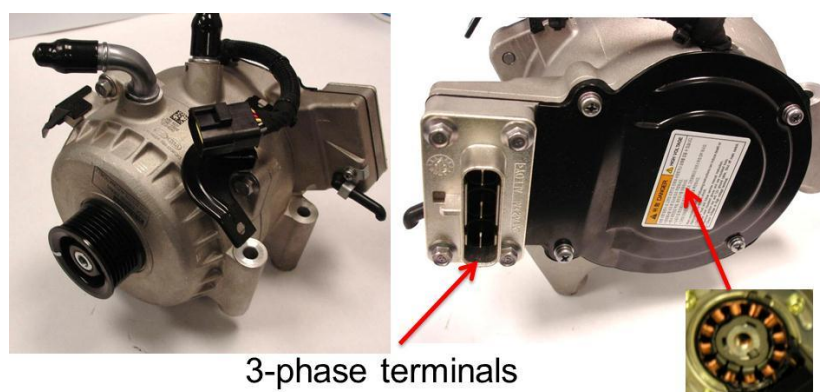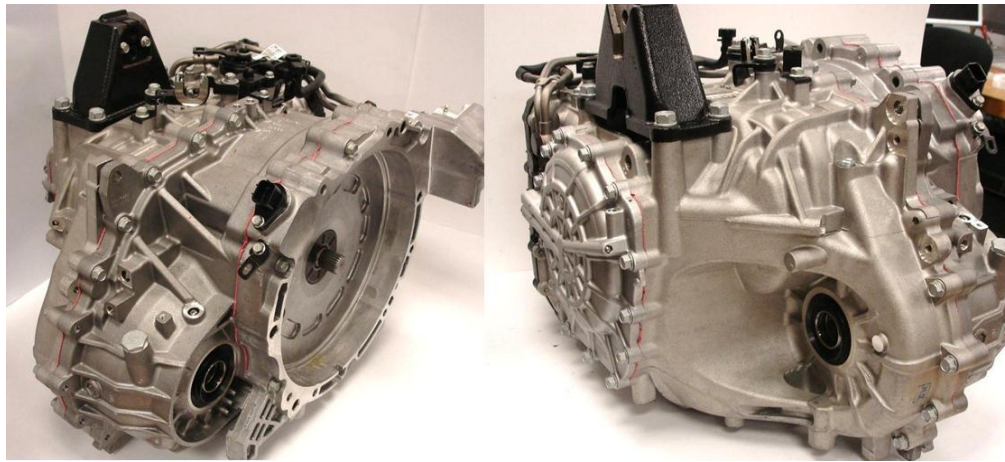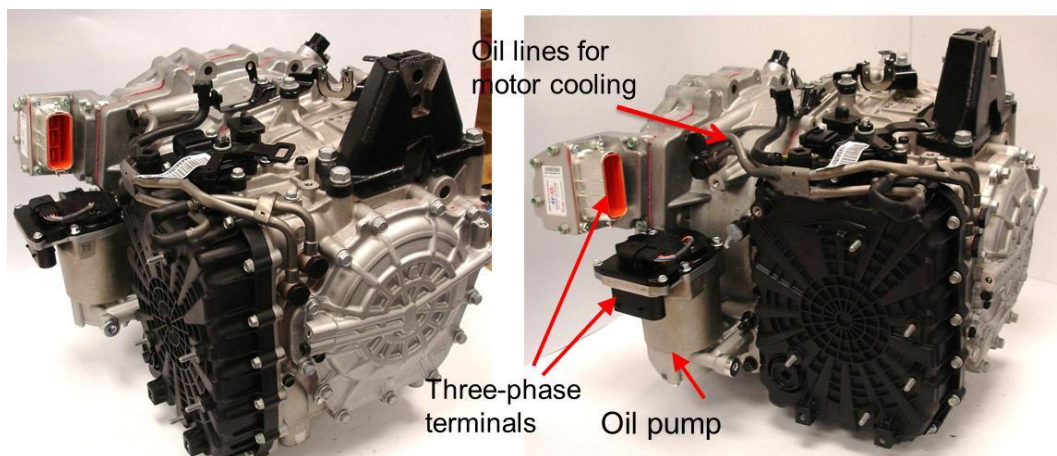
Fig. 9. 2011 Hyundai Sonata HSG.

Fig. 10. 2011 Hyundai Sonata HSG.

The 2011 Hyundai Sonata hybrid drivetrain includes a six speed automatic transmission (AT) which is similar in shape and size to most front wheel drive transmissions, which is reasonable as Hyundai also offers various non-hybrid versions of the Sonata. As received, the total mass of the transmission-transaxle (shown in Fig. 11) was 117.2 kg, which is slightly higher than that of the 2007 Camry at 108 kg. A 30 kW IPM machine is located inside the assembly, which also houses, among many things, a mechanical gear pump, drive gears, differential gears, etc. As shown in Fig. 12, a relatively large oil pump is located on the side of the transmission. This three phase PM-machine-driven pump may be necessary because (unlike the conventional AT) a clutch is located between the engine and the six speed transmission (and the internal mechanical pump), and thus the engine cannot help develop the hydraulic pressure needed to shift gear states if, for example, it is turned off at a stop light. Note that the primary electric motor essentially resides where a torque converter would normally be located, which is right at the transmission-engine interface. The torque converter aids in developing hydraulic pressure in a conventional AT. Three-phase terminals for the oil pump and the primary electric motor are indicated in Fig. 12. Substantial oil lines, also indicated in Fig. 12, are used to supply oil to actively cool the motor. As previously mentioned, the primary motor resides near the engine interface, and this section of the motor has been removed and is viewed from the rear in Fig. 13. This 30 kW motor can produce 205 Nm, with an approximate corner speed of 1,400 rpm. The stator has 24 concentrated windings with each stator

tooth being a separate piece but interlocked with its neighboring stator teeth (as shown in the left portion of Fig. 13). The rotor, shown in Fig. 14, has 16 poles, and in general, the stator and rotor laminations are nearly identical to that of Honda hybrid motor designs. A Honda Accord hybrid motor rotor lamination is shown in the bottom right portion of Fig. 14 for comparison. However, one considerable difference is the method of clutch integration into the center of the rotor. While the primary electric motor is always connected to the input of the six speed AT, a clutch located in the center of the rotor allows for the engine to be disengaged and stopped when the vehicle is stopped or operating in electric-only mode. Hyundai claims that the Sonata hybrid can operate up to 62 mph in electric-only mode. This is one advantage of this design over Toyota's Hybrid Synergy Drive system in which the primary electric motor is connected to the drive wheel through a fixed gear ratio.
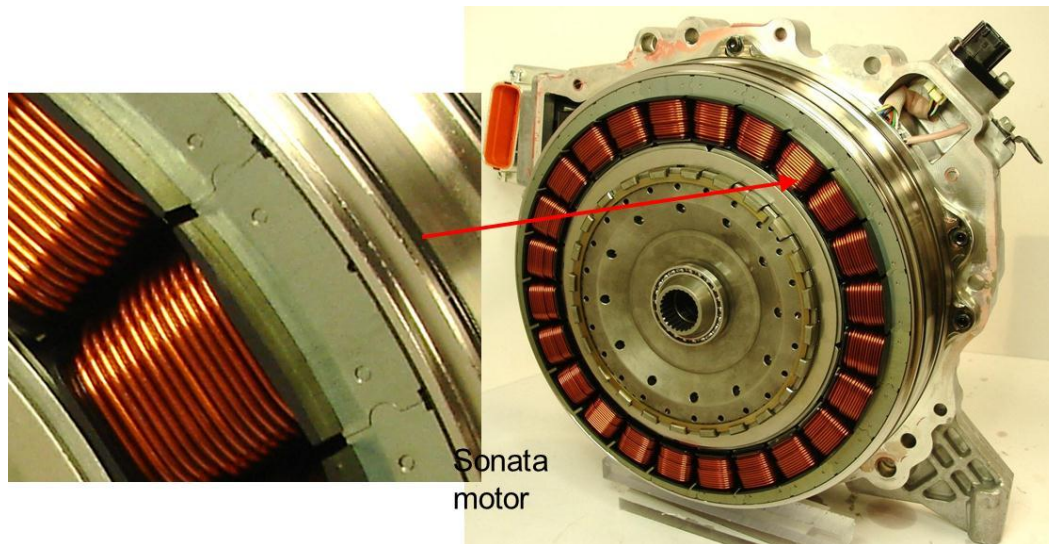

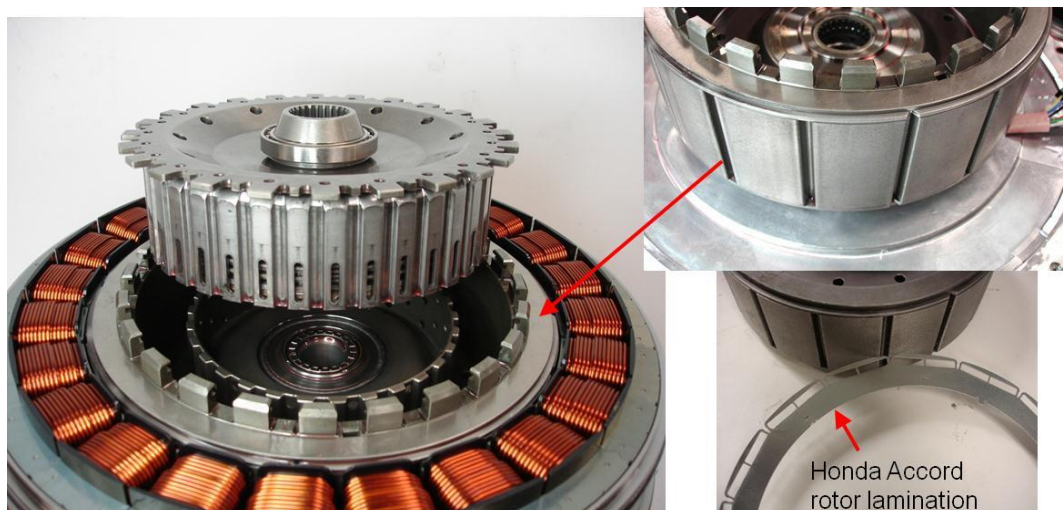**Fig. 11. 2011 Hyundai Sonata transmission-transaxle.**

Fig. 12. 2011 Hyundai Sonata transmission-transaxle.

Fig. 13. 2011 Hyundai Sonata motor.

Fig. 14. 2011 Hyundai Sonata motor.

Hydraulic pressure for the integrated clutch is provided by a port (shown in the upper left portion of Fig. 15), which is located in the center of the main transmission shaft. Also shown in Fig. 15 is the basic functionality of the motor cooling system. The previously mentioned oil lines serve as a supply and drain for the oil inlet and oil outlet labeled in Fig. 15. Two very large o-rings are located around the outer diameter of the stator. These o-rings form a seal with the chassis, and thus oil can be circulated around the entire perimeter of the motor stator before it exits the channel formed by the o-rings. While transmission oil is not the best transfer medium, this provides uniform cooling and mitigates potential thermal imbalances.

After removing the next section of the transmission, the mechanical oil pump, drive gears, and differential gear are visible, as shown in Fig. 16(a). Figure 16(b) is a view from the back of the transmission with the rear plate removed. The compound multiple planetary gear system in the forefront of the image carries out most of the functionalities of the six speed transmission. As shown in Fig. 17, a seal from the HSG and a seal for the differential gear output shaft were both damaged when the Sonata parts arrived. The HSG seal was pinched and likely maintained a proper seal when it was discovered.
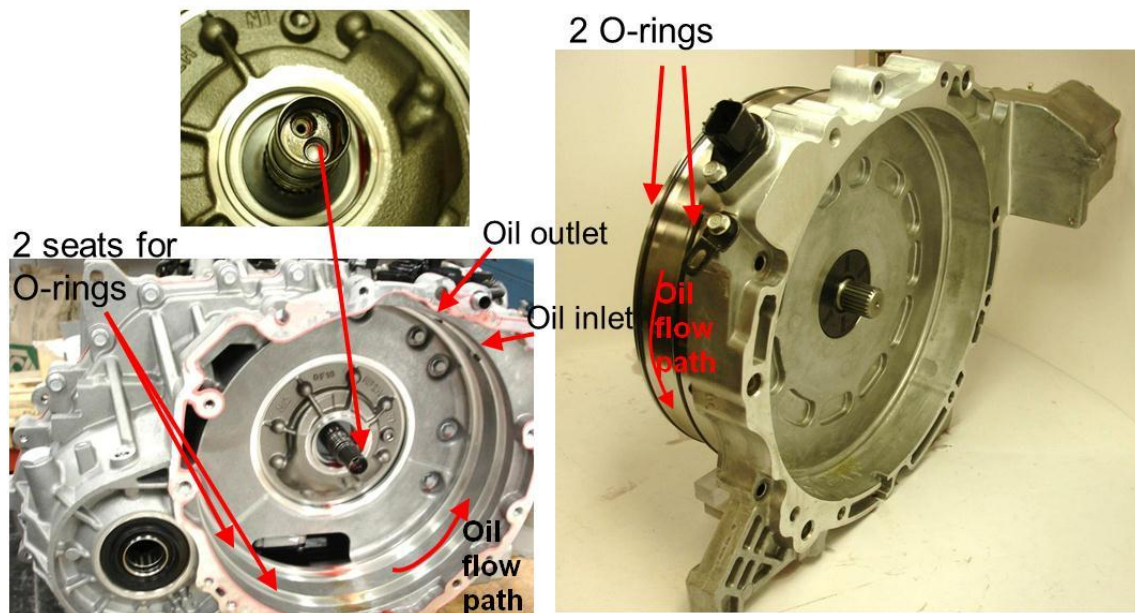
Fig. 15. 2011 Hyundai Sonata motor cooling system and hydraulic supply for clutch (upper left).
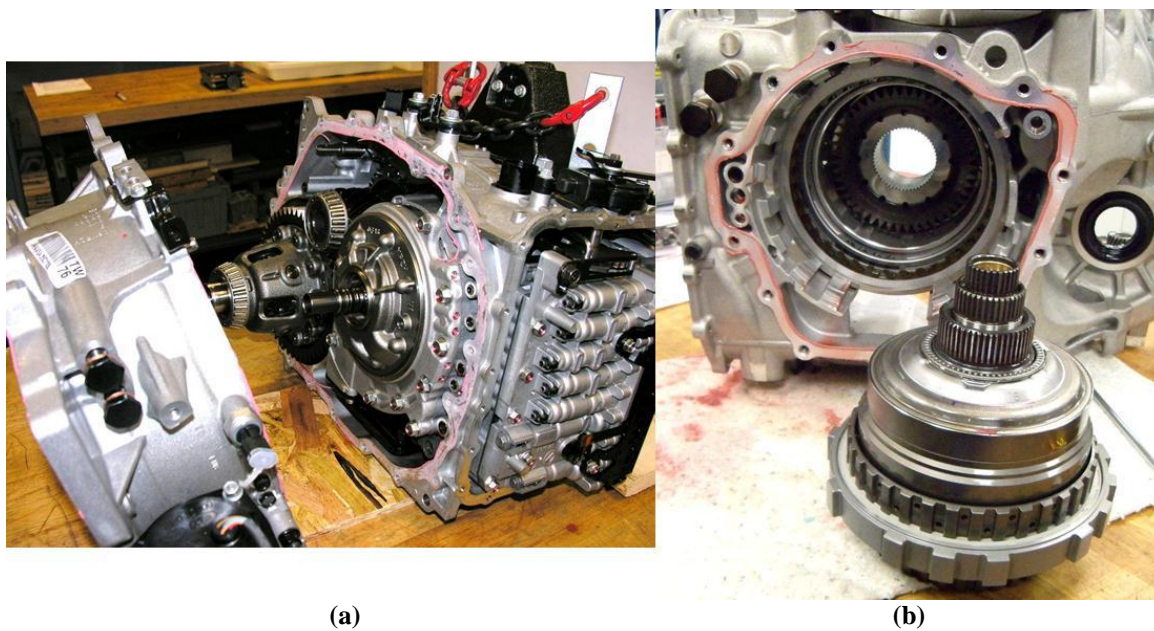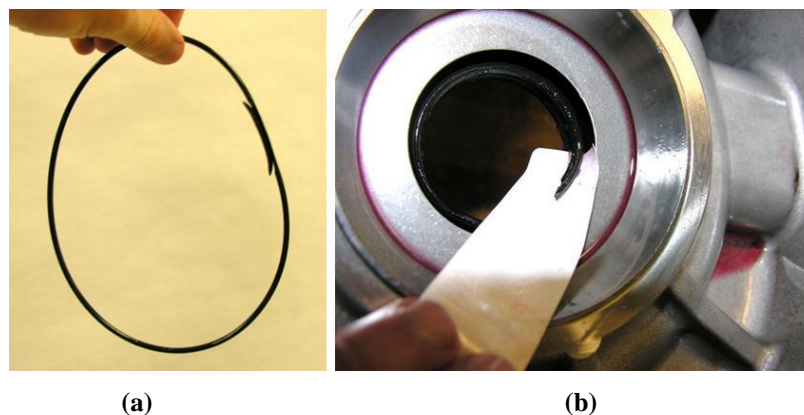

| (a) | (b) |

Fig. 16. 2011 Hyundai Sonata: (a) transaxle and (b) view from the back of the transmission showing the compound multiple planetary gear system.

(a)   (b)

Fig. 17. Damaged seals from (a) HSG and (b) transaxle differential shaft output (right).

In preparation for testing the Sonata subsystems in a dynamomter test cell, a mounting plate was designed and fabricated to access the output shaft of the primary electric motor while also providing proper mechanical support, cooling, and lubrication. The first section of the transmission-transaxle was mounted to the custom plate, with the engine-transmission bolt pattern facing away from the plate and unused as a clutch disengages the engine input from the electric motor. While seemingly simple, the design of the plate involved a complex design process which included high tolerance guidance and alignment mechanisms and bearing support and lubrication. As shown in Fig. 18(a), the stator was instrumented with thermocouples to monitor coil, core, oil port, and case temperatures during tests. Coil, core, and case thermocouples were strategically located to observe potential thermal gradient based on proximity to the oil inlet and outlet. Current transducers and voltage taps were installed on the input of the inverter and the output of the inverter. The Sonata motor and custom ORNL support plate were face-mounted to a Himmelstein torque transducer to measure mechanical power, and the torque transducer was mounted to the dynamometer [Fig. 18(b)]. Figure 19 shows back-electromotive force (emf) test results compared with those for the 2006 Honda Accord. At about 3,750 rpm, the line to neutral RMS voltage measurement reaches 120 V, which is roughly the maximum ac voltage output capability of the inverter with a 270 V dc link. Thus, operation above this speed will certainly require field weakening techniques. This characteristic is common among other hybrid systems, and optimal control of previously tested motors typically involved field weakening at relatively low speeds.

(a)   (b)
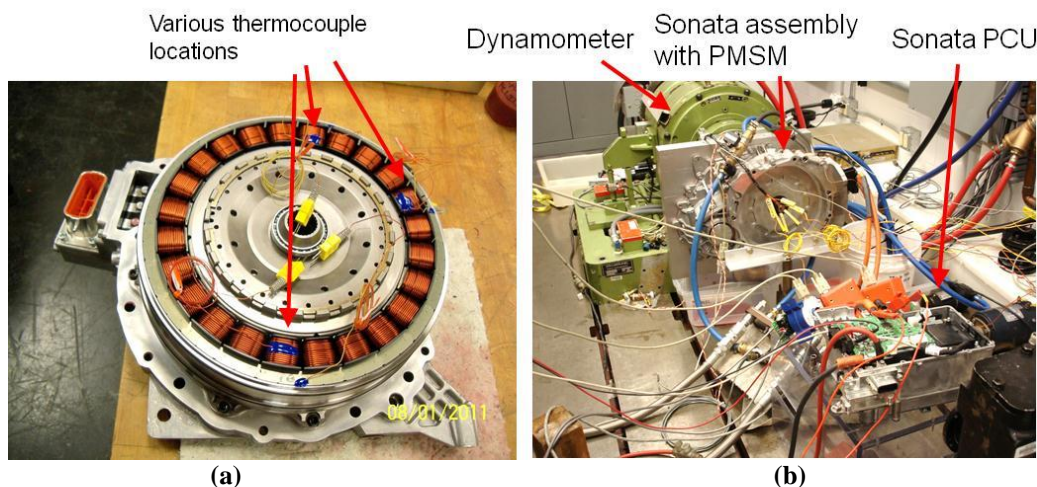
Fig. 18. Test setup showing (a) thermocouple installation locations and (b) dynamometer setup.
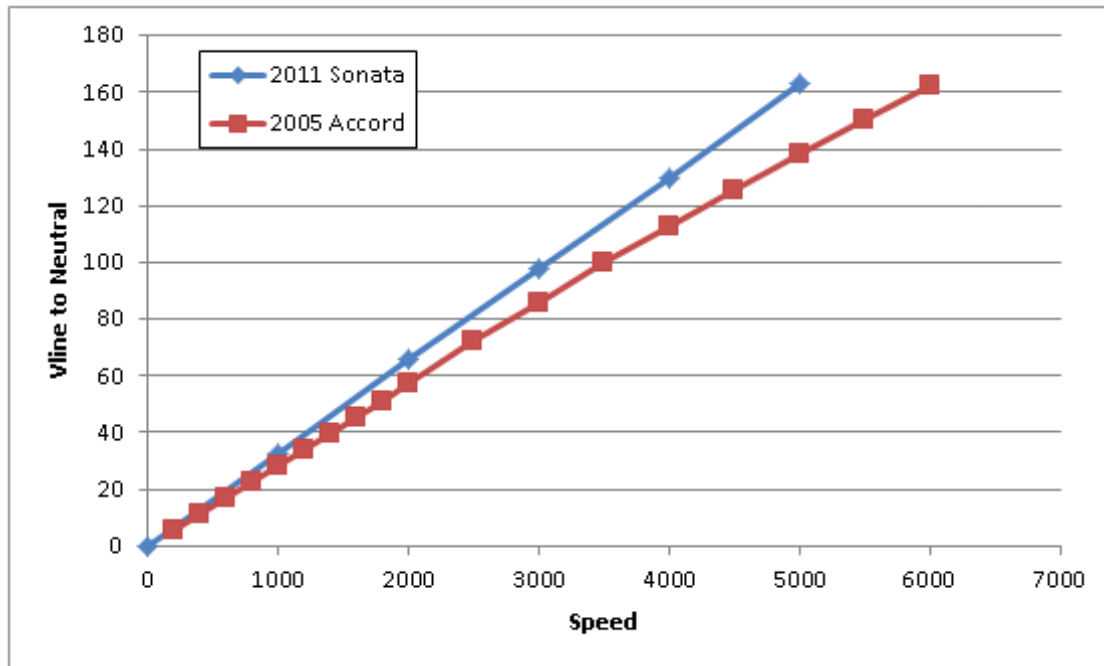
Fig. 19. Back-emf versus speed for 2011 Hyundai Sonata and 2006 Honda Accord motor.

Locked rotor torque measurements were made as the positive terminal of a dc supply was connected to phase "a" and the negative terminal of a dc supply was connected to phases "b" and "c" (in parallel). These tests were conducted as various current levels were applied and the rotor was incrementally locked in positions over a full electrical cycle. The results, shown in Fig. 20, indicate that like the 2006 Accord, the total torque does not include a considerable reluctance component in comparison with Toyota's designs. This is expected based on the layout of the magnets observed in Fig. 14. However, in comparison with the 2006 Accord, the locked rotor torque profile of the 2011 Sonata is much smoother. Peak torque values for each current level were selected and plotted versus current in Fig. 21. The results indicate that about 300 Adc was required to produce the published peak torque of 205 Nm. Figure 21 also indicates that the torque-per-current ratio of the motor remains approximately linear even up to 250 A and shows slight indications of saturation at 300 A. This is quite different from Toyota designs, which begin to operate in saturation at much lower current levels. Low speed efficiency mapping has been completed. Efficiency testing will be completed early in FY 2012. Fairly high efficiencies have been observed at low speeds. For example, at 500 rpm and 50 Nm, inverter and motor efficiencies were 92% and 93%, respectively, which is higher than most of the previously benchmarked systems in this operation region.

A comparison of power density (PD) and specific power (SP) for various systems benchmarked at ORNL is given in Table 1. The 2011 Sonata motor PD and specific power SP are more than 2 times those of the 2006 Accord motor (which has a similar topology). This is largely due to the increase of the dc-link voltage from the Accord's 144 V to the Sonata's 270 V. These PD and SP values are comparable to those of the 2004 Prius, even though the 2004 Prius uses a 500 V dc link. High speed ratings and a 650 V dc link provide high PD and SP values for recent Toyota designs. Inverter PD and SP values of the 2011 Sonata improved greatly over the 2006 Accord inverter. Increased dc-link voltage contributes to this improvement of PD and SP in the Sonata. The 2006 Accord has a large air cooled heat sink, whereas the Sonata uses an ethylene glycol cooling loop. Toyota motor inverters have two values each for PD and SP: one that includes the boost converter and one that does not. When the boost converter is included in the motor inverter PD and SP calculations, the 2011 Sonata surpasses all systems except the 2008 LS 600h. When the boost converter is not included in these calculations, the Sonata motor inverter PD and SP values are comparable to those for the 2004 Prius.
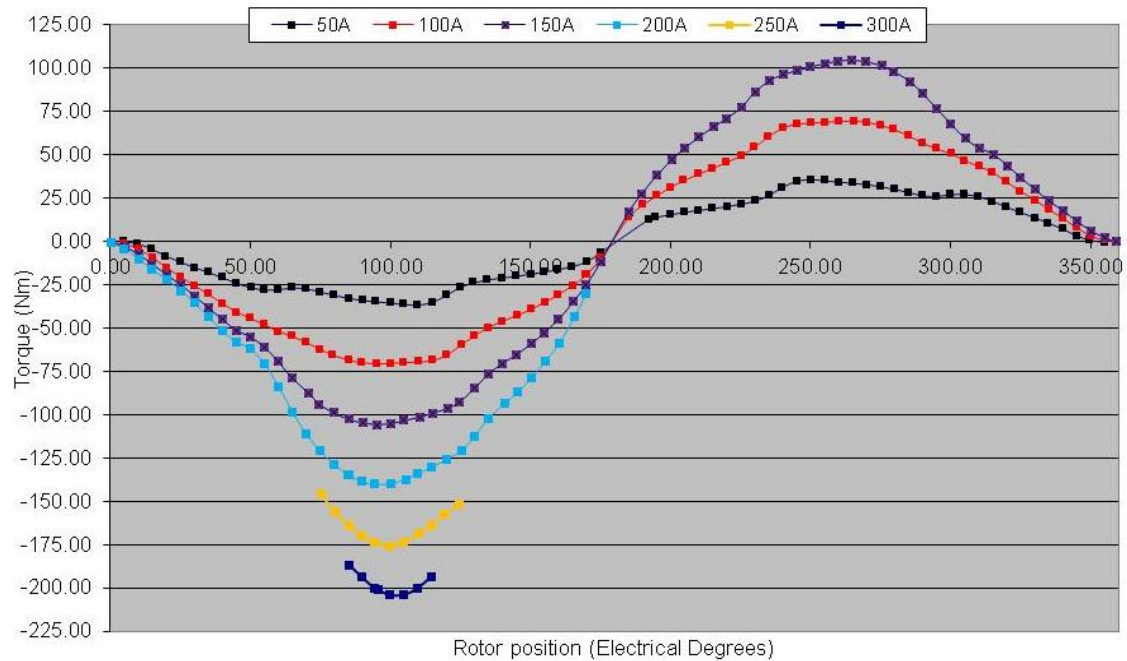
Fig. 20. Locked rotor torque versus position for the 2011 Hyundai Sonata motor.
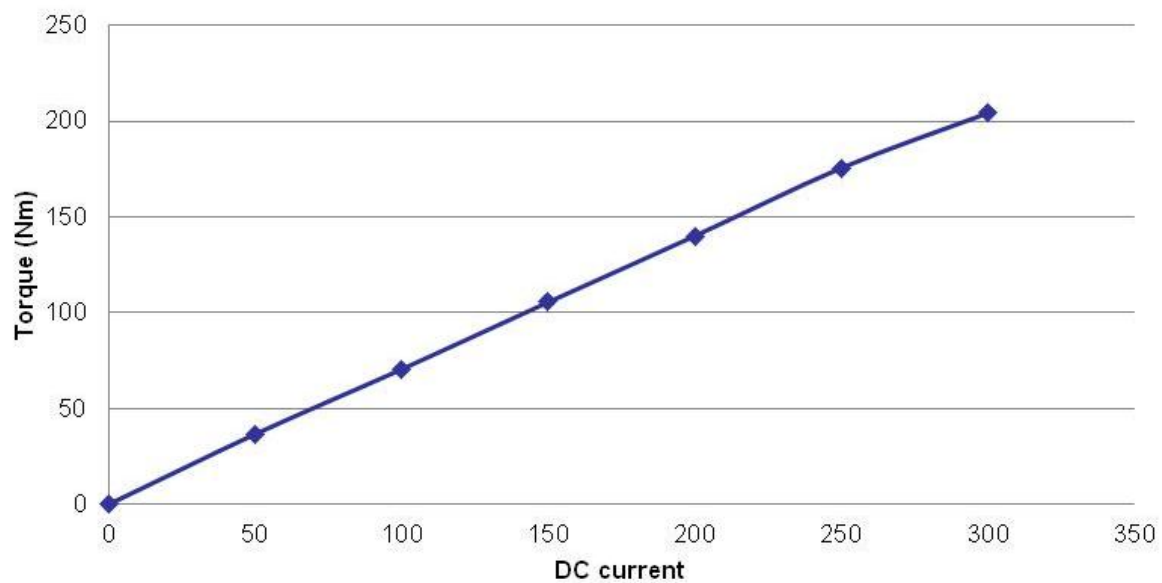

Fig. 21. Peak locked rotor torque versus current for the 2011 Hyundai Sonata motor.

Table 1. Comparison of specific power and power density for various HEV components

Component and parameter	2011 Sonata (30 kW)	2010 Prius (60 kW)	2008 LS600h Lexus (110 kW)	2007 Camry (70 kW)	2006 Honda Accord (12 kW)	2004 Prius (50 kW)
Motor						
Peak power density, kW/L	3.0	4.8	6.6	5.9	1.5	3.3
Peak specific power, kW/kg	1.1	1.6	2.5	1.7	0.5	1.1
Inverter—excluding generator inverter (parenthetical values do not include boost converter mass/volume)						
Peak power density, kW/L	7.3	5.9 (11.1)	10.6 (17.2)	7.4 (11.7)	2.9	4.5 (7.4)
Peak specific power, kW/kg	6.9	6.9 (16.7)	7.7 (14.9)	5.0 (9.3)	2.4	3.8 (6.2)

Conclusion

- The 2011 Hyundai Sonata hybrid and 2011 Kia Optima hybrids share the same drivetrain.

- Overall PCU slightly smaller than Toyota PCUs even though combined generator and motor power is only 38.5 kW versus ~90 kW for the 2010 Prius.

- PCU has many off-the-shelf components including what appears to be Infineon's HybridPack1 PEMs.

- PEMs are the same size for 8.5 kW HSG versus 30 kW motor, indicating potential for improved power density.

- The HSG and PCU share ethylene glycol coolant loop.

- The HSG is similar in size to alternator but has much higher power rating and efficiency because it uses a 270 V system (as opposed to 12 V).

- The HSG is cooled with a water jacket, and the primary motor has a dedicated oil path around the stator for cooling.

- The stator and rotor lamination design approach appears to be the same as the 2006 Accord, but with different design parameters

- Integrated clutch in motor rotor required significant engineering effort.

- The motor barely operates in saturation at peak torque.

- Efficiencies measured at low speeds are favorable (e.g., 92% inverter and 93% motor efficiency measured at 500 rpm and 50 Nm).

Patents

None.

Publications

None.

References

1. T. A. Burress, et al., *Evaluation of the 2010 Prius Hybrid Synergy Drive System*, ORNL/TM-2010/253 Oak Ridge National Laboratory, 2011.

2. T. A. Burress, et al., *Evaluation of the 2007 Toyota Camry Hybrid Synergy Drive System*, ORNL/TM-2007-190, Oak Ridge National Laboratory, 2007.

3. T. A. Burress, et al., *Evaluation of the 2008 Lexus LS600h Hybrid Synergy Drive System*, ORNL/TM-2008/185, Oak Ridge National Laboratory, 2008.

4.2   High Power Density Integrated Traction Machine Drive

Principal Investigator: Fred Wang
Oak Ridge National Laboratory
National Transportation Research Center
2360 Cherahala Boulevard
Knoxville, TN 37932
Voice: 865-946-012; Fax: 865-946-1262; E-mail: wangf@ornl.gov

DOE Technology Development Manager: Susan A. Rogers
Voice: 202-586-8997; Fax: 202-586-1600; E-mail: Susan.Rogers@ee.doe.gov

ORNL Program Manager: Mitch Olszewski
Voice: 865-946-1350; Fax: 865-946-1262; E-mail: olszewskim@ornl.gov

Objectives

- The overall objective is to develop a reliable, fault-tolerant, integrated modular motor drive (IMMD) that is capable of operating at 200°C junction and 150°C ambient temperatures.
- For FY 2011, the objectives are
  — to develop a demonstrator version of the IMMD with fault-tolerant controller using the most promising configuration to verify performance characteristics including power density and distributed control and
  — to develop the 10 kW phase leg power modules needed for implementing the full power IMMD. The modules should be based on low cost silicon and can operate at an ambient temperature of 150°C, with junction temperature up to 200°C.

Approach

- Analyze alternative fault-tolerant machine and controller configurations to identify the most promising candidates for future demonstration in prototype hardware.
- Apply the results of the initial analysis to design and build a preliminary 10 kW demonstrator integrated traction drive in FY 2011 followed by a full-scale 55 kW (peak) prototype unit in FY 2012 and FY 2013.
- Evaluate the ruggedness of the selected silicon insulated gate bipolar transistor (IGBT) for operation at 200°C considering latch-up immunity, short circuit capability, and dynamic avalanche capability.
- Design and fabricate a 10 kW phase leg module, aiming for 200°C junction temperature operation. Test the electrical and thermal characteristics of the high temperature power module.

Major Accomplishments

- Designed, built, and tested a 10 kW, six phase, 10-pole permanent magnet (PM) machine that is serving as a concept demonstrator in preparation for developing a full-scale 55 kW prototype IMMD unit.
- Developed a modular IMMD power converter that conforms to the dimensions of the 10 kW concept demo PM machine, providing a testbed for implementing the IMMD distributed control software.
- Tested ruggedness of selected IGBT at various temperatures, concluding that the device has good latch-up immunity and adequate short circuit capability for operation at 200°C.

- Designed and fabricated a 10 kW phase leg power module, and tested its electrical and thermal characteristics up to 200°C.
- Designed the gate driver boards and main board for the IGBT phase leg modules with which the continuous test is conducted with liquid cooling up to 10 kW.

Future Direction

- This project will not be funded by the DOE Vehicle Technologies Program beyond FY 2011.

Technical Discussion

Demonstrator IMMD Machine and Test Results

10 kW IMMD Machine

Based on the results of the IMMD analytical machine study completed in FY 2010, a six phase, 10-pole surface PM (SPM) machine was selected for further development during FY 2011 [1]. A 10 kW demonstrator SPM machine with the target six phase, 10-pole configuration [2-4] was built to verify key concepts before moving forward with the planned 55 kW version. To save both time and financial resources, a new stator was designed for an existing SPM rotor that was available at the University of Wisconsin (UW)-Madison. The only significant complication that had to be addressed was that the active length of the existing 10-pole SPM rotor is significantly longer than necessary because it was originally designed for a machine with a higher power rating. As a result, the rotor in the demonstrator 10 kW IMMD machine has 25 mm of rotor overhang on each side of the new stator stack. Although not ideal because of additional losses that the overhanging rotor magnets induce in the stator, this approach was adopted because it is consistent with the concept demonstration objectives for FY 2011.

New stator windings using multistrand, twisted magnet wire were designed to maintain the nominal dc bus voltage level at 325 V. Figure 1(a) shows the new demonstrator machine placed in its mounting fixture and 1(b) a cross-sectional view of the machine. Initial testing of the demonstrator machine is being carried out using a three phase inverter to measure the machine parameters and performance characteristics; Fig. 1(c) shows both parallel and series winding configurations that are being used during this initial testing. Table 1 provides a summary of machine dimensions, construction features, and rated operating conditions.

**(a)**   **(b)**   **(c)**
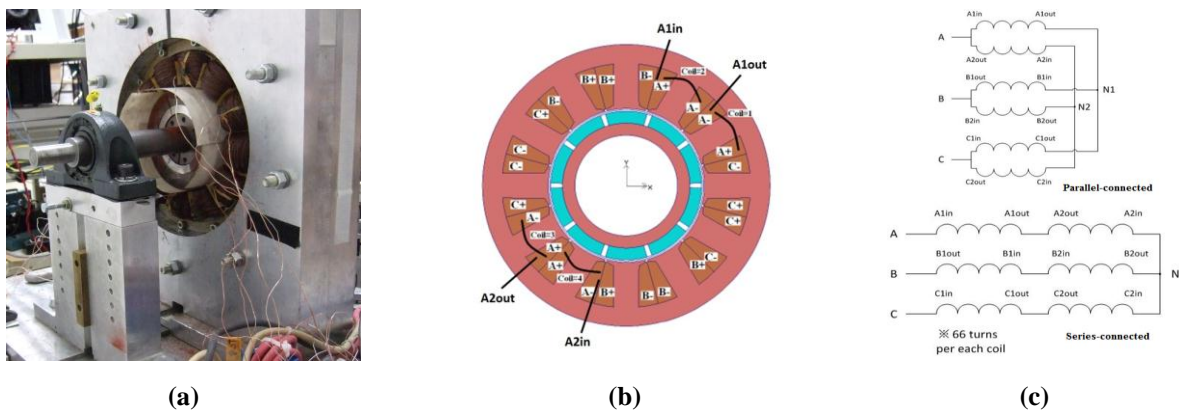
Fig. 1. 10 kW demonstrator IMMD machine (a) mounted in an open-frame fixture, (b) machine cross-section, and (c) three-phase parallel and series winding connections for the six phase machine.

Table 1. Demonstrator 10 kW machine dimensions and key design variables

Parameter	Value	Parameter	Value
Stator OD (mm)	280	Rated torque and speed (Nm/rpm)	34.3/2,800
Rotor OD (mm)	142	Peak torque and current (Nm/A$_{rms}$)	61.4/28.5
Stator active axial length (mm)	25	Number of turns per coil	66
Rotor active axial length (mm)	75	Number of strands per turn	20
Maximum speed (rpm)	14,000	Wire gauge (AWG)	24
Rated current/voltage (six phase configuration basis) (A$_{rms}$/V$_{rms}$)	14.2/132.7	Wire configuration	Transposed magnet wire

Dynamometer Test Configuration

A dynamometer with a 25 kW induction load machine rated at 6,000 rpm was selected for the demonstrator machine testing at UW-Madison. A Danfoss VLT-5202 three phase, adjustable-speed drive is used to excite the six phase demonstrator PM machine using both the series or parallel winding configurations shown in Fig. 1(c). The drive receives its gating signals from a dSPACE controller used as a rapid prototyping system. A block diagram of the dynamometer configuration is shown in Fig. 2.
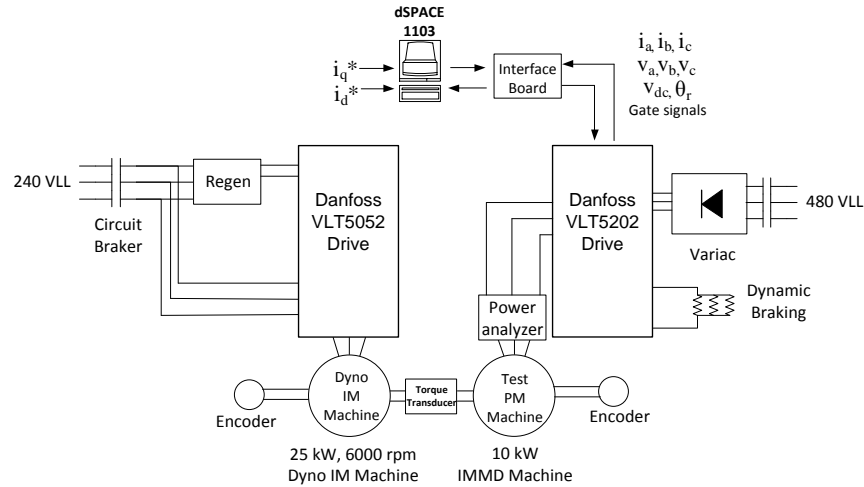

Fig. 2. Dynamometer test configuration for testing the 10 kW machine.

The dSPACE controller is programmed with a high performance synchronous-frame current regulator that makes it convenient to independently control the d-axis and q-axis currents, which, in turn, determine the torque developed by the demonstrator machine. The phase currents and voltages, dc link voltage, shaft torque, and thermocouple temperatures are measured and recorded during steady-state operating conditions. In addition, a three phase power analyzer is used to measure the terminal electrical performance of the machine including both real power input and power factor.

Demonstrator Machine Measured and Predicted Parameters

One of the first tests was to measure the machine's open-circuit back-electromotive force (emf) waveforms to determine its magnet flux linkage value in comparison to predictions. Figure 3(a) shows a comparison of the measured and finite element (FE) predicted back-emf voltage waveforms at 500 rpm. The frequency spectrum component amplitudes for the two back-emf waveforms are compared in Fig. 3(b), and plots of the fundamental component amplitudes of the back-emf voltage and magnet flux linkage as a function of rotor speed are provided in Fig. 3(c). The back-emf waveform is dominated by its

fundamental component, and this is expected because of the fractional-slot concentrated winding design. The measured experimental back-emf amplitudes are only 0.7% lower than the predicted values at 20°C. As indicated in Fig. 3(c), the magnet flux linkage is nearly constant with changes in the rotor speed.

| (a) | (b) | (c) |
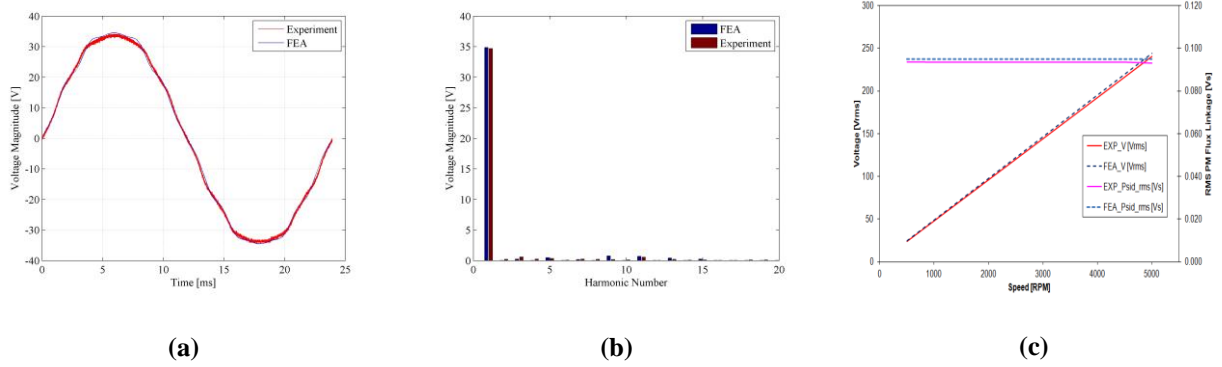
Fig. 3. Back-emf waveforms: (a) comparison of measured and FE predicted phase back-EMF waveforms for the parallel-connected IMMD machine at 500 rpm and 20°C, (b) frequency spectrum of back-emf waveforms at 500 rpm, and (c) measured and predicted back-emf and magnet flux linkage fundamental amplitudes vs speed at 20°C.

Static tests were carried out to measure the key machine parameters to populate the machine equivalent circuit. Table 2 presents a comparison of the measured and FE predicted machine parameters. The agreement between the predicted and measured machine parameters is generally very good.

Table 2. Comparison of measured and FE predicted machine parameters

Parameter	R_s (mΩ)	λ_{pm_rms} (V-s)	L_d (mH)	L_q (mH)
Measured value	53.3	0.0936	n/a	1.17
Predicted value	51.4	0.0949	n/a	1.35

Demonstrator Machine Load Tests

Machine testing has been carried out under loaded conditions to investigate the performance characteristics of the demonstrator 10 kW machine. Figure 4 provides plots of measured waveforms for operating conditions of iq = 20 A (peak) and id = 0 A at 1,000 rpm. This operating point corresponds to about 50% of rated torque for this machine. Table 3 provides a comparison of the predicted and measured performance characteristics with these same iq and id current commands at both 1,000 rpm and 2,800 rpm. Again, the agreement between the measured and predicted machine performance is generally very good.
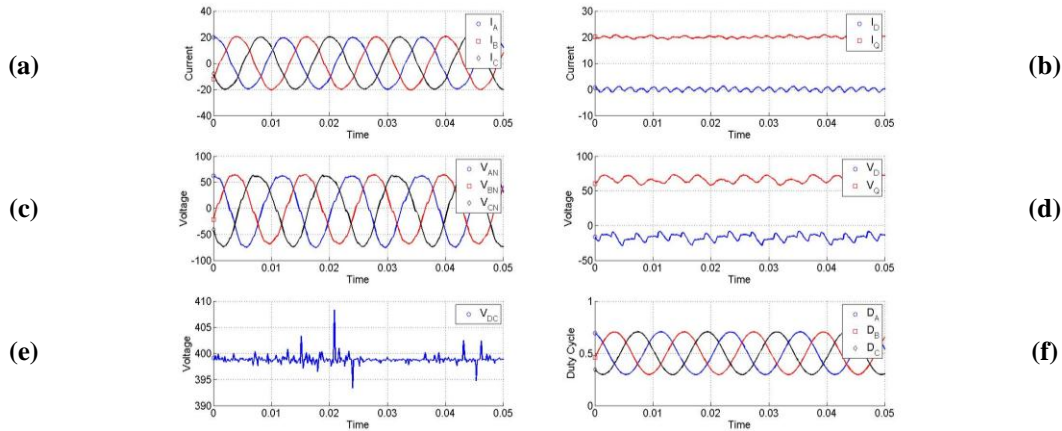
Fig. 4. Steady-state loaded machine operation with i_q = 20 A and i_d = 0 A at 1,000 rpm.
Graphs from top left: (a) phase currents; (b) synchronous frame currents, i_d, and i_q; (c) filtered phase voltages; d) filtered synchronous frame voltages, v_d, and v_q; (e) dc bus voltage, v_{dc}; and (f) commanded duty cycle.

Table 3. Comparison of measured and predicted machine performance for i_q = 20 A and i_d = 0 A

| Speed	1,000 RPM		2,800 RPM	
	FE analysis	**Experiment**	**FE analysis**	**Experiment**
Phase current [A peak]	20	19.4	20	20.1
Phase voltage [V peak]	72.0	68.3	194.8	192.0
Power factor	0.981	0.974	0.927	0.921
Output torque [Nm]	17.2	16.1	17.2	16.6
Efficiency [%]	85.2	87.4	92.0	90.8

Demonstrator IMMD Power Converter and Controller

Power Converter Configuration

Although the initial testing of the demonstrator 10 kW machine described in the preceding section is being carried out using a commercial three phase inverter drive, a demonstrator power converter that incorporates the IMMD principles [5] was also developed during FY 2011 to demonstrate key concepts during this phase of the project while establishing a design that can be easily upgraded to the full-scale 30 kW (55 kW peak) prototype unit scheduled for development during the next phase of this project. This power converter has been designed to consist of six separate phase modules that incorporate the power switches, gate drives, current sensor, and controller in each phase module. A view of this new power converter configuration is provided in Fig. 5(a), which shows that the phase modules have been shaped to conform to the dimensions of the six stator core segments corresponding to the six machine phases. Hardware selection for this power converter was carried out to balance costs, availability, and high temperature operation [6].

Fig. 5(b) provides a more detailed solid-model view of one phase module in the new power converter showing that it consists of a four-layer PC board that has a dc link film capacitor mounted on it and a smaller PC board that has the two phase leg IGBTs soldered to it. The IGBT subassembly uses a high current eight-pin connector that makes it easy to connect and disconnect IGBTs from the main converter

module board without soldering. This design achieves a power density of about 9 kW/L for the complete power converter while operating with 105°C water-ethylene glycol (WEG) coolant.
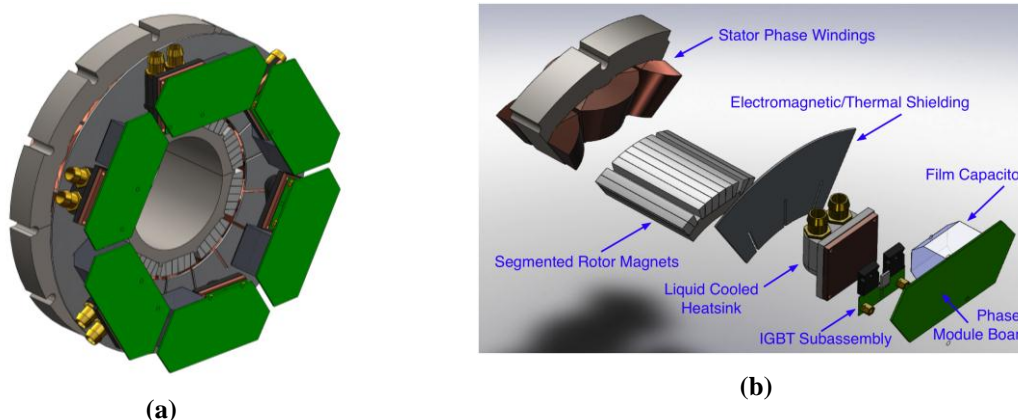
Fig. 5. Demonstrator 10 kW IMMD highlighting new six phase power converter configuration showing (a) complete power converter mounted on machine and (b) individual phase module.

The power switches for the 10 kW demonstrator are off-the-shelf IGBTs in TO-247 packages that have the power-handling capability and thermal performance needed for the 10kW power level. The IGBT subassembly is designed so that the IGBTs can be mounted on either liquid-cooled heatsink assemblies (as shown in Fig. 6) or air-cooled heat sinks, depending on the application. The adoption of the pin connector for the IGBT subassembly makes it straightforward to replace these commercial IGBTs with the new 200°C-rated power modules that are being developed as part of this project if they become available for testing in this demonstrator power converter in the future.
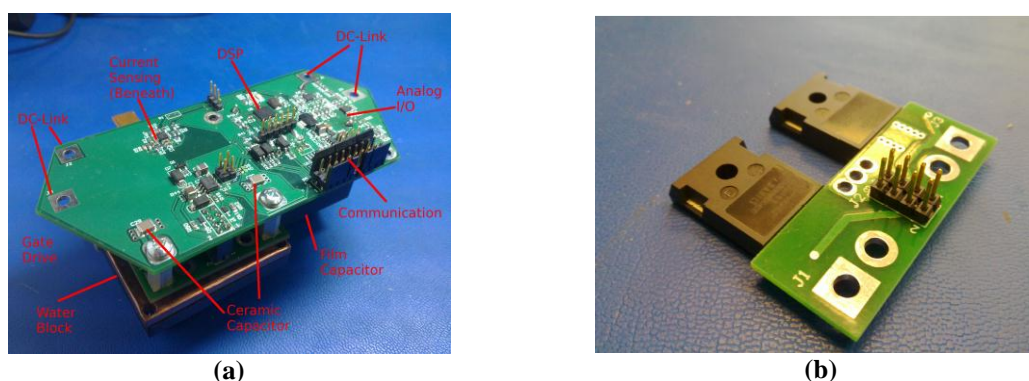
Fig. 6. Photos of new power converter hardware showing (a) complete phase module including film capacitor, IGBT subassembly, and water-cooled heat sink and (b) close-up view of IGBT subassembly.

Figure 7 shows the power circuit schematic for the demonstrator 10 kW IMMD. It shows that the six power converter phase modules are actually broken into two groups of three phases, with each group exciting a separate balanced wye-connected "star" set of stator windings. To improve the fault tolerance of the drive, the neutral points of the two star windings are not connected to each other [7].

A ring-and-star bus configuration with multiple layers of capacitance closely coupled to the switching nodes was adopted for the capacitors and dc bus structure for the IMMD. To this end, all IGBT half-bridges are decoupled directly at their power terminals by ceramic capacitors with large current-handling abilities and very low parasitics that help absorb switching transient energy in the megahertz range. Each module also has a 20 μF metalized film capacitor for bulk capacitance. Metalized film capacitors were chosen instead of electrolytics to increase the capacitor temperature limit to 125°C. These film capacitors provide

Fig. 7. Power circuit schematic for demonstrator 10 kW IMMD drive.

a total drive capacitance of 120 μF that is similar in value to several commercial drives with closely coupled high performance film capacitors. The power bus interconnections for the modules are provided by the bottom two layers of the main power converter board, which helps reduce power bus inductance and provides good decoupling for very high frequency noise.

Controller Configuration

Figure 8 shows the control architecture selected for implementing the IMMD's distributed control algorithm. Each phase is equipped with a dedicated digital signal processor that takes in analog measurements of current for its own phase as well as two adjacent phases. This information is then used to determine the complex current vector for the torque controller. Each phase controller is also provided the signals from a shaft encoder to determine rotor position. The neutral voltage for each phase is sensed and used to determine whether there are faults in any other phase winding of the star.

Fig. 8. Controller architecture for demonstrator 10 kW IMMD drive.

The drive commands, system status, and controller trim values are shared over a controller area network (CAN) bus between the phase modules and a user interface. Saturation of the CAN bus with critical control loop communications is avoided by using analog signals for sharing the current measurements.

The software architecture for each phase is modified from a standard field-oriented three phase drive for this distributed control algorithm. The control software uses the sensed currents and encoder position to regulate a complex current vector for each phase and assumes that the other phase controllers are doing the same. Fault tolerance is achieved externally to this loop as an error-checking function. Special attention is being devoted to designing the controller architecture to incorporate as many opportunities for enhancing the IMMD's fault tolerance as possible.

The dsPIC33 digital signal controller manufactured by Microchip was selected for implementing this control architecture. One of the attractive features of this processor is that it is available in a space-saving quad-flat, no-leads package and rated for operation at 140°C.

Si IGBT Ruggedness Evaluation at 200 ˚C

IGBTs are widely used in hard-switching applications where they are required to turn on or off rated current with full bus voltage across the terminals and also survive during malfunctions of systems such as short circuit conditions. To withstand the high stress conditions, these power devices are required to have robust safe operating areas. When temperature increases, the latch-up current is decreased because the current gains of the NPN and PNP transistors within an IGBT increase [8–9]. The static avalanche breakdown voltage increases with the temperature. However, the dynamic avalanche breakdown due to a current filament formation could deteriorate with high temperatures, which elevate the filament temperature before the self-heating [10–12]. In addition, the short circuit capability is also an important issue related to device ruggedness in high temperature operation, especially in practical motor drive applications [13–15].

To ensure the safe and reliable operation of the IGBT at 200°C, the high temperature IGBT ruggedness has to be verified by testing the safe operating area limits. The trench-gate field-stop IGBT with soft, fast recovery antiparallel diode from Infineon (IKW40N120H3) to be used in the IMMD power module was selected for ruggedness evaluation at high temperatures.
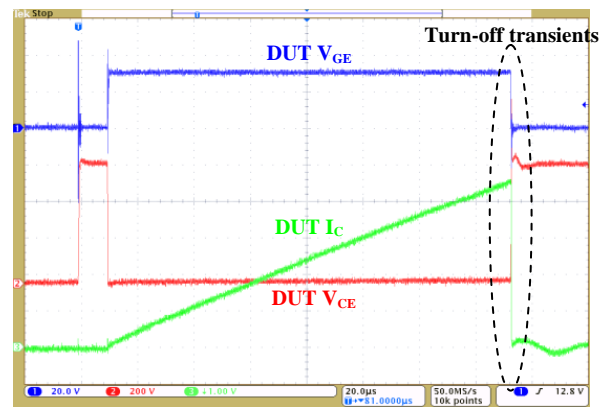
Latch-Up Immunity

"Latch-up" means the IGBT is tied to a state of continuous current conduction and gate voltage has no influence on output collector current. Today's commercial IGBTs have good latch-up immunity with latch-up suppressed designs. At high temperature operation, however, the latch-up current is decreased because the current gains of the NPN and PNP transistors increase.

Because of this, the following experiment was conducted to evaluate the latch-up immunity of the IGBT in extreme conditions. The gate voltage, V_{GE} was increased from 15 V to 30 V to prevent the IGBT from saturation at a low current level. The gate resistance was reduced from 12 Ω to 3 Ω to increase the turn-off speed. Also the ambient temperature was increased to 250°C. As shown in Fig. 9, the IGBT turned off the current of 300 A with a small gate resistance (3Ω) at 250°C. These experimental results demonstrated that the IGBT shows very good latch-up immunity even at very high temperatures.

Fig. 9. Latch-up immunity evaluation in extreme conditions: gate voltage, V_{GE} = 30 V; gate resistance, R_G = 3 Ω; and ambient temperature, T = 250 °C.

Short Circuit Capability

Short circuit capability is important especially for motor drive applications. When operating at high temperatures, the short circuit energy and short circuit withstand time are reduced due to the higher initial temperature. Therefore, for IGBT operation at the elevated temperature of 200°C, short circuit capability needed experimental evaluation.

Experiments were conducted to evaluate the short circuit capability of a trench-gate field stop IGBT operating at 200°C. Figure 10 shows the short circuit waveforms under hard switching fault condition at

25°C. In Fig. 10(a), the short circuit pulse is 32 μs. The device is turned off safely without destruction. In Fig. 10(b), the short circuit pulse is extended to 38 μs. The device looks as if it has safely turned off but destruction happens at 86 μs after the turn-off. A similar failure is reported in [13, 14]. At 200°C, the critical short circuit time is reduced to 22 μs.


(a) **(b)**
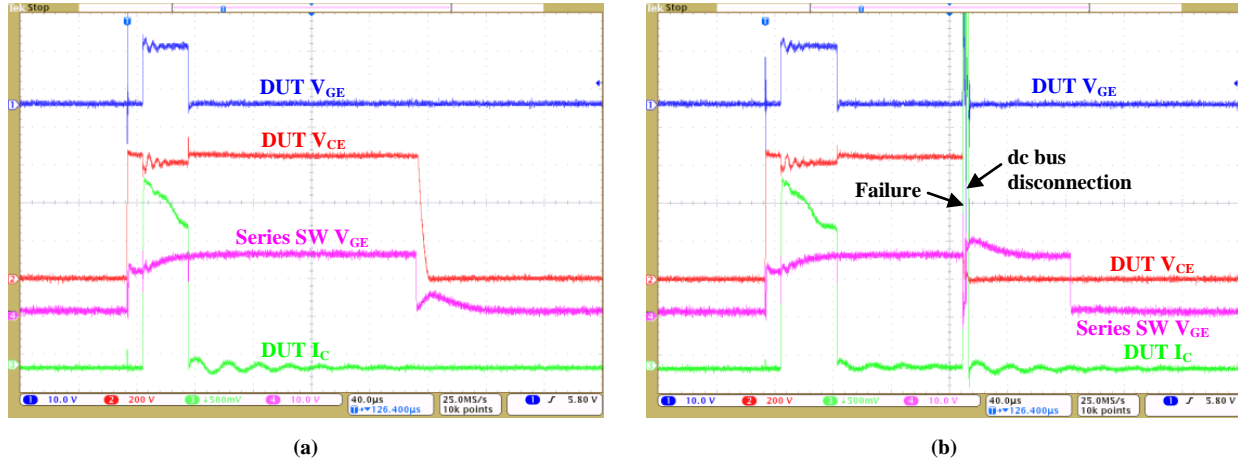
Fig. 10. Short circuit failure by thermal runaway at 25°C: (a) IGBT is turned off safely when short circuit pulse of 32 μs is applied at 25°C; (b) IGBT is destroyed at 86 μs after turn-off. The short circuit pulse of 38 μs is destroyed at 25°C.

Experimental results showed that the 1,200 V, 40 A field stop IGBT experiences short circuit failure by thermal runaway during the off state due to the high temperature leakage current caused by heat spreading after short circuit turn-off. The critical short circuit time is reduced to 22 μs when operating at 200°C compared with 32 μs at 25°C, but it is still adequate for protection.

Dynamic Avalanche Capability

During turn-off transients of IGBT, the high di/dt can cause the voltage to spike as a result of parasitic inductance. When the threshold electric field is reached with both voltage and current presented in the IGBT structure, the dynamic avalanche occurs [12].

A large stray inductance of 1.25 μH was used in the test circuit to evaluate the turn-off capability of the IGBT at various temperatures. Figure 11 shows the turn-off transients of the device under test (DUT) with various dc bus voltages. The dc bus voltage, V_{DC}, is increased from 600 V to 850 V in increments of 50 V while the current, I_C, is maintained at 40 A. In normal conditions, the voltage spike increases with higher dc bus voltage. In Fig. 11, however, it is observed that the voltage spike of V_{CE} is suppressed to 1,350 V when various dc bus voltages are applied, which means the dynamic avalanche occurs in the DUT. With V_{DC} increasing, the avalanche sustaining time increases to 70 ns until the DUT fails.
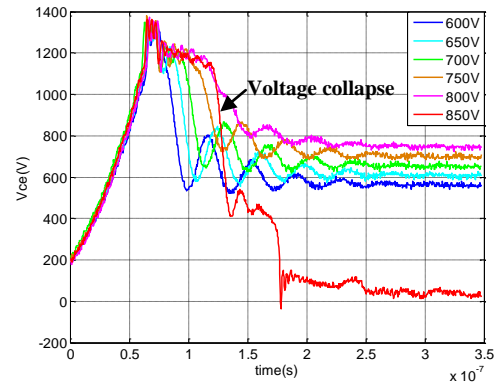
Fig. 11. V_{CE} voltage at turn-off with various V_{DC} applied when IGBT enters the dynamic avalanche mode at 25°C.

The avalanche capability of the DUT was further evaluated at 200°C where the avalanche sustaining time was reduced to 35 ns. These experimental results show that the 1,200 V IGBT under test has insufficient

avalanche capability and is very sensitive to overvoltage. It should not be operated exceeding the rated voltage in any cases from 25°C to 200°C.

Silicon IGBT Phase Leg Module for Operation at 200°C

This part of the report discusses suitable packaging and cooling for silicon IGBTs to achieve high temperature capability, high density, good thermal characteristics, and low cost.

IGBT Module Packaging Design

Wire-bonding technology was adopted for the design of the 10 kW phase leg power module. Two silicon IGBTs and two silicon diode dies from Infineon with maximum ratings of 1,200 V, 50 A, and 175°C were selected. A 10 mil aluminum wire with a maximum current rating of 22 A [16] was selected for wire bonding. Au80Sn20 solder was used for the die attachment, with optimized thickness of 200μm. Figure 12 shows the fabricated power module.
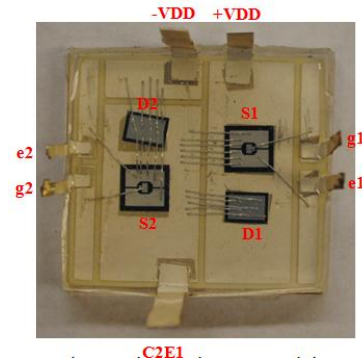
Fig. 12. Fabricated 10 kW power module.

IGBT Module Static Characterization

The static characterization of the fabricated power module was conducted with the curve tracer. Figure 13 shows the output characteristics of the IGBT at various temperatures. Figure 14 shows the leakage current at 650 V as a function of junction temperature. The leakage current is 3.98 mA at 200°C, which is smaller than that of the discrete device we characterized before (16.8 mA at 200°C).
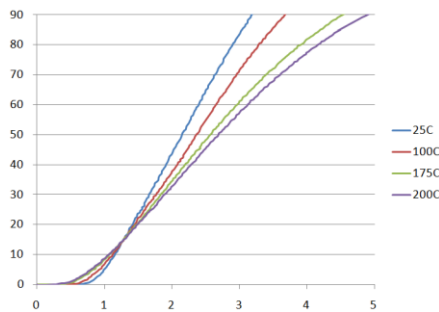
Fig. 13. Output characteristics of silicon IGBT module at various temperatures.
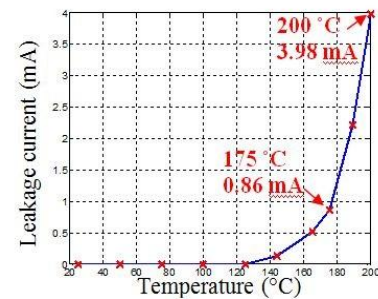
Fig. 14. Leakage current at 650 V as a function of junction temperature.

IGBT Module Switching Characterization

With the designed gate driver board and switching test board, the switching waveforms of the designed IGBT modules were tested and the switching losses estimated. Figure 15 shows the turn-on and turn-off waveforms at different temperatures, all at 650 Vdc and 70 A load current.

Figure 15 shows that the turn-on and turn-off time of the designed IGBT module increases with temperature, leading to higher switching loss for the IGBT module at higher temperatures. Furthermore, the reverse recovery of the diode is also worse at higher temperatures, also resulting in extra losses. The loss comparison is shown in Table 4.

(a)   **(b)**
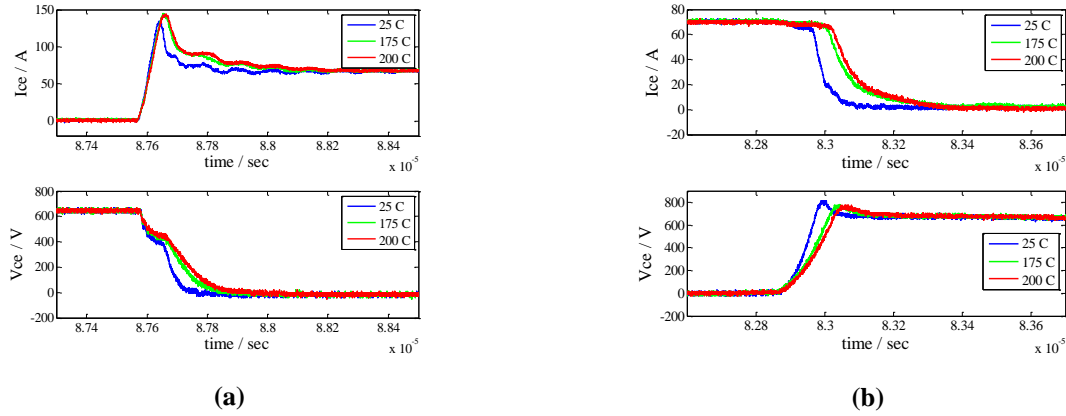
Fig. 15. Switching waveform comparison for designed IGBT phase leg module: (a) turn-on transients; (b) turn-off transients.

Table 4. Switching loss comparison (650 Vdc, 70 A case)

	Turn-on loss (mJ)	Turn-off loss (mJ)	Reverse recovery loss (mJ)
25°C	3.9	3.2	1.2
175°C	6.7	6.1	2.8
200°C	7.2	6.5	3.2

IGBT Module Loss Calculation

Based on the static characterization of the 10 kW power module, the losses were calculated with the switching frequency at 12 kHz and compared with those of a phase leg composed of discrete devices. As shown in Fig. 16, the fabricated module has smaller leakage current loss, but larger conduction loss and reverse recovery loss compared to the discrete devices phase leg. The total losses of the two are close. The total loss for the 10 kW phase leg composed of the discrete devices is 245.73 W, and the efficiency is 97.54%. The total loss for the power module is 248.33 W, and the efficiency is 97.52%.


(a)   **(b)**
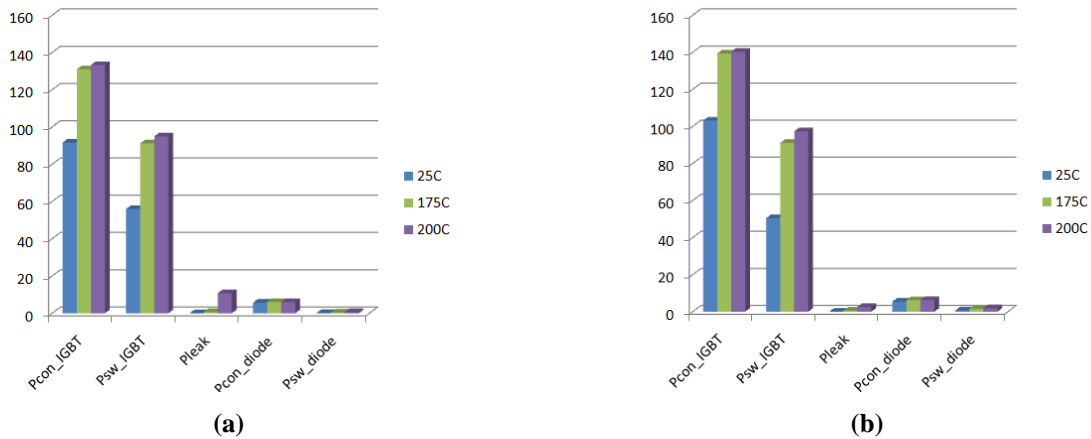
Fig. 16. Power losses in (a) a phase leg composed of discrete devices and (b) the fabricated phase leg power module (f_s=12 kHz).

IGBT Module Thermal Performance Evaluation

The thermal management system is one of the key challenges in the motor drive. In today's vehicles, the inverter and motor use different cooling loops and coolants. One objective of this project is to use a single liquid cooling loop and coolant for both the inverter and motor. A two-pass-tube cold plate from Aavid Thermalloy was used for the baseline design of the cooling system. A 105°C WEG coolant with a flow rate of 2.5 GPM is used to cool the module.

Comsol was used to characterize the thermal performance of the proposed package and cooling system. Figure 17 shows the cooling performance of the packaging design. The maximum IGBT junction temperature is 193.6°C. The thermal resistance is 0.738°C/W.
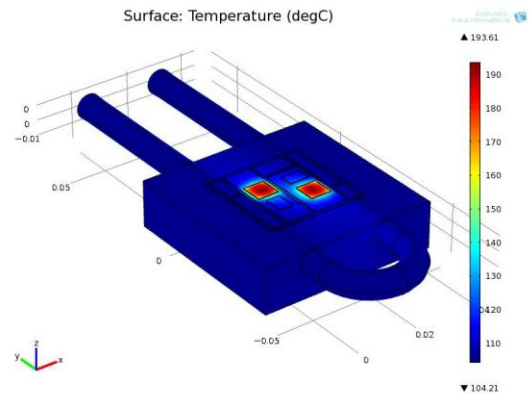
Experiments were also conducted to evaluate the thermal performance. In the experiments, the junction temperature was measured using the electrical parameters of the device. The forward voltage drop of the IGBT was used as the temperature-sensitive parameter. The losses were generated with a heating pulse. The thermal resistance measured was 1.417°C/W, significantly larger than the simulation results of 0.738°C/W. The increased thermal resistance is mainly caused by the attachment layer between the power module and the cold plate, which needs to be improved in future work.

Fig. 17. Cooling performance of the packaging design.

Design Approach for System-Level Electrical Architecture and Continuous Power Test

To test the designed IGBT phase leg module, gate-driver circuit, switching test (double-pulse-test) circuit, and main converter circuit are designed. To simplify the design and test, a flexible system-level electrical architecture that can accommodate both commercial IGBT modules and custom built modules was used. Figure 18 shows the gate driver board used for the custom IGBT modules.
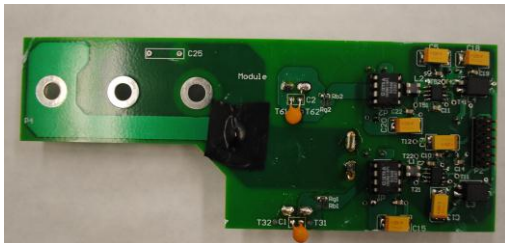
Fig. 18. Gate driver board for custom IGBT modules.

After the loss estimation and thermal design, a continuous power test for the custom IGBT phase leg module was conducted to verify the performance of the module in the converter. The test circuit, which is run as a buck converter, with the component parameters is shown in Fig. 19. With dc voltage of 650 V and duty cycle of 0.85, the converter runs with 10 kW output power and 12 kHz switching frequency. Liquid cooling is applied to the converter at a 2.5 GPM flow rate. Liquid at 25°C was used for preliminary evaluation due to the limitations of the fabricated module thermal performance.

Experimental results are shown in Fig. 20, with the V_{CE} and V_{GE} of bottom IGBT, load voltage, and inductor current. This test verified the 10 kW power conversion capability of the designed IGBT module.
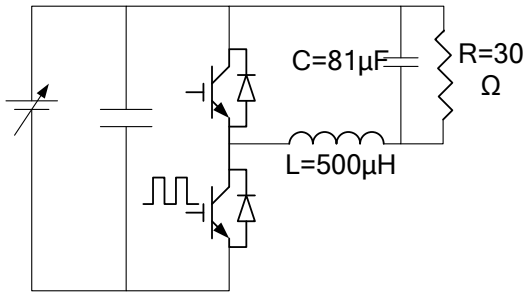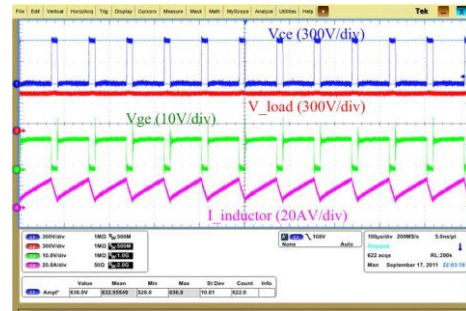
Fig. 19 Circuit for continuous test.

Fig. 20. Experimental results for 10 kW phase leg power module.

Conclusion

Significant progress has been made during FY 2011 toward demonstrating the key concepts associated with the integrated traction drive system. A 10 kW demonstrator version of the six phase, 10-pole SPM machine has been successfully fabricated and tested using a commercial three phase inverter for the initial tests. The matches between the predicted and measured machine parameters and torque production characteristics are very good, raising confidence in the machine modeling tools. A demonstrator version of the six phase modular power converter has also been developed for mounting immediately adjacent to the machine stator end windings. Each phase module includes a half-bridge IGBT power stage for exciting the associated phase winding and a dedicated controller chip and current sensor for controlling the phase excitation. The preferred heterarchical control architecture has been implemented to achieve the desired high levels of fault tolerance. According to this architecture, the loss of any one of the controllers does not affect the remaining five healthy controllers, providing the basis for achieving robust control of the integrated traction drive.

The silicon IGBT ruggedness operating at high temperatures was evaluated with a safe operating area test circuit, showing that the selected IGBT has good latch-up immunity and decreased but still adequate short circuit capability at 200°C. The IGBT has limited avalanche capability from 25°C to 200°C, so the rated voltage should not be exceeded in any cases. The 10 kW power module was designed and fabricated, and the electrical and thermal characteristics were tested. Compared to the discrete device tested in FY 2010, the module has smaller leakage current but large on-state voltage drop and reverse recovery current. The total losses of the two are very close. The thermal resistance of the fabricated power module is larger than the simulation results, caused by poor attachment between module and cold plate, which will be improved in future work. A continuous power test has been completed for the phase leg module. The module can work for 10 kW output power with 12 kHz switching frequency with the 25°C liquid cooling.

Patents

None.

Publications

G. Choi, Z. Xu, M. Li, S. Gupta, T. M. Jahns, F. Wang, N. A. Duffie, and L. Marlino, "Development of integrated modular motor drive for traction applications," *SAE International Journal of Engines*, vol. 4(1), pp. 286–300, June 2011.

Z. Xu, M. Li, F. Wang, and Z. Liang, "Investigation of Si IGBT operation at 200 ˚C for traction applications," in *IEEE Energy Conversion Congress and Expo (ECCE)*, 2011, pp. 2397–2404.

Z. Xu, and F. Wang, "Experimental investigation of Si IGBT short circuit capability at 200˚C," *IEEE APEC*, 2012, submitted.

Z. Xu, M. Li, P. Ning, F. Wang, and Z. Liang, "Si IGBT phase-leg module packaging and cooling design for operation at 200 ˚C in hybrid electrical vehicle applications," *IEEE APEC*, 2012, submitted.

References

1. G. Choi and T. M. Jahns, *Update on High Power Density Fractional Slot Concentrated Winding Modular PM Machine Design*, Integrated Modular Motor Drive Project Report, University of Wisconsin-Madison, April 2010.

2. A. M. EL-Refaie, *High Speed Operation of PM Machines,* PhD thesis, University of Wisconsin-Madison, 2005.

3. A. M. EL-Refaie and T. M. Jahns, "Comparison of synchronous PM machine types for wide constant-power speed range operation," in *Proc. IEEE IAS Annu. Meeting*, 2005, pp. 1015–1022.

4. J. K. Tangudu and T. M. Jahns, "Comparison of interior PM machines with concentrated and distributed stator windings for traction applications," in *Proc. of 2011 IEEE Vehicle Power and Propulsion Conference (VPPC'11),* 2011.

5. N. R. Brown, T. M. Jahns, and R. D. Lorenz, "Power converter design for an integrated modular motor drive," in *Rec. of 2007 IEEE Industry Applications Society Annual Meeting (IAS'07)*, 2007, pp. 1322–1328.

6. C. Buttay, D. Planson, B. Allard, D. Bergogne, P. Bevilacqua, C. Joubert, M. Lazar, C. Martin, H. Morel, D. Tournier, and C. Raynaud, "State of the art of high temperature power electronics," presented at *Microtherm 2009*, 2009, pp. 1–10.

7. B. A. Welchko, T. A. Lipo, T. M. Jahns, and S. E. Schultz, "Fault tolerance three-phase ac motor drive topologies: A comparison of features, cost, limitations," *IEEE Trans. Power Electron.*, vol. 19(4), pp. 1108–1116, July 2004.

8. A. Bhalla, S. Shekhawat, J. Gladish, J. Yedinak, and G. Dolny, "IGBT Behavior During Desat Detection and Short Circuit Fault Protection," in *Proc. IEEE ISPSD*, 1998, pp. 245–248.

9. A. Muller, F. Pfirsch, and D. Silber, "Trench IGBT Behaviour near to Latch-up Conditions," in *Proc. IEEE ISPSD*, 2005, pp. 255–258.

10. M. Trivedi and K. Shenai, "Failure Mechanisms of IGBTs under Short-Circuit and Clamped Inductive Switching Stress," *IEEE Trans. on Power Electronics*, vol. 14(1), pp. 108–116, January 1999.

11. K. H. Oh, Y. C. Kim, K. H. Lee, and C. M. Yun, "Investigation of Short-Circuit Failure Limited by Dynamic-Avalanche Capability in 600-V Punchthrough IGBTs," *IEEE Trans. on Device and Materials Reliability*, vol. 6(1), pp. 2–8, March 2006.

12. C. C. Shen, A. R. Hefner, D. W. Berning, and J. B. Bernstein, "Failure Dynamics of the IGBT during Turn-off for Unclamped Inductive Loading Conditions," *IEEE Trans. on Industry Applications*, vol. 36(2), pp. 614–624, March/April 2000.

13. M. Otsuki, Y. Onozawa, M. Kirisawa, H. Kanemaru, K. Yoshihara, and Y. Seki, "Investigation on the Short-Circuit Capability of 1200V Trench Gate Field-Stop IGBTs," in *Proc. IEEE ISPSD*, 2002, pp. 281–284.

14. A. Benmansour, S. Azzopardia, J. C. Martina, and E. Woirgarda, "Failure Mechanism of Trench IGBT under Short-circuit after Turn-off," *Microelectronics and Reliability*, vol. 46, no. 9-11, pp. 1778–1783, Sept.–Nov. 2006.

15. C. Abbate, G. Busatto, and F. Iannuzzo, "IGBT RBSOA non-destructive testing methods Analysis and discussion", *Microelectronics Reliability*, vol. 50, no. 9-11, pp. 1731-1737, Sept. –Nov. 2010.

16. W. W. Sheng and R. P. Colino, *Power Electronic Modules: Design and Manufacture*, CRC press, Boca Raton, 2005.

4.2.A Novel Packaging to Reduce Stray Inductance in Power Electronics

Principal Investigator: Leon M. Tolbert
Oak Ridge National Laboratory
National Transportation Research Center
2360 Cherahala Boulevard
Knoxville, TN 37932
Voice: 865-946-1332; Fax: 865-946-1262; E-mail: tolbertlm@ornl.gov

DOE Technology Development Manager: Susan A. Rogers
Voice: 202-586-8997; Fax: 202-586-1600; E-mail: Susan.Rogers@ee.doe.gov

ORNL Program Manager: Mitch Olszewski
Voice: 865-946-1350; Fax: 865-946-1262; E-mail: olszewskim@ornl.gov

---

Objectives

- Package devices in large power modules such that stray inductance is reduced.
- Reduce the stress on the insulated gate bipolar transistors (IGBTs) in hybrid electric vehicle (HEV) traction drives and dc-dc converters so that the IGBTs can work at higher power ratings and/or have better reliability and longer lifetimes.
- Reduce the distortion in output voltage.
- Improve reliability of converters.

Approach

- Layout design of phase leg module using P-cell and N-cell technique (i.e., series connection of IGBT and diode instead of antiparallel connection of IGBT and diode).
- Perform electromagnetic-field simulation of the package to extract the parasitics using Ansoft Q3D extractor.
- Perform circuit simulation for switching characterization with package parasitics.
- Use impedance analyzer to measure the parasitics in a prototype phase leg module.
- Use double pulse testing to experimentally test the switching behavior of the phase leg module.

Major Accomplishments

- Fabricated prototypes of the power modules.
- Obtained steady state characteristics for and measured the parasitics (stray inductance and resistance) of the modules.
- Built experimental setup for the double pulse test. Several methods were used to improve the accuracy of the measurement. The experimental results show 11 V lower overshoot voltage during IGBT turn-off in the proposed module than in the conventional module as a result of the reduction of the module stray inductance.
- Applied the novel switching cell concept in a multichip module (two chips in parallel for an individual switch position). The proposed layout and a conventional layout were designed in ANSYS Q3D Extractor.
- Studied switching characteristics under module inductance using Saber simulation.
- Fabricated modules for the multichip module, and measured the stray inductance in the modules experimentally.

Future Direction

- This project will not be funded by the DOE Vehicle Technologies Program beyond FY 2011.

Technical Discussion

In FY 2010, the module layout was designed and the parasitics were extracted using Q3D Extractor. Switching characterization was carried out using Saber simulation. The next step, which was the main work for FY 2011, was to fabricate the proposed module, measure the stray inductance, and build an experimental setup to verify the simulation.
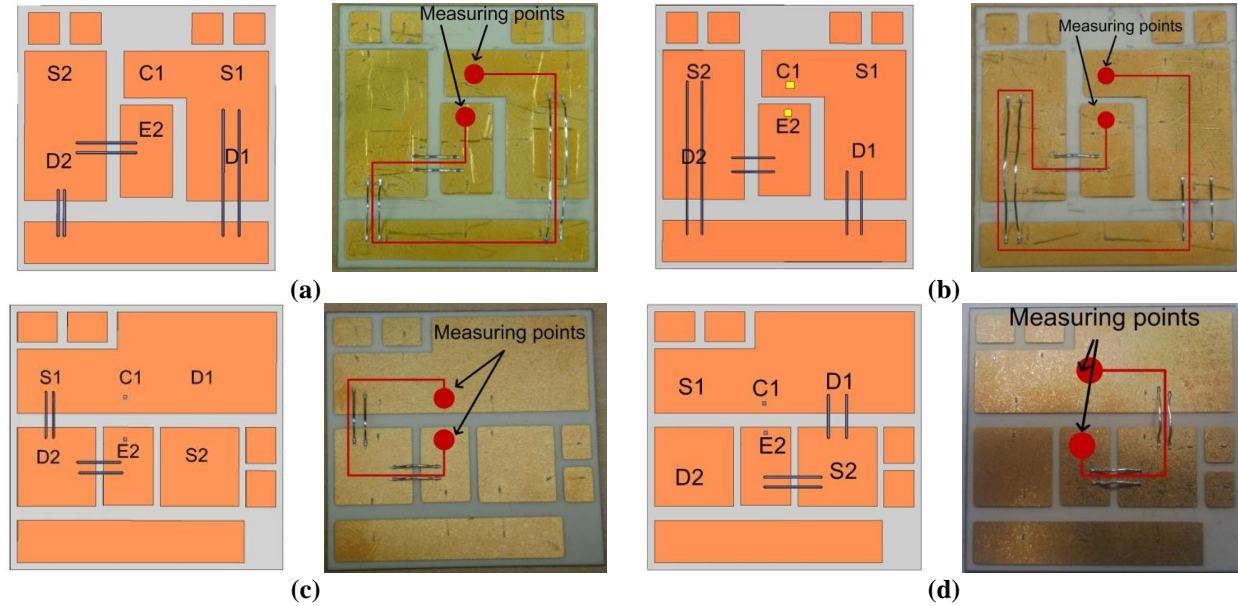
Parasitics Measurement

Because an IGBT is a normally off device, the commutation loop is not conducting by nature. Thus, the inductance should be measured part by part. However, because the inductance is so small (a few nanohenries), it is difficult to obtain an accurate measurement of the individual stray inductances. Also, it does not take the coupling effect between the pieces into account. In the Q3D simulation, the devices are set to copper to get a conductive commutation loop. Actually, this has the same effect as if the devices were set to conductor and the wires bonded directly to the direct bonded copper (DBC) substrate. Therefore, modules without devices were fabricated and the wires were bonded directly to the DBC. To measure the commutation loop formed by S1 and D2, the wires were bonded directly to the DBC where S1 and D2 seat, as shown in Fig. 1(a). The conducting trace actually is from terminal C1 through the DBC copper trace to S1 and through a group of bonding wires to the DBC, where the output terminal seats, and then through another set of wires to D2 and from D2 through another group of wires to the negative terminal E2.

Taking the same method, commutation Loop 2 in the conventional phase leg and commutation Loop 1 and Loop 2 in the proposed phase leg were fabricated as shown in Figs. 1(b), (c), and (d). Basically, they are the etched DBC patterns with wires which are bonded to the position of the devices that should conduct in the commutation loop. The commutation loops are made conductive this way and the stray inductance is measured.

Another concern is the measuring equipment. Because the inductance is very small, Agilent precision impedance analyzer 4294A was used. It has a wide measurement frequency range: from 40 Hz to 110 MHz. Meanwhile, using the correct probe fixture is also critical in this measurement. The commonly used alligator probe is not proper in this condition. The wires with the alligator probe introduce parasitics that are comparable to the one under test. Thus a pin probe was used; the shape of the probe is fixed. The parasitics with this probe is small and can be completely compensated using calibration.

Table 1 compares results of the measurement and simulation. The measurement value should compare with the ac simulation results because ac excitation is used in measurement.

Fig. 1. DBC pattern with bonding wires designed for parasitic measurement: (a) conventional module Loop 1, (b) conventional module Loop 2, (c) proposed module Loop 1, and (d) proposed module Loop 2.

**Table 1. Comparison of stray inductance measurement and simulation**

		Simulation results (nH)	Measurement results (nH)
Conventional module	Loop 1	20.5	25
	Loop 2	20.3	21
Proposed module	Loop 1	7.2	6.5
	Loop 2	8.6	6.0

Switching Characterization

Double Pulse Tester

Switching characterization can be conducted with only two pulses instead of a practical converter. The first pulse is used to charge the load inductor to the testing current, and then the device under test (DUT) is turned off. As a result, the turn-off characteristic can be captured. After a few microseconds the device is turned back on, and its turn-on characteristic is obtained. Figure 2 shows the double pulse tester (DPT) printed circuit board. A 450 V, 1,000 µF electrolytic capacitor is soldered at the back of the board. Three low inductance 300 nH film capacitors and twenty 100 nH ceramic capacitors together work as decoupling capacitors. A shunt resistor is used to measure current. The power module is attached at the back of the board. Also, the gate drive circuit is on the same board and close to the gate terminal of the power module. BNC (Bayonet-Neill-Concelman) connectors are used for accurate voltage measurement.

The DPT circuit parameters and testing condition are shown in Table 2. A large electrolytic capacitor is necessary as energy storage. Actually, a large part of the load current draws from this capacitor as there is usually a long cable connected from the dc voltage source and impedance is much higher. During switching transitions, the dc source and C_{bulk} will not be able to provide adequate energy quickly enough due to high values of equivalent series resistance (ESR) and equivalent series inductance (ESL), leading to large ringing of the voltage across the positive and negative buses. Decoupling capacitors with low ESR and ESL must be added to provide a low impedance path for the transient current 1. Film and ceramic capacitors, which have low ESR and ESL, were selected for this purpose. Paralleling of the decoupling capacitor is also useful, to reduce the ESR and ESL of the decoupling capacitors themselves.
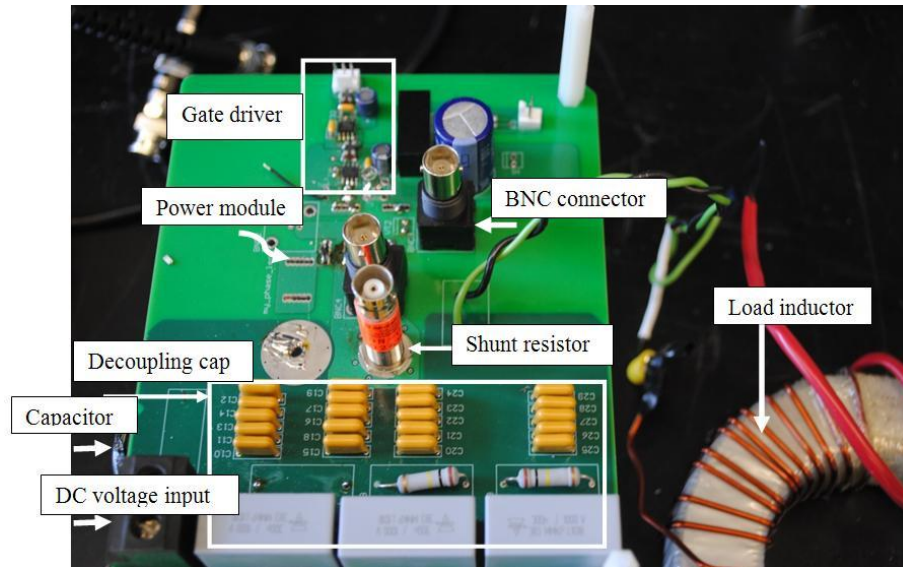
Fig. 2. Printed circuit board of DPT.

Table 2. Circuit Parameters

Parameters	Value/Rating
dc electrolytic capacitor C_{bulk}	1,000 µF, 450 V
dc decoupling capacitors C_{dec}	2.9 µF
Gate resistor	3 Ω
IGBT 5SMY 12J1280	1,200 V, 75 A
Diode 5SLY12F1200	1,200 V, 75 A
Load inductor	47 µH
dc link voltage	300 V
Testing current	75 A

The current measured here is IGBT current, I_C. During transition, the current slope is very sharp (from the datasheet of the ABB IGBT, the rise time is 50 ns while the fall time is 75 ns). This equals a frequency of $f = 0.5 / t_r = 5$ MHz 1. Typically a frequency margin of 5 times is maintained, so the current sensor should have a bandwidth of at least 25 MHz. A coaxial shunt resistor was selected as the current sensor. The connection to the oscilloscope was through a coaxial cable, which eliminates the probe connection. The voltage across the resistor has to be less than 10 V as there is no attenuation for the coaxial cable. This voltage was directly connected to the oscilloscope. In this experiment the testing current was 75 A; during reverse recovery, the current can be as high as 150 A. The resistance should be less than 0.06 Ω. A 0.025 Ω shunt resistor from T&M research was selected for this experiment. The bandwidth is 1,200 MHz, and the power rating is 3 mJ.

The input impedance of the voltage probe can be modeled as a capacitor of around 10 nF and a resistor of 10 MΩ in parallel. The ground lead of the voltage probe introduces stray inductance, which forms an LC resonant circuit with the input capacitor. If a step voltage is applied at the probe, high frequency resonance can occur. Then the detected voltage is not the step voltage itself but the resonance at the capacitor. This phenomenon is obvious when measuring high dv/dt. For accurate voltage measurement in this experiment, the grounding leads were removed and tip adaptors were used. When measuring gate voltage using P6139, a tip adaptor, Tek 131 5031 00, is used. The high voltage probe has a different tip to BNC adaptor, Tek 013 0291 01. Then a BNC jack is used on the printed circuit board. The use of a tip adaptor eliminates the grounding lead, which reduces the stray inductance in the probe.

IGBT Die Voltage Measurement

In the past, any voltage measurement was from the terminals of the module or device; however, that will not work in this case because it does not take the voltage drop of the module stray inductance into account, and one of the purposes of this project is to compare the difference of the voltage drop of the stray inductance for different layout techniques. Therefore, the voltage that should be measured here is the true stress on the IGBT die.

As part of this research, a new method was proposed to measure the die voltage. Two wires are attached to the collector and emitter side of the die. Then the wires are twisted and connected to the board, where the BNC connector and adapter are used to connect to the oscilloscope. As shown in Fig. 3(a), one wire is soldered to the DBC near the IGBT die under test to get the collector signal of point A. Because the top emitter pad cannot be soldered, the other wire is soldered to the auxiliary emitter for the gate signal, point B in Fig. 3(a). Attention should be paid here that there are two groups of bonding wires connected out from the emitter side of the die, power emitter, and auxiliary emitter. Because the gate drive current is very small, point B can represent the voltage of the IGBT emitter because the voltage drop associated with this small current through the bonding wires is negligible.

(a)   (b)
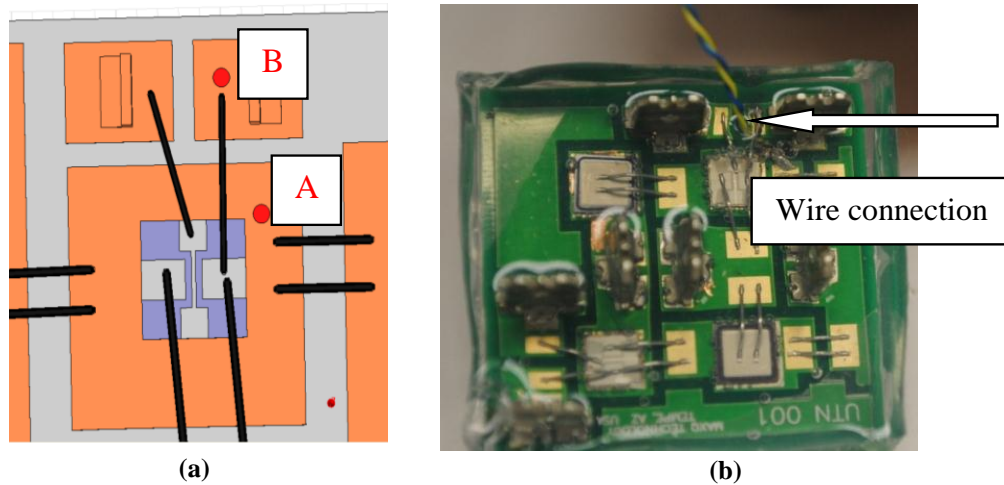
Fig. 3. Module with wire connection from IGBT die: (a) wire soldering schematic and (b) photo of finished module.

Using the method described above, the voltage was measured across the IGBT die. At the same time, voltage across the terminals was also measured, as shown in Fig. 4. Taking the measurement for the conventional module as an example, the voltage across the IGBT die is 392 V, while the voltage at the terminal is 376 V, which indicates that there is a 16 V voltage drop across the module stray inductance. It is the same for the proposed module measurement, but because the module stray inductance in the proposed module is reduced, the difference is only 10 V.

Experimental Results

The turn-off current and voltage waveforms for both the conventional and proposed modules are shown in Fig. 5. At the test condition of 300 V and 75 A, the overshoot voltage in the conventional module [Fig. 5(a)] was higher than that in the proposed module [Fig. 5(b)]. It is clear in these two figures that the overshoot voltage is 92 V and 81 V, respectively, for the conventional and the proposed modules.
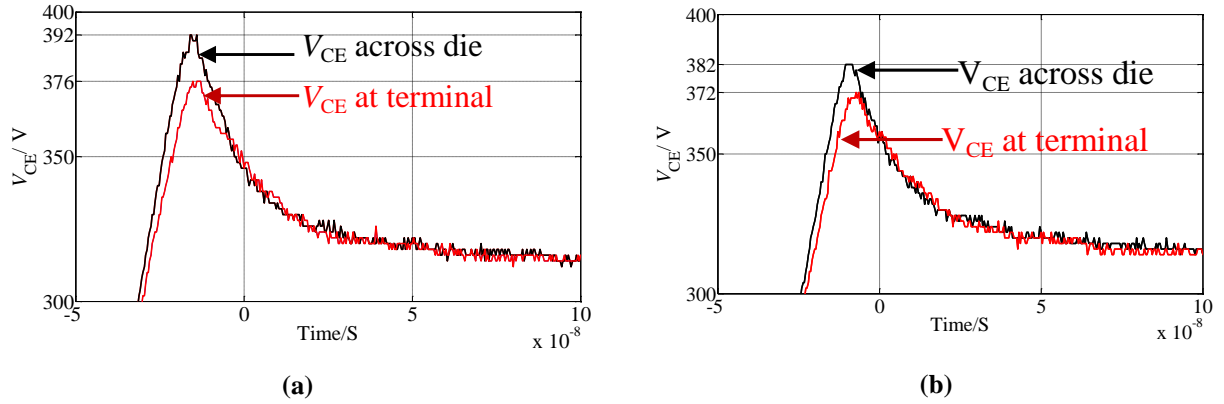
Fig. 4. Enlarged waveform of turn-off voltage of IGBT die at different measuring points: (a) conventional module and (b) proposed module.
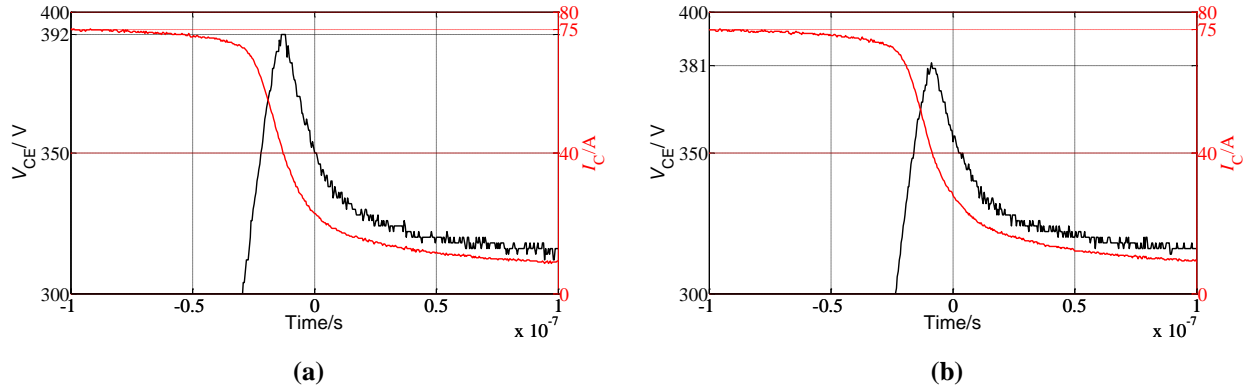
Fig. 5. Voltage overshoot during turn-off for (a) conventional module and (b) proposed module.

The turn-off current slope was also calculated (Fig. 6). The slope in the conventional module was 2,550 A/µs, while in the proposed module it was 2,650 A/µs. The reduction of stray inductance can accelerate the switching speed.

During turn-on, the space charge stored in the depletion region because of the large reverse-bias voltage is removed by the forward current. Then the excess-carrier distribution in the drift region grows. As the forward current grows in time, there is an increasingly large voltage drop across the drift region because there is no conductivity modulation of the region until the space charge layer is discharged to its thermal equilibrium value at around 40 V. This voltage is measured at the module terminals; therefore it also includes the voltage drop at the module stray inductance. It is difficult to separate the two parts.

The switching loss is calculated using the math function on the oscilloscope. To get an accurate measurement of the loss, synchronization of the voltage (channel one) and current signal (channel 2) is necessary. The propagation delay of the high voltage probe P5100, which is 14.9 ns, can be detected automatically by the scope. The propagation delay of the current channel was 7.4 ns. First, the voltage and current are multiplied using math function and saved to R1. Then the R1 signal is integrated as the red waveform (Fig. 7). The energy increase from cursor "a" to cursor "b" is the turn-off loss. In the conventional module it was 3.16 mJ, and in the proposed module it was 3.10 mJ.
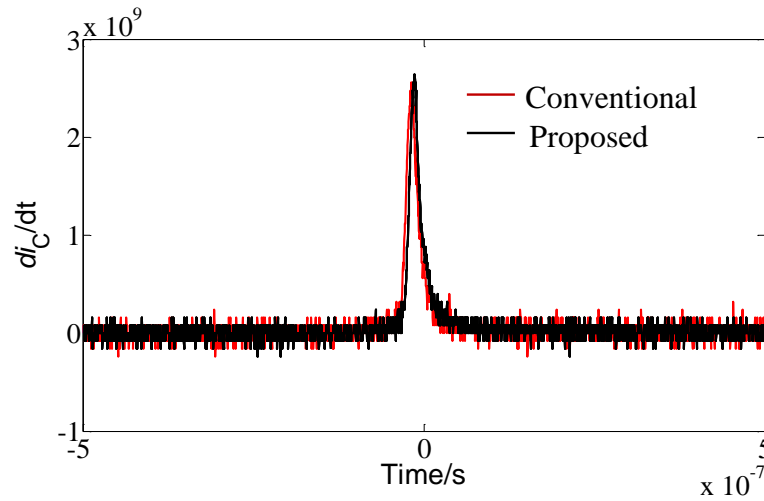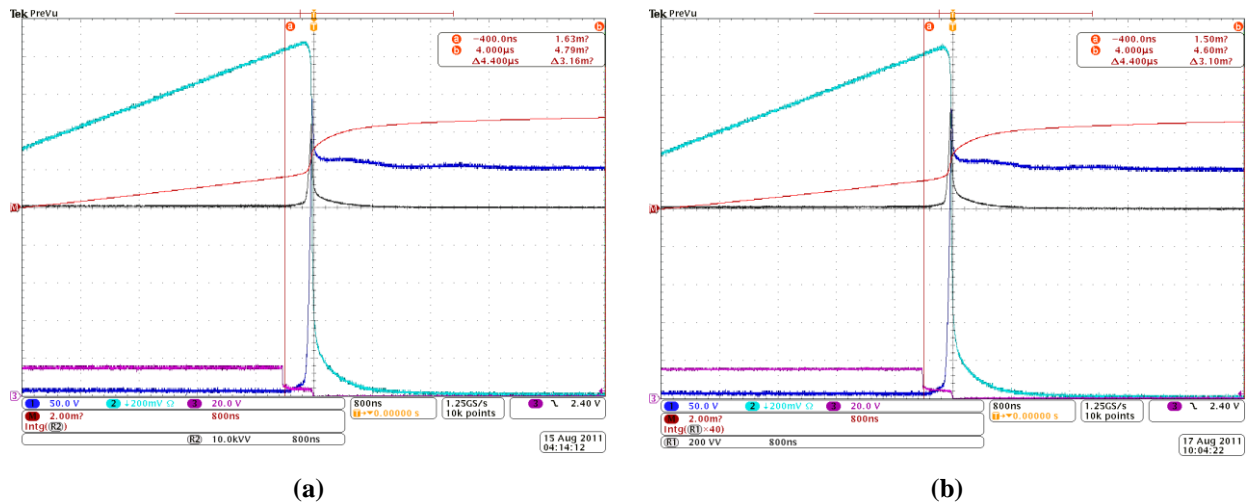
Fig. 6. Slope of the turn-off current.

| (a) | (b) |

**Fig. 7. Turn-off loss calculation for (a) conventional module and (b) proposed module.**

Using Novel Switching Cells in IGBT Module with Paralleled Chips

In mid or high power areas, such as HEVs, many IGBTs and diode chips are connected in parallel inside the module to increase the current capability. In the packaging of multichip IGBT modules, except reducing loop stray inductance, another concern is the mismatch of the parameters of the two paralleled loops. More uniform parasitics and dice characteristics in the module offer more even distribution of current and commutation voltage conditions between chips, which helps to keep the components inside the module at similar temperatures, enables better use of silicon, and minimizes potential early wear out failures due to degradation over module lifetime 2. Power modules with two devices in parallel were studied using a conventional layout designed according to a commercial module and a multichip module designed using the P-cell–N-cell concept. Parasitics were extracted for both modules, and Saber simulation was conducted for the electrical characteristics under different parasitics.

Layout Design of Multichip Power Modules

A commercial module from a hybrid electrical vehicle 3 was used for the conventional layout [Fig. 8(a)]. The antiparalleled IGBT and diode form the upper and lower cells. The upper cell is in one piece of the DBC, while the lower cell is in another.

The parasitic model of the commercial multichip power module is shown in Fig. 8(b). The parasitic model is based on the physical layout. The parasitic inductance was extracted piece by piece. The commutation loop inductance can be calculated by adding them together, which is 24 nH for one of the die and 25.4 nH for the second die. The mismatch of the inductance is 1.4 nH. The parasitic resistance was also extracted. Because the resistance doesn't affect transient behavior much but does affect the steady state current distribution, the resistance was extracted under the condition of dc excitation. The resistances of the paralleled upper branch are 1.0 mΩ and 1.1 mΩ for each of the two die; while in the two lower branches, they are 0.9 mΩ and 1.0 mΩ respectively.

(a)   (b)
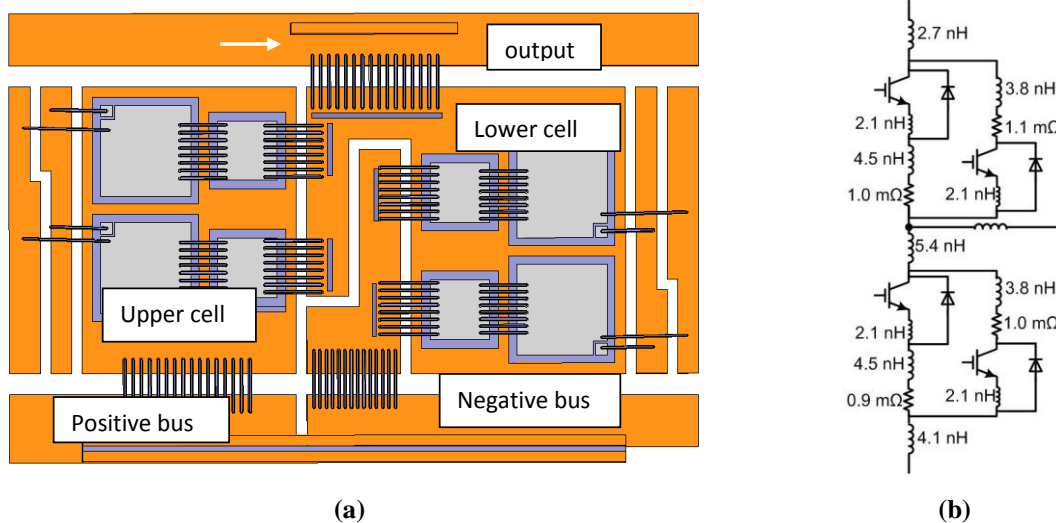
Fig. 8. Commercial IGBT module showing (a) layout with paralleled dice and (b) parasitics extraction.

Another layout using P-cell and N-cell was also designed [Fig. 9(a)]. In this design, the commutating IGBTs and diodes, identified as P-cell or N-cell, are arranged together. The parasitics was modeled differently from the conventional module, as shown in Fig. 9(b). In this arrangement, the stray inductance has been reduced to some extent. In P-cell the loop inductances were 14.2 nH and 24.3 nH, respectively, for the two die; in N-cell the loop inductances were 21.4 nH and 16.5 nH, respectively, for the two die. The dc resistance was also extracted and is reflected in the model. It is worthwhile to point out that the resistance is between the output and positive or negative bus. For example, if the IGBTs in P-cell are conducting, the paths are shown in Fig. 9 as the white and black lines. From the layout, it can be seen that the two conducting paths have similar lengths. Therefore, the resistance in the paralleled branches, about 1 mΩ, is similar.

Comparing the two layouts, it can be concluded that, in general, the proposed method has short commutation loops for some branches; however, the length of each paralleled loop is different, and this creates inductance mismatch. The mismatch can become serious as the paralleled branches increase. The conventional layout has similar loop length for each parallel loop, although the stray inductance value is at the level of the largest in the proposed layout. As for dc resistance, the two layouts have similar values and there is no mismatch either design. The effect during the transient activity is discussed in the next section.
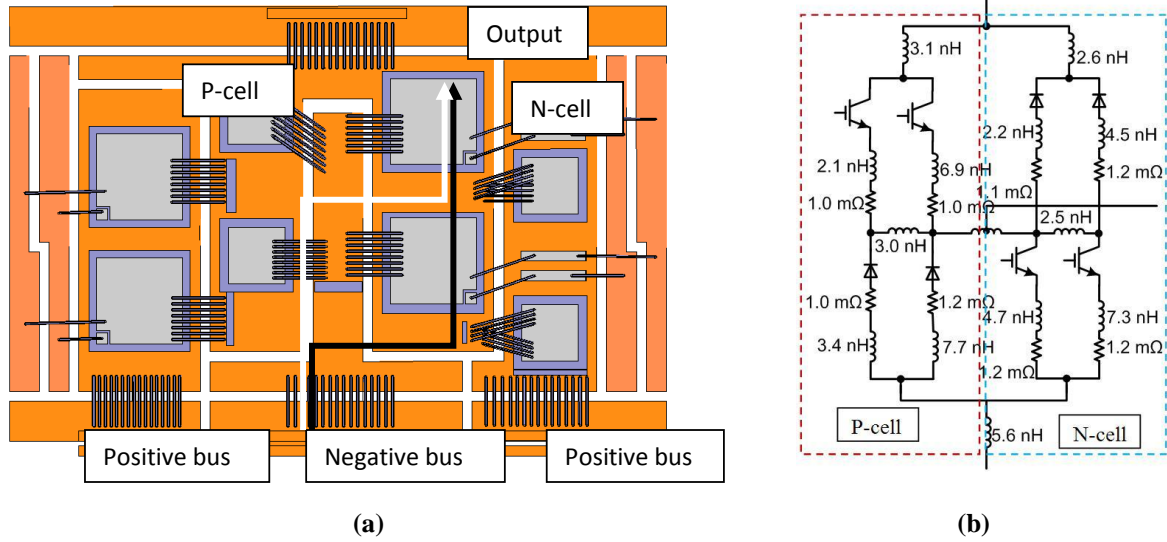
Fig. 9. Novel IGBT module: (a) layout showing switching cells and (b) parasitics extraction.

Electrical Evaluation of Switching Characteristics of Multichip Module

To study the switching behavior of the multichip modules under different parasitics, a DPT with detailed module parasitics was built in Synopsys Saber.

The transient voltages and currents on the IGBTs and diodes are shown in Figs. 10, 11, and 12. In each figure, there are four waveforms, which are the two paralleled devices in two layouts. The green and orange lines are from the conventional design, and the blue and purple lines are for the proposed layout. The turn-off voltages on the IGBTs are shown in Fig. 10. The overshoot voltage is higher in the conventional layout. The reason is that there is some common stray inductance between the upper and lower cells; the whole current 150 A flows through this path and the voltage drop is thus higher. In the proposed layout, the two paralleled paths and their parasitics are relatively separated. The turn-off voltage in the two paralleled devices in the proposed module is not the same, caused by the mismatch of the parasitic inductance of the two loops. Although it is not serious, it might cause loss mismatch in the long run. This compromises the benefit of the proposed layout.
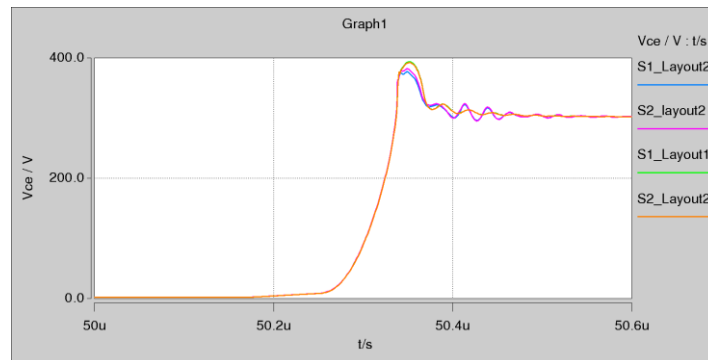

Fig. 10. Turn-off voltages of IGBTs.

Figure 11 shows the turn-on currents of the IGBTs. The currents peak because the reverse recovery is higher, and the oscillation after turn-on is more severe in the conventional module. However, as expected there is some mismatch for the transient current in the proposed module.
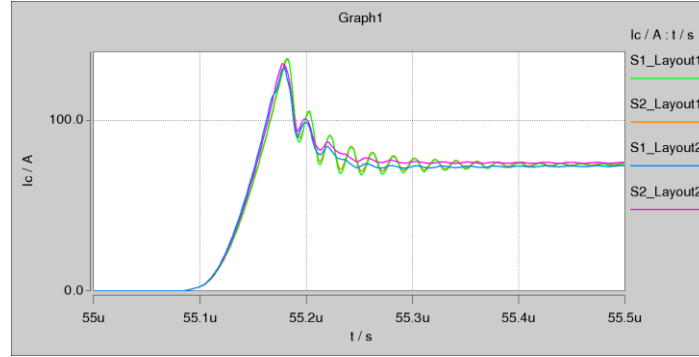
Fig. 11. Turn-on currents of IGBTs.

Figure 12 shows the turn-on currents of the diodes. It can be seen that the diode currents are significantly affected by the stray inductance. Therefore, the mismatch between the two devices in the proposed layout is around 25 A. Because the two paralleled loops in the conventional module are not identical, there is also some mismatch in this module.
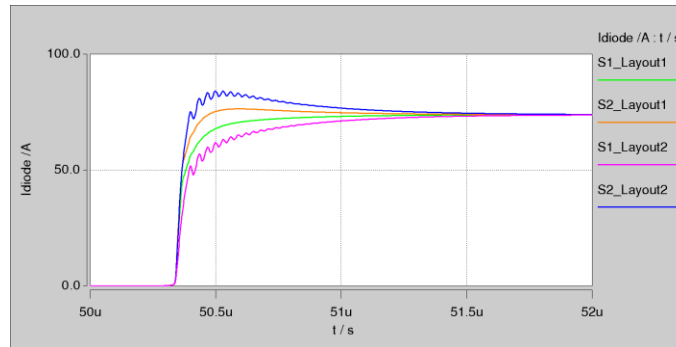
Fig. 12. Turn-on currents of diodes.

**Measurement of the Parasitics in the Multichip Modules**

Figure 13 shows different commutation loops in the conventional layout design. To ease the measurement, the bus bars have been removed and only the substrate inductance is taken into account. It should be mentioned that the identified loops are not exactly the current path. For example, in Fig. 13(a), the current which goes through IGBT A, does not exactly pass diode B. It would be more accurate to model the module inductance as shown in Fig. 13(b); however, it is not realistic to measure the stray inductance part to part in practice. Figures 13(a) and (b) show the two paralleled paths, Loop 1 and Loop 2, that are formed by devices A, B and C, D. Figures 13(c) and (d) show the other two paralleled loops, Loop 3 and Loop 4.

| (a) | (b) | (c) | (d) |
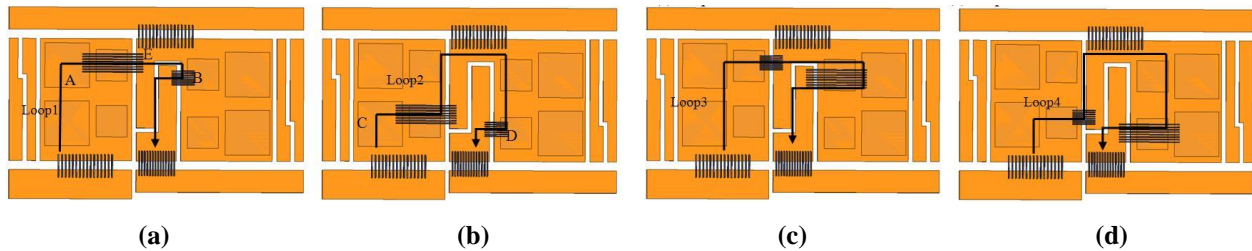
Fig. 13. Commutation loops in the conventional layout: (a) Loop 1, (b) Loop 2, (c) Loop 3, and (d) Loop 4.

Figure 14 shows the different loops in the proposed layout design. The four figures (a), (b), (c), and (d) represent the four commutation loops. It is obvious that in this design the two paralleled loops, for example Loop 1 in (a) and Loop 2 in (b), have different covered areas, and therefore the stray inductance for the two loops is different. It is the same thing for the two paralleled loops in N-cell, as shown in Figures 14(c) and 14(d).

| (a) | (b) | (c) | (d) |
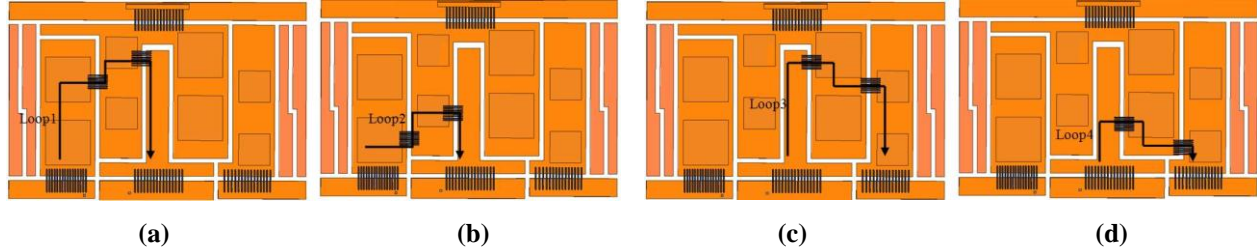
Fig. 14. Commutation loops in the proposed layout: (a) Loop 1, (b) Loop 2, (c) Loop 3, and (d) Loop 4.

For measurement, the two designed substrate patterns were etched and the wires bonded. Figure 15(a) shows Loop 1 of the conventional design, and Fig. 15(b) shows the longer loop, Loop 1, and the shorter loop, Loop 4, for the proposed design. Table 3 compares the results for the detailed simulation and measurement of inductance.

| (a) | (b) |

Fig. 15. Fabricated commutation loops for (a) the conventional design and (b) the proposed design.

Table 3. Comparison of the inductance value simulation and measurement results

	Conventional layout (nH)		Proposed layout (nH)	
	Simulation	**Measurement**	**Simulation**	**Measurement**
Loop 1	23.4	22.2	21.8	18.6
Loop 2	21.6	20.1	13.0	11.8
Loop 3	21.3	19.8	20.5	17.9
Loop 4	22.0	20.2	13.5	12.7

Conclusion

The project for FY 2011 mainly focused on measurement of the stray inductance inside the power module and the experimental work on characterizing the switching performance of the power module. The measurement results of the stray inductance agree with the simulation results; the commutation loop inductances in the proposed layout design are smaller than in the conventional layout. The experimental setup for a DPT was built. Several methods were used to improve the accuracy of the measurement. To measure the voltage drop on the stray inductance, two wires were attached as close as possible to the collector and emitter of the IGBT die. Voltage was measured both across the die and across the module

terminal. There is a difference of more than 10 V for the two measurements, which shows the effectiveness of this method. The experimental results show an 11 V lower overshoot voltage during IGBT turn-off in the proposed module than in the conventional module, which results from the reduction of the module stray inductance.

A novel switching cell concept was applied in a multichip (two parallel devices) module. The proposed layout and a conventional layout were designed in Q3D Extractor. Under this layout design, the dc buses are arranged at one side of the module; this causes the proposed layout to have a disadvantage of uneven loop inductance. Although the loop inductance can be reduced, the effect is not significant. The mismatch in the parasitics causes imbalance in the switching voltage and current of the paralleled branches. The current dice metallization is made in a certain pattern: the collector of the IGBT and the cathode of the diode are made of silver alloy for solder attachment; the emitter of the IGBT and the anode of the diode are made of aluminum alloy for wire bonding. This requires the two devices in P-cell and N-cell to be arranged on separate DBC substrates, which takes more substrate area. This shows that additional effort is needed to ensure the stray inductance is even for paralleled die in a module.

Patents

None.

Publications

S. Li, L. M. Tolbert, F. Wang, and F. Peng, "Reduction of Stray Inductance in Power Electronic Modules Using Basic Switching Cells," in *Proc. IEEE Energy Conversion Congress and Exposition,* 2010, pp. 2686–2691.

S. Li, L. M. Tolbert, F. Wang, and F. Peng, "P-cell and N-cell based IGBT module: Layout design, parasitic extraction, and experimental verification," in *Proc. IEEE Applied Power Electronics Conference and Exposition,* 2011, pp. 372–378.

References

1. J. Witcher, *Methodology for Switching Characterization of Power Devices and Modules,* M.S. thesis, Dept. Electrical Eng., Virginia Polytechnic Institute and State University, Blacksburg, Virginia, 2002.

2. L. Schnur, G. Debled, S. Dewar, and J. Marous, "Low Inductance, Explosion Robust IGBT Modules in High Power Inverter Applications," in *Proc. IEEE Industry Applications Conference*, 1998, pp. 1056–1060.

3. T. A. Burress, R. H. Staunton, and C. L. Coomer, *Evaluation of the 2007 TOYOTA Camry Hybrid Synergy Drive System,* ORNL/TM-2007/190, 2007.

4.3   Integration of Novel Flux Coupling Motor and Current Source Inverter

Principal Investigator: John Hsu
Oak Ridge National Laboratory
National Transportation Research Center
2360 Cherahala Boulevard
Knoxville, TN 37932
Voice: 865-946-1325; Fax: 865-946-1262; E-mail: hsujs@ornl.gov

DOE Technology Development Manager: Susan A. Rogers
Voice: 202-586-8997; Fax: 202-586-1600; E-mail: Susan.Rogers@ee.doe.gov

ORNL Program Manager: Mitch Olszewski
Voice: 865-946-1350; Fax: 865-946-1262; E-mail: olszewskim@ornl.gov

---

Objectives

- Produce an integrated motor and inverter assembly that marries two ORNL technologies, the novel flux coupling motor (NFC-motor) and the current source inverter (CSI), to eliminate the inductor in the CSI topology.

Approach

- Design an excitation core that can take high frequency.
- Fabricate prototype core and coil for test.
- Test the prototype core with inverter.
- Find out the pros and cons from test.
- Repeat the loop for improvement until the goal is reach.

Major Accomplishments

- Validated the concept of the integration of the NFC-motor and the CSI through laboratory tests.
- Determined through test that the efficiency needs to be improved.

Future Direction

- Identify the source of the losses associated with the winding and the soft-iron-wire core of the NFC-motor.
- Simulate potential improvements.
- Fabricate and test the improvements for the integration.
- Repeat the loop for improvement until the goal is reached.

Technical Discussion

The CSI [1–7] circuit diagram is shown in Fig. 1. It does not have the huge dc link capacitor bank of the voltage source inverter but has an additional inductor, L_{dc}. A CSI prototype is shown in Fig. 2.

Figure 3 shows the prototype NFC-motor. It contains two stationary excitation cores that produce dc excitation flux to the rotor.
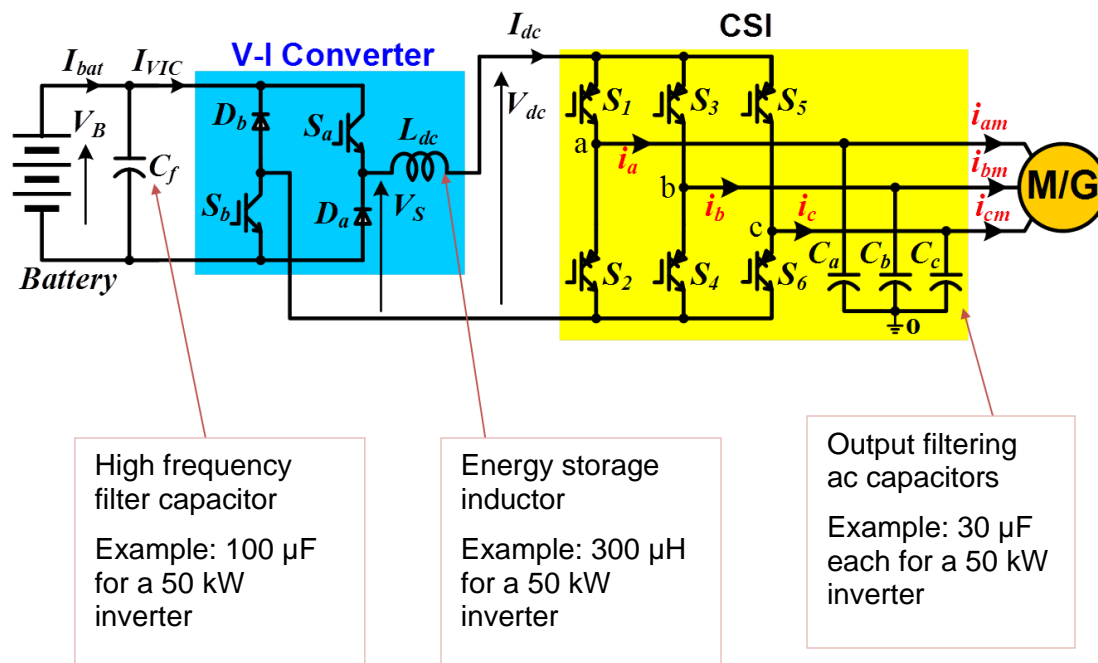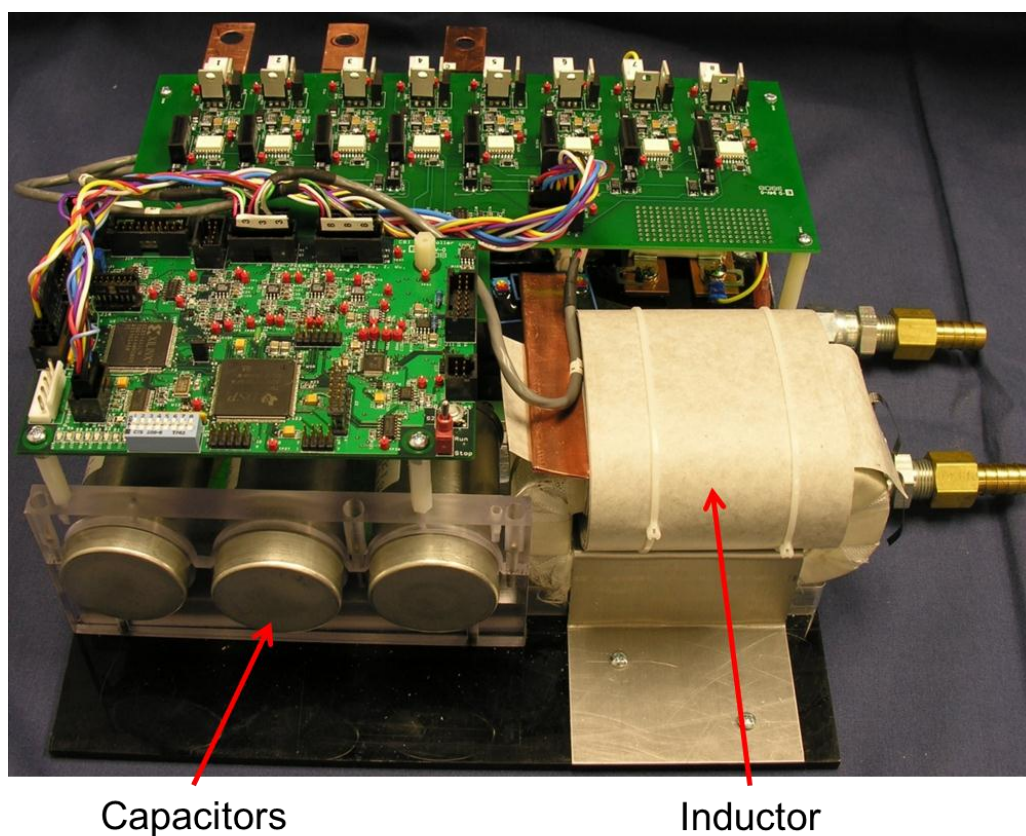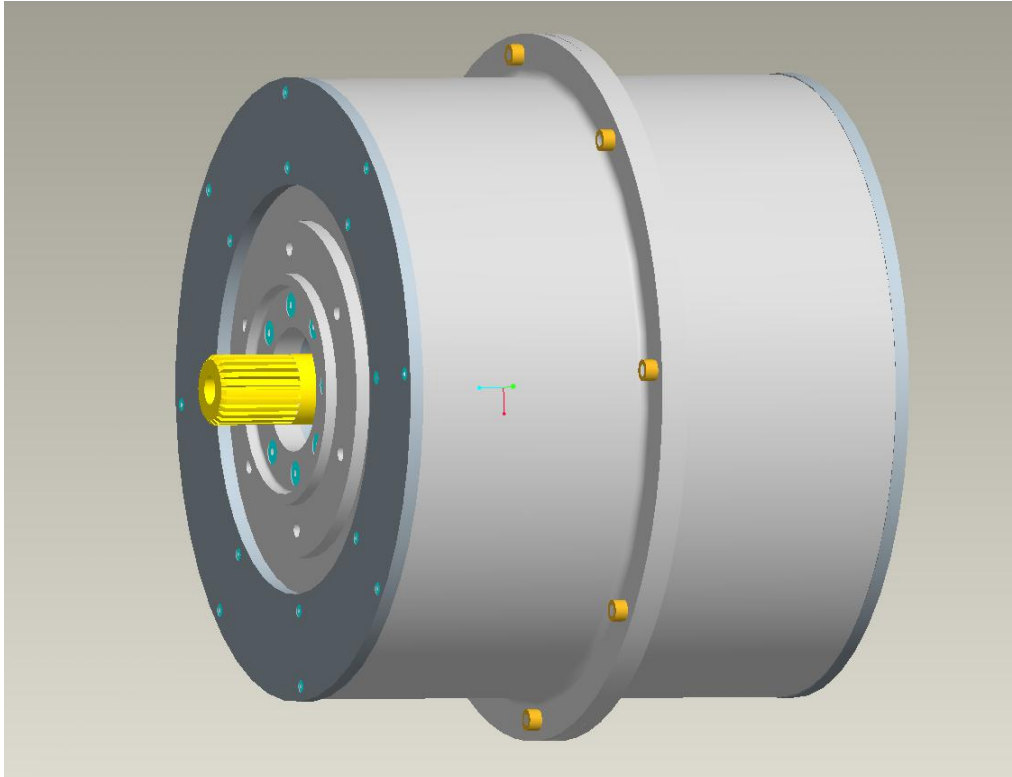
Fig. 1. CSI circuit diagram.

Fig. 2. CSI prototype.

Fig. 3. Prototype NFC-motor.

Figure 4 shows the experimental setup used to determine the feasibility of using the excitation coils of the motor to eliminate the CSI inductor. It includes an excitation core that is made of thin, soft iron wires coated with thin surface insulation. The reason to use the thin, soft iron wires for the excitation core is to reduce the core loss associated with the high frequency current component in the inductor.

Figures 5 and 6 show the results for the tests with the old inductor of the CSI prototype and with the NFC-motor excitation coil functioning as the inductor. The test traces of the input current (100 A/div), two output voltages (500 V/div), two output currents (50 A/div), and input voltage (500 V/div) for the two cases show very little difference. This validates the concept of integration of the NFC machine and the CSI.

Figure 7 shows the power electronic system (excluding load) efficiency curves with different dc bus inductors (measured with a PZ4000 power meter) versus the modulation index. The V_{dc2} and V_{dc} used for the modulation index are shown in Fig. 8. Three efficiency curves are shown, corresponding to the following scenarios: (1) the old inductor of the CSI used, (2) the old inductor of the CSI replaced by the new wound core of the NFC-motor, and (3) an additional short-circuit coil ("SC ring" in the figure) placed on top of the new wound core. The efficiency curves indicate that the efficiencies for either of the two NFC-CSI integration scenarios described [(2) or (3) above] are low and need to be increased before this concept would be acceptable for commercial products.

Fig. 4. Experimental setup for integration of NFC-motor and CSI.
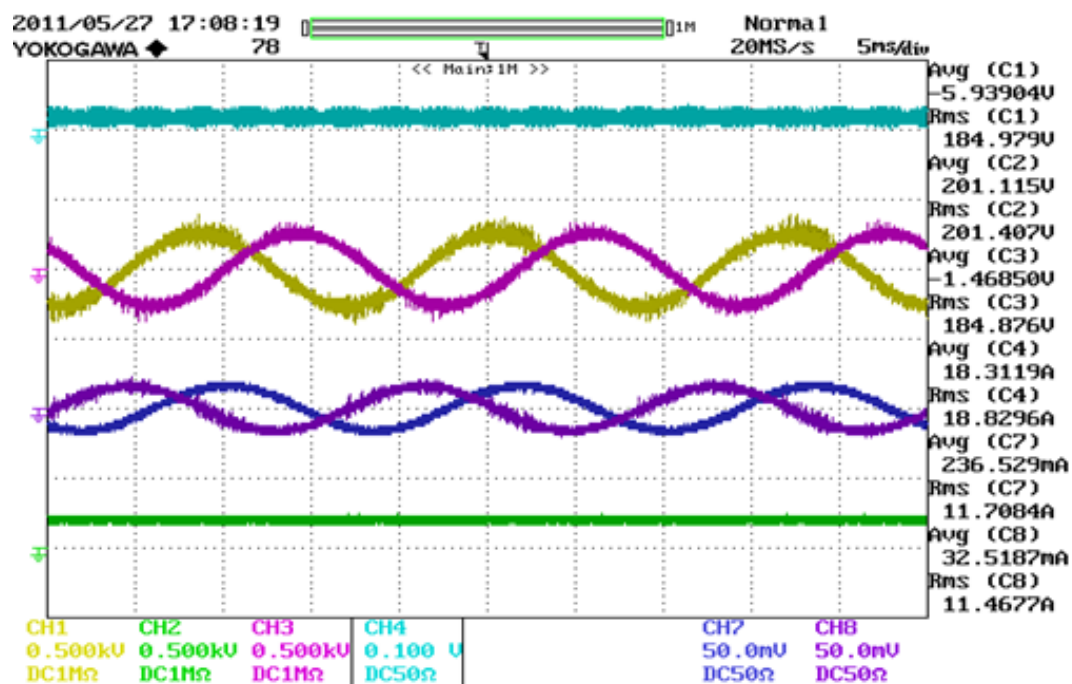

Fig. 5. Test of old inductor under the following conditions: input current (100 A/div), two output voltages (500 V/div), two output currents (50 A/div), and input voltage (500 V/div).
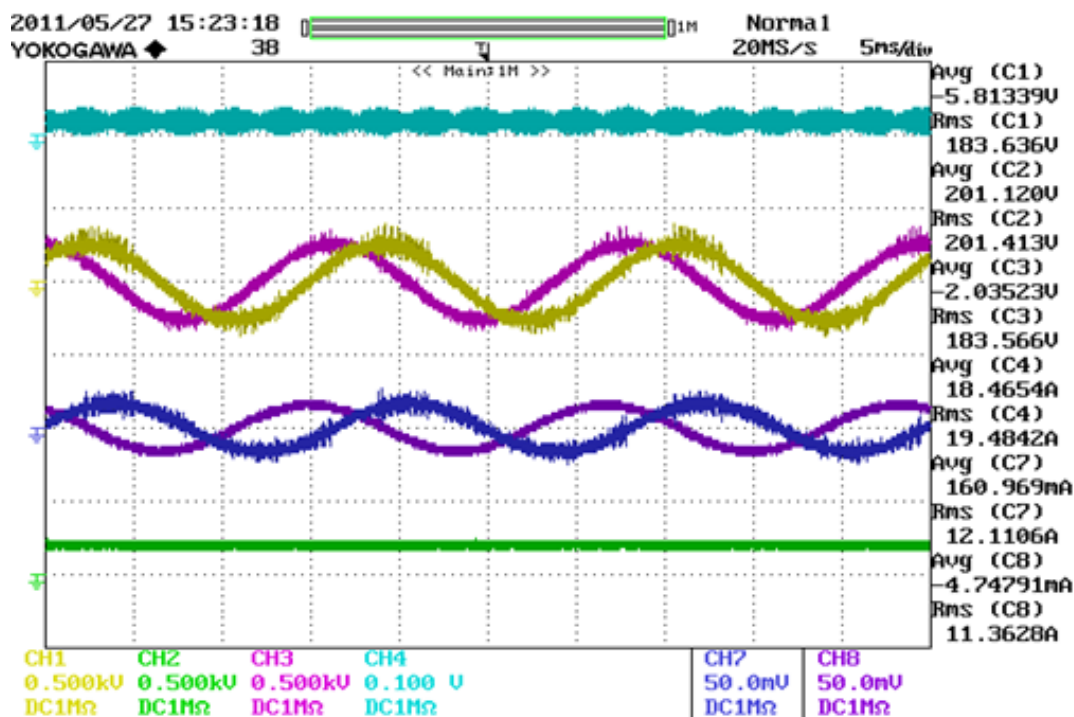
Fig. 6. Test of NFC-motor excitation inductor under the following conditions: input current (100 A/div), two output voltages (500 V/div), two output currents (50 A/div), and input voltage (500 V/div).
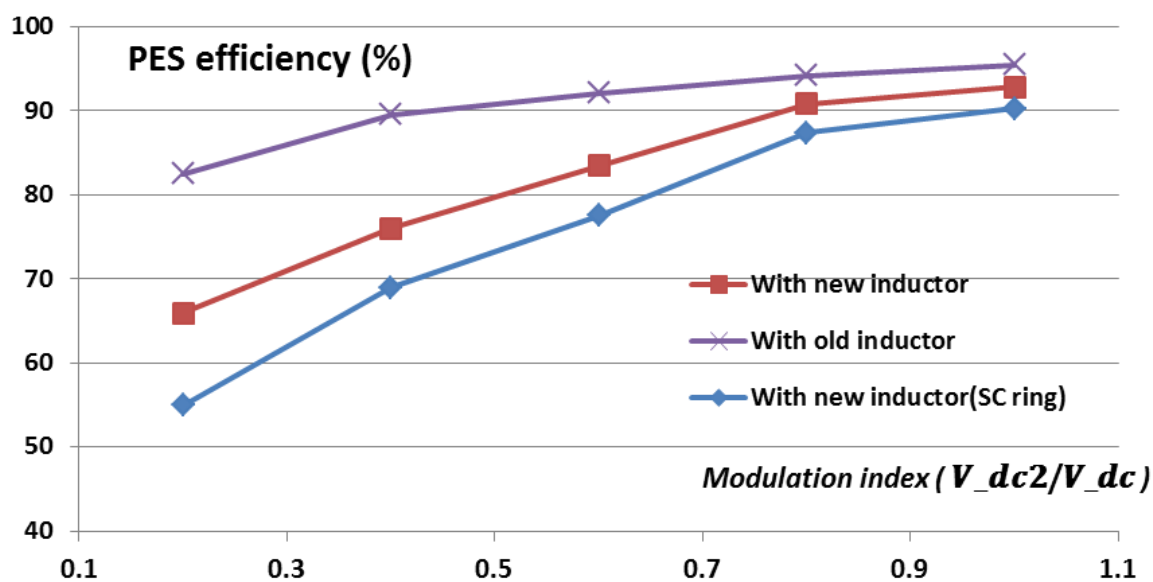

Fig. 7. Power electronic system (PES) efficiency (excluding load) with different dc bus inductors (measured with a PZ4000 power meter).
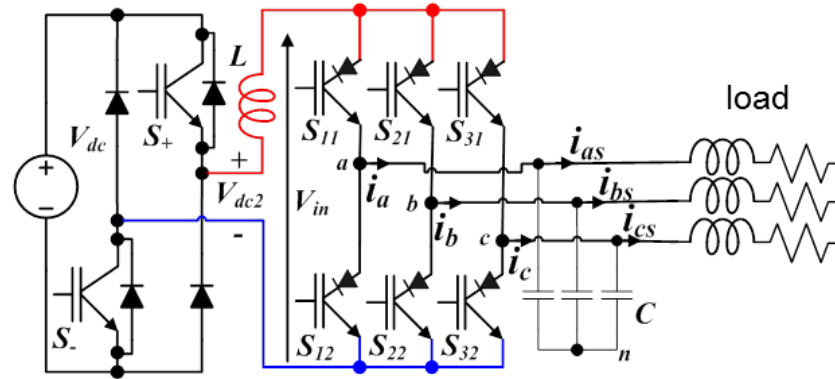
Fig. 8. Locations of *Vdc2* and *Vdc*.

Conclusion

The concept of integration of the NFC machine and the CSI has been validated through test.

Low efficiency numbers indicate further work is needed for acceptable performance.

Patents

None.

Publications

Internal and DOE review meeting publications only.

References

1. A. E. Fitzgerald, Charles Kingsley, Jr., and Stephen D. Umans, *Electric Machinery,* McGraw-Hill Book Company, Fourth Edition, 1983.

2. T. A. Burress, C. L. Coomer, S. L. Campbell, L. E. Seiber, L. D. Marlino, R. H. Staunton, and J. P. Cunningham, *Evaluation of the 2007 Toyota Camry Hybrid Synergy Drive System,* ORNL/TM-2007/190, Revised: April 2008, Publication Date: January 2008.

3. T. A. Burress, C. L. Coomer, S. L. Campbell, A. A. Wereszczak, J. P. Cunningham, L. D. Marlino, L. E. Seiber, and H. T. Lin, *Evaluation of the 2008 LEXUS LS Hybrid Synergy Drive System,* ORNL/TM-2008/185, January 2009.

4. Gui-Jia Su, L. Tang, and Z. Wu, "Extended Constant-Torque and Constant-Power Speed Range Control of Permanent Magnet Machine Using a Current Source Inverter," in *Proceedings of the 2009 Vehicle Power and Propulsion Conference* (VPPC 2009), Dearborn Michigan, September 7–11, 2009 pp. 109–115.

5. L. Tang and Gui-Jia Su, "Boost Mode Test of a Current-Source-Inverter-Fed Permanent Magnet Synchronous Motor Drive for Automotive Applications," in *Proceedings of the Twelfth IEEE Workshop on Control and Modeling for Power Electronics* (COMPEL 2010), Boulder, Colorado, June 2010.

6. L. Tang and Gui-Jia Su, "Novel Current Angle Control of a Current Source Inverter Fed Permanent Magnet Synchronous Motor Drive for Automotive Applications," in *Proceedings of the 2011 Energy Conversion Congress Expo* (ECCE2011), Phoenix, Arizona, September 2011.

7. Gui-Jia Su and L. Tang, "Current Source Inverter Based Traction Drive for EV Battery Charging Applications," in *Proceedings of the 2011 Vehicle Power and Propulsion Conference* (VPPC 2011), Chicago, Illinois, September 2011.

DISTRIBUTION

Internal

1. K. P. Gambrell
2. J. B. Green, Jr.
3. L. D. Marlino
4. M. Olszewski

5. B. Ozpineci
6. Laboratory Records
   Authors
   Coauthors

External

7. R. Al-Attar, DCX, raa9@chrysler.com.

8. S. J. Boyd, U.S. Department of Energy, EE-2G/Forrestal Building, 1000 Independence Avenue, S.W., Washington, D.C. 20585.

9. J. Cox, Chrysler, LLC, john.cox@chrysler.com.

10. J. Czubay, General Motors Corporation, GM Powertrain Headquarters, Mail Code: 483-710-270, 895 Joslyn Avenue, Pontiac, Michigan 48340.

11. H. Dadkhah, Chrysler, LLC, CIMS 526-00-00, 1960 Technology Drive, Building D, Troy, Michigan 48083.

12. P. B. Davis, U.S. Department of Energy, EE-2G/Forrestal Building, 1000 Independence Avenue, S.W., Washington, D.C. 20585.

13. R. R. Fessler, BIZTEK Consulting, Inc., 820 Roslyn Place, Evanston, Illinois 60201-1724.

14. S. Gopalakrishnan, General Motors Corporation, RMB-356, Mail Code 480-106-390, 30500 Mound Road, Warren, Michigan 48090.

15. G. Hagey, 501 Randolph St., Williamsburg, Virginia 23185.

16. E. Jih, Ford Motor Company, Scientific Research Laboratory, 2101 Village Road, MD-1170, Rm. 2331, Dearborn, Michigan 48121.

17. F. Leonardi, Ford Motor Company, 15050 Commerce Drive, North, Dearborn, Michigan 48120-1261.

18. F. Liang, Ford Motor Company, Scientific Research Laboratory, 2101 Village Road, MD1170, Rm. 2331/SRL, Dearborn, Michigan 48121.

19. M. W. Lloyd, Energetics, Inc., 7164 Columbia Gateway Drive, Columbia, Maryland 21046.

20. F. P. McCluskey, National Renewable Energy Laboratory, 1617 Cole Boulevard, Golden, Colorado 80401.

21. M. Mehall, Ford Motor Company, Scientific Research Laboratory, 2101 Village Road, MD-2247, Rm. 3317, Dearborn, Michigan 48124-2053.

22. N. Olds, United States Council for Automotive Research (USCAR), nolds@uscar.org.

23. S. A. Rogers, U.S. Department of Energy, EE-2G/Forrestal Building, 1000 Independence Avenue, S.W., Washington, D.C. 20585.

24. G. S. Smith, General Motors Advanced Technology Center, 3050 Lomita Boulevard, Torrance, California 90505.